

## REPORT DOCUMENTATION PAGE

Form Approved  
OMB No. 0704-0188

Public reporting burden for this collection of information is estimated to average 1 hour per response, including the time for reviewing instructions, searching existing data sources, gathering and maintaining the data needed, and completing and reviewing the collection of information. Send comments regarding this burden estimate or any other aspect of this collection of information, including suggestions for reducing this burden, to Washington Headquarters Services, Directorate for Information Operations and Reports, 1215 Jefferson Davis Highway, Suite 1204, Arlington, VA 22202-4302, and to the Office of Management and Budget, Paperwork Reduction Project (0704-0188), Washington, DC 20503.

1. AGENCY USE ONLY (Leave blank)	2. REPORT DATE	3. REPORT TYPE AND DATES COVERED DISSERTATION	
4. TITLE AND SUBTITLE "SPATIALLY RESOLVED SUB-DOPPLER OVERTONE GAIN MEASUREMENTS IN A SMALL SCALE SUPERSONIC HF LASER		5. FUNDING NUMBERS	
6. AUTHOR(S) MAJ WISNIEWSKI CHARLES F			
7. PERFORMING ORGANIZATION NAME(S) AND ADDRESS(ES) UNIVERSITY OF NEW MEXICO		8. PERFORMING ORGANIZATION REPORT NUMBER CI02-1285	
9. SPONSORING/MONITORING AGENCY NAME(S) AND ADDRESS(ES) THE DEPARTMENT OF THE AIR FORCE AFIT/CIA, BLDG 125 2950 P STREET WPAFB OH 45433		10. SPONSORING/MONITORING AGENCY REPORT NUMBER	
11. SUPPLEMENTARY NOTES			
12a. DISTRIBUTION AVAILABILITY STATEMENT Unlimited distribution In Accordance With AFI 35-205/AFIT Sup		12b. DISTRIBUTION CODE <b>DISTRIBUTION STATEMENT A</b> Approved for Public Release Distribution Unlimited	
13. ABSTRACT (Maximum 200 words)			
14. SUBJECT TERMS			15. NUMBER OF PAGES 255
			16. PRICE CODE
17. SECURITY CLASSIFICATION OF REPORT	18. SECURITY CLASSIFICATION OF THIS PAGE	19. SECURITY CLASSIFICATION OF ABSTRACT	20. LIMITATION OF ABSTRACT

20030923 112

THE VIEWS EXPRESSED IN THIS ARTICLE ARE THOSE OF  
THE AUTHOR AND DO NOT REFLECT THE OFFICIAL  
POLICY OR POSITION OF THE UNITED STATES AIR  
FORCE, DEPARTMENT OF DEFENSE, OR THE U.S.  
GOVERNMENT

## **DEDICATION**

To Shayleen, Natalie, Nicole and Nathaniel

Bloom Where You Are Planted

## ACKNOWLEDGEMENTS

This work was funded by the United States Air Force and performed at the Air Force Research Laboratory's High Power Gas and Chemical Laser Branch (AFRL/DEL) at Kirtland Air Force Base, Albuquerque New Mexico. I am sincerely grateful to all the government and contractor personnel within the branch for providing the assistance necessary to insure the success of this research project. In particular, thanks go out to Dr. Gordon D. Hager whose knowledge and enthusiasm guided all aspects of this research and to Professor C. Randall Truman for his efforts in helping organize and edit the manuscript into a readable form.

I am also indebted to Gen. Michael Smith (Ret) and Col. Neal Barlow of the USAF Academy Aeronautics Department for giving me the opportunity to earn this degree and return to teach at the Academy.

The views expressed in this dissertation are those of the author and do not reflect the official policy or position of the United States Air Force, Department of Defense, or the U.S. Government.

# **SPATIALLY RESOLVED SUB-DOPPLER OVERTONE GAIN MEASUREMENTS IN A SMALL SCALE SUPERSONIC HF LASER**

Charles F. Wisniewski

B.S., Mechanical/Aerospace Engineering,  
Illinois Institute of Technology, 1988

M.S., Mechanical Engineering, University of New Mexico, 1995  
Ph.D., Mechanical Engineering, University of New Mexico, 2003

## **Abstract**

The overtone gain of a small-scale HF laser was measured using a sub-Doppler tunable diode laser system. Two-dimensional spatially resolved small signal gain and temperature maps were generated, which show a highly inhomogeneous gain medium indicating the dominant role that mixing of the fuel and oxidizer streams has in HF laser performance. The measured gain and temperature data were analyzed with the aid of a two-dimensional computational fluid dynamics code. To reduce uncertainty of important modeling input parameters, novel measurements of reactant concentration, flow velocity and gain length were made. Results show that reactant mixing mechanisms such as turbulence and large-scale vortex structures have a large effect on the gain averaged over a vertical profile while kinetic rate mechanisms such as reaction rate constants and reactant concentration have a greater effect on the maximum system gain. Overtone gain data measured while operating the laser saturated on the fundamental transitions are compared with fundamental lasing output spectra. In all cases, the data are consistent with an equilibrium rotational distribution.

**DISTRIBUTION STATEMENT A**  
Approved for Public Release  
Distribution Unlimited

## Table of Contents

List of Figures .....	xi
List of Tables .....	xx
Chapter 1: Introduction .....	1
1.1 History of HF Lasers .....	2
1.2 HF Laser Basics .....	3
1.3 Previous Investigations .....	5
Chapter 2: Background .....	7
2.1 HF Rotational-Vibrational Energy Levels .....	7
2.1.1 Non-Rigid Rotor/Anharmonic Oscillator .....	14
2.1.2 Radiative Processes.....	15
2.1.3 Quantum Mechanical Link to Einstein Coefficients.....	18
2.1.4 Small Signal Gain/Absorption .....	22
2.1.5 Spectral Line Broadening.....	26
2.1.6 Transition Selection Rules .....	28
2.1.7 Thermal Population.....	32
2.1.8 Ro-Vibrational Spectrum.....	33
2.2 HF Laser Chemistry .....	35
2.2.1 Cold Pumping Reaction .....	38
2.2.2 Hot Pumping Reaction.....	42
2.2.3 R-R Energy Transfer.....	43
2.2.4 V-V Energy Transfer.....	44

a. HF.....	45
b. H <sub>2</sub> .....	46
c. F <sub>2</sub> .....	47
2.2.5 V-T Energy Transfer.....	47
a. Self Deactivation.....	47
b. H <sub>2</sub> .....	48
c. H atoms .....	50
d. F atoms.....	51
e. He and F <sub>2</sub> .....	52
2.2.6 Reactive Quenching.....	52
2.2.7 Fluorine Dissociation and Recombination.....	53
2.2.8 Reverse Reactions.....	55
2.3 Hydrodynamic Mixing in HF Lasers .....	58
2.3.1 Transverse Injection Vortex Structures.....	60
2.3.2 Turbulence .....	63
2.3.3 Binary Diffusion .....	68
Chapter 3: Experimental Apparatus and Procedure.....	70
3.1 HF Laser Device .....	70
3.1.1 Fluid Supply and Vacuum System.....	75
3.1.2 Data Acquisition and Control System.....	78
3.2 Gain Diagnostic .....	80
3.3 Data Collection and Analysis.....	85
3.4 Discharge Tube Characterization (F atom Titration).....	88

3.5 Velocity and Mach Number Measurements.....	93
3.5.1 Pitot-Static Tube .....	93
3.5.2 Doppler Velocity.....	96
3.6 Power and Out-coupled Spectrum Measurements .....	99
3.7 Saturated Gain Measurements .....	105
Chapter 4: Modeling-Code Description.....	107
4.1 NEP Starting Conditions.....	113
4.2 Comparison of Measured and Predicted Gain .....	116
Chapter 5: Results .....	119
5.1 Discharge Tube Characterization (F atom Titration).....	119
5.2 Velocity and Mach Number Measurements.....	123
5.2.1 Horizontal Mach Number Profiles.....	123
5.2.2 Vertical Pitot Tube and Doppler Velocity Profiles .....	125
5.3 Vertical Gain and Temperature Mapping .....	134
5.4 Data and Model Comparison .....	152
5.4.1 Premix Model Sensitivity to Kinetics .....	152
5.4.2 Model Turbulence Effect .....	155
5.4.3 Model Injection Scheme Effect.....	163
5.4.4 Mixing Model Sensitivity to Kinetics.....	175
a. Pressure and Temperature .....	177
b. Cold Pumping Rate Constant.....	180
c. Molar Flow Rates .....	182

d. V-V Energy Transfer.....	184
5.4.5 Model Velocity and Mach Number Predictions.....	200
5.4.6 Cavity Shock and Expansion Fans.....	205
5.5 Fundamental Power and Spectra.....	212
5.6 Saturated Gain.....	231
Chapter 6: Conclusions .....	241
References.....	247

## List of Figures

<b>Figure 2.1</b> Solid curve is a typical potential energy function of a diatomic molecule in the electronic ground state .....	12
<b>Figure 2.2</b> HF rotational energy level distribution in $v=2$ at 100 K and 400 K .....	33
<b>Figure 2.3</b> Relative gain distribution of HF $v=2$ to $v=0$ overtone transition .....	34
<b>Figure 2.4</b> Potential energy contour map of collinear three-atom reaction, A+BC $\rightarrow$ AB+C. $R_{AB}$ and $R_{BC}$ represent the AB and BC bond lengths, respectively .....	39
<b>Figure 2.5</b> $F+H_2 \rightarrow HF+H$ reaction path along the minimum potential energy surface showing the vibrational distribution of the products .....	41
<b>Figure 2.6</b> $HF(v)+HF \rightarrow HF(v-1)+HF$ energy transfer routes .....	49
<b>Figure 2.7</b> Shock and vortex structure of transverse sonic injection into supersonic crossflow .....	61
<b>Figure 2.8</b> Side view of transverse sonic injection into a supersonic crossflow .....	61
<b>Figure 3.1</b> Assembly diagram for the HF laser device slit nozzle .....	71
<b>Figure 3.2</b> Photograph of HF laser device .....	72
<b>Figure 3.3</b> HF laser supersonic nozzle .....	74
<b>Figure 3.4</b> Side view of important nozzle injection dimensions .....	75
<b>Figure 3.5</b> Schematic diagram of flow injection locations .....	76
<b>Figure 3.6</b> Example of flow control system for an individual flow species .....	77
<b>Figure 3.7</b> Front panel of LabView fluid supply system control program .....	79
<b>Figure 3.8</b> Diagram of tunable diode laser system .....	81
<b>Figure 3.9</b> Front panel display of tunable diode laser control LabView program .....	83
<b>Figure 3.10</b> Transition lineshape of the P(3) ro-vibrational line of the first HF overtone ( $v'=2, J'=2$ $v=0, J=3$ ) .....	87

<b>Figure 3.11</b> Normalized time response of [F] and [HF] for titration reaction F+HCl $\rightarrow$ HF+Cl for F <sub>2</sub> and HCl flow rates of 1 mmol s <sup>-1</sup> and 2.5 mmol s <sup>-1</sup> , respectively .....	90
<b>Figure 3.12</b> Pitot-static tube modification used for horizontal Mach number profiles ..	94
<b>Figure 3.13</b> Diagram of double pass Doppler velocity optical set-up.....	97
<b>Figure 3.14</b> Schematic representation of power versus outcoupling fraction .....	100
<b>Figure 3.15</b> Time traces of fundamental output power and fluorine flow rate for the (F <sub>2</sub> =2, H <sub>2</sub> =10) flow conditions taken 3.2 cm downstream of the NEP .....	103
<b>Figure 3.16</b> Experimental set-up for power extraction and output laser beam spectrum measurements.....	104
<b>Figure 3.17</b> Experimental set-up of overtone gain measurement while lasing on fundamental transitions .....	106
<b>Figure 4.1</b> Flow distribution with mixing options a) premixed b) mixing with imesh=2 and c) mixing with imesh=3 injection schemes .....	114
<b>Figure 5.1</b> F atom titration data using HCl .....	120
<b>Figure 5.2</b> Dissociation fraction and F atom flow rate for several different F <sub>2</sub> flow rates .....	121
<b>Figure 5.3</b> Vertical Mach number profile at several downstream locations measured using a Pitot-static probe.....	124
<b>Figure 5.4</b> Lineshapes from Doppler velocity measurement .....	125
<b>Figure 5.5</b> Vertical Pitot-static tube Mach number profile taken 2 cm downstream of the NEP .....	127
<b>Figure 5.6</b> Vertical Mach number and velocity profiles taken 4 cm downstream of the NEP .....	128
<b>Figure 5.7</b> Vertical Mach number and velocity profiles taken 4.5 cm downstream of the NEP .....	128
<b>Figure 5.8</b> Vertical Mach number and velocity profiles taken 5 cm downstream of the NEP .....	129

<b>Figure 5.9</b> Vertical Mach number and velocity profiles taken 6 cm downstream of the NEP .....	129
<b>Figure 5.10</b> Vertical Mach number and velocity profiles taken 7 cm downstream of the NEP .....	130
<b>Figure 5.11</b> Vertical Mach number and velocity profiles taken 8 cm downstream of the NEP .....	130
<b>Figure 5.12</b> Centerline Doppler velocity and Mach number measurements along with Pitot-static tube Mach number measurements taken on the vertical centerline at various downstream locations.....	132
<b>Figure 5.13</b> Vertical P3 overtone small signal gain profiles 0.5 cm downstream of NEP .....	138
<b>Figure 5.14</b> Vertical P3 overtone small signal gain profiles 2.0 cm downstream of NEP .....	139
<b>Figure 5.15</b> Vertical P3 overtone small signal gain profiles 3.5 cm downstream of NEP .....	139
<b>Figure 5.16</b> Vertical P3 overtone small signal gain profiles 5.5 cm downstream of NEP .....	140
<b>Figure 5.17</b> P3 overtone small signal gain measured at the peak gain location.....	143
<b>Figure 5.18</b> P3 overtone small signal gain measured at the vertical centerline .....	143
<b>Figure 5.19</b> Vertical location of the peak gain shown in Figure 5.17 .....	144
<b>Figure 5.20</b> Measured P3 overtone small signal gain averaged over the vertical profile between $\pm 5$ mm from the vertical centerline .....	146
<b>Figure 5.21</b> Vertical static temperature profiles 0.5 cm downstream of NEP .....	148
<b>Figure 5.22</b> Vertical static temperature profiles 2.0 cm downstream of NEP .....	148
<b>Figure 5.23</b> Vertical static temperature profiles 3.5 cm downstream of NEP .....	149
<b>Figure 5.24</b> Vertical static temperature profiles 5.5 cm downstream of NEP .....	149
<b>Figure 5.25</b> Static temperature measured at the peak gain locations of Figure 5.19....	151

<b>Figure 5.26</b> Predicted small signal gain for premixed ( $F_2=2$ , $H_2=10$ ) flow conditions for kinetics cases specified in Table 5.4 .....	152
<b>Figure 5.27</b> Predicted vertical concentration profiles 0.025 cm downstream of the NEP for the ( $F_2=2$ , $H_2=10$ ) flow conditions .....	157
<b>Figure 5.28</b> Predicted vertical concentration profiles 2.0 cm downstream of the NEP for the ( $F_2=2$ , $H_2=10$ ) flow conditions.....	157
<b>Figure 5.29</b> Predicted vertical concentration profiles 4.0 cm downstream of the NEP for the ( $F_2=2$ , $H_2=10$ ) flow conditions .....	158
<b>Figure 5.30</b> Predicted vertical concentration profiles 6.0 cm downstream of the NEP for the ( $F_2=2$ , $H_2=10$ ) flow conditions.....	158
<b>Figure 5.31</b> Measured and predicted peak gain for ( $F_2=2$ , $H_2=10$ ) flow conditions ....	160
<b>Figure 5.32</b> Measured and predicted centerline gain for ( $F_2=2$ , $H_2=10$ ) flow conditions .....	160
<b>Figure 5.33</b> Predicted vertically-average gain for ( $F_2=2$ , $H_2=10$ ) flow conditions .....	162
<b>Figure 5.34</b> Predicted F atom utilization for ( $F_2=2$ , $H_2=10$ ) flow conditions .....	163
<b>Figure 5.35</b> Predicted imesh=2 and imesh=3 concentration profiles 0.025 cm downstream of the NEP for the ( $F_2=2$ , $H_2=10$ ) flow conditions with 1% initial turbulence intensity.....	166
<b>Figure 5.36</b> Predicted imesh=2 and imesh=3 concentration profiles 0.5 cm downstream of the NEP for the ( $F_2=2$ , $H_2=10$ ) flow conditions with 1% initial turbulence intensity .....	166
<b>Figure 5.37</b> Predicted imesh=2 and imesh=3 concentration profiles 2.0 cm downstream of the NEP for the ( $F_2=2$ , $H_2=10$ ) flow conditions with 1% initial turbulence intensity .....	167
<b>Figure 5.38</b> Predicted imesh=2 and imesh=3 concentration profiles 4.0 cm downstream of the NEP for the ( $F_2=2$ , $H_2=10$ ) flow conditions with 1% initial turbulence intensity .....	167
<b>Figure 5.39</b> Measured and predicted Gain profiles 0. 5 cm downstream of the NEP for the ( $F_2=2$ , $H_2=10$ ) flow conditions.....	169
<b>Figure 5.40</b> Measured and predicted gain profiles 2.0 cm downstream of the NEP for the ( $F_2=2$ , $H_2=10$ ) flow conditions.....	169

<b>Figure 5.41</b> Measured and predicted gain profiles 4.0 cm downstream of the NEP for the ( $F_2=2$ , $H_2=10$ ) flow conditions.....	170
<b>Figure 5.42</b> Measured and predicted peak gain for the ( $F_2=2$ , $H_2=10$ ) flow conditions.....	171
<b>Figure 5.43</b> Measured and predicted centerline gain for the ( $F_2=2$ , $H_2=10$ ) flow condition .....	171
<b>Figure 5.44</b> Measured and predicted locations of peak gain shown in Figure 5.42 for the ( $F_2=2$ , $H_2=10$ ) flow conditions.....	172
<b>Figure 5.45</b> Predicted F atom utilization for the ( $F_2=2$ , $H_2=10$ ) flow conditions .....	174
<b>Figure 5.46</b> Predicted average gain for the ( $F_2=2$ , $H_2=10$ ) flow conditions.....	174
<b>Figure 5.47</b> Predicted optimized injection scheme concentration profiles 0.025 cm downstream of NEP for ( $F_2=2$ , $H_2=10$ ) flow conditions.....	175
<b>Figure 5.48</b> Measured and predicted peak gain at different cavity pressures for the ( $F_2=2$ , $H_2=10$ ) flow conditions.....	178
<b>Figure 5.49</b> Measured and predicted centerline gain at different cavity pressures for the ( $F_2=2$ , $H_2=10$ ) flow conditions.....	178
<b>Figure 5.50</b> Measured and predicted peak gain at different cavity temperatures for the ( $F_2=2$ , $H_2=10$ ) flow conditions.....	179
<b>Figure 5.51</b> Measured and predicted centerline gain at different cavity temperatures for the ( $F_2=2$ , $H_2=10$ ) flow conditions.....	180
<b>Figure 5.52</b> Measured and predicted peak gain at different cold pumping reaction rate constants for the ( $F_2=2$ , $H_2=10$ ) flow conditions .....	181
<b>Figure 5.53</b> Measured and predicted centerline gain at different cold pumping reaction rate constants for the ( $F_2=2$ , $H_2=10$ ) flow conditions .....	182
<b>Figure 5.54</b> Measured and predicted peak gain at different F atom flow rates for the ( $F_2=2$ , $H_2=10$ ) flow conditions.....	183
<b>Figure 5.55</b> Measured and predicted centerline gain at different F atom flow rates for the ( $F_2=2$ , $H_2=10$ ) flow conditions.....	183

<b>Figure 5.56</b> Measured and predicted peak gain for different HF V-V rate constants for the ( $F_2=2$ , $H_2=10$ ) flow conditions.....	184
<b>Figure 5.57</b> Measured and predicted centerline gain for different HF V-V rate constants for the ( $F_2=2$ , $H_2=10$ ) flow conditions .....	185
<b>Figure 5.58</b> Measured and predicted vertical gain profiles 0.5 cm downstream of NEP for the ( $F_2=2$ , $H_2=10$ ) flow conditions .....	186
<b>Figure 5.59</b> Measured and predicted vertical gain profiles 2.0 cm downstream of NEP for the ( $F_2=2$ , $H_2=10$ ) flow conditions .....	187
<b>Figure 5.60</b> Measured and predicted vertical gain profiles 4.0 cm downstream of NEP for the ( $F_2=2$ , $H_2=10$ ) flow conditions .....	187
<b>Figure 5.61</b> Measured and predicted vertical gain profiles 6.0 cm downstream of NEP for the ( $F_2=2$ , $H_2=10$ ) flow conditions .....	188
<b>Figure 5.62</b> Measured and predicted vertical temperature profiles 0.5 cm downstream of NEP for the ( $F_2=2$ , $H_2=10$ ) flow conditions.....	189
<b>Figure 5.63</b> Measured and predicted vertical temperature profiles 2.0 cm downstream of NEP for the ( $F_2=2$ , $H_2=10$ ) flow conditions.....	189
<b>Figure 5.64</b> Measured and predicted vertical temperature profiles 4.0 cm downstream of NEP for the ( $F_2=2$ , $H_2=10$ ) flow conditions.....	190
<b>Figure 5.65</b> Measured and predicted vertical temperature profiles 6.0 cm downstream of NEP for the ( $F_2=2$ , $H_2=10$ ) flow conditions.....	190
<b>Figure 5.66</b> Measured and predicted temperatures at peak gain locations for ( $F_2=2$ , $H_2=10$ ) flow conditions.....	191
<b>Figure 5.67</b> Measured and predicted vertical locations of peak gain of Figure 5.56 for the ( $F_2=2$ , $H_2=10$ ) flow conditions.....	192
<b>Figure 5.68</b> Measured and predicted peak gain with V-V rate constant adjustment for the ( $F_2=1$ , $H_2= 5$ ) flow conditions.....	193
<b>Figure 5.69</b> Measured and predicted centerline gain with V-V rate constant adjustment for the ( $F_2=1$ , $H_2= 5$ ) flow conditions .....	193
<b>Figure 5.70</b> Measured and predicted peak gain with V-V rate constant adjustment for the ( $F_2=2$ , $H_2= 27$ ) flow conditions.....	194

<b>Figure 5.71</b> Measured and predicted centerline gain with V-V rate constant adjustment for the ( $F_2=2$ , $H_2= 27$ ) flow conditions .....	194
<b>Figure 5.72</b> Measured and predicted peak gain with V-V rate constant adjustment for the ( $F_2=3$ , $H_2=10$ ) flow conditions .....	195
<b>Figure 5.73</b> Measured and predicted centerline gain with V-V rate constant adjustment for the ( $F_2=3$ , $H_2=10$ ) flow conditions .....	195
<b>Figure 5.74</b> Measured and predicted average gain with V-V rate constant adjustment for the ( $F_2=1$ , $H_2= 5$ ) flow conditions.....	197
<b>Figure 5.75</b> Measured and predicted average gain with V-V rate constant adjustment for the ( $F_2=2$ , $H_2=10$ ) flow conditions.....	197
<b>Figure 5.76</b> Measured and predicted average gain with V-V rate constant adjustment for the ( $F_2=2$ , $H_2= 27$ ) flow conditions .....	198
<b>Figure 5.77</b> Measured and predicted average gain with V-V rate constant adjustment for the ( $F_2=3$ , $H_2= 10$ ) flow conditions .....	198
<b>Figure 5.78</b> Vertical velocity profile 4 cm downstream of the NEP for the ( $F_2=2$ , $H_2=10$ ) flow conditions.....	202
<b>Figure 5.79</b> Vertical Mach number profile 4 cm downstream of the NEP for the ( $F_2=2$ , $H_2=10$ ) flow conditions.....	202
<b>Figure 5.80</b> Streamwise velocity at the vertical centerline for the ( $F_2=2$ , $H_2=10$ ) flow conditions.....	203
<b>Figure 5.81</b> Streamwise Mach number at the vertical centerline for the ( $F_2=2$ , $H_2=10$ ) flow conditions.....	204
<b>Figure 5.82</b> Example of over-expanded oblique shock and expansion fan pattern .....	206
<b>Figure 5.83</b> Example of under-expanded oblique shock and expansion fan pattern ...	207
<b>Figure 5.84</b> Oblique shock and expansion fan pattern for each of the four flow conditions based on computer model prediction of total properties at the secondary He nozzle injection point and the measured cavity pressure .....	209
<b>Figure 5.85</b> Fundamental power as a function of downstream location for the ( $F_2=1$ , $H_2=5$ ), ( $F_2=2$ , $H_2=10$ ) and ( $F_2=3$ , $H_2=10$ ) flow conditions .....	213

<b>Figure 5.86</b> Spectra of fundamental output beam for the ( $F_2=1$ , $H_2=5$ ) flow conditions at optical axis positions of 2.7, 4.7 and 8.7 cm downstream of the NEP .....	214
<b>Figure 5.87</b> Spectra of fundamental output beam for the ( $F_2=2$ , $H_2=10$ ) flow conditions at optical axis positions of 2.7, 4.7 and 8.7 cm downstream of the NEP.....	215
<b>Figure 5.88</b> Spectra of fundamental output beam for the ( $F_2=3$ , $H_2=10$ ) flow conditions at optical axis positions of 2.7, 4.7 and 8.7 cm downstream of the NEP.....	216
<b>Figure 5.89</b> Intensity saturation curve at several downstream locations for the ( $F_2=1$ , $H_2=5$ ) flow conditions.....	218
<b>Figure 5.90</b> Intensity saturation curve at several downstream locations for the ( $F_2=2$ , $H_2=10$ ) flow conditions.....	219
<b>Figure 5.91</b> Intensity saturation curve at several downstream locations for the ( $F_2=3$ , $H_2=10$ ) flow conditions.....	219
<b>Figure 5.92</b> Spectra of fundamental output beam for the ( $F_2=1$ , $H_2=5$ ) flow conditions at optical axis positions 4.7 cm downstream of the NEP for OC reflectivities of 95%, 70% and 50% .....	221
<b>Figure 5.93</b> Spectra of fundamental output beam for the ( $F_2=2$ , $H_2=10$ ) flow conditions at optical axis positions 4.7 cm downstream of the NEP for OC reflectivities of 95%, 70% and 50% .....	222
<b>Figure 5.94</b> Spectra of fundamental output beam for the ( $F_2=3$ , $H_2=10$ ) flow conditions at optical axis positions 4.7 cm downstream of the NEP for OC reflectivities of 95%, 70% and 50% .....	223
<b>Figure 5.95</b> Fundamental small signal gain determined from the I-Sat curves shown in Figures 5.89, 5.90 and 5.91 for the dominate threshold transition of the ( $F_2=1$ , $H_2=5$ ), ( $F_2=2$ , $H_2=10$ ) and ( $F_2=3$ , $H_2=10$ ) flow conditions shown in Figures 5.92, 5.93 and 5.94 .....	225
<b>Figure 5.96</b> Measured and predicted P3 $\nu=2-1$ fundamental small signal gain as a function of streamwise location for the ( $F_2=1$ , $H_2=5$ ) flow conditions.....	226
<b>Figure 5.97</b> Measured and predicted P3 $\nu=2-1$ fundamental small signal gain as a function of streamwise location for the ( $F_2=2$ , $H_2=10$ ) flow conditions.....	227
<b>Figure 5.98</b> Measured and predicted P4 $\nu=2-1$ fundamental small signal gain as a function of streamwise location for the ( $F_2=3$ , $H_2=10$ ) flow conditions.....	227

**Figure 5.99** Streamwise distribution of the predicted overtone ( $P_3 v=2-0$ ) and fundamental ( $P_3 v=2-1$ ) peak gain for the ( $F_2=2$ ,  $H_2=10$ ) flow conditions..... 229

**Figure 5.100** Streamwise distribution of the predicted overtone ( $P_3 v=2-0$ ) and fundamental ( $P_3 v=2-1$ ) centerline gain for the ( $F_2=2$ ,  $H_2=10$ ) flow conditions ..... 229

**Figure 5.101**  $P_1$ ,  $P_2$ ,  $P_3$ ,  $P_4$  and  $P_5$   $v=2-0$  overtone gain distribution under small signal gain conditions ( $R_1=0\%$ ) and saturated conditions ( $R_1=80\%$ )..... 235

**Figure 5.102** Fundamental output beam spectra for the ( $F_2=2$ ,  $H_2=10$ ) flow conditions with optical axis positioned 2.7 cm downstream of the NEP for  $R_1=80\%$ ..... 236

**Figure 5.103** Temperature as a function of OC reflectivity for the ( $F_2=2$ ,  $H_2=10$ ) flow conditions 2.7 cm downstream of the NEP and 3.0 mm above the vertical centerline... 239

## List of Tables

<b>Table 2.1</b> Spectroscopic constants for HF.....	15
<b>Table 2.2</b> HF ro-vibrational energies (cm <sup>-1</sup> ) in the electronic ground state .....	15
<b>Table 2.3</b> Einstein A coefficient and wavelength for HF fundamental and overtone transitions.....	23
<b>Table 2.4</b> HF laser chemical kinetic rate constants (center column). Equations give rate constants in units of cm <sup>3</sup> molecules <sup>-1</sup> s <sup>-1</sup> .....	56
<b>Table 2.5</b> HF laser chemical kinetic rate constants at 300 K. Equations give rate constants in units of cm <sup>3</sup> molecules <sup>-1</sup> s <sup>-1</sup> .....	57
<b>Table 3.1</b> Description of laser flow species. Injection location of each species is shown in Figure 3.5 .....	76
<b>Table 3.2</b> Location of laser cavity pressure transducers.....	78
<b>Table 5.1.</b> Doppler velocity measurement parameters taken 4 cm downstream of the NEP on the vertical centerline .....	126
<b>Table 5.2</b> Nominal flow rates (mmol s <sup>-1</sup> ) for gain and temperature mapping flow conditions.....	135
<b>Table 5.3</b> Nominal pressures (torr) for flow conditions listed in Table 5.2 .....	136
<b>Table 5.4</b> Results of small signal gain and temperature precision uncertainty analysis.....	137
<b>Table 5.5</b> Premix kinetics cases .....	153
<b>Table 5.6</b> Comparison of measured and predicted maximum average gain.....	196
<b>Table 5.7</b> Flow parameters for various flow cases .....	205
<b>Table 5.8</b> Parameters predicted by oblique shock/expansion fan system shown in Figure 5.84.....	209
<b>Table 5.9</b> Results of lineshape and saturated gain data analysis .....	238

## **Chapter 1**

### **Introduction**

The hydrogen fluoride (HF) laser and its cousin the deuterium fluoride (DF) laser are chemical lasers that have significant potential for use in many applications (Kiernan 2001; Smith and Wall 2000; Wollmann 2003). The hydrogen fluoride laser, which was invented over 35 years ago, continues to be investigated because of its ability to generate high power laser beams with relatively high chemical conversion efficiency. However, despite enormous efforts expended to fully characterize the HF laser, questions regarding its performance relative to theoretical predictions and fundamental properties such as small signal gain and reactant mixing remain. In general, this is because the bulk of the experimental work in the last 10-15 years has gone into technological and engineering development. The goal of this research is to gain a better understanding of the physical mechanisms that dominate the performance of HF laser systems. In order to achieve this goal, an advanced tunable diode laser diagnostic system was used to probe the cavity of an active HF laser to measure small signal gain of the HF overtone transitions, static flow temperature, and flow velocity. The analysis of this data in conjunction with a two-dimensional computational fluid dynamics code has provided insight into the complex fluid mechanics and chemical kinetics of the HF laser. This research represents the first ever sub-Doppler small signal gain measurements in an active HF laser.

## 1.1 History of HF Lasers

The first demonstrations of the fundamental HF chemical laser were reported in the late 1960's. While the first HF lasers were pulse initiated (Basov et al. 1969; Batovskii et al. 1969; Deutsch 1967; Gross et al. 1968; Kompa and Pimentel 1967; Parker and Pimentel 1968), continuous wave HF lasers were also demonstrated as early as 1970 (Airey and McKay 1969; Gross et al. 1969; Spencer et al. 1969). Over the past 35 years, the development of HF laser technology has advanced to the point where multi-megawatt lasers can be constructed (Hecht 1993). It is widely recognized that the fundamental HF laser, which operates at a wavelength from  $2.7 - 3.0 \mu\text{m}$ , has limited utility for low-altitude, long-range propagation applications due to strong absorptions in the atmosphere. This limitation can be overcome by operating on HF overtone transitions, from  $1.25 - 1.35 \mu\text{m}$ . The first demonstrations of HF overtone lasing were reported by Hon and Novak (1975) and Bashkin et al (1977). The overall power efficiency (i.e.,  $P_{\text{fundamental}}/P_{\text{overtone}}$ ) of these demonstrations was rather poor, most likely due to less than ideal optics. A scalable HF overtone laser, built by Jeffers in 1984, possessed significantly enhanced efficiency with 20-30% of the fundamental power extracted on the overtone (Jeffers 1988). The use of HF combustion technology coupled with improved mirrors led to demonstrations of multi-kW HF overtone lasers during the mid- to late-1980's (Duncan et al. 1989; 1991; 1990). Further development of HF overtone technology has been limited by the availability of optical coatings for the mirrors. As the technology to manufacture these coatings, which must simultaneously suppress fundamental lasing and enable overtone lasing, has improved, so have the prospects for developing high power HF overtone lasers.

## 1.2 HF Laser Basics

A chemical laser is defined by the "Handbook of Chemical Lasers" *as a laser operating on a population inversion produced--directly or indirectly--in the course of an exothermic chemical reaction* (Pimentel and Kompa 1976). To produce a laser with high power requires a chemical reaction with a large energy release in which a large portion of that energy is channeled into excited states of the reaction products. The reaction of atomic fluorine with hydrogen is such a reaction. This reaction produces 14.7 kJ/g of fluorine with approximately 60% of the energy going into excited vibrational states of the hydrogen fluoride (HF) molecule making it relatively easy to create the population inversions required for lasing (Cohen and Bott 1976). This is why much attention was given to HF in the early development of chemical lasers.

There are two basic types of HF lasers: combustor-driven and electric discharge driven. The main difference between these systems is the method of molecular fluorine dissociation. In a combustor-driven HF laser, the combustion of deuterium ( $D_2 + F_2$ ) is used to produce the thermal energy required to dissociate excess molecular fluorine supplied to the combustion chamber. Hydrogen can also be used in the combustion chamber to dissociate the  $F_2$ . However, the byproduct of this reaction, ground state HF, has been shown to be an efficient deactivator of the excited state HF in the laser cavity. In contrast, the byproduct of  $D_2 + F_2$ , has been shown to have little effect on laser cavity kinetics. Alternatively, F atoms can also be produced by direct electric discharge in a discharge tube. This process is relatively inefficient requiring very large power supplies to produce modest F atom flow rates. As a result, electric discharge driven lasers have inherently low power. They are, however, quite simple to operate and have proven very

useful in the investigation of basic chemical kinetics of chemical lasers. In either type of laser, the F atoms are accelerated through a nozzle, typically to supersonic speeds, where a secondary stream of hydrogen ( $H_2$ ) is injected into the flow. The primary reaction of the oxidizer (F) with the fuel ( $H_2$ ) produces hydrogen fluoride (HF) molecules in the first three excited vibrational states. Lasing occurs on the radiation emitted from molecular transitions between the vibrational energy levels.

Excited state HF can be deactivated by collisions with other species inside the laser cavity at rates nearly as fast as the pumping mechanism that produces the excited state. This is why the fuel and oxidizer are kept separate until they reach the optical cavity inlet where the mixing of the two streams initiates the pumping. The efficiency of the laser system therefore depends heavily on the rate of mixing. Herein lies the main conflict in the design of HF laser systems: Creating an environment where the pumping mechanism dominates over the deactivation mechanism is in direct opposition to creating a healthy mixing environment. The chemical kinetics requires the flow to be at a very high velocity and low pressure. This tends to drastically reduce the Reynolds number resulting in laminar flow and very long mixing lengths. HF system designers have traditionally attempted to overcome this conflict by injecting 2 to 5 times the stoichiometric requirement of  $H_2$ . This gives diffusional mixing mechanisms more opportunities to bring the reactants in contact. Despite efforts such as this, these systems still can only achieve between 25 and 50% of the theoretical maximum (completely mixed) power output.

### 1.3 Previous Investigations

A major impediment to HF overtone laser development has been the lack of high fidelity small signal gain data. Small signal gain is the fundamental property of the laser flow field that determines the amplification of coherent radiation as it traverses the laser cavity. Previous investigations have used commercially available arc-driven HF lasers as probes to measure the small signal gain. These types of probe lasers are typically stabilized and locked to the line center of a HF overtone transition but have proven difficult and expensive to operate resulting in large uncertainty for this type of measurement. Alternatively, Rigrod theory, which relates the small signal gain to the output laser power, has been used in lieu of a direct gain probe (Rigrod 1965). However, this technique cannot generate spatially resolved gain or temperature maps, which are strongly needed since the rate of mixing can dominate HF laser efficiency. Furthermore, Rigrod theory cannot be used to measure gain on individual ro-vibrational lines because the measured small signal gain is only associated with the strongest line in the multi-line overtone spectrum.

The difficulty in measuring the small signal gain in previous work has been further complicated by the uncertainty in the gain length. In single nozzle experiments, this uncertainty is due to expansion of the gain medium as it flows downstream. In nozzle bank experiments, the regions of gain are interspersed with base regions that have no gain. Thus the geometric length is only an upper bound on the actual gain length.

A third major difficulty in previous work is the lack of a precise measurement of the fluorine atom concentration in the laser cavity. This critical parameter determines how much HF can be formed and consequently how much power can be extracted from a

laser. A great deal of work has gone into fitting HF laser experimental data with theoretical models to indirectly estimate the F atom concentration. This is done by altering the dissociation fraction of the F atom precursor molecule (SF<sub>6</sub>, F<sub>2</sub>, etc.) until the model agrees with the experimental data (Carroll et al. 1993; Sentman et al. 1987).

Given the chemical and physical complexity of a typical HF laser, this technique can result in erroneous conclusions.

This investigation addresses the previous experimental shortcomings primarily through the use of a tunable diode laser system that is capable of resolving the lineshape of individual HF overtone ro-vibrational transitions thereby ensuring high fidelity of the centerline gain measurement. Resolution of the transition lineshape also allows for the determination of the static flow temperature. A novel titration experiment is used to measure the F atom flow rate and Pitot-static probe measurements are made to greatly reduce the ambiguity of the gain length.

## Chapter 2

### Background

The HF laser is an enormously complex system that spans the disciplines of quantum mechanics, chemical kinetics and fluid dynamics. The following sections of this chapter discuss the effect these three fundamental disciplines have on the performance of an HF laser systems. Quantum mechanics describes the rotational/vibrational energy spectrum of the HF molecule. Included is a discussion of the relevant radiative energy transfer processes and the small signal gain, which is the fundamental parameter that defines the lasing potential of the medium. The section on chemical kinetics describes the reactions that create the nonequilibrium (i.e., inverted) population distribution of the HF molecular system and the collisional deactivation reactions that work to restore equilibrium to the system. The fluid mechanics section covers the operation of the supersonic nozzle used to mix the reactants and create favorable lasing conditions within the laser cavity.

#### 2.1 HF Rotational-Vibrational Energy Levels

Solutions of the Schrödinger equation define the quantum mechanical energy states of a molecular system:

$$\hat{H}\psi_m(\mathbf{r}, \mathbf{R}) = E_m \psi_m(\mathbf{r}, \mathbf{R}) \quad (2.1)$$

where  $\hat{H}$  is the Hamiltonian operator,  $\psi_m$  is the molecular wave function and  $E_m$  is the total molecular energy, which includes translational, vibrational, rotational, and

electronic energies (Lowe 1993). The vectors  $\mathbf{r}$  and  $\mathbf{R}$  represent the locations of the electrons and nuclei, respectively. The Hamiltonian operator for a diatomic molecule is:

$$\hat{\mathbf{H}} = -\frac{\hbar^2}{2m_a} \nabla_a^2 - \frac{\hbar^2}{2m_b} \nabla_b^2 - \frac{\hbar^2}{2m_e} \sum_i \nabla_i^2 - \sum_i \frac{Z_a e^2}{\mathbf{r}_{a,i}} - \sum_i \frac{Z_b e^2}{\mathbf{r}_{b,i}} + \frac{Z_a Z_b e^2}{\mathbf{R}} + \sum_{i,j} \frac{e^2}{\mathbf{r}_{ij}} \quad (2.2)$$

where  $\hbar$  is Plank's constant,  $m_a$  and  $m_b$  are the masses of the two nuclei,  $m_e$  is the electron mass,  $Z_a$  and  $Z_b$  are the charges of the two nuclei, and  $e$  is the electron charge. The first three terms represent the kinetic energy of the two nuclei and the electrons, respectively (Levine 1975). The fourth and fifth terms represent the attractive potentials between the nuclei and the electrons while the last two terms represent the nuclei-nuclei and electron-electron repulsive potentials.

The first step in obtaining an approximate solution to the Schrödinger equation is to assume the molecular wavefunction is separable into electronic and nuclear parts:

$$\psi_m(\mathbf{r}, \mathbf{R}) = \psi_{el}(\mathbf{r}, \mathbf{R})\psi_N(\mathbf{R}) \quad (2.3)$$

Substituting this form of the wavefunction into the Schrödinger equation gives:

$$\begin{aligned} -\frac{\hbar^2}{2m_a} \nabla_a^2 \psi_{el} \psi_N - \frac{\hbar^2}{2m_b} \nabla_b^2 \psi_{el} \psi_N - \frac{\hbar^2}{2m_e} \sum_i \nabla_i^2 \psi_{el} \psi_N \\ + [\hat{V}_{eN} + \hat{V}_{NN} + \hat{V}_{ee}] \psi_{el} \psi_N = E_m \psi_{el} \psi_N \end{aligned} \quad (2.4)$$

where  $\hat{V}_{eN}$ ,  $\hat{V}_{NN}$ , and  $\hat{V}_{ee}$  are the electron-nuclei, nuclei-nuclei and electron-electron potentials, respectively. By utilizing the vector calculus identity:

$$\nabla^2 fg = f \nabla^2 g + 2\nabla f \nabla g + g \nabla^2 f$$

Equation (2.4) expands into:

$$\begin{aligned}
& -\frac{\hbar^2}{2m_a} (\psi_{el} \nabla_a^2 \psi_N + 2\nabla_a \psi_{el} \nabla_a \psi_N + \psi_N \nabla_a^2 \psi_{el}) \\
& -\frac{\hbar^2}{2m_b} (\psi_{el} \nabla_b^2 \psi_N + 2\nabla_b \psi_{el} \nabla_b \psi_N + \psi_N \nabla_b^2 \psi_{el}) \\
& -\frac{\hbar^2}{2m_e} \sum_i (\psi_{el} \nabla_i^2 \psi_N + 2\nabla_i \psi_{el} \nabla_i \psi_N + \psi_N \nabla_i^2 \psi_{el}) \\
& + (\hat{V}_{eN} + \hat{V}_{NN} + \hat{V}_{ee}) \psi_{el} \psi_N = E_m \psi_{el} \psi_N
\end{aligned} \tag{2.5}$$

The initial separation assumption separated the nuclear motion from the electronic motion. This assumption is justified because the electron mass is so much smaller than the nuclear mass that the electrons can respond virtually instantaneously to the nuclear motion. Under this assumption the derivatives of the electronic wavefunction with respect to the nuclear coordinates vanish as do the derivatives of the nuclear wavefunctions with respect to the electronic coordinates:

$$\begin{aligned}
\nabla_{a,b}^2 \psi_{el} &= 0, \quad \nabla_{a,b} \psi_{el} = 0 \\
\nabla_i^2 \psi_N &= 0, \quad \nabla_i \psi_N = 0
\end{aligned}$$

This simplification, commonly termed the Born-Oppenheimer approximation, reduces Equation (2.5) to (Levine 1975):

$$\begin{aligned}
& -\frac{\hbar^2}{2m_a} (\psi_{el} \nabla_a^2 \psi_N) - \frac{\hbar^2}{2m_b} (\psi_{el} \nabla_b^2 \psi_N) - \frac{\hbar^2}{2m_e} \sum_i (\psi_N \nabla_i^2 \psi_{el}) \\
& + (\hat{V}_{eN} + \hat{V}_{NN} + \hat{V}_{ee}) \psi_{el} \psi_N = E_m \psi_{el} \psi_N
\end{aligned} \tag{2.6}$$

At a given inter-nuclear separation, the potential energy operators do not affect the nuclear wavefunction so it can be brought in front of the operators. Then by dividing through by  $\psi_{el}$  and  $\psi_N$  and rearranging terms, Equation (2.6) becomes:

$$\frac{1}{\psi_N} \left[ -\frac{\hbar^2}{2m_a} (\nabla_a^2 \psi_N) - \frac{\hbar^2}{2m_b} (\nabla_b^2 \psi_N) - E_m \right] + \frac{1}{\psi_{el}} \left[ -\frac{\hbar^2}{2m_e} \sum_i (\nabla_i^2 \psi_{el}) + (\hat{V}_{eN} + \hat{V}_{NN} + \hat{V}_{ee}) \psi_{el} \right] = 0 \quad (2.7)$$

Since the first term is only a function of  $\psi_N$  and the second term is only a function of  $\psi_{el}$ , separation of variables has been achieved. Each term must equal  $\pm$  the same constant resulting in separate electronic and nuclear Schrödinger equations:

$$\left[ -\frac{\hbar^2}{2m_e} \sum_i \nabla_i^2 + \hat{V}_{eN} + \hat{V}_{NN} + \hat{V}_{ee} \right] \psi_{el} = C \psi_{el} \quad (2.8)$$

$$\left[ -\frac{\hbar^2}{2m_a} \nabla_a^2 - \frac{\hbar^2}{2m_b} \nabla_b^2 \right] \psi_N = -C \psi_N + E_m \psi_N$$

where the separation constant, C, can now be defined as the total electronic energy including nuclear-nuclear repulsion,  $U(R)$ . The electronic equation can be written more succinctly as:

$$[\hat{H}_e + \hat{V}_{NN}] \psi_{el} = U(R) \psi_{el} \quad (2.9)$$

where  $\hat{H}_e$  is the electronic Hamiltonian:

$$\hat{H}_e = -\frac{\hbar^2}{2m_e} \sum_i \nabla_i^2 + \hat{V}_{eN} + \hat{V}_{ee}$$

Equation (2.9) can be solved for a particular electronic configuration at a given inter-nuclear separation, R. Then by parametrically varying R, the total electronic energy, including nuclear repulsion, can be determined as a function of inter-nuclear separation. Using the electronic solution and rearranging the terms of the nuclear Schrödinger equation gives:

$$\left[ -\frac{\hbar^2}{2m_a} \nabla_a^2 - \frac{\hbar^2}{2m_b} \nabla_b^2 + U(R) \right] \psi_N = E_m \psi_N \quad (2.10)$$

Since  $U(R)$  is only a function of the inter-nuclear separation, the two-particle system can be reduced to a one-particle system by moving to an internal reference frame. This separates the translational motion of the molecule from the internal motion of the nuclei relative to each other. The nuclear Schrödinger equation then becomes:

$$\left[ -\frac{\hbar^2}{2\mu} \nabla^2 + U(R) \right] \psi_N = E \psi_N \quad (2.11)$$

where  $\mu$  is the reduced mass of the nuclei,  $R$  is the inter-nuclear separation and  $E$  is the total energy of the molecule, excluding translational energy.

In spherical polar coordinates Equation (2.11) has a separable solution of the form:

$$\psi_N = F(R) Y_J^M(\theta_N, \phi_N) \quad (2.12)$$

The angular part of the solution,  $Y_J^M$ , are spherical harmonics and can be written in terms of Legendre polynomials. The quantum number  $J$  represents the angular momentum and is restricted to positive integers or zero. The quantum number  $M$  represents the projection of the angular momentum onto the z-axis and is restricted to integer values between  $J$  and  $-J$ . The energies associated with the spherical harmonics are those of the rigid rotor (McQuarrie and Simon 1997):

$$E_{rot} = \frac{\hbar^2}{2I} J(J+1) \quad (2.13)$$

where  $I (= \mu R^2)$  is the molecule's moment of inertia. Since the rotational energy is not a function of  $M$ , and because  $M$  can vary between  $\pm J$ , the rotational energy levels are  $2J+1$

degenerate. The energy of the rigid rotor depends on the square of the quantum number  $J$ , so the energy level spacing increases as the  $J$  value increases.

The potential energy function,  $U(R)$ , must be known in order to solve for the radial component of the nuclear wave function. For bound electronic states of diatomic molecules,  $U$  has the general shape of the solid curve in Figure 2.1. The curve rises steeply to the left of the minimum, indicating the difficulty of pushing the two nuclei closer together. The curve to the right of the equilibrium position rises initially but eventually levels off to the molecular bond energy. When the internal energy of the molecule exceeds the bond energy the molecule will dissociate into separate atoms.

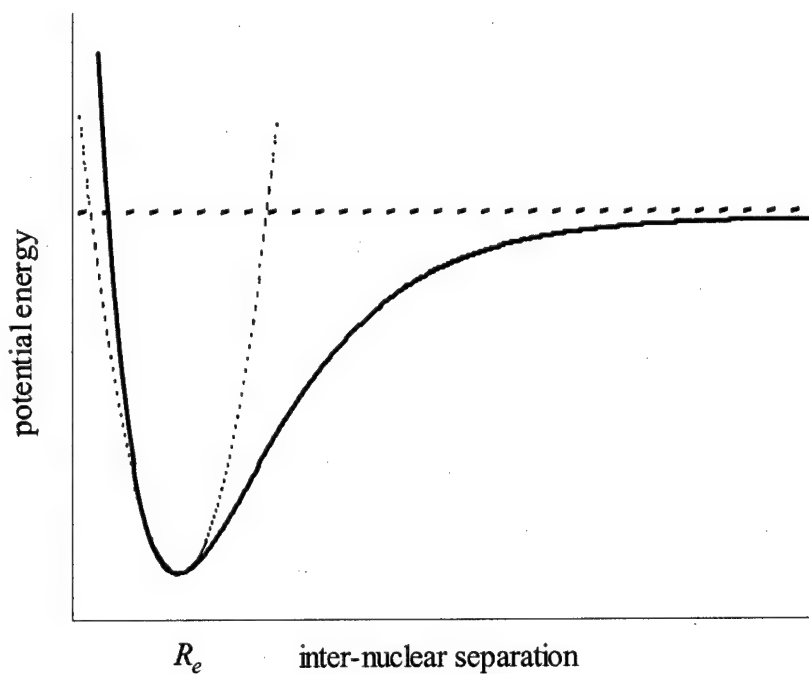


**Figure 2.1** Solid curve is a typical potential energy function of a diatomic molecule in the electronic ground state. Dotted curve is the parabolic harmonic oscillator approximation. Dashed curve represents the dissociation energy.  $R_e$  represents the equilibrium bond length between the nuclei.

Expanding  $U(R)$  in a Taylor series about the equilibrium inter-nuclear separation gives:

$$U(R) = U(R_e) + U'(R_e)(R - R_e) + \frac{1}{2!}U''(R_e)(R - R_e)^2 + \frac{1}{3!}U'''(R_e)(R - R_e)^3 + \frac{1}{4!}U^{(4)}(R_e)(R - R_e)^4 + \dots \quad (2.14)$$

The first derivative of  $U$  vanishes at the equilibrium separation,  $R_e$ :

$$U'(R_e) = 0 \quad (2.15)$$

Keeping only the parabolic term gives the simplest approximation to  $U$ :

$$U(R) \approx U(R_e) + \frac{1}{2}k_e(R - R_e)^2 \quad (2.16)$$

where  $k_e$  ( $= U''(R_e)$ ) is the equilibrium molecular force constant. This approximation is justified for small oscillations about  $R_e$  and amounts to replacing the solid curve in Figure 2.1 with the dashed curve. Equation (2.16) represents the potential energy of a harmonic oscillator and is equivalent to a mechanical system in which two masses connected by a spring oscillate about an equilibrium position.

Solving for the radial component of the wavefunction gives:

$$F(R) = \frac{S_v(R - R_e)}{R} \quad (2.17)$$

where the function  $S_v$  can be written in terms of Hermite polynomials. The corresponding vibrational energies are:

$$E_{vib} = \omega_e(v + \frac{1}{2}) \quad (2.18)$$

where the vibrational quantum number,  $v$ , is restricted to positive integer values (Levine 1975). The zero point energy,  $\omega_e$  is given by:

$$\omega_e = \hbar \left( \frac{k}{\mu} \right)^{1/2}$$

where  $k$  is the vibrational force constant. The vibrational energy levels of the harmonic oscillator are evenly spaced and are typically 100 to 1000 times farther apart than the rigid-rotor energy levels.

### 2.1.1 Non-Rigid Rotor/Anharmonic Oscillator

The higher order terms neglected in Equation (2.14) in the previous section must be retained in order to adequately model the energy levels of the HF molecule. Because the neglected terms are small they can be considered perturbations to the rigid-rotor/harmonic-oscillator model (Levine 1975). The corrected expression for the vibrational energy in terms of band spectrum coefficients common in spectroscopic literature is:

$$E_{vib} = \omega_e(v + \frac{1}{2}) - \omega_e x_e(v + \frac{1}{2})^2 + \omega_e y_e(v + \frac{1}{2})^2 + \dots \quad (2.19)$$

The coefficients ( $\omega_e$ ,  $\omega_e x_e$  and  $\omega_e y_e$ ) are experimentally determined and represent the weakening of the inter-nuclear force constant as the vibrational energy level increases.

Similar corrections to the rigid-rotor expression correct for the changing of the inter-nuclear separation as the rotational energy level increases:

$$E_{rot} = B_v J(J+1) - D_e J^2 (J+1)^2 + \dots \quad (2.20)$$

Coupling between the vibrational and rotational energies also needs to be considered. As the vibrational energy increases, the average separation between the nuclei grows increasing the rotational inertia. Also, the lengthening of the inter-nuclear separation at higher rotational levels decreases the vibrational force constant. Vibrational-rotational coupling enters the energy expression through  $B_v$  in Equation (2.20):

$$B_v = B_e - \alpha_e(v + \frac{1}{2}) + \dots \quad (2.21)$$

With these corrections the rotational-vibrational energy of a diatomic molecule becomes:

$$E_{ro-vib} = \omega_e(v + \frac{1}{2}) - \omega_e x_e(v + \frac{1}{2})^2 + \omega_e y_e(v + \frac{1}{2})^3 + [B_e - \alpha_e(v + \frac{1}{2})]J(J+1) - D_e J^2(J+1)^2 + \dots \quad (2.22)$$

Table 2.1 lists the HF spectroscopic constants and the associated ro-vibrational energies are listed in Table 2.2 (Wilkins 1977).

### 2.1.2 Radiative Processes

Einstein identified three radiative processes that affect the concentrations of molecules in individual energy states: spontaneous emission, stimulated absorption and stimulated emission (Verdeyen 1995). As the name implies, spontaneous emission is the

**Table 2.1** Spectroscopic constants for HF (Wilkins 1977)

Constant	Value (cm <sup>-1</sup> )
$\omega_e$	4138.73
$\omega_e x_e$	90.05
$\omega_e y_e$	0.932
$B_e$	20.9555
$D_e$	2.15E-03
$\alpha_e$	0.7958

**Table 2.2** HF ro-vibrational energies (cm<sup>-1</sup>) in the electronic ground state. (Wilkins 1977)

	v=0	v=1	v=2	v=3
<b>J=0</b>	2046.97	6008.55	9797.96	13419.96
<b>1</b>	2088.08	6048.12	9836.02	13456.55
<b>2</b>	2170.25	6127.20	9912.10	13529.70
<b>3</b>	2293.39	6245.70	10026.09	13639.29
<b>4</b>	2457.33	6403.47	10177.86	13785.19
<b>5</b>	2661.88	6600.32	10367.20	13967.22
<b>6</b>	2906.78	6835.99	10593.89	14185.15
<b>7</b>	3191.73	7110.20	10857.63	14438.68
<b>8</b>	3516.38	7422.60	11158.10	14727.51

spontaneous decay of a molecule from energy state 2 to 1 by radiation. In doing so the excess energy is released in the form of a photon. The change in the population density of state 2 due to spontaneous emission can be written in terms of a simple rate expression:

$$\frac{dN_2}{dt} \bigg|_{\substack{\text{spontaneous} \\ \text{emission}}} = -A_{21}N_2 = A_{21}N_1 \quad (2.23)$$

where  $N_2$  and  $N_1$  are the populations of molecules in energy states 2 and 1, respectively, and  $A_{21}$  is termed the Einstein A coefficient. The solution to this equation shows that if no other process took place the population of state 2 would decrease exponentially with a time constant  $\tau = (A_{21})^{-1}$ . The Einstein A coefficient is therefore the radiative lifetime of the molecules in energy state 2.

In the absorption process, a molecule in energy state 1 absorbs a photon from a radiation field and is promoted to state 2. The rate which this process takes place depends on the density of the radiation field and the concentration of the absorbing molecules:

$$\frac{dN_2}{dt} \bigg|_{\text{absorption}} = B_{12}N_1\rho(\nu)f(\nu) = -\frac{dN_1}{dt} \bigg|_{\text{absorption}} \quad (2.24)$$

where  $\rho(\nu)$  is the radiation field energy density and  $f(\nu)$  is the lineshape function. The lineshape function is the frequency dependence of the radiative transfer between energy states 1 and 2. Section 2.1.7 gives a detailed explanation of the causes and consequences of the broadening of the lineshape function. In the applications discussed here, the frequency bandwidth of the interacting radiation field is many orders of magnitude narrower than the spectral lineshape of the transition. Therefore,  $\rho(\nu)$  can be considered a

delta function existing at only a single frequency. The radiating field will then interact only with the fraction of molecules transitioning between states 1 and 2 that correspond to that frequency. That fraction of molecules is defined by the lineshape function (Verdeyen 1995).

Stimulated emission is the reverse of absorption. In this process a molecule in state 2 is stimulated by a radiation field to give up its excess energy and in the process drops down to state 1:

$$\frac{dN_2}{dt} \bigg|_{\substack{\text{stimulated} \\ \text{emission}}} = -B_{21}N_2\rho(\nu)f(\nu) = -\frac{dN_1}{dt} \bigg|_{\substack{\text{stimulated} \\ \text{emission}}} \quad (2.25)$$

The photon that is released in the process is at the same frequency, at the same phase, in the same polarization, and in the same direction as the stimulating wave. This coherent radiation addition is the fundamental process by which all lasers operate. Here again the stimulating wave will interact only with the fraction of molecules dictated by the lineshape function.

Einstein used a thermodynamic equilibrium argument to show the relationship between the different coefficients (Verdeyen 1995):

$$g_2B_{21} = g_1B_{12} \quad (2.26)$$

$$\frac{A_{21}}{B_{21}} = \frac{8\pi h\nu^3}{c^3} \quad (2.27)$$

where  $g_1$  and  $g_2$  are the degeneracies of the upper and lower energy levels, respectively and  $\nu$  is the photon transition frequency between the upper and lower energy levels. Therefore by knowing one coefficient, all three are known. It is important to note that the coefficients are physical properties of the molecule and as such do not depend on whether or not it is in equilibrium or on the intensity of the radiation field or on the existence of

any other energy transfer mechanisms. Therefore the likelihood of any radiative transition is quantified by the Einstein A coefficient.

### 2.1.3 Quantum Mechanical Link to Einstein Coefficients

The previous section defined the observed macroscopic transition rate coefficients (i.e., Einstein coefficients) of radiative energy transfer. This section derives the relationship between these rate coefficients and the quantum mechanical state functions described earlier. On the quantum mechanical level, a radiative energy transfer involves the interaction between the radiation field and the electric dipole moment of the molecule. A molecule consisting of nuclei and electrons at positions  $\mathbf{r}_i = (x_i, y_i, z_i)$  with charge  $q_i$  will have a net dipole moment,  $\mu$ , with Cartesian components (Hollas 1998):

$$\mu = \begin{cases} \mu_x = \sum_i x_i q_i \\ \mu_y = \sum_i y_i q_i \\ \mu_z = \sum_i z_i q_i \end{cases} \quad (2.28)$$

The classic potential energy of a system of charges having a dipole moment in a radiation field is given by:

$$V = -\mathbf{E}(t) \cdot \mu \quad (2.29)$$

where  $\mathbf{E}$  is the oscillating electric field vector. If the oscillating field is in the z direction and the dipole system is located at the origin, Equation (2.29) can be written as:

$$V = -E_{oz} \cos(\omega t) \mu_z \quad (2.30)$$

where  $\omega$  is the frequency of the electromagnetic wave. This classical energy potential can be written as a time-dependent perturbation Hamiltonian to the quantum mechanical system (Levine 1975):

$$\hat{H}'(t) = -E_{oz} \cos(\omega t) \mu_z \quad (2.31)$$

The transition probability is then obtained by solving the time-dependent Schrödinger equation:

$$i\hbar \frac{\partial \Psi(t)}{\partial t} = [\hat{H}^0 + \hat{H}'(t)] \Psi(t) \quad (2.32)$$

where  $\Psi(t)$  is the time dependent wavefunction for the perturbed system and  $\hat{H}^0$  is the Hamiltonian for the unperturbed system.

Consider now a simple two-level system described by upper and lower stationary state wavefunctions  $\psi_2$  and  $\psi_1$ , respectively, in which the stimulating wave is absorbed by the molecule and promoted from state 1 to state 2. Solutions to the unperturbed time-dependent Schrödinger equation (Equation (2.32) with  $\hat{H}' = 0$ ) give the time-dependent wavefunctions for the upper and lower energy states in terms of the stationary state solutions:

$$\begin{aligned} \Psi_1 &= \psi_1 e^{-iE_1 t/\hbar} \\ \Psi_2 &= \psi_2 e^{-iE_2 t/\hbar} \end{aligned} \quad (2.33)$$

The wavefunction for the perturbed system is then given by the linear combination of the complete set of solutions to the unperturbed system:

$$\Psi(t) = a_1(t) \psi_1 e^{-iE_1 t/\hbar} + a_2(t) \psi_2 e^{-iE_2 t/\hbar} \quad (2.34)$$

where  $a_1(t)$  and  $a_2(t)$  are time-dependent coefficients. The squares of the coefficients,  $|a_1(t)|^2$  and  $|a_2(t)|^2$ , are the probabilities of the system being in state 1 and 2,

respectively. Substitution of Equation (2.34) into Equation (2.32) gives, after much simplification, two coupled differential equations for the time-dependent coefficients:

$$\frac{da_2}{dt} = a_1 \frac{\mu_{21z} E_{oz}}{2i\hbar} e^{-i(\omega-\omega_{21})t} \quad (2.35)$$

$$\frac{da_1}{dt} = a_2 \frac{\mu_{12z} E_{oz}}{2i\hbar} e^{i(\omega-\omega_{21})t}$$

where  $\omega_{21} = (E_2 - E_1)/\hbar$  is the transition frequency between the upper and lower energy states. The z component of the transition dipole moment is:

$$\mu_{21z} = \int \psi_2 \hat{\mu}_z \psi_1 d\tau \quad (2.36)$$

where the dipole moment operator,  $\hat{\mu}_z$ , is given by:

$$\hat{\mu}_z = \sum_i z_i q_i \quad (2.37)$$

To solve Equations (2.35), first assume that the system of molecules is initially in state 1 and then at  $t=0$  a weak electric field, with a frequency near the transition frequency, is turned on to induce a transition from state 1 to state 2. This gives initial conditions of:

$$a_1(t=0) \approx 1 \quad \text{and} \quad a_2(t=0) \approx 0$$

If the growth of  $a_2$  is examined for short enough times so that the approximation  $a_1 \approx 1$  is still valid, then the state 2 occupation probability is:

$$|a_2(t)|^2 = \frac{|\mu_{21z}|^2 E_{oz}^2}{4\hbar^2} \left[ \frac{\sin^2 \frac{(\omega - \omega_{21})t}{2}}{\left( \frac{\omega - \omega_{21}}{2} t \right)^2} \right] \quad (2.38)$$

The bracketed term in Equation (2.38) peaks sharply when  $\omega \approx \omega_{21}$  and is very small everywhere else. This indicates that an absorptive transition is only likely to occur when

the radiating field is at or near resonance with the quantum mechanical transition frequency. Consideration must also be given to the fact that the transition frequency itself is not a delta function but instead is spread over a frequency range defined by the lineshape function. Since we are assuming a monochromatic radiating wave, the relative probability that a transition is possible is also given by the lineshape function:

$$f(\nu) d\nu$$

By incorporating the lineshape function, Equation (2.38) can be integrated over all frequencies to give the total transition probability:

$$|a_2(t)|^2 = \frac{|\mu_{21z}|^2 E_{oz}^2}{4\hbar^2} f(\nu) t \quad (2.39)$$

The z component of the dipole moment is related to the total dipole moment and the electric field amplitude to the energy density by:

$$\begin{aligned} |\mu_{21z}|^2 &= \frac{1}{3} |\mu_{21}|^2 \\ E_{oz}^2 &= \frac{2\rho(\nu)}{\epsilon_0} \end{aligned}$$

The transition rate per molecule is thus given by:

$$\frac{d(|a_2(t)|^2)}{dt} = \frac{2\pi^2}{3\epsilon_0 h^2} |\mu_{21z}|^2 \rho(\nu) f(\nu) \quad (2.40)$$

In the previous section the time rate of change of the excited state population was written in terms of the absorption coefficient  $B_{12}$  (Equation (2.27)). For the case of the weak field in which we are concerned only with the initial population rate change, the population of the ground state is essentially the same as the total population ( $N_1 \approx N$ ).

The transition probability per molecule can then be written as:

$$\frac{1}{N} \frac{dN_2}{dt} = B_{12} \rho(v) f(v) \quad (2.41)$$

By comparing Equations (2.41) and (2.40) we obtain a relation between the absorption coefficient and the transition dipole moment:

$$B_{12} = \frac{2\pi^2}{3\epsilon_0 h^2} |\mu_{21}|^2 \quad (2.42)$$

To complete the circle with Section 2.1.2, the Einstein A coefficient is written in terms of the transition dipole moment:

$$A_{21} = \frac{64\pi^4 \nu_{21}^3}{3hc^3} \left( \frac{1}{4\pi\epsilon_0} \right) |\mu_{21}|^2 \quad (2.43)$$

where  $\nu_{21}$  and  $\mu_{21}$  are the transition frequency and transition dipole moment from the upper to the lower states, respectively. As the value of the transition dipole moment increases, the likelihood of the transition increases. So, we see again, if the transition dipole moment is zero that transition will have a zero probability of occurring. Table 2.3 lists the HF overtone and fundamental Einstein A coefficients.

#### 2.1.4 Small Signal Gain/Absorption

Gain is the amplification that an electromagnetic wave receives as it traverses a medium. The intensity of a laser beam used to probe a gain medium will change according to:

$$\frac{dI(v)}{dy} = \gamma(v) I(v) \quad (2.44)$$

where  $I(v)$  is the laser intensity,  $\gamma(v)$  is the gain coefficient of the medium, and  $y$  is the laser propagation direction (Verdeyen 1995). It is important to note that  $I$  and  $\gamma$  are

**Table 2.3** Einstein A coefficient and wavelength for HF fundamental and overtone transitions (Arunan et al. 1992).

HF Overtone $\nu=2$ to $\nu=0$			HF Fundamental $\nu=2$ to $\nu=1$		
P branch	A (s <sup>-1</sup> )	wavelength (nm)	P branch	A (s <sup>-1</sup> )	wavelength (nm)
J <sub>lower</sub>			J <sub>lower</sub>		
1	23.68	1297.04	1	199.28	2666.78
2	15.90	1304.50	2	135.42	2696.27
3	14.39	1312.56	3	123.93	2727.47
4	13.77	1321.22	4	119.72	2760.44
5	13.43	1330.50	5	117.78	2795.22
6	13.22	1340.41	6	116.75	2831.89
7	13.06	1350.96	7	116.09	2870.52
8	12.93	1362.17	8	115.55	2911.18
R branch	A (s <sup>-1</sup> )	wavelength (nm)	R branch	A (s <sup>-1</sup> )	wavelength (nm)
J <sub>lower</sub>			J <sub>lower</sub>		
0	7.76	1283.85	0	63.43	2612.69
1	9.21	1278.12	1	74.08	2588.00
2	9.75	1272.94	2	77.03	2564.83
3	9.98	1268.32	3	77.30	2543.14
4	10.06	1264.24	4	76.28	2522.88
5	10.06	1260.71	5	74.48	2504.02
6	10.00	1257.73	6	72.20	2486.55
7	9.90	1255.28	7	69.57	2470.41

functions of the laser frequency and that the laser will only interact with the gain medium when it is at or near resonance with a quantum mechanical energy transition. Equation (2.44) can easily be solved for  $\gamma(\nu)$  to give the well-known integrated Beer-Lambert law:

$$\gamma(\nu) = \frac{1}{L} \ln \left[ \frac{I_e(\nu)}{I_o(\nu)} \right] \quad (2.45)$$

where  $L$  is the gain length,  $I_e(\nu)$  is the beam intensity at the exit of the gain region and  $I_o(\nu)$  is the beam intensity at the inlet. If the beam intensity decreases as it traverses the medium,  $\gamma(\nu)$  becomes negative and is then referred to as the absorption coefficient. Therefore, by measuring the input and output beam intensity, Equation (2.45) can be used to determine the gain or absorption of the medium.

The beam intensity increases due to stimulated and spontaneous emission and decreases due to absorption as it interacts with the molecules inside the gain medium. The rate equation for the change in population of the excited state molecules caused by the radiative processes is:

$$\frac{dN_u}{dt} \Big|_{\text{rad}} = -A_{ul}N_u - B_{ul}N_u\rho_v f(v) + B_{lu}N_l\rho_v f(v) \quad (2.46)$$

where the  $u$  and  $l$  subscripts represent the upper and lower energy states, respectively.

The radiation field energy density is related to the beam intensity by:

$$\rho_v = \frac{\text{beam intensity}}{\text{photon velocity}} = \frac{I_v}{c} \quad (2.47)$$

Using this expression and the relationships between the Einstein coefficients (Equations (2.26) and (2.27)), Equation (2.46) can be rewritten as:

$$\frac{dN_u}{dt} \Big|_{\text{rad}} = -A_{ul}N_u - \frac{\sigma(v)}{hv} I_v \left[ N_u - \frac{g_u}{g_l} N_l \right] \quad (2.48)$$

where  $\sigma(v)$  is the stimulated emission cross section:

$$\sigma(v) = A_{ul} \frac{\lambda^2}{8\pi n^2} f(v) \quad (2.49)$$

Because  $hv$  is so small, the second term in Equation (2.48) is an order of magnitude larger than the first term. This allows the spontaneous emission term to be dropped even when the stimulating beam intensity,  $I_v$ , is small. Spontaneous emission of photons plays the important role of initiating laser oscillation but is not significant when calculating gain.

Equation (2.48) can then be written as:

$$hv \frac{dN_u}{dt} \Big|_{\text{rad}} = -\sigma(v) \left[ N_u - \frac{g_u}{g_l} N_l \right] I_v \quad (2.50)$$

The term on the left hand side of Equation (2.50) is the energy of a photon times the rate of change of population density of the excited molecules. Since each photon released adds coherently to the beam intensity and each photon absorbed subtracts from the beam intensity, this term must be equal to the change of intensity of the beam as it propagates through the gain medium:

$$h\nu \frac{dN_u}{dt} \Big|_{\text{rad}} = -\frac{dI_\nu}{dy} \quad (2.51)$$

Substituting this expression into Equation (2.50) gives:

$$\frac{dI_\nu}{dy} = \sigma(\nu) \left[ N_u - \frac{g_u}{g_l} N_l \right] I_\nu \quad (2.52)$$

Comparing the above expression to Equation (2.44) gives the gain (or absorbance) of the medium as a function of population of the upper and lower quantum energy states:

$$\gamma(\nu) = \sigma(\nu) \left[ N_u - \frac{g_u}{g_l} N_l \right] \quad (2.53)$$

If the probing beam intensity is low, it will not affect the population of the excited state energy levels (Verdeyen 1995).  $\gamma(\nu)$  is then referred to as the small signal gain with units of % cm<sup>-1</sup> or cm<sup>-1</sup>.

Clearly for gain to be present:

$$N_u > \frac{g_u}{g_l} N_l \quad (2.54)$$

When this condition is met, a system is said to have a population inversion because it is contrary to the normal state of affairs such as that given by the Boltzmann relationship. It is possible to have gain on a particular ro-vibrational transition without having an inversion of the vibrational levels. However, in typical HF lasers, the vibrational levels

are inverted while the rotational levels within those vibrational levels have Boltzmann distributions (Pimentel and Kompa 1976). There are many different ways to produce a population inversion and much of laser research is dedicated to improving the efficiency of those pumping mechanisms. In HF lasers the population inversion is created by a chemical reaction between atomic fluorine and molecular hydrogen. The kinetics of this reaction as well as other competing chemical reactions within the HF laser is discussed in Section 2.2.

Equations (2.45) and (2.53) relate the measurable quantities ( $I_e/I_o$ ) to the physical properties of the gain medium (populations of upper and lower energy states). This is a key point and the reason for the development of this section. Much of the rest of this research revolves around the measurement of small signal gain and how it relates to the fundamental mechanisms responsible for creating a population inversion inside an HF laser.

### **2.1.5 Spectral Line Broadening**

A transition between two quantum energy levels implies a single distinct frequency ( $\nu = (E_2 - E_1)/\hbar$ ). However, the uncertainty principle dictates that there will be a distribution in the energy related to the lifetime of the excited states. The uncertainty in the energy levels gives rise to the natural linewidth of the transition. The natural linewidth of the HF transitions investigated in this research is very small ( $\sim 10\text{Hz}$ ) and has a negligible effect on the gain. It would in fact be extremely difficult to actually measure the natural linewidth of the HF overtone transitions. There are, however, other transition lineshape broadening mechanisms that will have an effect on the measured gain.

The two main contributors to the broadening of the spectral lineshape are pressure (collisional) broadening and Doppler broadening (Hollas 1998). Pressure broadening is caused by elastic molecular collisions in the flow that cause the phase of the emitting radiation to take discontinuous jumps. This, in turn, shows up as a broadening in the frequency domain. Because the absorption and emission profile of the macroscopic assembly of atoms is the same as that of each individual atom, pressure broadening is termed homogeneous broadening and gives rise to a Lorentzian spectral lineshape:

$$f(v) = \frac{Aw_l}{2\pi \left[ (v - v_c)^2 + \left( \frac{w_l}{2} \right)^2 \right]} \quad (2.55)$$

where  $A$  is the spectral area,  $v_c$  is the line center frequency, and  $w_l$  is the Lorentzian linewidth (full width at half maximum). Since the frequency of molecular collisions is a function of the flow temperature and pressure,  $w_l$  can be written as:

$$w_l = \frac{NQ}{\pi} \sqrt{\frac{16kT}{\pi M}} \quad (2.56)$$

where  $N$  is the number density of the excited species which incorporates the flow pressure dependence,  $Q$  is the collisional cross section,  $k$  is Boltzmann's constant,  $T$  is the static temperature, and  $M$  is molar mass (Demtroder 1982).

Doppler broadening is a form of inhomogeneous broadening because it depends on the motion of the atoms relative to the probing beam. The random motion of the molecules toward or away from the probe beam source creates an apparent shift in the beam frequency, as seen by the molecule, due to the Doppler effect. A Maxwell-Boltzmann distribution of molecular velocities yields a Gaussian lineshape:

$$f(v) = \frac{A}{w_G} \sqrt{\frac{4 \ln(2)}{\pi}} \exp \left[ -4 \ln(2) \left( \frac{v - v_c}{w_G} \right)^2 \right] \quad (2.57)$$

where  $w_G$  is the Gaussian linewidth (FWHM). Since the random molecular velocity is a function of temperature, the Gaussian linewidth can be written as:

$$w_G = 2v_c \sqrt{\frac{2\check{R}T \ln 2}{Mc^2}} \quad (2.58)$$

where  $c$  is the speed of light and  $\check{R}$  is the universal gas constant (Demtroder 1982).

The observed lineshape of a Doppler and pressure broadened transition is called a Voigt lineshape and is a convolution of Gaussian and Lorentzian profiles. Fitting a Voigt profile to the measured lineshape could deconvolve the Gaussian and Lorentzian linewidths (Ward et al. 1974). However, under conditions investigated here, Doppler broadening dominated pressure broadening. This is because the laser cavity pressure is very low (~2-3 torr) and the pressure broadening coefficient for a collision between HF and He is only 0.75 MHz Torr<sup>-1</sup> (Chou et al. 1999a; Chou et al. 1999b). Collisions with other flow species had a negligible effect even though their pressure broadening coefficients are much larger because the cavity flow is over 90% He. The temperature inside the laser cavity is expected to be in the 200 to 500 K range. This gives Doppler broadened Gaussian widths between 400 and 700 MHz.

### 2.1.6 Transition Selection Rules

By absorbing or emitting radiation an HF molecule can transition between the ro-vibrational energy levels listed in Table 2.2. However, this movement is not unrestricted. Transitions between energy levels are governed by the interaction of the radiation field and the electric transition dipole moment of the molecule as stated in Section 2.1.3. In

order for an electromagnetic wave to interact with a molecule it must be at or near resonance with a quantum mechanical energy transition. As a result of this interaction the molecule will undergo transitions. A change in the dipole moment as a function of inter-nuclear separation therefore becomes the criterion for defining the selection rules for the allowed ro-vibrational transitions of diatomic molecules. Time-dependent perturbation theory is needed to quantify this criterion into the requirement that transitions only occur between states for which the transition dipole moment,  $(\mu)_{12}$ , is nonzero:

$$(\mu)_{12} = \int \psi^2 \hat{\mu} \psi^1 d\tau \neq 0 \quad (2.59)$$

where  $\psi^1$  and  $\psi^2$  are the molecular wavefunctions of the initial and final states,  $\hat{\mu}$  is the dipole moment operator, and  $d\tau$  is a differential volume. The molecular wavefunctions can be separated into electronic and nuclear parts ( $\psi_{el}$  and  $\psi_N$ ) by invoking the Born-Oppenheimer approximation. Also, since we are only interested in ro-vibrational transitions within the electronic ground state, the electronic wavefunctions of state 2 and 1 are the same and Equation (2.59) can then be rewritten as:

$$(\mu)_{12} = \int \psi_N^2 \psi_N^1 \int \psi_{el} \hat{\mu} \psi_{el} d\tau_{el} d\tau_N \neq 0 \quad (2.60)$$

Integration over the electronic coordinates reduces Equation (2.60) to:

$$(\mu)_{12} = \int \psi_N^2 \psi_N^1 \mu(R) d\tau_N \neq 0 \quad (2.61)$$

where  $\mu(R)$  is the permanent electric dipole moment function corresponding to the electronic ground state.  $\mu$  is a function of the inter-molecular separation and is directed along the inter-nuclear axis:

$$\mu(R) = \mu(R)(i \sin \theta_N \cos \phi_N + j \sin \theta_N \sin \phi_N + k \cos \theta_N) \quad (2.62)$$

where  $\theta_N$  and  $\phi_N$  are the orientation of the molecule with respect to the z and x axis, respectively. Equation (2.61) becomes:

$$\int_0^{2\pi} \int_0^{\pi} \int_0^{\infty} \psi_2 \psi_1 \mu(R) (\mathbf{i} \sin \theta_N \cos \phi_N + \mathbf{j} \sin \theta_N \sin \phi_N + \mathbf{k} \cos \theta_N) R^2 \sin \theta_N dR d\theta_N d\phi_N \neq 0 \quad (2.63)$$

Substituting the separated form of the rigid-rotor/harmonic oscillator wavefunctions into Equation (2.63) gives:

$$\int_0^{\infty} S_v(q)_2 S_v(q)_1 \mu(R) dR \int_0^{2\pi} \int_0^{\pi} (Y_J^M)_2 (Y_J^M)_1 (\mathbf{i} \sin \theta_N \cos \phi_N + \mathbf{j} \sin \theta_N \sin \phi_N + \mathbf{k} \cos \theta_N) \sin \theta_N d\theta_N d\phi_N \neq 0 \quad (2.64)$$

Notice that  $\mu$  must be nonzero for the transition moment to be nonzero. Therefore, within the rigid-rotor/harmonic oscillator approximation, a molecule must have a permanent dipole moment to have a ro-vibrational spectrum.

Owing to the orthogonality of the spherical harmonics, the three angular integrals in Equation (2.64) vanish unless  $M_2=M_1$  and  $J_2=J_1\pm 1$ . Thus the selection rules for changes in the rotational quantum numbers of a diatomic molecule with no change in electronic state are:

$$\Delta J = \pm 1, \quad \Delta M = 0 \quad (2.65)$$

To solve for the vibrational selection rules, we first must expand  $\mu$  in a Taylor series about the equilibrium bond length,  $R_e$ :

$$\mu(R) = \mu(R_e) + \mu'(R_e)(R - R_e) + \frac{1}{2}\mu''(R_e)(R - R_e)^2 + \dots \quad (2.66)$$

Substituting this expression into the radial part of Equation (2.64) and changing to the variable  $q$  ( $=R-R_e$ ) gives:

$$\begin{aligned}
 & \mu(R_e) \int_{-\infty}^{\infty} S_{\nu}(q)_2 S_{\nu}(q)_1 dq + \mu'(R_e) \int_{-\infty}^{\infty} S_{\nu}(q)_2 q S_{\nu}(q)_1 dq + \\
 & \frac{1}{2} \mu''(R_e) \int_{-\infty}^{\infty} S_{\nu}(q)_2 q^2 S_{\nu}(q)_1 dq + \dots \neq 0
 \end{aligned} \tag{2.67}$$

Because of the orthogonality of the Hermite polynomials, the first integral is nonzero only when  $\nu_2 = \nu_1$ . Likewise the second integral is nonzero only when  $\nu_2 = \nu_1 \pm 1$  and the third integral is nonzero when  $\nu_2 = \nu_1 \pm 2$  or  $\nu_2 = \nu_1$ . Therefore by keeping the higher order terms in the expansion of  $\mu$ , the selection rules for vibrational transitions are:

$$\Delta\nu = 0, \pm 1, \pm 2, \pm 3, \pm \dots \tag{2.68}$$

For most molecules the contributions of the higher order terms is much smaller than the  $\mu'(R_e)$  term which decreases the probability for transitions of  $|\Delta\nu| > 1$  to occur. In HF,  $\Delta\nu = 1$  transitions are  $\sim 100$  times more likely than  $\Delta\nu = 2$  transitions which are in turn much more probable than  $\Delta\nu = 3$  transitions. Single vibrational energy level changes are referred as fundamental transitions and  $\Delta\nu \geq 2$  are termed overtone transitions.

It should be noted that the radial wavefunctions used in Equation (2.64) are those of the harmonic oscillator. The neglected anharmonic perturbation terms of Equation (2.14) produce small changes in the radial part of the nuclear wavefunctions. The actual radial wavefunctions contain contributions from the harmonic oscillator wavefunctions with quantum numbers other than  $\nu$ . Therefore the first term in Equation (2.64) will have a small value for transitions where  $\nu_2 \neq \nu_1$ . Likewise the second term will not be zero when  $\nu_2 \neq \nu_1 \pm 1$  and so on for the other terms. Therefore the anharmonicity corrections further add to the probability of overtone transitions.

### 2.1.7 Thermal Population

Collisions between molecules can also cause transitions between quantum mechanical energy states. These collisional processes work to maintain thermal equilibrium by converting ro-vibrational internal energy into translational kinetic energy.

The Boltzmann relationship describes the thermal equilibrium population distribution:

$$F_s = \frac{g_s e^{-E_s/kT}}{\sum_j g_j e^{-E_j/kT}} \quad (2.69)$$

where  $F_s$  represents the fraction of molecules in energy level  $s$ ,  $E_s$  is the energy value of level  $s$ , and  $g_s$  is the number of degenerate states in level  $s$  (McQuarrie and Simon 1997).

The Boltzmann distribution shows that a level's population depends on the energy required to reach that level relative to  $kT$ . At room temperature,  $kT \approx 205 \text{ cm}^{-1}$ . Since the energy gap between electronic and vibrational energy level is  $60,600 \text{ cm}^{-1}$  and  $3960 \text{ cm}^{-1}$ , respectively, solving Equation (2.69) shows that practically all room temperature HF

molecules are in the ground electronic and vibrational levels (Dunning 1976). In contrast, the rotational levels have small energy gaps and are significantly populated.

Figure 2.2 shows the population distribution of the rotational levels within the  $v = 2$  vibrational level in HF at 100K and at 400 K. As the temperature increases, the number of populated rotational levels increases and the J level with the highest population fraction shifts to a higher value.

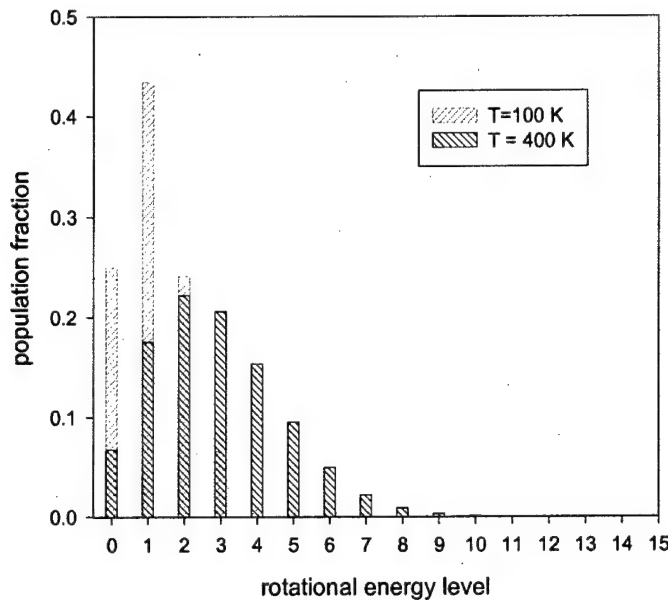


**Figure 2.2** HF rotational energy level distribution in  $\nu=2$  at 100 K and 400 K.

### 2.1.8 Ro-Vibrational Spectrum

Ro-vibrational transitions are identified by the change in the rotational level (McQuarrie and Simon 1997). The letter P is assigned to transitions in which the upper state J value is one less than the lower state J value. The particular transition is identified by including the lower state J value in parentheses: P( $J_{\text{lower}}$ ). For example, a transition from  $\nu=2$ ,  $J=6$  to  $\nu=0$ ,  $J=7$  is a P(7) transition. Specification of the vibrational transition (i.e., fundamental or overtone) is typically not stated requiring the reader to infer this from the context of the text. The letter R is assigned to transitions whose upper state J value is one greater than the lower state value. The transition from  $\nu=2$ ,  $J=8$  to  $\nu=0$ ,  $J=7$  is an R(7) transition. This nomenclature applies whether the radiation is absorbed or emitted by the molecule. The frequency and wavelength of the absorbed or emitted radiation is determined from the difference in quantum energy levels:

$$E_2 - E_1 = h\nu = h\frac{c}{\lambda} \quad (2.70)$$

where  $h$  is Planck's constant,  $c$  is the speed of light, and  $\nu$  and  $\lambda$  are the frequency and wavelength of the radiation, respectively. Since R branch transitions have greater energy change they have lower wavelengths than P branch transitions. Table 2.3 lists the wavelengths for the fundamental and overtone P and R branch transitions of HF (Arunan et al. 1992). Figure 2.3 shows the relative gain distribution of the HF overtone transition ( $\nu=2$  to  $\nu=0$ ) for a given population inversion when the upper and lower ro-vibrational manifolds have Boltzmann distributions with a temperature of 400 K. The P branch transitions have higher gain due to the higher transition probability given by the Einstein A coefficients. However, even though the Einstein A coefficient is larger for P1 than for P2 or P3, it has less gain due to the Boltzmann population distribution of the vibrational levels. The fundamental gain distribution is the same as the overtone distribution with the only difference being a shift along the x-axis to the fundamental wavelengths.

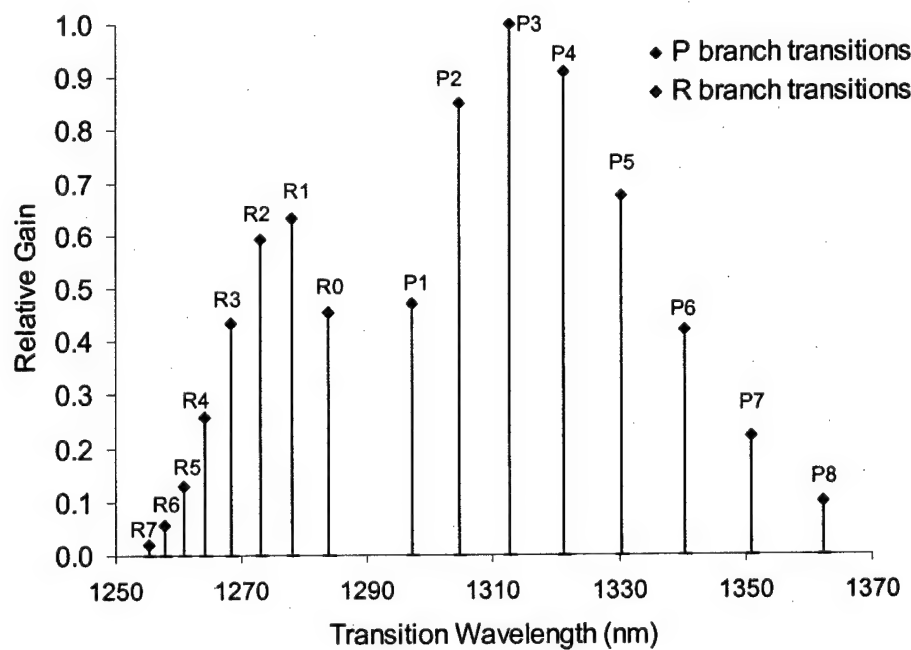


**Figure 2.3** Relative gain distribution of HF  $\nu=2$  to  $\nu=0$  overtone transition at 300K.

## 2.2 HF Laser chemistry

Excited HF molecules are produced inside HF lasers by two different chemical reactions. The *Cold Pumping Reaction*, which is the primary pumping mechanism for producing the population inversion, is the reaction between atomic fluorine and molecular hydrogen. The reaction between molecular fluorine and atomic hydrogen can also produce excited HF molecules. This reaction has a much higher heat of reaction than the *Cold Pumping Reaction* and is therefore referred to as the *Hot Pumping Reaction*. Both of these reactions are in the category of three-atom exchange reactions:

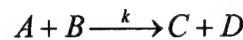


where *A*, *B* and *C* are different atomic species. These types of reactions will be exothermic if the *AB* chemical bond is stronger than the *BC* chemical bond. Such reactions are generally extremely fast because the activation energies are small and there are no significant restrictive geometrical requirements for a collision to be reactive. For a chemical reaction to create a population inversion there must be some dynamical constraint in the forming of the products that prevents a purely statistical (Boltzmann) distribution and selectively channels part of the reactive energy into one or more higher energy states. In the case of the primary HF pumping reaction, the reaction exothermicity preferentially populates the vibrational energy levels of the reaction products.

Beside the need for a population inversion, the production of laser gain also depends upon the stimulated emission cross section. The stimulated emission cross section is related to the Einstein coefficient which is a measure of the probability of a radiative energy transfer as discussed in Section 2.1.3. The radiative processes compete for the energy stored in the population inversion with collisional processes that work to restore

thermal equilibrium to the system. Therefore in order to create a laser, the rate of energy extraction by stimulated emission must be greater than the rate of energy transfer by collisional processes. In HF lasers the collisional deactivation processes of interest are reactive quenching and direct energy transfer. In reactive quenching the excited molecules react with another species to form a new chemical compound. Direct energy transfer can occur by R-R, V-V, or V-T mechanisms. R-R energy transfer involves transfer of energy between rotational levels of the excited molecules within the same vibrational level. V-T energy transfer involves conversion of the vibrational energy of the excited molecules into translation energy of the collision partners. V-V energy transfer involves the direct vibrational energy exchange between the excited molecules and other vibrationally excited species.

Nearly all the chemical reactions in HF lasers have the form:



where A, B, C and D are different atomic or molecular species and  $k$  is the characteristic rate constant for the reaction. The rate of reaction,  $R$ , is defined by:

$$R = -\frac{d[A]}{dt} = -\frac{d[B]}{dt} = \frac{d[C]}{dt} = \frac{d[D]}{dt} = k[A][B] \quad (2.71)$$

where the brackets indicate species concentration. For an isolated reaction, the rate of reactant consumption and the rate of product generation are dependent on the rate constant and the concentrations of the reactants. Solutions to Equation (2.71) show an exponential decay in reactant concentration and an exponential increase in product concentration. Inside the laser cavity, the reactions are not isolated which requires simultaneously solving the rate equation for every possible chemical reaction. There are only 6 chemical species present in the discharge driven HF laser considered here: F, F<sub>2</sub>,

H, H<sub>2</sub>, HF and He. However, each of the three molecular species can appear in different ro-vibrational energy levels. To completely represent the HF laser chemical system, each ro-vibrational energy level must be treated as a separate species with individual rate constants for each state-to-state reaction. This creates a nearly intractable number of chemical reactions.

Further adding to the complexity of the HF laser chemical system is the temperature dependence of the rate constants. The temperature dependence is typically written in the Arrhenius form:

$$k(T) = A(T)e^{-E_A/RT} \quad (2.72)$$

where  $T$  is absolute temperature,  $E_A$  is the activation energy and  $R$  is the gas constant (Steinfeld et al. 1989). The pre-exponential factor,  $A(T)$ , may have a weak temperature dependence, typically no more than some fractional power of  $T$ . The activation energy can be thought of as the amount of energy that must be supplied to the reactants in order to get them to react with each other. Since  $E_A$  is a positive energy quantity, the majority of reactions have  $k$  increasing with temperature. The following sections describe the temperature-dependent rate constants for the chemical reactions currently thought to represent the kinetic system of the HF laser. The primary reference for these rate constants is the recent review article by Manke and Hager (2001). All of the rate constants presented here have units of (cm<sup>3</sup> molecules<sup>-1</sup> s<sup>-1</sup>) with temperature in units of (K). A summary of the functional form of the rate constants and a comparison of the room temperature rate constants are given in Tables 2.4 and 2.5, respectively, at the end of this section.

### 2.2.1 Cold Pumping Reaction

As stated previously the principal pumping reaction in continuous wave HF chemical lasers is the reaction between atomic fluorine and molecular hydrogen:



The dynamics of the reaction are governed by the interaction of the electronic potential energy (including nuclear-nuclear repulsion) functions of the individual reactants and products. Combining of these potential energy curves produces a multi-dimensional surface in which the potential energy is given in terms of reaction coordinates. For the collinear three-atom exchange reaction, F-H-H, the reaction coordinates are the H-H bond length and the H-F bond length. As the F atom moves closer to the H<sub>2</sub> molecule, the H<sub>2</sub> bond stretches and the H-F bond begins to form. After the HF bond forms, the freed H atom recoils from the newly formed molecule, lengthening the H-H distance. Figure 2.4 gives an example of a potential energy contour surface for a generic three-atom exchange reaction (A+BC → AB+C). The dashed line in Figure 2.4 represents the reaction path along a line of minimum potential energy. The F+H<sub>2</sub> reaction is of the general type in which there is a potential energy barrier between the reactants and products. This is evident in Figure 2.4 by the increase in potential energy along the reaction path and the formation of a saddle point. The height of the saddle point is the required activation energy for the reaction. The saddle point is also termed the transition point because the H-H bond has been broken and H-F bond has not yet formed. The transition point for the HF reaction occurs when the reactants are approaching each other, which tends to favor vibrational excitation of the products (Steinfeld et al. 1989). The

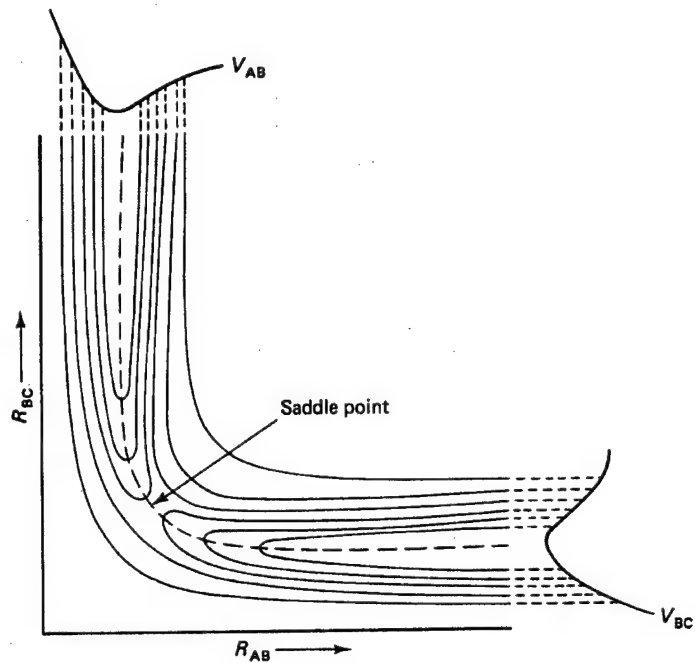


**Figure 2.4** Potential energy contour map of collinear three-atom reaction,  $A+BC \rightarrow AB+C$ .  $R_{AB}$  and  $R_{BC}$  represent the  $AB$  and  $BC$  bond lengths, respectively. The dashed line represents the reaction path along the minimum potential energy and the saddle point lies at the transition state (Steinfeld et al. 1989).

reason for this is that the H-F distance is still decreasing when the energy of the exothermicity is released. This causes the freed H atom to recoil away from the newly formed molecule depositing a large fraction of the energy into the vibrational modes of the HF bond. The average values for the partition of the energy among the various degrees of freedom of the reaction products are:

$$\langle f_v \rangle = 0.66$$

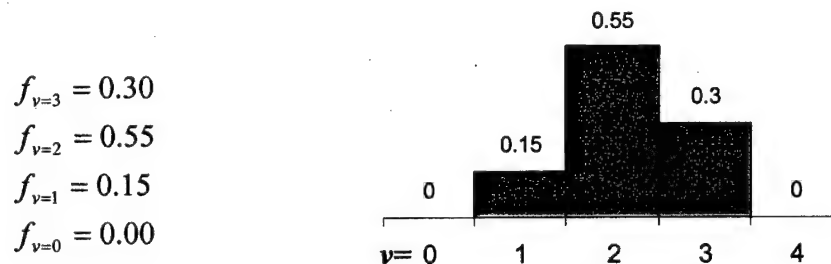
$$\langle f_R \rangle = 0.08$$

$$\langle f_T \rangle = 0.26$$

where  $\langle f_v \rangle$ ,  $\langle f_R \rangle$  and  $\langle f_T \rangle$  are the average fractions of energy deposited into the vibrational, rotational and translational degrees of freedom, respectively (Steinfeld et al.

1989). Therefore, the HF molecules are produced with appreciable vibrational excitation, but relatively little rotation and translation.

Figure 2.5 shows a slice of the potential energy contour surface along the reaction path of minimum potential energy for the  $\text{F}+\text{H}_2$  reaction. The heat of reaction,  $\Delta\text{H}$ , and activation energy,  $E_A$ , are  $32.0 \text{ kcal mol}^{-1}$  and  $1.6 \text{ kcal mol}^{-1}$ , respectively (Cohen and Bott 1976). If all this energy ( $\Delta\text{H}+E_A$ ) is available to populate the ro-vibrational energy levels of the formed HF molecules, then the highest ro-vibrational level that can be reached is  $v=3$   $J=3$ . There is, therefore, some probability that excited HF molecules will be formed in the first three vibrational bands. The fraction of molecules channeled into each vibrational band is (Cohen and Bott 1976):



The vibrational levels are therefore inverted and the possibility of building a laser between the vibrational manifolds exists. Even though the largest population inversion exists for the  $v = 2$  to  $v = 0$  overtone transition, the largest gain ends up being on the  $v = 2$  to  $v = 1$  fundamental transition due to differences in the Einstein coefficients.

Despite being extensively studied, both theoretically and experimentally, there is still some uncertainty in the overall rate constant for the cold pumping reaction. The accepted value is (Manke and Hager 2001):

$$k(T) = f_v (1.1 \pm 0.1) \times 10^{-10} e^{-(450 \pm 50)/T} \quad [\text{cm}^3 \text{ molecules}^{-1} \text{ s}^{-1}] \quad (2.74)$$

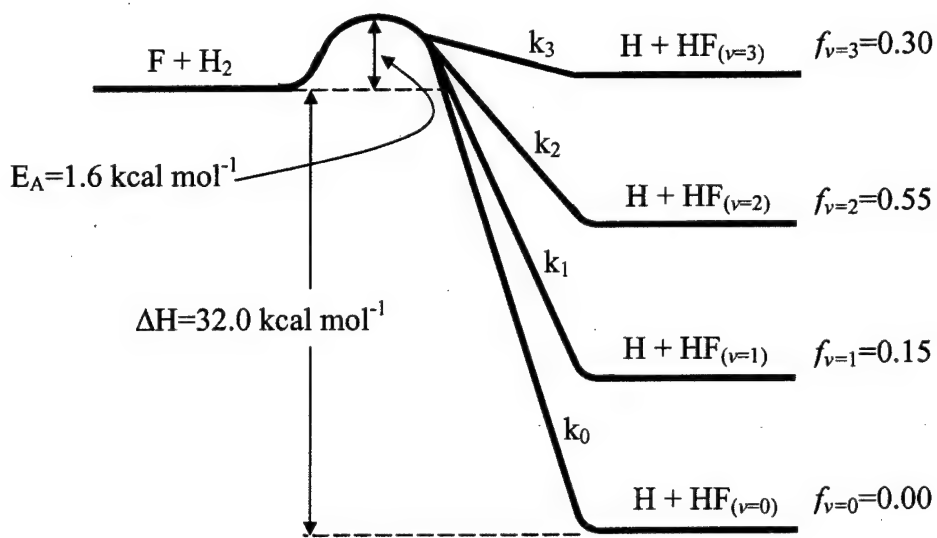


**Figure 2.5**  $\text{F} + \text{H}_2 \rightarrow \text{HF} + \text{H}$  reaction path along the minimum potential energy surface showing the vibrational distribution of the products.

over the temperature range  $190 \text{ K} \leq T \leq 376 \text{ K}$ . However, the overall rate constant has also been experimentally determined to be (Manke and Hager 2001):

$$k(T) = f_v (2.2 \pm 0.4) \times 10^{-10} e^{-(595 \pm 50)/T} \quad [\text{cm}^3 \text{ molecules}^{-1} \text{ s}^{-1}] \quad (2.75)$$

over the temperature range  $295 \text{ K} \leq T \leq 765 \text{ K}$ . At 295 K, Equation (2.74) gives a value 18% larger than Equation (2.75) and the difference grows to 27% at 376 K. For a rate constant this is not a large discrepancy and the error bars for each expression overlap for this temperature range. The temperature in the laser flow investigated here can be expected to vary from as low as 150 K up to 500 K and even higher for a combustor-driven system. A single rate expression over this temperature range would be beneficial. Since this is not available, it is generally accepted to use Equation (2.74) for temperatures below 376 K and Equation (2.75) for temperatures above 376 K (Manke and Hager 2001).

## 2.2.2 Hot Pumping Reaction

The hot pumping reaction:



is a three-atom exchange reaction with dynamics similar to those of the cold pumping reaction. The heat of reaction and activation energy are  $98.0 \text{ kcal mol}^{-1}$  and  $2.4 \text{ kcal mol}^{-1}$ , respectively (Cohen and Bott 1976). The significantly higher heat of reaction comes from the breaking of the F-F bond, as opposed to the much stronger H-H bond in the cold reaction, and results in population of vibrational levels up to  $v=9$ . The fraction of molecules channeled into each vibrational band is (Manke and Hager 2001):

$$f_{v=9} = 0.04$$

$$f_{v=8} = 0.08$$

$$f_{v=7} = 0.14$$

$$f_{v=6} = 0.28$$

$$f_{v=5} = 0.22$$

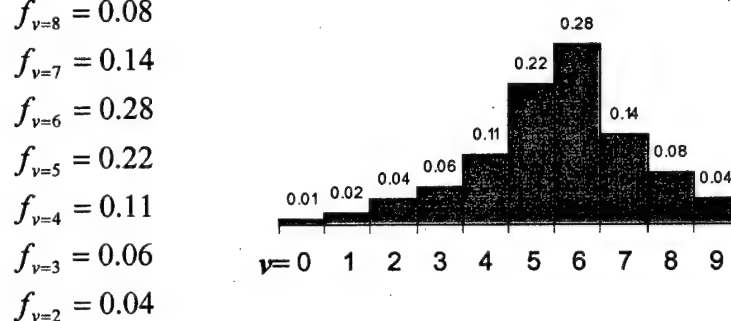
$$f_{v=4} = 0.11$$

$$f_{v=3} = 0.06$$

$$f_{v=2} = 0.04$$

$$f_{v=1} = 0.02$$

$$f_{v=0} = 0.01$$



Because the increased exothermicity is spread over a much larger range of vibrational energy levels, the population inversion created in this case is not as strong as that created by the cold pumping reaction.

A recent review of relevant HF laser kinetics by Manke and Hager (2001) gives two temperature-dependent expressions for the rate constant of the hot pumping reaction. One is attributed to Cohen and Bott (1982) and the other to Baulch (1981). At room temperature these expressions differ by  $\sim 40\%$  and in lieu of more information Manke and

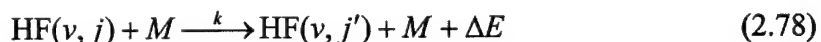
Hager chose to adopt the more widely used Cohen and Bott expression. However, more recently Manke et al (2002) conducted an independent experiment in which they measured a room temperature rate constant more in line with the Baulch value and subsequently changed their recommendation. The recommended rate constant is then given by (Manke and Hager 2001):

$$k(T) = f_v 1.46 \times 10^{-10} e^{-1210/T} \quad [\text{cm}^3 \text{ molecules}^{-1} \text{ s}^{-1}] \quad (2.77)$$

over the temperature range from 290 K  $\leq T \leq 570$  K. At room temperature the overall rate constant (i.e.,  $f_v = 1.0$ ) for the hot pumping reaction is an order of magnitude slower than the overall rate constant for the cold pumping reaction. Along with the weaker population inversion, this greatly increases the difficulty of building a laser based solely on the hot pumping reaction. The hot pumping reaction does help the population inversion of the cold pumping reaction and provides a path for creating more F atoms needed by the cold pumping reaction. However, population of the higher vibrational levels also produces more pathways for vibrational deactivation.

### 2.2.3 R-R Energy Transfer

The R-R energy transfer between a ro-vibrationally excited HF molecule and a collision partner changes the rotational level but not the vibrational level of the HF molecule and is accompanied by a small energy release:

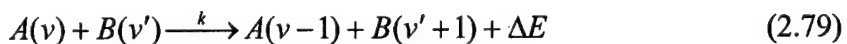


where  $M$  represents nearly any flow species. Because the energy gap between the rotational levels is so small, the collision partners do not exchange significant energy. The probability of a collision exchanging this small amount of energy is very high,

corresponding to a rate constant that is very fast. Experimental and theoretical investigations both show that the rotational relaxation rate constants are 10-100 times larger than vibrational relaxation rate constants (Manke and Hager 2001). Therefore on the vibrational relaxation time frame, the rotational levels can approximately be considered in thermal equilibrium with the translational degrees of freedom. To a good approximation, the ro-vibration energy distribution can be described by a Boltzmann distribution of the rotational levels within each vibrational band. This allows a single rate constant to be assigned to reactions within each ro-vibrational manifold, thus greatly reducing the number of state-to-state chemical reactions in the system.

#### 2.2.4 V-V Energy Transfer

V-V energy transfer involves direct vibrational energy exchange between the excited molecules and other vibrationally excited species (Yardley 1980). Typically one molecular species increases one vibrational quantum level while the other decreases one vibrational quantum level:



Multi-quantum level changes are generally allowed but typically occur at much smaller rates. In these processes the total number of vibrational quanta is conserved. If the energy transitions of the two molecules are nearly resonant with each other,  $\Delta E$  is small and the reaction is only slightly exothermic or endothermic. In this case the barrier to the reaction is small and the reaction will have a large rate constant. If  $\Delta E$  is large, the translational modes of one of the collision partners must absorb (or release) a lot of energy, greatly decreasing the probability of reaction and reducing the rate constant.

Near-resonant V-V energy transfers typically have much larger rate constants than V-T energy transfers but smaller rate constants than those for R-R energy transfer mechanisms. As a result, V-V energy transfers are a primary source of deactivation, which will work to quickly establish a Boltzmann statistical distribution of the initially inverted HF vibrational levels. Vibrational temperatures of the Boltzmann distribution, which can be determined from Equation (2.69), can reach as high as 10,000 K in HF lasers. Since the HF vibrational energy is essentially isolated from the translation energy due to the much slower V-T rate constants, this vibrational temperature can be associated with the population inversion created by the cold pumping reaction and is indicative of the large heat of reaction a large portion of which is deposited into the vibrational modes. However, even at these very high vibrational temperatures the majority of the HF molecules will be in the vibrational ground state ( $v=0$ ) after equilibrium is reached between the vibrational energy levels. V-V energy transfer will only occur between flow species that can be vibrationally excited. This gives three possible V-V combinations: HF( $v$ )+HF( $v$ ), HF( $v$ )+H<sub>2</sub> and HF( $v$ )+F<sub>2</sub>.

**a. HF** HF molecules exchange vibrational energy through the reaction:

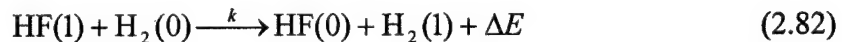


where it is assumed that  $v' \geq v$ . For a true harmonic oscillator, the vibrational levels are evenly spaced and therefore  $\Delta E = 0$  which would result in extremely fast rate constants. The anharmonicity of the HF molecule creates unevenly spaced vibrational levels and reduces the rate constant for V-V energy transfer (Manke and Hager 2001):

$$k(T) = 4.5 \times 10^{-9} (v+1)^{0.35} T^{-1} \quad [\text{cm}^3 \text{ molecules}^{-1} \text{ s}^{-1}] \quad (2.81)$$

At 300 K for  $v=2$  this rate constant is about 50% larger than the cold pumping rate constant into  $v=2$ . As more and more excited HF is produced by the pumping reaction, the effect of deactivation will increase and eventually dominate the pumping reaction. It is important to note that the rate constant has only been measured for  $v=v'=1$  (i.e.,  $\text{HF}(1)+\text{HF}(1) \rightarrow \text{HF}(2)+\text{HF}(0)$ ) and the measurements may include significant V-T energy transfer contributions. As a result, the rate constant is highly uncertain for all vibrational quantum numbers. This is very unfortunate because V-V energy transfer between the HF vibrational bands is clearly a dominant deactivation mechanism and laser performance will be sensitive to these rate constants.

**b.  $\text{H}_2$**  The transition energies between  $v = 0$  and  $v = 1$  for  $\text{H}_2$  and HF are  $4160 \text{ cm}^{-1}$  and  $3962 \text{ cm}^{-1}$ , respectively. This makes the V-V energy transfer:



somewhat endothermic with an energy defect,  $\Delta E = -198 \text{ cm}^{-1}$ . This energy deficit can be overcome by the translational energy of the collision partners, which is  $kT \approx 205 \text{ cm}^{-1}$  at room temperature, resulting in a room-temperature rate constant of (Manke and Hager 2001):

$$k(T) = (5.2 \pm 0.4) \times 10^{-13} \quad [\text{cm}^3 \text{ molecules}^{-1} \text{ s}^{-1}] \quad (2.83)$$

The anharmonicity of HF increases the energy deficit for  $v \geq 2$ , which in turn decreases the rate constant. Therefore, the dominant energy transfer mechanism for  $v \geq 2$  is believed to be through V-T processes, which are discussed in the following section. In lieu of more temperature-dependent data, the room-temperature rate constant is recommended for reaction (2.82).

**c.  $F_2$**  The transition energy between  $v=0$  and  $v=1$  for  $F_2$  is  $893\text{ cm}^{-1}$  (Chase 1998). This creates a large energy deficit with HF and suggests a very low rate constant for V-V energy transfer. Therefore V-V energy transfer by  $\text{HF}(v)+F_2$  is not expected to have a significant impact on HF laser kinetics. The V-T energy transfer between  $\text{HF}(v)$  and  $F_2$  is discussed in the following section.

### 2.2.5 V-T Energy Transfer

V-T energy transfer involves conversion of the vibrational energy of the excited molecules into translation energy of the collision partners (Yardley 1980). These processes tend to be much slower than the other direct energy transfer mechanisms because the collision partners have to absorb whole quanta of vibrational energy, which is nearly  $4000\text{ cm}^{-1}$  for HF.

**a. Self Deactivation** Deactivation of vibrationally excited HF by ground state HF is a principal relaxation mechanism in the HF laser:

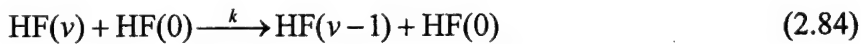


Figure 2.6 shows an example of the possible energy transfer routes for  $\text{HF}(v=2)$ . The possible mechanisms include “true” V-T relaxation (the solid arrow in Figure 2.6) and near-resonant V-R redistribution (broken arrows in Figure 2.6). During a “true” V-T relaxation process the rotational quantum number of the excited molecule remains fixed while the vibrational level decreases. The released energy is transferred to the translational modes of the ground state quenching molecule. A near-resonant V-R redistribution relaxes the excited molecule to a lower vibrational level with a much higher rotational level. Since the final state has nearly the same energy as the initial state,

very little energy is transferred to the quenching molecule and as a result the rate of reaction is very fast. The rotational levels of the lower vibrational manifold would then be brought into thermal equilibrium by the very fast R-R energy transfer mechanism.

Regardless of the actual mechanism, the end result is the same and the rate constant for the overall deactivation process has been determined as (Manke and Hager 2001):

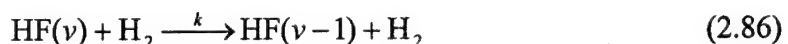
$$k(T) = 9.0 \times 10^{-12} A(v) T^{-0.8} \quad [\text{cm}^3 \text{ molecules}^{-1} \text{ s}^{-1}] \quad (2.85)$$

where  $v$  is the vibrational quantum number of the initial energy state. The coefficients for the different vibrational levels are given by (Manke and Hager 2001):

$$\begin{aligned} A(1) &= 12.0 \\ A(2) &= 218.0 \\ A(3) &= 315.2 \\ A(4) &= 764.0 \\ A(5) &= 1610.3 \\ A(6) &= 3107.0 \\ A(7) &= 4339.0 \end{aligned}$$

Although multi-quantum vibrational level changes are possible, the majority of evidence indicates that they account for a very small fraction of the total relaxation rate and therefore only single vibrational quantum transitions will be tracked. At 300 K, the self-deactivation rate constant for  $v=2$  is actually 50% larger than that for the cold pumping reaction into  $v=2$ . Fortunately, the cold pumping reaction does not populate the  $v=0$  level, so self-deactivation has to wait until some other mechanism creates ground state HF before it can begin to compete with the pumping reaction.

**b.  $\text{H}_2$**  The V-T energy transfer between molecular hydrogen and HF is given by:



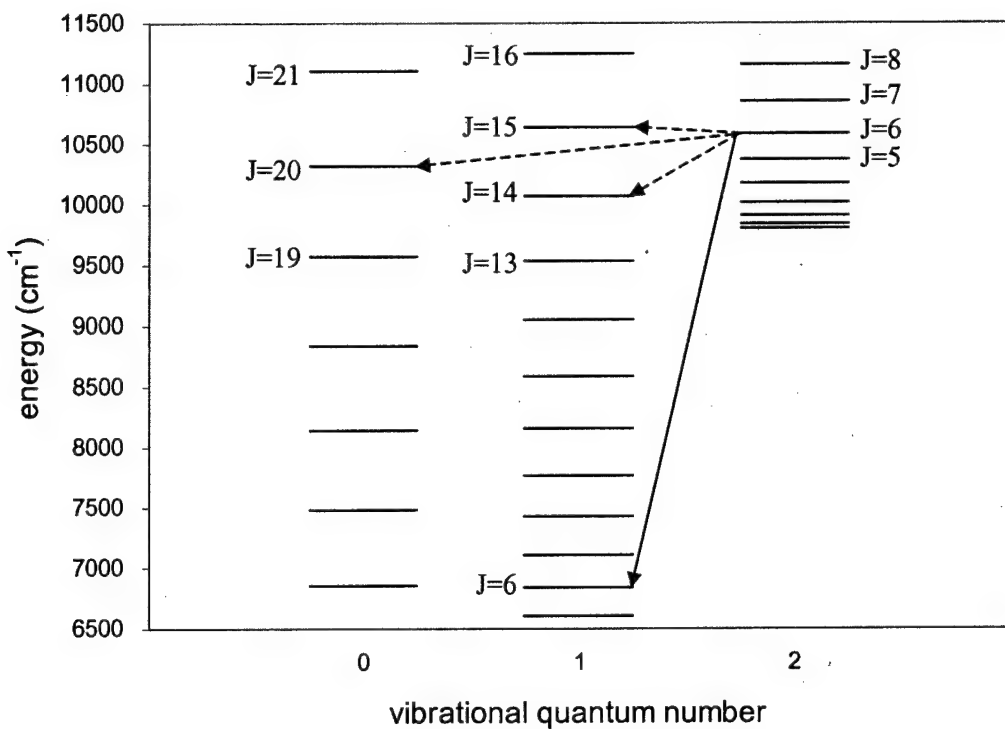


**Figure 2.6**  $\text{HF}(v) + \text{HF} \rightarrow \text{HF}(v-1) + \text{HF}$  energy transfer routes. Solid arrow represents “true” V-T energy relaxation process. Broken arrows represent near-resonant V-R energy transfer.

Experimental investigations have shown the rate constant of this reaction to be

independent of temperature (Manke and Hager 2001):

$$k = A(v)1 \times 10^{-12} \quad [\text{cm}^3 \text{ molecules}^{-1} \text{ s}^{-1}] \quad (2.87)$$

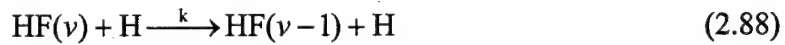
where the vibrational quantum level specific coefficients are given by (Manke and Hager 2001):

$$\begin{aligned}
 A(2) &= 0.2 \pm 0.1 \\
 A(3) &= 0.35 \pm 0.04 \\
 A(4) &= 0.50 \pm 0.2 \\
 A(5) &= 1.6 \pm 0.3 \\
 A(6) &= 3.5 \pm 1.0 \\
 A(7) &= 9.1 \pm 2.7
 \end{aligned}$$

The rate constant for the deactivation of  $\text{HF}(v=2)$  is  $\sim 2 \times 10^{-13}$ , which is two orders of magnitude smaller than the rate constant for the cold pumping reaction into  $v=2$ .

However, the  $\text{H}_2$  flow rate is typically set much higher than the stoichiometric requirement for the pumping reaction in order to speed the rate of reaction. The excess  $\text{H}_2$  will increase deactivation by the above process.

**c. H atoms** H atoms can remove vibrationally excited HF from the flow by reactive quenching and by V-T energy transfer:



Here again multi-quantum vibrational energy level changes are possible but at a much lower rate and are therefore ignored. The rate constant is then given by (Manke and Hager 2001):

$$k(T) = 1.7 \times 10^{-8} A(v) T^{-1} + 1.7 \times 10^{-12} B(v) e^{-352/T} \quad [\text{cm}^3 \text{ molecules}^{-1} \text{ s}^{-1}] \quad (2.89)$$

where the vibrational quantum level specific coefficients are (Manke and Hager 2001):

$A(1)=0.0$	$B(1)=0.4$
$A(2)=0.0$	$B(2)=0.7$
$A(3)=1.4$	$B(3)=0.7$
$A(4)=2.0$	$B(4)=0.7$
$A(5)=2.7$	$B(5)=0.7$
$A(6)=3.5$	$B(6)=0.7$

At 300 K and  $v = 2$ ,  $k \sim 10^{-13}$  which is two orders of magnitude smaller than the rate constant for the cold pumping reaction. However,  $k \sim 10^{-11}$  for  $v = 3$  at 300 K making the deactivation of  $\text{HF}(v = 3)$  into  $v = 2$  much faster than deactivation of  $\text{HF}(v = 2)$  into  $v = 1$ . This energy transfer process therefore actually helps the population inversion. Also, since H atoms are produced by the cold pumping reaction, they are present at the formation of the excited HF making a collision highly probable. This reaction essentially takes all of the  $\text{HF}(v \geq 3)$  and very quickly puts it in  $v = 2$ . Since the cold pumping

reaction channels 30% of the HF into  $v = 3$ , this reaction could have an enormous effect on both the fundamental and overtone gains.

The rate constants presented here are based on the experiments of Heidner and Bott (1978). The only other experimental investigation into reaction (2.88) is by Bartoszek et al (1978), which refutes some of the previous claims. Heidner and Bott used laser-induced fluorescence to monitor the removal rate of HF( $v=3$ ) mixed with varying H atom concentration. They attributed the total HF( $v=3$ ) removal rate to a combination of reactive quenching ( $H + HF(v=3) \rightarrow H_2 + F$ ) and vibrational deactivation ( $H + HF(v=3) \rightarrow H + HF(v=2)$ ). After calculating the reactive quenching rate constant from the equilibrium constant and the cold pumping reaction rate constant, the vibrational deactivation reaction was shown to account for ~80% of the total HF( $v=3$ ) removal. Bartoszek et al conducted a similar experiment in which they monitored the chemiluminescence of HF( $v=3$ ) and HF( $v=2$ ) and determined the relative rate constants. These experiments did not show an increase in HF( $v=2$ ) signal corresponding to HF( $v=3$ ) removal, thus calling into question vibrational deactivation as the dominant reaction path. Over the past 25 years most HF laser kinetics models have used some form of the Heidner and Bott relation and in lieu of more data it will also be adopted here.

**d. F atoms** F atoms deactivate vibrationally excited HF according to:



with a rate constant of (Manke and Hager 2001):

$$k(T) = 2.7 \times 10^{-11} v e^{-1359/T} \quad [\text{cm}^3 \text{ molecules}^{-1} \text{ s}^{-1}] \quad (2.91)$$

where  $v$  is the vibrational quantum number.  $k \sim 10^{-13}$  for  $v=2$  at 300 K. This again is two orders of magnitude smaller than the pumping rate constant. However, since F atoms are

also present at the formation of the excited HF, they could play a key role by creating initial concentrations of ground state HF that begin the very fast self-deactivation mechanism.

**e. He and F<sub>2</sub>** He and fluorine molecules can deactivate excited HF according to:



with a rate constant given by (Manke and Hager 2001):

$$k(T) = 1.7 \times 10^{-29} A(\text{M}) \nu T^{4.5} \quad [\text{cm}^3 \text{ molecules}^{-1} \text{ s}^{-1}] \quad (2.93)$$

where M= He or F<sub>2</sub> and the species specific coefficients are given by (Manke and Hager 2001):

$$\begin{aligned} A(\text{He}) &= 3.7 \\ A(\text{F}_2) &= 2.0 \end{aligned}$$

Both of these rate constants are on the order of 10<sup>-17</sup> at 300 K for v=2. F<sub>2</sub> is present in the laser due to incomplete dissociation in the discharge tube. In general the dissociation fraction is high making the F<sub>2</sub> concentration a small fraction of the F atom concentration further reducing the F<sub>2</sub> deactivation effect. He, on the other hand, is the biggest constituent of the flow with concentrations 100 to 1000 times greater than any other flow species. This gives the rate of deactivation by He the same order of magnitude as deactivation by F atoms. Therefore He may also play a role in the initial production of ground state HF.

### 2.2.6 Reactive Quenching

Reactive quenching of HF by H atoms:



is the reverse of the cold pumping reaction and therefore described by the same potential energy surface. Figure 2.4 shows that the barrier for  $v=0, 1$  or  $2$  is very large suggesting very slow reaction rates. The rate for the higher vibrational levels is given by (Manke and Hager 2001):

$$k(T) = 3.0 \times 10^{-11} T^{0.179} e^{-382/T} \quad [\text{cm}^3 \text{ molecules}^{-1} \text{ s}^{-1}] \quad \text{for } v = 3 \quad (2.95)$$

and

$$k(T) = g(v, v') 1.0 \times 10^{-10} e^{-252/T} \quad [\text{cm}^3 \text{ molecules}^{-1} \text{ s}^{-1}] \quad \text{for } v = 4 - 6 \quad (2.96)$$

$$\begin{aligned} g(4,0) &= 0.5 & g(4,1) &= 0.5 \\ g(5,0) &= 0.5 & g(5,1) &= 1.0 \\ g(6,0) &= 0.5 & g(6,1) &= 0.5 & g(6,2) &= 1.5 \end{aligned}$$

At 300 K,  $k \sim 10^{-11}$  for  $v=3$  and is twice as large as the rate for the cold pumping reaction into  $v=3$ . This indicates that the reactive quenching barrier is smaller than the barrier for the cold pumping reaction into  $v=3$ . However, as discussed previously, the H atom concentration is small and therefore not likely to have a significant affect on laser performance. In addition, the reactive quenching does not directly affect the population of HF  $v=2$  and  $v=1$  which is the primary population inversion. Furthermore, a benefit of reactive quenching is the creation of an additional F atom source. The higher HF vibrational levels are converted into F atoms that can react to produce more HF( $v=2$ ).

### 2.2.7 Fluorine Dissociation and Recombination

Few parameters are as important to HF laser performance as the efficiency of F atom generation. The complex interplay of thermal  $F_2$  dissociation, three-body F atom recombination, and heterogeneous (wall) recombination determines the initial F atom concentration, and thus the maximum concentration of vibrationally excited HF.

The thermal dissociation of fluorine is:



where  $\Delta E$  is the dissociation energy and  $K_{equi}$  is the equilibrium constant. The dissociation energy for molecular fluorine is firmly established at  $36.94 \pm 0.14 \text{ kcal mol}^{-1}$  (Vasiliev et al. 1999). Likewise, the equilibrium constant has also been firmly established (Vasiliev et al. 1999):

$$K_{equi} = 1.855 \times 10^1 e^{-18920/T} \quad [\text{mole cm}^3] \quad (2.98)$$

The equilibrium constant is the ratio of the forward and reverse rate constants. The large negative exponential factor indicates that the temperature must be very high in order to drive the reaction to the right and get substantial thermal dissociation. The discharge tube used in this research does not thermally dissociate the  $F_2$  as described by Equation (2.97). Instead it uses the kinetic energy of a stream of electrons to bombard the fluorine and break it apart. This is an extremely complex problem in plasma physics and no attempt is made here to model this process. A titration experiment (discussed in Section 3.4) is instead used to measure the dissociation fraction of the fluorine exiting the discharge tube and attention is turned to the chemistry within the nozzle and laser cavity.

F atoms can recombine to form fluorine molecules through three body collisions:



Because of their complexity, these processes have not been well characterized. For the F atoms to recombine they must collide with a third body at nearly the same instant and deposit the dissociation energy, suggesting very slow rate constants. The accepted rate constant is given by (Manke and Hager 2001):

$$k = A(M) \times 10^{-34} \quad [\text{cm}^3 \text{ molecules}^{-1} \text{ s}^{-1}] \quad (2.100)$$

where M= He or F<sub>2</sub> and the species specific coefficients are given by:

$$\begin{aligned}A(\text{He}) &= 6 \pm 1 \\A(\text{F}_2) &= 4.7 \pm 1.2\end{aligned}$$

Therefore, recombination of F atoms as they travel from the discharge tube through the nozzle throat to the laser cavity should not be significant.

### 2.2.8 Reverse Reactions

All of the reactions previously discussed can, to a greater or lesser degree, proceed in forward or reverse directions:



where  $v_A$ ,  $v_B$ ,  $v_C$  and  $v_D$  are equilibrium stoichiometric coefficients. The equilibrium constant,  $K_{equi}$ , is the ratio of the forward and reverse rate constants (Cengel and Boles 1994):

$$K_{equi} = \frac{k_f}{k_r} \quad (2.102)$$

The equilibrium constant can be written in terms of the Gibbs function for the reactants and products:

$$K_{equi} = e^{-\Delta G^*(T)/RT} \quad (2.103)$$

where:

$$\Delta G^*(T) = v_C \bar{g}_C^*(T) + v_D \bar{g}_D^*(T) - v_A \bar{g}_A^*(T) - v_B \bar{g}_B^*(T) \quad (2.104)$$

and  $\bar{g}_i^*(T)$  represent the Gibbs function for component  $i$  at 1 atm pressure and temperature T. Therefore by knowing the forward rate constant and the state properties of the reactants and products, the rate constant for the reverse reaction can be determined.

**Table 2.4** HF laser chemical kinetic rate constants (center column). Equations give rate constants in units of  $\text{cm}^3 \text{ molecules}^{-1} \text{ s}^{-1}$  (Manke and Hager 2001).

<b>Cold Pumping Reaction</b>		
$\text{F} + \text{H}_2 \rightarrow \text{HF}(v) + \text{H}$	$190 \text{ K} \leq T \leq 376 \text{ K}$ $1.1 \pm 0.1 \times 10^{-10} g(v) e^{-(450 \pm 50)/T}$ $376 \text{ K} < T$ $2.2 \pm 0.4 \times 10^{-10} g(v) e^{-(595 \pm 50)/T}$	$g(0)=0.0 \quad g(1)=0.15$ $g(2)=0.55 \quad g(3)=0.30$
<b>Hot Pumping Reaction</b>		
$\text{H} + \text{F}_2 \rightarrow \text{HF} + \text{F}$	$5.0 \times 10^{-15} T^{1.5} e^{-845/T}$	
<b>V-V energy transfer</b>		
$\text{HF}(1) + \text{H}_2(0) \rightarrow \text{HF}(0) + \text{H}_2(1)$	$5.2 \pm 0.4 \times 10^{-13}$	
$\text{HF}(v) + \text{HF}(v') \rightarrow \text{HF}(v+1) + \text{HF}(v'-1)$	$4.5 \times 10^{-9} (v+1)^{0.35} T^{-1}$	
<b>V-T energy transfer</b>		
$\text{HF}(v) + \text{HF} \rightarrow \text{HF}(v-1) + \text{HF}$	$\pi d^2 \sqrt{\frac{8RT}{\pi\mu}} A(v) T^{-1.3}$ $d = 1.25 \times 10^{-10} \text{ m}$	$A(1)=12.0 \quad A(2)=218.0$ $A(3)=315.2 \quad A(4)=764.0$ $A(5)=1610.3 \quad A(6)=3107$ $A(7)=4339$
$\text{HF}(v) + \text{H} \rightarrow \text{HF}(v') + \text{H}$	$1.7 \times 10^{-8} A(v) T^{-1} +$ $1.7 \times 10^{-12} B(v) e^{-352/T}$	$A(3)=1.4 \quad A(4)=2.0$ $A(5)=2.7 \quad A(6)=3.5$ $B(1)=0.4 \quad B(2-6)=0.7$
$\text{HF}(v) + \text{F} \rightarrow \text{HF}(v-1) + \text{F}$	$2.7 \times 10^{-11} g(v) e^{-1359/T}$	$g(v)=v$
$\text{HF}(v) + \text{M} \rightarrow \text{HF}(v-1) + \text{M}$	$1.7 \times 10^{-29} A(\text{M}) v T^{4.5}$	$A(\text{F}_2)=2.0$ $A(\text{He})=3.7$
$\text{HF}(v) + \text{H}_2 \rightarrow \text{HF}(v') + \text{H}_2$	$1.0 \times 10^{-12} A(v)$	$A(2)=0.2 \pm 0.1$ $A(3)=0.35 \pm 0.04$ $A(4)=0.50 \pm 0.2$ $A(5)=1.6 \pm 0.3$ $A(6)=3.5 \pm 1.0$ $A(7)=9.1 \pm 2.7$
<b>Reactive Quenching</b>		
$\text{HF}(v) + \text{H} \rightarrow \text{H}_2(v') + \text{F}$	$3.0 \times 10^{-11} T^{0.179} e^{-382/T} \quad v=3$ $g(v, v') 1.0 \times 10^{-10} e^{-252/T} \quad v=4-6$	$g(4,0)=0.5 \quad g(4,1)=0.5$ $g(5,0)=0.5 \quad g(5,1)=1.0$ $g(6,0)=0.5 \quad g(6,1)=0.5$ $g(6,2)=1.5$
<b>F atom recombination</b>		
$\text{F} + \text{F} + \text{M} \rightarrow \text{F}_2 + \text{M}$	$A(\text{M}) \times 10^{-34}$	$A(\text{He})=6 \pm 1$ $A(\text{F}_2)=4.7 \pm 1.2$

**Table 2.5** HF laser chemical kinetic rate constants at 300 K. Equations give rate constants in units of  $\text{cm}^3 \text{ molecules}^{-1} \text{ s}^{-1}$  (Manke and Hager 2001).

<b>Cold Pumping reaction</b>		
$\text{F} + \text{H}_2 \rightarrow \text{HF}(\nu) + \text{H}$	$1.35 \times 10^{-11}$	$\nu=2$
<b>Hot Pumping reaction</b>		
$\text{H} + \text{F}_2 \rightarrow \text{HF} + \text{F}$	$1.03 \times 10^{-13}$ $7.24 \times 10^{-13}$	$\nu=2$ $\nu=6$
<b>V-V energy transfer</b>		
$\text{HF}(1) + \text{H}_2(0) \rightarrow \text{HF}(0) + \text{H}_2(1)$	$5.2 \pm 0.4 \times 10^{-13}$	
$\text{HF}(\nu) + \text{HF}(\nu') \rightarrow \text{HF}(\nu+1) + \text{HF}(\nu'-1)$	$2.20 \times 10^{-11}$	$\nu=2$
<b>V-T energy transfer</b>		
$\text{HF}(\nu) + \text{HF} \rightarrow \text{HF}(\nu-1) + \text{HF}$	$2.05 \times 10^{-11}$	$\nu=2$
$\text{HF}(\nu) + \text{H} \rightarrow \text{HF}(\nu-1) + \text{H}$	$3.710^{-13}$ $8.0 \times 10^{-11}$	$\nu=2$ $\nu=3$
$\text{HF}(\nu) + \text{F} \rightarrow \text{HF}(\nu-1) + \text{F}$	$5.82 \times 10^{-13}$	$\nu=2$
$\text{HF}(\nu) + \text{M} \rightarrow \text{HF}(\nu-1) + \text{M}$	$1.76 \times 10^{-17}$ $9.54 \times 10^{-18}$	$\nu=2, \text{He}$ $\nu=2, \text{F}_2$
$\text{HF}(\nu) + \text{H}_2 \rightarrow \text{HF}(\nu-1) + \text{H}_2$	$2.0 \times 10^{-13}$	$\nu=2$
<b>Reactive Quenching</b>		
$\text{HF}(\nu) + \text{H} \rightarrow \text{H}_2(\nu') + \text{F}$	$2.33 \times 10^{-11}$	$\nu=3$
<b>F atom recombination</b>		
$\text{F} + \text{F} + \text{M} \rightarrow \text{F}_2 + \text{M}$	$6 \times 10^{-34}$ $4.6 \times 10^{-34}$	$\text{He}$ $\text{F}_2$

### 2.3 Hydrodynamic Mixing in HF lasers

In the previous section the V-T and V-V energy transfer mechanisms that compete with stimulated emission for the energy stored in the population inversion were shown to be as fast as, and in some cases faster than, the primary cold pumping reaction. Therefore, in order to construct an effective laser system, an injection scheme must be devised that quickly mixes the fuel and oxidizer inside the optical cavity and then quickly removes the spent reactants. Expanding the F atom flow through a converging-diverging nozzle and injecting the H<sub>2</sub> through a series of small holes in the supersonic region of the nozzle typically accomplishes this (Grosh and Emanuel 1976). The efficiency of the laser system therefore strongly depends on the rate of mixing and consequently, the optical, kinetic, and gas dynamic processes within the laser are coupled. The primary mechanisms that affect the rate of mixing in the optical cavity are molecular diffusion, turbulence and large-scale vortex structures. These mechanisms are in turn influenced by heat release from the cold pumping reaction, shear stresses between injected and primary flows, and the flow pressure, density, temperature and viscosity.

In addition to providing a means to rapidly mix the fluorine oxidizer and hydrogen fuel flows, the nozzle is also designed to produce supersonic flow at a temperature and pressure substantially lower than that in the combustor or discharge tube. This lowers the reactant concentrations and therefore slows the rates of reaction for the cold pumping and deactivation mechanisms to allow more time for the reactants to mix. The nozzle thus establishes the appropriate pressure, temperature and composition of reactants in the laser cavity. The large nozzle exit velocity produced by the supersonic expansion stretches the

lasing-zone in the downstream direction and provides the potential for pressure recovery reducing the required pumping capacity.

Heat generated by the cold pumping reaction causes the pressure and temperature to increase and the supersonic Mach number to decrease. If the Mach number decreases to unity, thermal choking of the flow occurs and a strong shock system develops that forces the upstream flow to readjust. The shock system will reduce the flow velocity and increase the static pressure and temperature. This compresses the gain region by speeding up the reaction kinetics while reducing the flow velocity and the rate of mixing resulting in a dramatic drop in laser efficiency and power (Grosh and Emanuel 1976). Thermal choking of the flow can be avoided by providing a base relief region or by increasing the diluent ratio to absorb the excess heat generated by the pumping reaction. A base relief region is typically a rear-facing step in the nozzle contour just downstream of the hydrogen injection location so that the nozzle flow expands into a larger cavity. A small subsonic diluent flow is typically used as a purge for the base relief region to prevent recirculation of the reactants. A nozzle with base relief has the added complexity of free expansion of the nozzle flow, which will create an oblique shock/expansion fan system that can only be eliminated by pressure matching the nozzle and laser cavity. For a fixed nozzle geometry, pressure matching can only occur for a single set of flow conditions and is thus very difficult to attain in practice. Therefore, some oblique shock/expansion fan structure is likely to occur in an HF laser cavity that utilizes base relief.

### 2.3.1 Transverse Injection Vortex Structures

HF lasers typically utilize a nozzle geometry in which the H<sub>2</sub> is transversely injected through a series of sonic injectors into the supersonic F atom flow. This type of injection scheme produces a complex 3-dimensional flow field containing several different types of vortex and shock structures. The mixing qualities of transverse injection in crossflow have been extensively investigated at high Reynolds number in the compressible regime (Blanchard et al. 1999; Gruber et al. 1997; Hollo et al. 1994) and at low Reynolds number for incompressible flows (Fric and Roshko 1994; VanLerberghe et al. 1999). The injectant stream in these experimental investigations were all injected perpendicular to the crossflow whereas the HF laser fuel is typically injected at a shallow angle. The shallow angle injection will reduce the strength of the vorticity generated by the shear between the injected stream and the crossflow but should produce similar vortex structures.

Figures 2.7 and 2.8 show schematics of an under-expanded transverse jet injected perpendicular into a supersonic crossflow. The disturbance in the crossflow caused by the jet creates a bow shock that curves around the plume of the jet and interacts with the crossflow boundary layer producing a separated flow region upstream of the jet. The under-expanded jet accelerates through a Prandtl-Meyer expansion fan and is then compressed by a barrel shock and Mach disk. The jet plume is quickly bent toward the downstream direction by the momentum of the crossflow. In the near field of the jet, where the three-dimensional interaction between the jet and crossflow is most intense, there are four discernable vortex structures: (i) jet shear-layer vortices; (ii) a system of

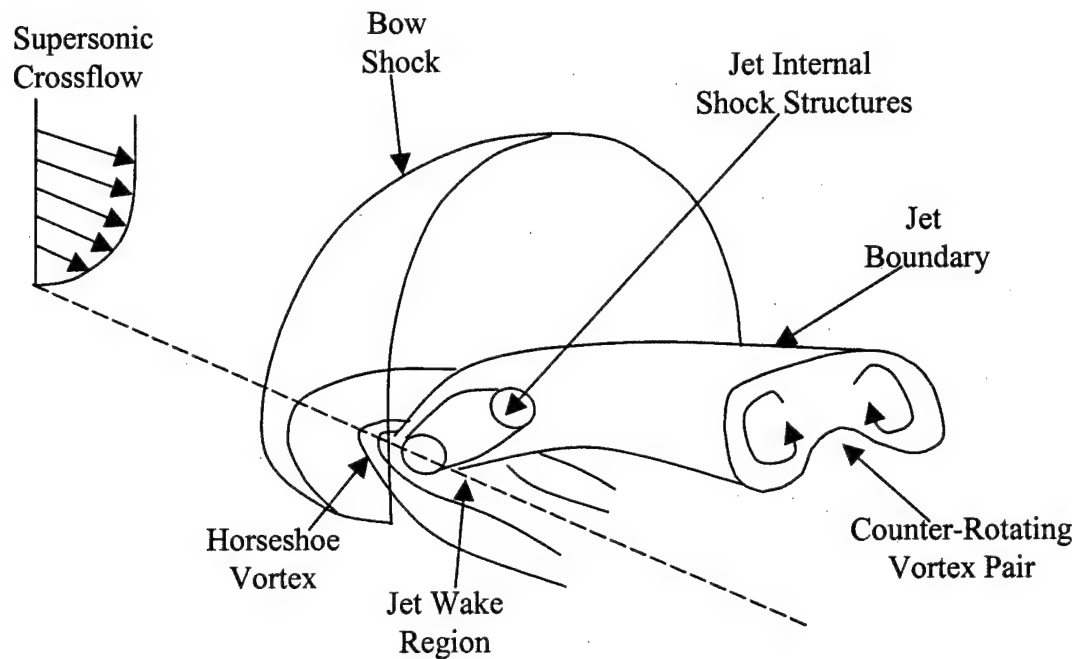


**Figure 2.7** Shock and vortex structure of transverse sonic injection into supersonic crossflow.

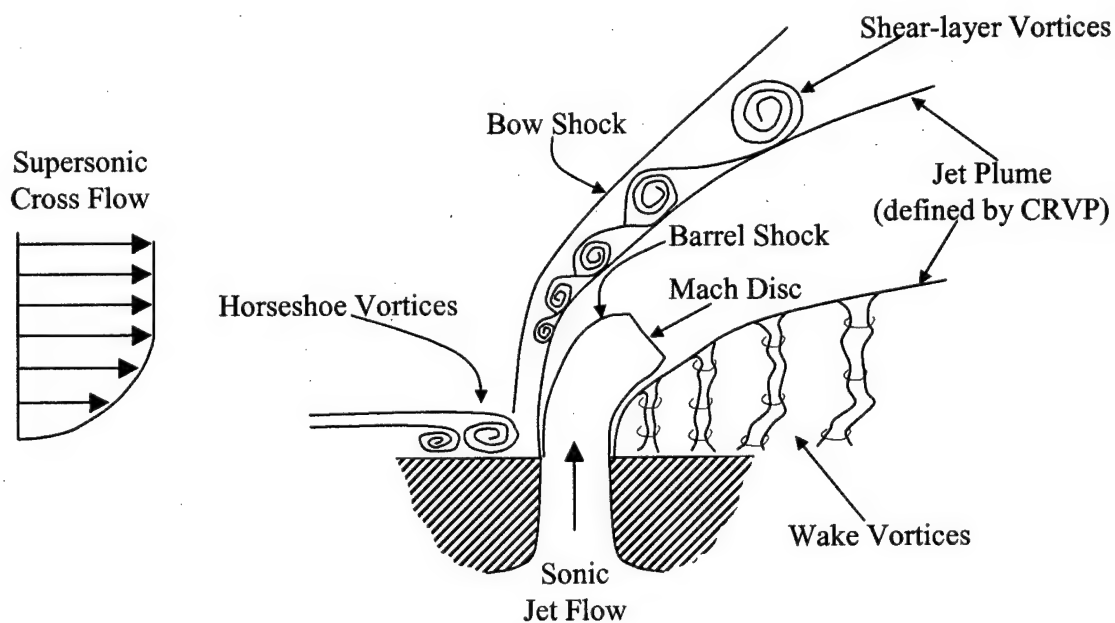


**Figure 2.8** Side view of transverse sonic injection into a supersonic crossflow.

horseshoe vortices; (iii) a counter-rotating vortex pair (CRVP); and (iv) wake vortices (Fric and Roshko 1994). The jet shear-layer vortices are the result of the Kelvin-Helmholtz instability of the annular shear layer that forms between the jet plume and the crossflow as the jet fluid passes through the oblique shocks defined by the sides of the barrel shock. This annular shear layer creates a system of small-scale vortices around the periphery of the jet plume that contribute to the mixing between the jet and crossflow by actively entraining freestream fluid. The horseshoe vortex system forms upstream of the injection point near the wall and wraps around the jet and trailing downstream where it interacts with the wake vortices. The horseshoe vortices are created by the reverse flow resulting from the adverse pressure gradient caused by blockage of the crossflow by the jet in the boundary layer upstream of the injection point. These vortex structures are similar to the horseshoe-vortex system that forms around the base of a wall-mounted circular cylinder.

The dominant vortex structure that develops in the jet is the counter-rotating vortex pair (CRVP). In most regards the CRVP can be considered the structure that actually defines the boundary of the jet plume. The CRVP is formed when the crossflow, which is deflected laterally around the jet, shears the jet fluid along its edges and folds the face of the jet over itself. These large-scale vortices entrain the freestream fluid into the jet transporting coherent packets of fluid from above the jet into the wake region downstream of the barrel shock where small-scale instantaneous mixing occurs.

The wake vortices are tornado-like structures that connect the CRVP to the boundary layer and have some characteristics similar to the periodic vortices shed in the wake of a solid cylinder in crossflow. The most notable difference between the wake

vortices of a jet in crossflow and a circular cylinder in crossflow is that the plume of the jet follows the wake downstream. Therefore, as the vortical structure convects downstream it stretches across the widening gap between the jet and the wall. Fric and Roshko (1994) determined that the vorticity in the jet wake is not shed from the jet itself, as it would be from a solid cylinder, but instead originates in the separation of the crossflow boundary layer caused by the adverse pressure gradient created by the disruption of the crossflow by the jet (Fric and Roshko 1994). The ‘separation event’ on the crossflow wall occurs alternately on each side of the jet and results in eruptions of the horseshoe vortex away from the wall. Once the horseshoe vortex separates from the wall it rotates perpendicular to the wall with one end becoming entrained into the jet and the other end remaining attached to the boundary layer creating the distinctive tornado-like structure of the wake vorticity. This fundamental difference has profound impact of the mixing qualities of a jet in crossflow and in particular the transition of the coherent vortex structures that dominate the near field into small-scale turbulence that dominate in the far field, which is discussed in the next section.

### **2.3.2 Turbulence**

It is very difficult to give a precise definition of turbulence. Listing some of the characteristics of turbulent flows is typically all one can do to gain insight into the effect that turbulence has on the flow field. Turbulence is random and inherently three-dimensional in nature making deterministic solutions to realistic turbulent flows impossible. Turbulence is diffusive and dissipative. Turbulence can quickly diffuse throughout the flow field, however turbulence will dissipate quickly without a source of

energy to fuel the motion. Turbulent flow fields typically originate from instabilities in laminar flows that grow as the Reynolds number increases. The laminar instabilities are related to interactions between viscous and non-linear inertial terms in the equations of motion (White 1991).

Turbulent motion within a flow field can simultaneously exist on several length scales, all of which are much smaller than the length scale of the bulk fluid motion. It is this small-scale random motion that gives turbulence its diffusive characteristic, which is the most important feature with respect to mixing. The diffusivity of turbulence allows it to transport or mix momentum, kinetic energy and species concentrations at rates several orders of magnitude greater than the rates due to molecular diffusion alone (Tennekes and Lumley 1972). However, the viscous shear stresses produced by the mixing motion of the turbulence perform deformation work that increases the internal energy of the fluid at the expense of the turbulent kinetic energy. The turbulence therefore needs a continuous supply of energy to make up for the viscous losses. This energy is typically supplied through shear stresses that result from the large-scale bulk motion of the flow field.

The dimensionless parameter governing the transition between laminar flow and turbulent flow is usually represented by the Reynolds number:

$$\text{Re} = \frac{\rho V L}{\mu} \quad (2.105)$$

where  $\rho$  is the local fluid density,  $V$  is the streamwise velocity,  $\mu$  is the local viscosity and  $L$  is a characteristic length scale of the flow field. The Reynolds number indicates the ratio of inertia forces to viscous forces. At high Reynolds number the inertia forces dominate and the flow is turbulent. At low Reynolds numbers the viscous forces

dominate and the flow is laminar. The magnitude of the Reynolds number at which a flow transitions from laminar to turbulent is referred to as the critical Reynolds number and is a function of the flow field geometry. When discussing transition, the characteristic length scale is typically defined as the streamwise distance from the point of flow field disturbance (i.e., leading edge for flow over a flat plate). The Reynolds number therefore increases in the downstream direction and the critical Reynolds number defines the downstream location where the flow field transitions to turbulent. HF laser cavities operate at very low pressures, typically 2 to 20 torr, resulting in low cavity densities and therefore low Reynolds number. As a result, the laser cavity can be expected to be laminar over relatively long distances downstream of the injection point.

In HF lasers that utilize base relief to prevent thermal choking, there are two shear flows. One is between the injected  $H_2$  and F atom flow streams inside the nozzle that produce the complex vortex structures described in the previous section and the other occurs between the supersonic nozzle flow and the subsonic purge flow used to fill the base relief region. According to stability analysis, these types of free shear flows are unconditionally unstable at all Reynolds numbers and it is therefore difficult to establish a streamwise transition location (White 1991). The mixing layer between the base purge and the primary nozzle flow can be approximated as a planar two-dimensional mixing layer, which reaches a self-similar profile at  $Re \approx 40,000$  based on downstream location (Tennekes and Lumley 1972). In the self-similar region the mixing layer spreads linearly as the flow moves downstream and preferentially grows into the slow side of the mixing layer. However, at the flow conditions inside the HF laser cavity, self-similarity will not be achieved until about 50 cm downstream of the NEP, or well downstream of the active

gain region of the flow field. The interaction between the base purge flow and the nozzle flow is therefore in a transitional regime making it very difficult to predict the growth rate of the mixing layer.

Growth of instabilities and subsequent transition to a turbulent flow regime of the coherent vortex structures created by the transverse injection scheme are the result of a very complex interaction of the large-scale and small-scale vortex structures within the flow field (Blanchard et al. 1999; Camussi and Stella 2002). For high Reynolds number ( $Re \approx 10^6$ ), transverse injection into a Mach 2 crossflow, the transition of the dominant mixing mechanism from vortex-driven mixing in the near field to small-scale turbulent mixing in the far field, has been found to occur in the region 8 to 10 diameters downstream of the injectors (Gruber et al. 1997; Hollo et al. 1994). At low Reynolds number ( $Re \approx 10^3$ ) in the incompressible flow regime, coherent large-scale vortex structures have been observed 60 injection diameters downstream (Blanchard et al. 1999). The Reynolds number of the HF laser cavity can be expected to lie somewhere between these two flow regimes and have the additional complications of compressibility and heat release from the cold pumping reaction. Compressibility should have a stabilizing effect on the vortex structures within the flow field (Givi et al. 1991; Gruber et al. 1997). This delays turbulent transition leading to suppressed mixing and, therefore, to reduced reaction conversion rate. Because of the high diluent to reactant ratio of the experimental conditions in this investigation, heat release from the cold pumping reaction has a relatively small effect on the bulk temperature of the flow field. However, local heating within the flow field may be significant. The local heat release will lead to volumetric expansion of the coherent vortex structures creating a small rate of mixing

increase in the near field while suppressing turbulent transition and therefore reducing the rate of mixing in the far field (Givi et al. 1991). Therefore the combination of low Reynolds number, heat release and compressibility make it difficult to determine whether or not the large-scale vortex structures dissipate or transition to a fully turbulent flow field. To provide a definitive answer to this question, visualization of the flow field and, if possible, velocity field measurements would be required.

The near field vortex structures appear to be dependent on the injection geometry while the far field turbulent mixing is insensitive to the injection geometry (Hollo et al. 1994). This suggests that the best way to increase the overall mixing rate of the entire flow field is to maximize vortex generation in the injector near field. At a given injection velocity, shear stress and vorticity will increase as the injection angle is increased with respect to the crossflow direction. However, since the downstream momentum that the jet acquires must come at the expense of the crossflow momentum, increasing the injection angle will also increase total pressure loss and lower the freestream velocity. This creates a major tradeoff decision when applying transverse injection to HF laser systems. Increased vortex generation will increase the near field mixing rate tending to increase the F atom utilization and improve laser performance. However, the corresponding loss of downstream momentum will compress the streamwise gain distribution thus shifting the location where deactivation begins to dominate the kinetics closer to the injection point and decrease laser performance. Therefore, the maximum allowable H<sub>2</sub> injection angle in HF laser nozzles depends on the crossflow Mach number. This restricts the transverse H<sub>2</sub> injection in HF laser nozzles to very shallow injection angles.

### 2.3.3 Binary Diffusion

At the smallest scale, the mechanism that brings a fluorine atom and hydrogen molecule together inside an HF laser cavity so that the cold pumping reaction can occur is molecular diffusion. Diffusional mixing occurs on the smallest length scales and is typically much slower than bulk fluid mixing produced by turbulence or large-scale vortex structures. However, the large concentration gradients found in HF lasers can produce substantial diffusional velocities that are particularly important in the highly viscous HF cavity flow field in which turbulence is likely to play a small role. In computer modeling of the COIL flow field, which has many similarities to the HF laser cavity flow field, Madden has shown that an accurate description of molecular diffusion is essential to predicting cavity gain distributions (Madden 1997).

The driving potential of molecular diffusion can be supplied by concentration, pressure, or temperature gradients. An external force that does not act equally on all the components of the flow can also cause a diffusional mass flux but this situation is not applicable to the HF laser flow field. Thermal diffusion coefficients are typically very small and are therefore neglected in most situations unless the temperature gradients are unusually large. Even the temperature gradients created by injecting room temperature H<sub>2</sub> into the high temperature F atom flow from the combustor or discharge along with the heat release from pumping reaction are not expected to contribute significantly to the overall diffusional mass flux. This is particularly true for the conditions investigated here in which the reactant flows are highly diluted with He. Pressure gradients are also expected to be small except in the injection region where a 2:1 pressure ratio must exist

for sonic injection to be achieved. Therefore, most of the flow field will be dominated by diffusional mass flux created by concentration gradients.

The diffusional mass flux of each flow species can be formulated in terms of the multi-component diffusion coefficients and the gradients of the driving potentials (Hirschfelder et al. 1954). However, the multi-component diffusion coefficients that depend on the concentration of each flow species are not typically known. A more convenient formulation is represented by the Stefan-Maxwell equations, which relate the multi-component diffusion coefficients to the more readily available binary diffusion coefficients and the diffusion velocity of each species (Hirschfelder et al. 1954). This calculation can be rather cumbersome because it requires the solution of an NxN linear system of equations for the diffusion velocities, where N is the number of flow species. Bird et al (1960) outlines a procedure for replacing the binary diffusion coefficients with a set of effective binary diffusion coefficients. In this procedure the velocity of the  $i^{\text{th}}$  component is calculated assuming an average velocity for the remaining (N-1) flow components. In diffusion model studies for a COIL flow field, Crowell (1983; 1989) has shown that the effective binary diffusion model is in excellent agreement with the more detailed Stefan-Maxell equations. The 2-D CFD code used to predict the small signal gain as described in Chapter 4 uses the effective binary diffusion model.

## Chapter 3

### Experimental Apparatus and Procedure

The HF laser device and optical diagnostic system used to measure the small signal gain are described in the following sections. The laser nozzle design and experimental conditions are very similar to those of Sentman and co-workers (Carroll et al. 1993; Sentman et al. 1989b). The two most important differences are that in this research a slit nozzle rather than a nozzle bank is used, and the discharge used 20% F<sub>2</sub> in helium rather than SF<sub>6</sub> + O<sub>2</sub> as the F atom source. The significant advancement in this research is the use of a sub-Doppler tunable diode laser source to probe the HF overtone transitions. Previous investigations used a commercially available arc-driven HF laser as a probe stabilized and locked to the line center of one of a limited number of HF overtone lines. These systems proved difficult to use and without the ability to resolve the transition lineshape, lead to ambiguous or deceptive answers when making comparisons with computational fluid dynamics calculations. The diagnostic system used in this research provided high fidelity, spatially resolved small signal gain data for individual HF ro-vibrational lines.

#### 3.1 HF Laser Device

A small-scale HF laser was constructed by the Air Force Research Laboratory Chemical Laser Branch to generate an inversion on the first overtone frequencies of HF at 1.27 - 1.40  $\mu\text{m}$  (Wisniewski et al. 2003a). The principal component of the laser was a 5 cm wide supersonic slit nozzle, where F atoms generated by a discharge tube reacted

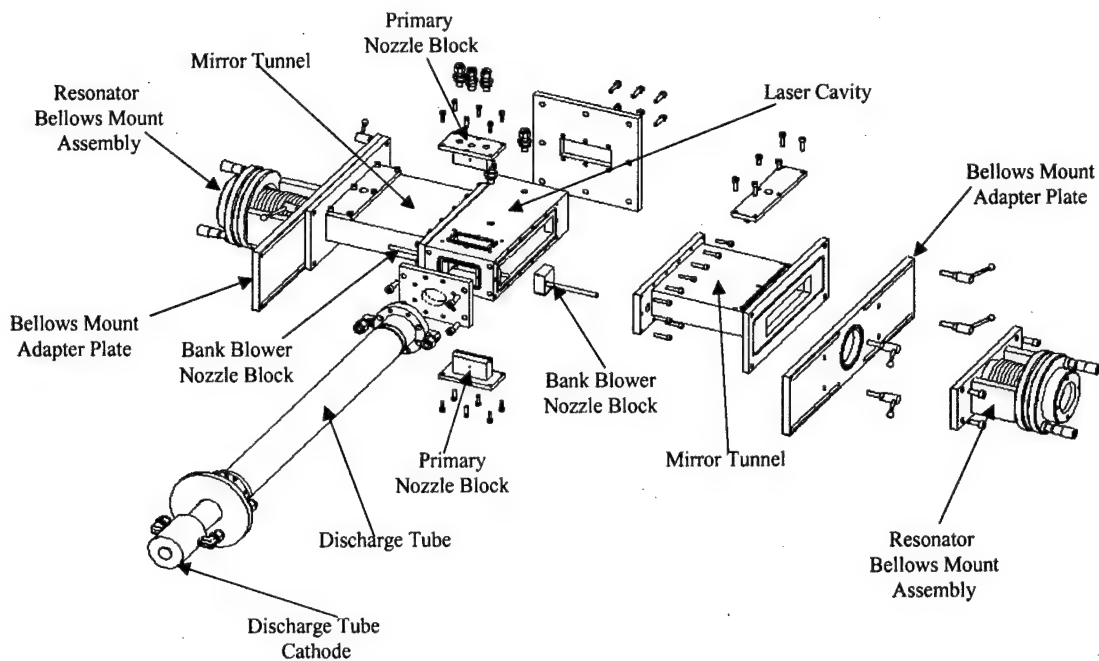


**Figure 3.1** Assembly diagram for the slit nozzle HF laser device. Fluorine atoms are generated by the discharge tube and enter the plenum region before passing through the 3 mm high slit nozzle. Laser mirrors or glass windows can be mounted along the sides of the cavity to accommodate laser demonstrations or gain measurements, respectively.

with molecular hydrogen to generate vibrationally excited HF. A schematic representation of the experimental apparatus is shown in Figure 3.1 along with a photograph in Figure 3.2. The top and bottom nozzle blocks form the throat of the supersonic nozzle while the bank blower nozzle blocks form the sides. Each bank blower is a Mach 5 nozzle that was designed to create an aerodynamic curtain between the laser cavity flow and the mirror tunnel to prevent the reactive laser flow from reaching the resonator optics. The mirror tunnels extend perpendicular from the laser cavity and mate with the resonator bellows mount assembly. The resonator could be repositioned in the flow direction by loosening the bolts in the adapter plates and sliding the assembly along the slotted holes. The fine threads of the 2-axis gimbals on the bellows mount assembly

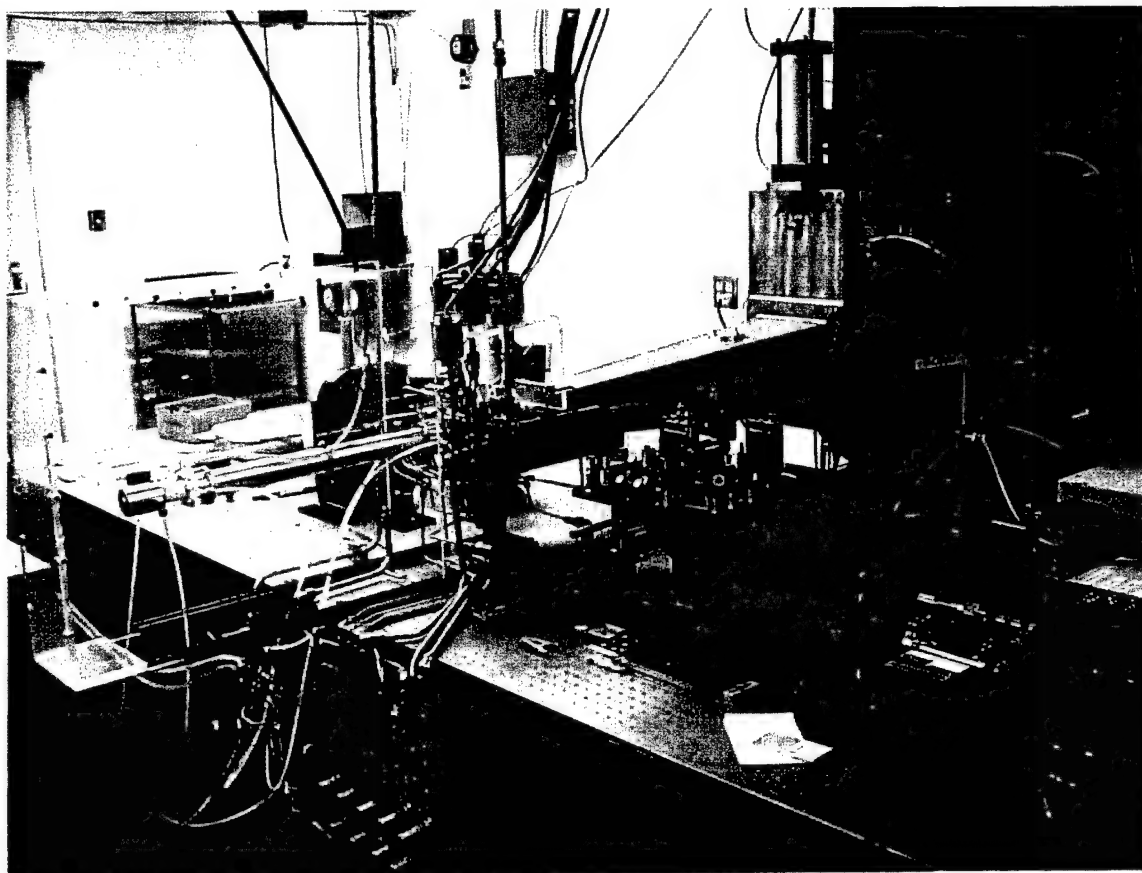


**Figure 3.2** Photograph of HF laser device.

allowed the resonator to be precisely aligned. The assembly adapter plate and bellows mount assembly were replaced with 2.5° wedged windows to allow probe beam access to the laser cavity. The internal laser cavity was 2.85 cm high and extended 13 cm downstream of the nozzle.

The discharge tube was powered by a 3mA 10kV power supply. It was supplied with fluorine molecules from a gas cylinder that was 20% F<sub>2</sub> and 80% He by volume. This flow was further diluted with He before injection into the cathode end of the discharge tube. An additional small He purge was always maintained in the discharge tube cathode to prevent the tube from overheating when the power was turned on but the fluorine flow had not reached the tube. The pressure in the discharge was controlled by

the primary He diluent flow injected downstream of the discharge anode but upstream of the nozzle throat. The discharge tube had a fairly narrow range of operating pressures and was kept between 25 and 30 torr for all fluorine flow rates. Circulating chilled water through an external water jacket actively cooled the discharge tube. The combination of fluorine and He diluent and purge flows exiting the discharge tube are referred to as the primary flow and the pressure in the discharge tube is termed the plenum pressure.

Figure 3.3 shows the view from the downstream end of the nozzle looking back into the plenum region. The slit nozzle is 5cm wide and has a 2.96 mm throat height that expands with a  $20^{\circ}$  half angle to 9.56 mm at the nozzle exit plane (NEP). As the primary flow expands through the nozzle it encounters two rows of injectors on the top and on the bottom of the nozzle. The first row injects He into the primary flow of F atoms,  $F_2$  and He and is referred to as the secondary He injection flow. In some references the secondary He injection is described as a mechanism to increase mixing and in other references it is designed to shield the primary F atom flow from the  $H_2$  flow within the nozzle. The second row injects  $H_2$  fuel into the primary flow.  $H_2$  is supplied by gas cylinder and is diluted with He before injection. The He diluent flow rate varied depending on the  $H_2$  flow rate with the intention of keeping the momentum of the total injected flow constant. The injection holes have 0.508 mm diameter and there are 28 in each row on the top and on the bottom of the nozzle for a total of 56 secondary He injectors and 56  $H_2$  injectors. The injection holes are drilled through to plenum regions inside the nozzle block that are supplied with pressures high enough to ensure sonic conditions at each injection point. The secondary He injection and diluted  $H_2$  flows were

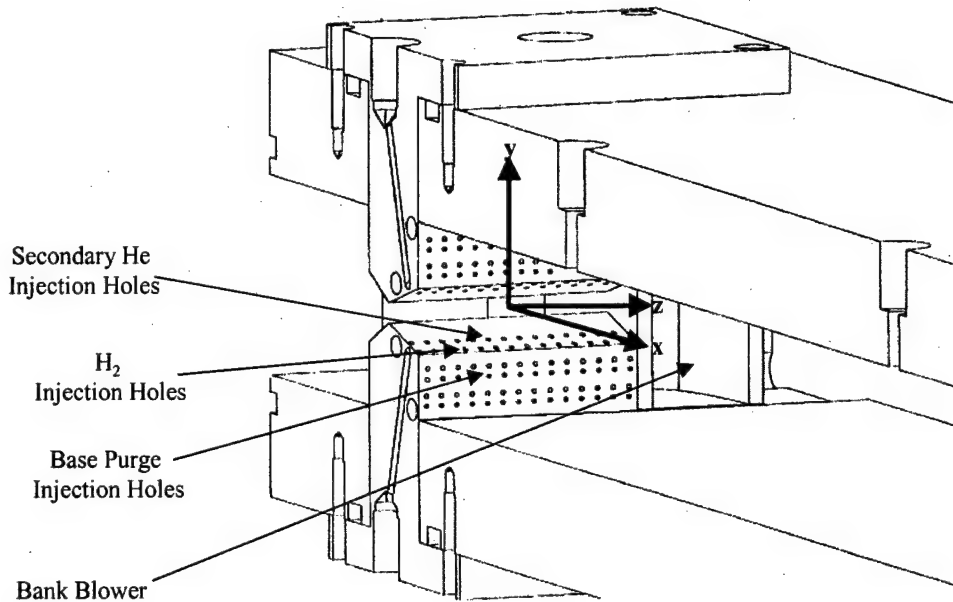


**Figure 3.3** HF laser supersonic nozzle. View is from the downstream direction looking back up the nozzle into the plenum region. Near side Bank Blower nozzle block is not shown. Origin of axis system is shown at the NEP on the vertical centerline.

injected into the primary flow at a  $15^\circ$  angle to the horizontal. Due to this shallow injection angle, the injected flows do not penetrate to the nozzle centerline. The absence of  $H_2$  at the nozzle centerline is evident by zero measured gain at the nozzle centerline near the NEP. Figure 3.4 shows the important dimensions of the nozzle injection scheme.

The primary reaction of  $F+H_2$  is highly exothermic and could cause thermal choking of the flow. To alleviate this, the flow is allowed to expand into a rearward-facing step at the NEP. The step is 9.45 mm deep at top and at bottom and is referred to as the base relief region. A small He purge flow is injected into this base region to prevent recirculation of the primary flow in the corner. The base relief region at the top

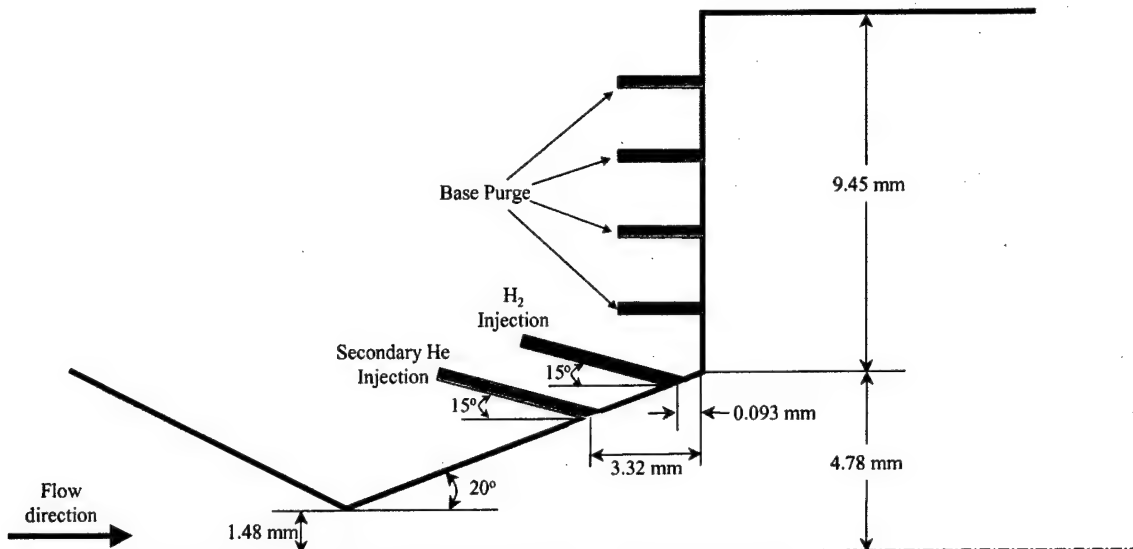


**Figure 3.4** Side view of important nozzle injection dimensions.

of the cavity has four rows of evenly spaced 0.37 mm diameter holes with 28 holes in each row, with an identical arrangement at the bottom of the cavity. This nozzle/injection scheme is designed to approximate two-dimensional behavior to help simplify the modeling requirements.

### 3.1.1 Fluid Supply and Vacuum System

The 10 separate flows used when operating the laser device with their designated names and descriptions are listed in Table 3.1. A schematic of the injection locations of these flows, with the exception of the bank blower and tunnel purge flows, is shown in Figure 3.5. F<sub>2</sub> and H<sub>2</sub> are supplied to the device from gas cylinders secured in coffins outside the lab while He is supplied from the facility high-pressure system. Switches from a control panel actuate each flow remotely. Controlling the pressure upstream of a

**Table 3.1** Description of laser flow species. Injection location of each species is shown in Figure 3.5.

Flow designation	Flow Name	Description
MFHE1	Cathode He	He flow injected into the upstream end of the discharge tube just downstream of the cathode.
MFHE2	F <sub>2</sub> diluent	He flow mixed with MFFO1 flow before injection into discharge tube.
MFHE3	Primary He Diluent	He flow injected into the discharge tube just upstream of the primary nozzle.
MFHE4	Secondary He Injection	Total He flow injected through first row of holes in primary nozzle.
MFHE5	H <sub>2</sub> diluent	He flow mixed with MFH21 before injection into nozzle.
MFSRD	Base Purge Flow	Total He flow injected into base purge region at the nozzle exit plane.
MFCUR	Curtain Flow	Total He flow to the two bank blowers on either side of the nozzle.
MFTUN	Tunnel Purge	Total He flow to the two mirror tunnels on either side of the laser cavity.
MFFO1	F <sub>2</sub>	20% F <sub>2</sub> and 80% He flow injected into discharge tube.
MFH21	H <sub>2</sub>	Total 100% H <sub>2</sub> injected through second row of holes in primary nozzle.

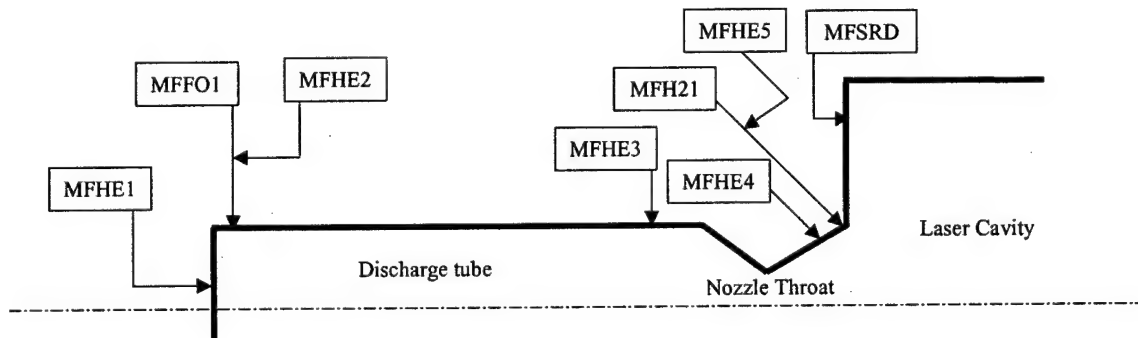


**Figure 3.5** Schematic diagram of flow injection locations. Bank blower and tunnel purge flows not shown. Flow designations are described in Table 3.1.

sonic orifice sets the flow rate of each species. Figure 3.6 shows a schematic of the control system for an individual flow species. A signal from the data acquisition/control computer commanded the proportion air to load the top of the dome regulator to a specified pressure. The pressure on top of the dome regulator controlled the pressure in the fluid supply line. The species flow rate was determined by monitoring the pressure and temperature upstream of the sonic orifice. The data acquisition/control computer recorded and displayed the orifice pressure, temperature and calculated flow rate so the operator could verify proper operation. The inlet edges of the orifices were either rounded or beveled and ranged in size from 0.254 mm to 1.83 mm diameter. The discharge coefficient of each orifice was calibrated using a Flow-Dyne venturi type critical flow nozzle to give an overall flow rate uncertainty of less than 5% (Schmidt 1996). The cavity pressure inside the laser was maintained by the facility pumping system, which consists of 4 Kinney 850 mechanical pumps in parallel preceded by 4 stages of 0.61 m diameter vacuum line. The entire system has a pumping capacity of nearly  $51,000 \text{ m}^3 \text{s}^{-1}$ , which was ample for this application.

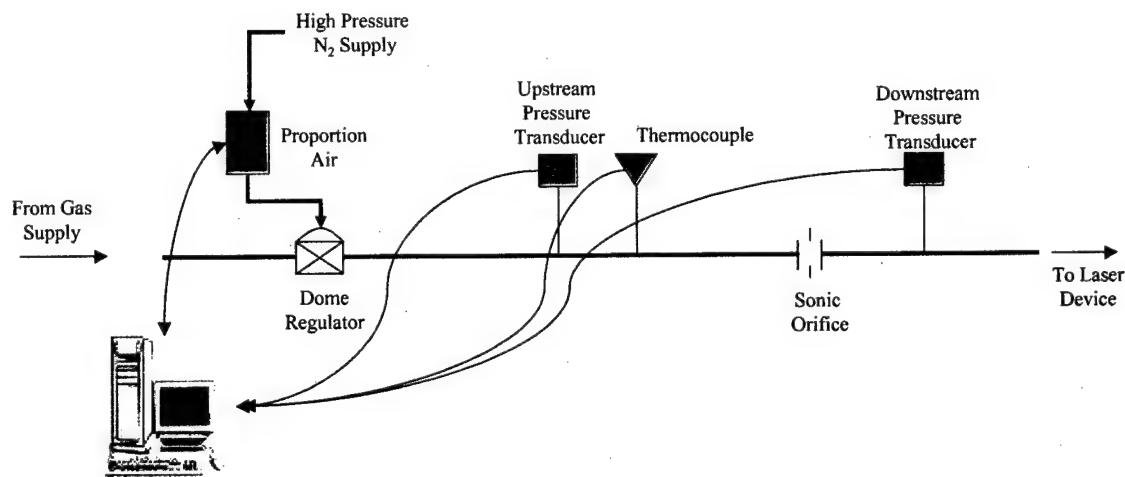


**Figure 3.6** Example of flow control system for an individual flow species.

### 3.1.2 Data Acquisition and Control System

The primary function of the data acquisition and control system was to control and monitor the fluid supply system and record all fluid supply system related data. The system also recorded signals from pressure transducers located on the laser device itself. Table 3.2 lists the name and location of each pressure transducer on the device. The system itself consisted of a PC running a National Instruments LabView program and the associated A/D or D/A converters and input/output channel hardware. Figure 3.7 shows the front panel display of the LabView program. The LabView program includes scroll bars and input windows to set the proportion air voltage for each flow species. This set the pressure upstream of each flow orifice. The LabView program used the upstream pressure and temperature and the orifice calibration curve from a database to calculate each flow rate. The program also monitored the downstream orifice pressure to insure the pressure ratio across the orifice was greater than 2 so that the sonic assumption would hold. The active display was updated at 50Hz and data was recorded at 2Hz. A typical laser hot fire was accomplished by first establishing the He purge/injection flows and verifying cavity and plenum pressures. The acquisition and control computer was then set to record and the discharge tube turned on. This created a He plasma that could be

**Table 3.2** Location of laser cavity pressure transducers.

Transducer Designation	Location	range
PVCA1	Cavity ceiling, 9cm downstream of NEP	10 torr
PVCA2	Cavity ceiling, 7cm downstream of NEP	10 torr
PVCA3	Right mirror tunnel	100 torr
PVCA4	Left mirror tunnel	100 torr
PVCA5	Cavity ceiling, 5cm downstream of NEP	10 torr
PVCA6	Cavity ceiling, 3cm downstream of NEP	10 torr
PVCA7	Plenum, upstream of primary nozzle throat	100 torr

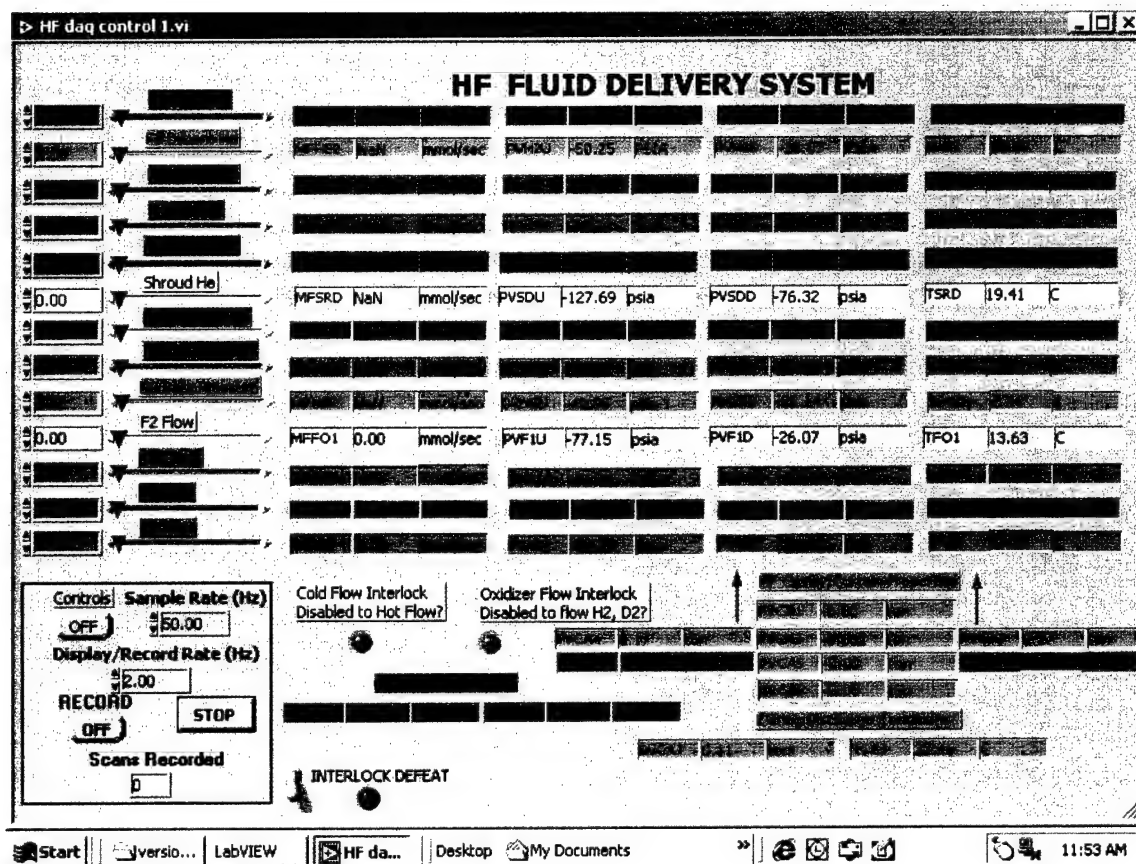


**Figure 3.7** Front panel of LabView fluid supply system control program.

seen using a video camera directed at the laser cavity. The fluorine flow was then activated followed by the hydrogen flow. Shutting off the flows in the reverse order and then turning off the discharge tube terminated the hot fire. A typical hot fire lasted 10 to 15 sec but some of the power extraction runs went as long as 60 sec with the only limit being the discharge tube temperature. The plenum temperature and the discharge tube water return temperature were monitored to prevent overheating of the discharge tube.

### 3.2 Gain Diagnostic

The principal diagnostic tool for this experiment was a tunable diode laser system. This system was initially developed to investigate the fundamental transition of the electronically excited iodine atom ( $I^*$ ) in a chemical oxygen iodine laser (COIL) (Nikolaev et al. 2000; Tate et al. 1995). It is fortunate that the wavelength of the HF overtone transition is nearly identical to the  $I^*$  transition so the system could be used for the present study with only minor modifications. The main component of the system was a New Focus model 6324 tunable diode laser. This laser has a maximum power of 9 mW. A drive screw mechanism inside the laser provides a coarse tunable wavelength range from 1272 to 1342 nm, which covers several R and P branch transitions of the first HF overtone. A piezoelectric transducer (PZT) was capable of repetitively scanning across a precise sub-angstrom wavelength range. The bandwidth of the diode is reported by the vendor to be less than 500 kHz, which is several orders of magnitude smaller than the broadened linewidth of the HF transition making it possible to resolve the HF transition lineshape. The resolution of the lineshape allowed the calculation of static flow temperature as described in Section 2.1.5.

A diagram of the tunable diode laser system is shown in Figure 3.8. The light from the diode was split several times with part of the beam going to a Fabry-Perot interferometer, part to an HF reference cell and the main part going toward the laser cavity. The output of the Fabry-Perot interferometer is used as a frequency reference for the time sequence of the main beam. The Fabry-Perot interferometer had a free spectral range of 300 MHz with a Finesse of 100. The Finesse,  $F$ , provides a measure of the filtering properties of a Fabry-Perot cavity and is defined as (Verdeyen 1995):

$$F = \frac{\text{free spectral range}}{\Delta\nu_{1/2}}$$

where  $\Delta\nu_{1/2}$  is the bandwidth, full width at half maximum, of the interference fringes.

As the diode laser repetitively scanned over a large frequency range it would go in and out of resonance with the Fabry-Perot cavity. This created a Fabry-Perot output that looked like a series of narrow peaks with each peak separated by 300 MHz in the frequency domain. This allowed the scan rate of the diode to be precisely calibrated (Manke 2002).

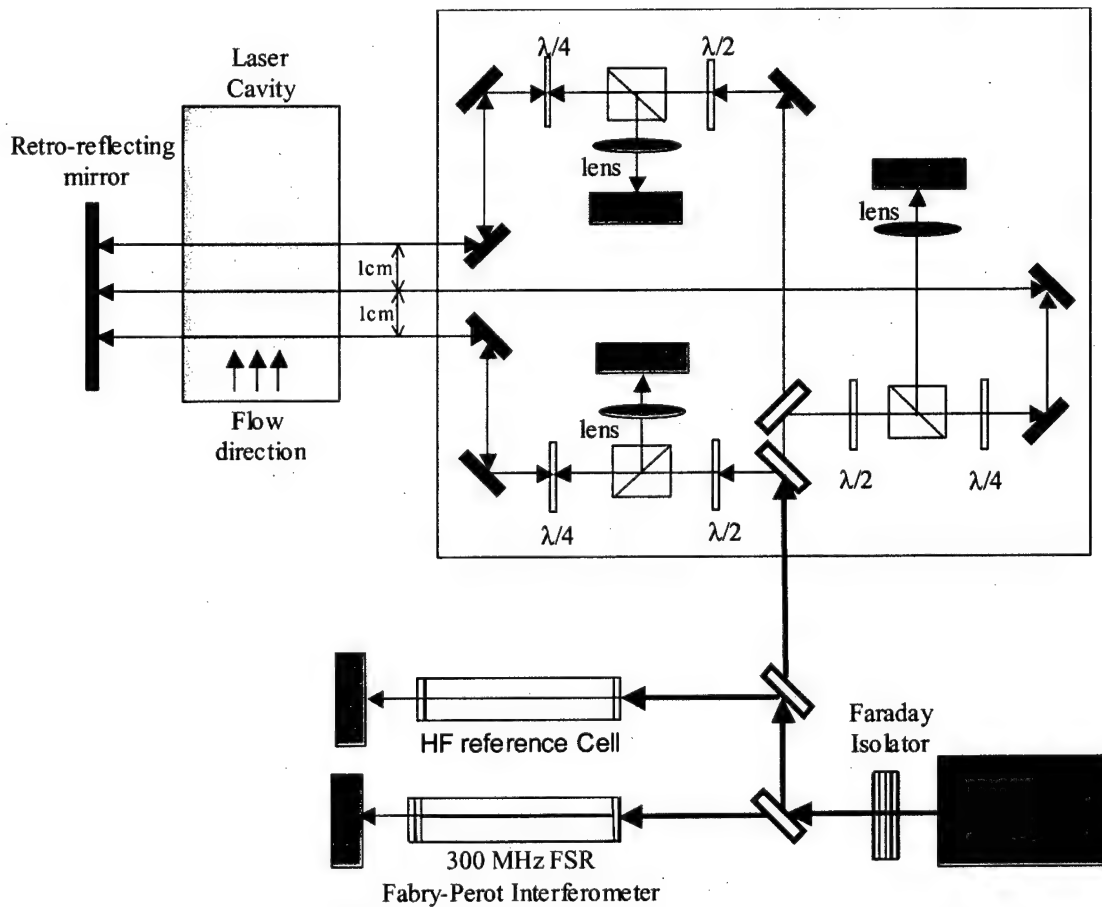


**Figure 3.8** Diagram of tunable diode laser system.

The HF reference cell was filled at low partial pressure of ground state HF and was used to locate the wavelength of the desired transition. The wavelengths of the HF overtone transitions are known to high precision (Wilkins 1977). However, because the diode was scanned over sub-angstrom range, the wavelength controller on the diode could not be used to accurately locate the transition of interest. Day-to-day variations in wavelength for a particular transition, as indicated by the diode controller, were less than 1nm. Since the diode was typically scanned over a range of 0.01 nm, the desired transition could not be found without the HF cell.

The main beam, which is about 2 mm in diameter, is split into three separate beams which enter the laser cavity perpendicular to the flow and are reflected back onto themselves making a double pass through the laser cavity. The three beams are at the same vertical location and evenly spaced 1 cm apart in the streamwise direction. The probing beam optics were attached to a platform that could be translated independently in the vertical direction and in the downstream direction so that two-dimensional gain maps of the cavity could be developed.

A separate data acquisition and control computer for the tunable diode system consisted of a PC running a Labview program with the associated A/D or D/A converters and input/output channel hardware. This system recorded the signal from the three cavity detectors, the HF cell detector and the Fabry-Perot detector and controlled the diode wavelength and scanning span. The Labview display is shown in Figure 3.9. The bottom graph showed the output of the HF cell detector and the top graph could be toggled between outputs of the three cavity detectors and the Fabry-Perot detector. The sweep rate, which was typically set to 50Hz, controlled how fast the diode scanned across the

wavelength range. 500 samples per sweep were usually recorded and the gain length was always set to 10 cm. The wavelength could be adjusted depending on which HF overtone transition was to be probed on a given test. Since, 50 sweeps were averaged to increase the signal-to-noise ratio it took 1 sec to get one complete lineshape. About 5 sec of data was collected for each hot fire giving 5 separate lineshapes from each detector. This allowed verification of steady state operation and further post-process averaging. The scroll bars at the bottom of the display could adjust the centerline wavelength and the scanning span of the diode. Having the span set properly proved to be important when

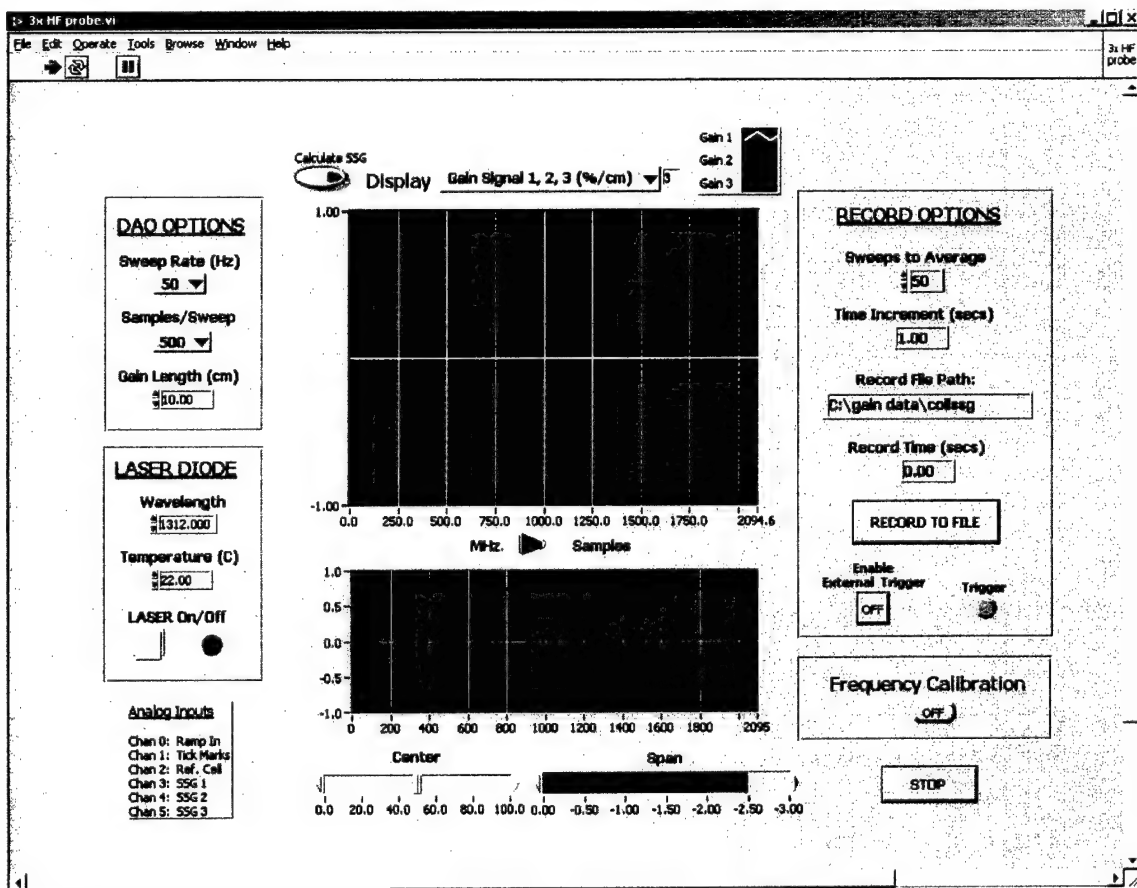


**Figure 3.9** Front panel display of tunable diode laser control LabView program.

fitting the recorded lineshapes. If the span were set too small the wings of the lineshape would be cut off and if the span was set too wide there would be too few points to adequately resolve the peak. The span was typically set to scan across 2 to 3 GHz with typical transition lineshape widths of 400 to 600 MHz.

### 3.3 Data Collection and Analysis

The small signal gain (or absorption) coefficient,  $\gamma(v)$ , is defined by the change of the probe beam signal as it traverses the laser cavity which is in turn a function of the population of the upper and lower energy states:

$$\gamma(v) = \frac{1}{L} \ln \left[ \frac{I_e(v)}{I_o(v)} \right] = \sigma_{stim} f(v) \left( N_u - \frac{g_u}{g_l} N_l \right) \quad (3.1)$$

where  $L$  is the gain length,  $I_e(v)$  is the beam intensity at the exit of the gain region,  $I_o(v)$  is the beam intensity at the inlet,  $\sigma_{stim}$  is the stimulated emission cross section,  $f(v)$  is the lineshape function, and  $N_u$ ,  $g_u$  and  $g_l$ ,  $N_l$  are the number densities and degeneracies of the upper and lower states, respectively (Verdeyen 1995). The measured gain therefore has a frequency dependence defined by the spectral lineshape of the quantum mechanical transition. In general, the two main contributors to the broadening of the spectral lineshape are pressure (collisional) broadening and Doppler broadening. The observed lineshape of a Doppler and pressure broadened transition would be a combination of Gaussian and Lorentzian profiles, which could be deconvolved by fitting a Voigt profile to the measured lineshape (Ward et al. 1974). However, under conditions investigated here, Doppler broadening dominated pressure broadening. Voigt fits to the measured lineshapes confirmed this by predicting Lorentzian widths less than 1 MHz with Gaussian widths in the 400 to 700 MHz range. The Lorentzian widths were therefore ignored and the practice of fitting the measured lineshapes with simple Gaussian profiles was adopted.

The Gaussian profile gives the peak small signal and Gaussian width, which is related to the static flow temperature through Equation (2.58). Figure 3.10 shows an

example of an HF( $v=2$  to  $v=0$ ) P3 transition lineshape fitted with a Gaussian profile. The lower panel of the graph shows the residuals of the fit, which indicate excellent agreement. The fit gives a peak gain of  $0.141\text{ % cm}^{-1}$  and a width (FWHM) of 619.2 MHz, which corresponds to a temperature of 289 K. The residual plot shown in the lower panel of Figure 3.10 demonstrates that the Gaussian line function adequately fits the entire lineshape and that Doppler broadening dominates over pressure broadening. If pressure broadening had been significant, the residual plot would have non-random structure.

Each cavity detector recorded about 5 lineshapes per hot fire. The data reduction consisted of importing the data into a data analysis and plotting software program called Origin. Origin was used due to its ease of plotting multiple data sets at one time. The lineshapes from a single detector were plotted at the same time to check steady state operating conditions, fluctuations in the baseline signal, and signal-to-noise ratio. The lineshape was then fit with a Gaussian function. The PeakFit program uses a slightly different form for the Gaussian expression:

$$f(v) = \frac{A}{w_G \sqrt{2\pi}} \exp\left[-\frac{1}{2}\left(\frac{v-v_c}{w_G}\right)^2\right] \quad (3.2)$$

This expression gives the same profile and peak value as the accepted Gaussian function (Equation (2.57)) but reports a different linewidth:

$$\frac{w_G \text{ (accepted formula, Equation (2.57))}}{w_G \text{ (PeakFit formula, Equation (3.2))}} = 2\sqrt{2\ln(2)} \approx 2.355$$

All of the linewidths reported here have been corrected by this factor. The peak value of the small signal gain, the Gaussian width,  $w_G$ , and the  $R^2$  value of the fit reported by

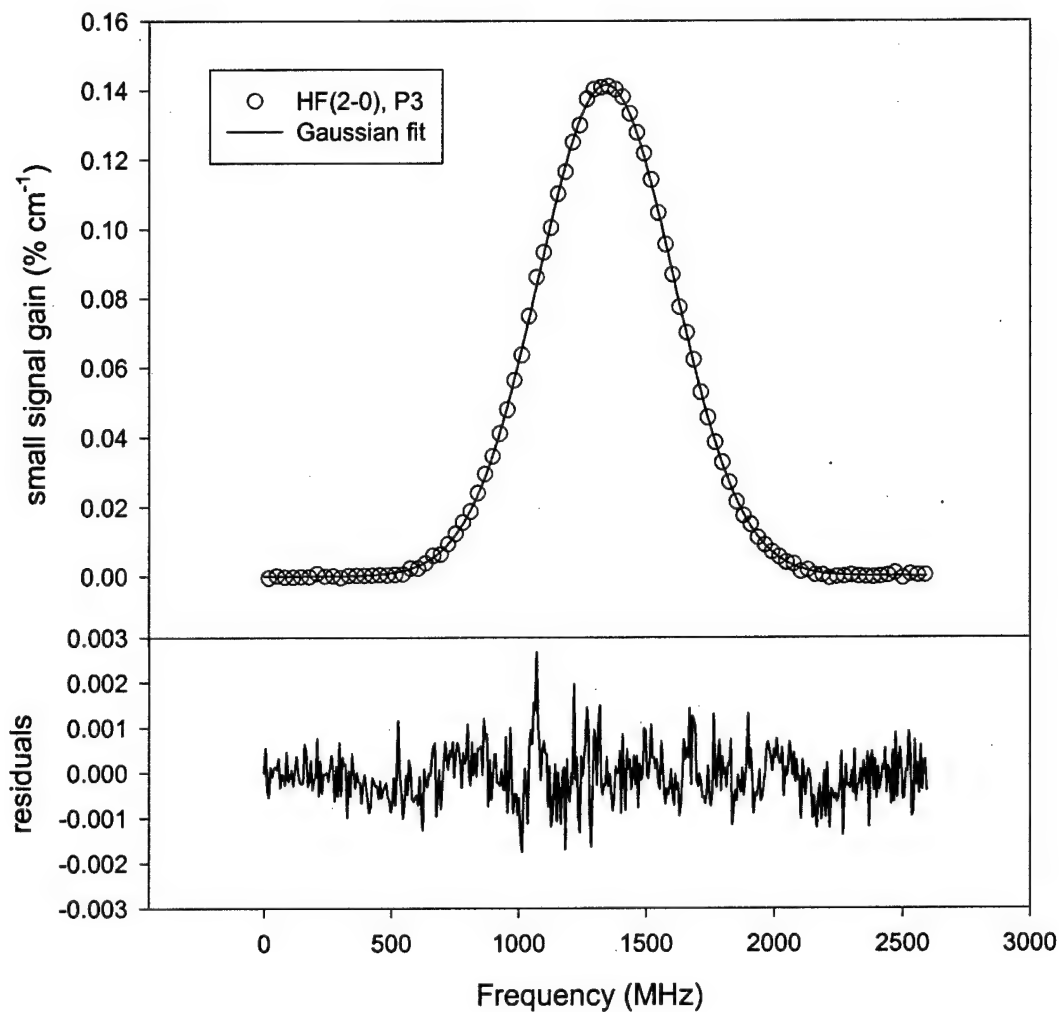


**Figure 3.10** Transition lineshape of the P(3) ro-vibrational line of the first HF overtone ( $v'=2, J'=2$   $v=0, J=3$ ). The experimental conditions for the upper panel are the ( $F_2=2$ ,  $H_2=10$ ) flow conditions,  $x = 2.5$  cm downstream of the NEP, and  $z = 0.15$  cm above the centerline. For purposes of clarity, only every 5<sup>th</sup> data point is shown. The residual plot shown in the lower panel represents the residual difference between all the data and the curve fit and demonstrates that the Gaussian line function adequately fits the entire lineshape.

PeakFit were recorded into a spreadsheet. The vertical and downstream location of the detector was also recorded in the spreadsheet. The static temperature of the flow was then determined from Equation (2.58). This process was then completed for the other two detectors. So in mapping out the cavity gain and temperature, each hot fire produced data at three different downstream locations for a given vertical location.

### 3.4 Discharge Tube Characterization (F atom Titration)

The fluorine atom concentration in the primary flow was determined via gas-phase titration with HCl (Wisniewski et al. 2003c). Electronic grade HCl (99.997%, Air Products) was injected through a ring injector installed in the plenum region between the discharge tube and the nozzle. The titration reaction



( $k$  is  $4.4 \times 10^{-11} e^{-420/T} \text{ cm}^3 \text{ molecules}^{-1} \text{ s}^{-1}$ ) quickly consumes the F atoms and generates HF with significant populations in vibrational levels up to  $v=3$  (Wurzberg and Houston 1980). The tunable diode laser system was configured to monitor the HF absorbance just downstream of the NEP. From the stoichiometry of Equation (3.3), it is evident that, for a given F atom flow rate, the amount of HF in the flow increases linearly with increases in HCl flow rate until all of the F atoms are consumed. Since the absorbance (or gain) measured by the tunable diode laser system is a linear function of the HF concentration (Equation 3.1), the absorbance signal will also increase linearly with increasing HCl flow rate. Once the HCl flow rate is increased to the point where it equals the F atom flow rate, the maximum amount of HF will be produced. Further increases in HCl will not produce more HF because all the F atoms have been consumed. The F atom flow rate is therefore equal to the HCl flow rate at the point where the HF absorbance signal plateaus to a constant value.

It is critical for the titration reaction to go to completion before reaching the nozzle throat. This can be assured if the time for the reaction is much shorter than the resident time of the reactants in the plenum region. By making one-dimensional and ideal gas assumptions, the flow velocity in the plenum region can be estimated as:

$$V = \frac{\dot{m}RT}{PA} \quad (3.4)$$

where  $\dot{m}$  is the mass flow rate,  $R$  is the gas constant,  $T$  and  $P$  are the plenum temperature and pressure, and  $A$  is the cross sectional area of the plenum. Typical values for  $\dot{m}$ ,  $T$ , and  $P$  for these titration experiments are  $0.0004 \text{ kg s}^{-1}$ ,  $400 \text{ K}$  and  $29 \text{ torr}$ , respectively. The average cross-sectional area from the injection point to the nozzle throat is  $3.8 \text{ cm}^2$ . This gives a velocity of approximately  $200 \text{ m s}^{-1}$ , which corresponds to a Mach number of about 0.2. The residence time,  $t_{res}$ , of the reactants in the plenum is:

$$t_{res} = \frac{L}{V}$$

where  $L$  is the distance from the injection point to the nozzle throat, which is about  $8 \text{ cm}$ , and  $V$  is the plenum velocity. The residence time is then on the order of  $400 \mu\text{s}$ .

The titration reaction is a nearly irreversible second-order reaction with a rate of reaction,  $R$ , defined by:

$$R = -\frac{d[F]}{dt} = \frac{d[HF]}{dt} = k[F][HCl] \quad (3.5)$$

where the brackets indicate species concentration and  $k$  is the rate constant. This equation indicates that the rate of F atom consumption is equal to the rate of HF production. Solving Equation (3.5) gives the time dependence of the F atom and HF concentrations

$$[F] = ([HCl]_o - [F]_o) \left( \frac{[HCl]_o}{[F]_o} e^{([F]_o - [HCl]_o)kt} - 1 \right)^{-1} \quad (3.6)$$

$$[HF] = [F]_o - [F]$$

where the subscript “*o*” indicates initial concentration (Steinfeld et al. 1989). Figure 3.11 shows the time evolution of the normalized  $[F]$  and  $[HF]$  for a  $1 \text{ mmol s}^{-1}$  of  $F_2$  flow case with an excess of  $HCl$ . If the reaction is considered complete when the  $[F]$  is within 1% of its final value, then the time for the reaction to reach completion is on the order of 40  $\mu\text{s}$ , an order of magnitude less than the residence time of the reactants in the plenum. The titration reaction is therefore assured of reaching completion provided the primary and injected flows are thoroughly mixed before reaching the throat. As a check of the mixing performance, a series of tests were conducted in which the probe beam was traversed in the vertical direction for fixed fluorine (MFFO1) and  $HCl$  flow rates. These

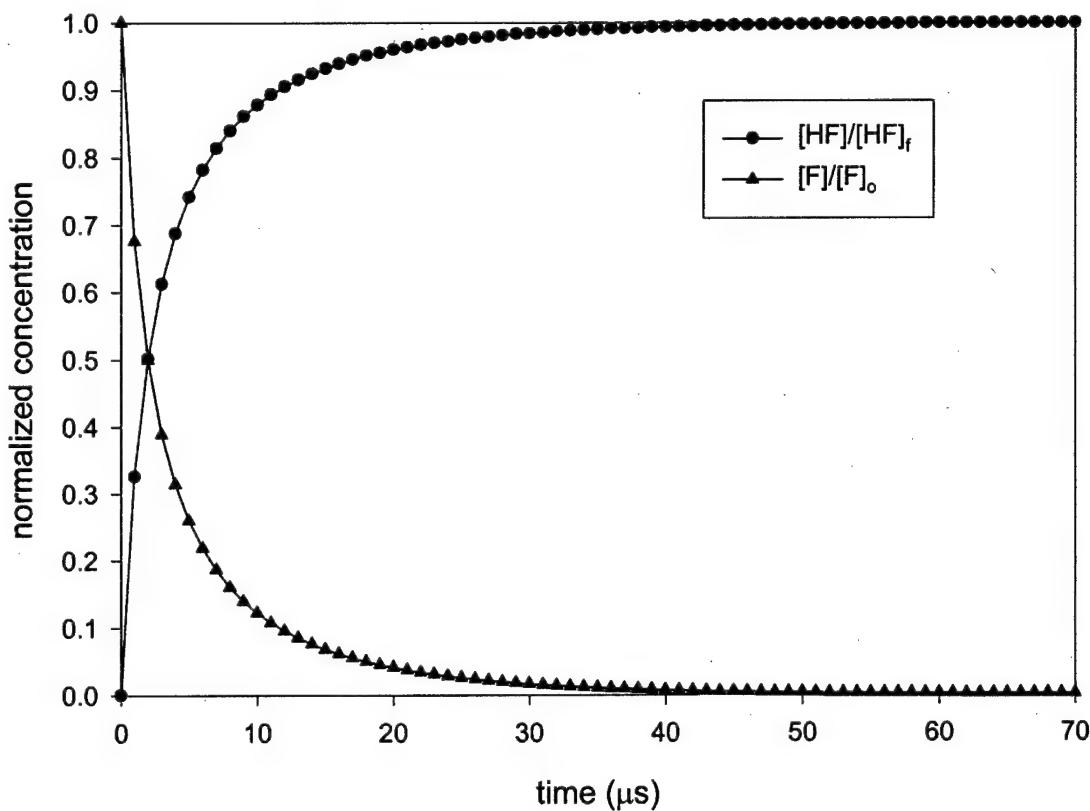


**Figure 3.11** Normalized time response of  $[F]$  and  $[HF]$  for titration reaction  $F+HCl \rightarrow HF+Cl$  for  $F_2$  and  $HCl$  flow rates of  $1 \text{ mmol s}^{-1}$  and  $2.5 \text{ mmol s}^{-1}$ , respectively. Time for reaction to go to completion  $< 40 \mu\text{s}$ .

tests showed a uniform absorbance profile indicating excellent mixing. It was therefore determined that a single point measurement at the vertical centerline would be sufficient to represent the absorbance for the given flow rates.

The vibrational distribution of the HF created by the titration reaction is another complication in the analysis of the data. The primary deactivation mechanism of the vibrationally excited HF, at the concentrations encountered in these titration experiments, is through self-relaxation with ground state HF:



This reaction has rate constants on the order of  $10^{-12} \text{ cm}^3 \text{ molecules}^{-1} \text{ s}^{-1}$  for  $v=1,2$ , or 3, which correspond to reaction completion times of about  $70 \mu\text{s}$  (Manke and Hager 2001).

Therefore significant deactivation will take place and much of the HF will be in the ground state by the time it reaches the nozzle throat. It is important to note that complete deactivation is not necessary to obtain useful data. This is because we are looking for the HCl flow rate where the HF absorbance signal plateaus and the absorbance signal is a function of the population difference between the upper and lower energy levels. So, it is only necessary for the relative populations to remain unchanged as the total HF concentration is increased. This will be the case because the deactivation reaction is a nearly irreversible second order reaction, just like the primary titration reaction (3.1), making the rate of reaction a function of the concentration difference between the upper and lower vibrational states and not of the total HF concentration. So, even though we do not know exactly how the primary and deactivation reactions populate the different HF vibrational levels, the distribution into those levels will not change as the HCl flow rate increases.

The titration experiments were conducted with the probe beam approximately 3 mm downstream of the NEP on the vertical centerline. The fluorine flow rate (MFFO1) was kept constant and the HCl flow was increased while monitoring the absorbance of the HF P3 ( $\nu=2, J=2$  to  $\nu=0, J=3$ ) overtone transition. The F<sub>2</sub> diluent (MFHE2) and Cathode He (MFHE1) flow rates were set to those used during a hot fire for the given fluorine flow rate. The addition of HCl upstream of the nozzle throat tended to raise the plenum pressure. To correct for this, the primary He diluent (MFHE3) was adjusted to maintain the proper hot-fire pressure (25 to 30 torr). The nozzle injection flows (MFH21, MFHE5, and MFHE4) were not used during the titration test series.

### 3.5 Velocity and Mach Number Measurements

#### 3.5.1 Pitot-Static Tube

Horizontal (z-direction) and vertical (y-direction) Mach number profiles of the laser cavity flow were determined from Pitot-static tube measurements (Wisniewski et al. 2003c). The Pitot-static tube used for all of these measurements was a Dwyer model 167-12 which is 30.5 cm long with a 3.175 mm (1/8 in) diameter and has separate internal channels for total and static pressures. Teflon tubing was used to connect the total and static ports of the Pitot-static tube to 100 torr and 10 torr pressure transducers, respectively.

For horizontal profiles, the Pitot-static tube was inserted through the bellows mount adapter plate and mirror tunnel. This was a span of over 25 cm, which allowed the tube to vibrate violently when the primary flows were activated. To eliminate the vibrations, a piece of 3.175 mm (1/8 in) stainless steel tubing was attached to the end of the Pitot-static tube at the point where it makes the 90° turn into the flow as shown in Figure 3.12. The extra tubing was long enough to extend through the opposite window tunnel and out the bellows mount adapter plate on the other side so that the Pitot-static tube was supported at both ends. The Pitot-static tube was attached to a translation stage that could move the tube in the horizontal or z-direction. The Pitot-static tube could be moved in the flow direction by loosening the bolts in the adapter plates and sliding it along the slotted holes.

For the vertical profiles the Pitot-static tube (without modification) was inserted through a 3.175 mm (1/8 in) pipe thread fitting screwed into a pressure port in the top of the laser cavity. There were 4 ports in the cavity spaced 2 cm apart in the downstream

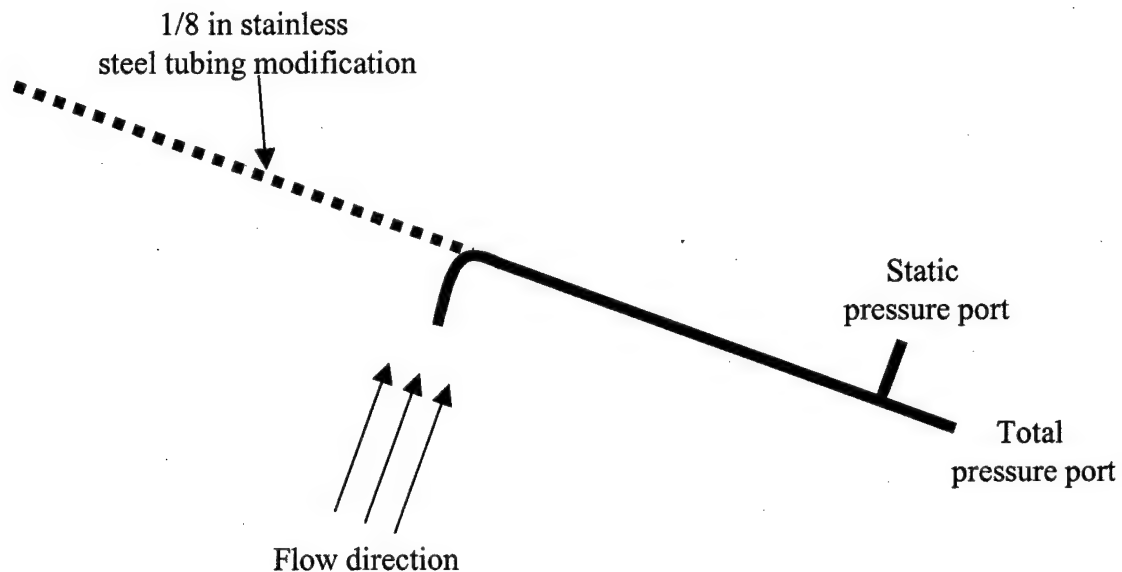


**Figure 3.12** Pitot-static tube modification used for horizontal Mach number profiles. Stainless steel tubing was attached to support the tube from both sides to eliminate vibrations during testing.

(x) direction with the tip of the tube 2 cm downstream of the NEP when placed in the first port. The end of the Pitot-static tube was attached to a translation stage that could move the tube in the vertical (z) direction.

For the horizontal Mach number profile test series, the Pitot-static tube was placed as close as possible to the vertical centerline. However, due to the bow in the tube over the large horizontal span, the exact vertical location was not known. The distance from the NEP was determined by removing the pressure port plate in the top to the laser cavity (not shown in Figure 3.1) and placing a small ruler in the bottom of the cavity. A check of this distance at the end points of the horizontal travel showed that the tube traversed straight across the flow. The angle of the tube about the horizontal axis (y-direction) was set to maximize total pressure during cold flow operation. The Pitot-static

tube was clamped securely to the translation stage to insure this angle did not change. A horizontal profile was collected by placing the tube at a particular horizontal location and then activating the hot-fire flows. The total pressure from the Pitot-static tube was monitored to ensure a steady state condition was reached. Due to the relatively long lengths of tubing between the Pitot-static tube and the pressure transducers, it took as long as 10-15 sec for the total pressure to reach a steady state value. The long tube time constant precluded an automated translation of the tube across the cavity, so we were restricted to collecting one data point per hot fire. The vertical profiles were collected in a similar manner (i.e., one data point per hot fire). The tube angle about the vertical axis (z-direction) was set to maximize the total pressure during cold flow and clamped secure to the vertical translation stage. The short vertical span of the tube did not present the same vibrations problems as for the horizontal profile measurements.

In supersonic flow, a normal shock is formed just upstream of the Pitot-static tube. The Pitot-static tube measurements are related to the flow Mach number though the Rayleigh Pitot-static tube relation (Benedict 1983):

$$\frac{P_t}{P} = \left[ \left( \frac{\gamma - 1}{2} \right) M^2 \right]^{\gamma/(\gamma-1)} \left[ \frac{\gamma + 1}{2\gamma M^2 - (\gamma - 1)} \right]^{1/(\gamma-1)} \quad (3.8)$$

where  $P_t$  and  $P$  are the total and static pressures measured by the Pitot-static tube,  $M$  is the freestream Mach number upstream of the normal shock, and  $\gamma$  is the ratio of specific heats. Equation (3.8) is a transcendental equation and cannot be solved analytically for Mach number. However, a numerical solution is easily attained by iterating on  $M$  until the calculated and measured pressure ratios are equal.

Several errors creep into the analysis of the Pitot-static tube data. The first is that because the exact constituency of the flow is unknown, the flow parameters  $\gamma$  and molecular weight (which will be needed for the Doppler velocity measurements) are also unknown. However, since the flow is approximately 90% He, the range of possible values is small. Assuming all of the F atoms in the flow channel are converted to HF gives an upper limit to the flow properties with the molecular weight and  $\gamma$  equal to 4.36 and 1.66, respectively. The lower limit is found by assuming none of the F atoms are converted to HF, which gives a molecular weight and  $\gamma$  of 4.33 and 1.63, respectively. Thus varying the flow constituents has less than a 1% effect on the calculated Mach number. Other sources of error include flow channel blockage, Pitot-static tube heating from chemical reactions in the flow, and Pitot tube alignment. The magnitude of these errors is more difficult to assess, however each will have the effect of lowering the measured Mach number.

### 3.5.2 Doppler Velocity

The optical set-up of the tunable diode laser system described in Section 3.2 was modified for its use as a velocity measuring device (Wisniewski et al. 2003b). By probing the laser cavity at an angle to the flow, the transition lineshape is Doppler shifted by the component of the flow velocity in the beam direction. The optical set-up used to measure this effect is shown in Figure 3.13. This approach is a slight modification to the technique used by Nikolaev et al (2000) to measure velocity in an oxygen-iodine laser. Here the diode beam is split into three separate beams. Two of the beams were rotated  $\pm 7.85^\circ$  from the direction normal to the flow. The third beam, directed normal to the

flow, intersected the other beams in the center of the flow channel. The angled beams were directed back through the laser cavity in a “bow tie” crossing pattern. The resulting double pass arrangement significantly improves the signal-to-noise ratio making this approach better suited for gain mediums than the technique used by Nikolaev et al (2000).

The HF spectroscopic line was shifted to a higher frequency for the downstream-directed beam and to a lower frequency for the upstream-directed beam. Both lines, however, had the same Doppler and pressure broadened characteristics. The frequency difference between the shifted peaks is directly proportional to the flow velocity. Translation stages were incorporated into the optical set-up so that the velocity could be measured at different locations along the vertical axis. The beam that probed the laser

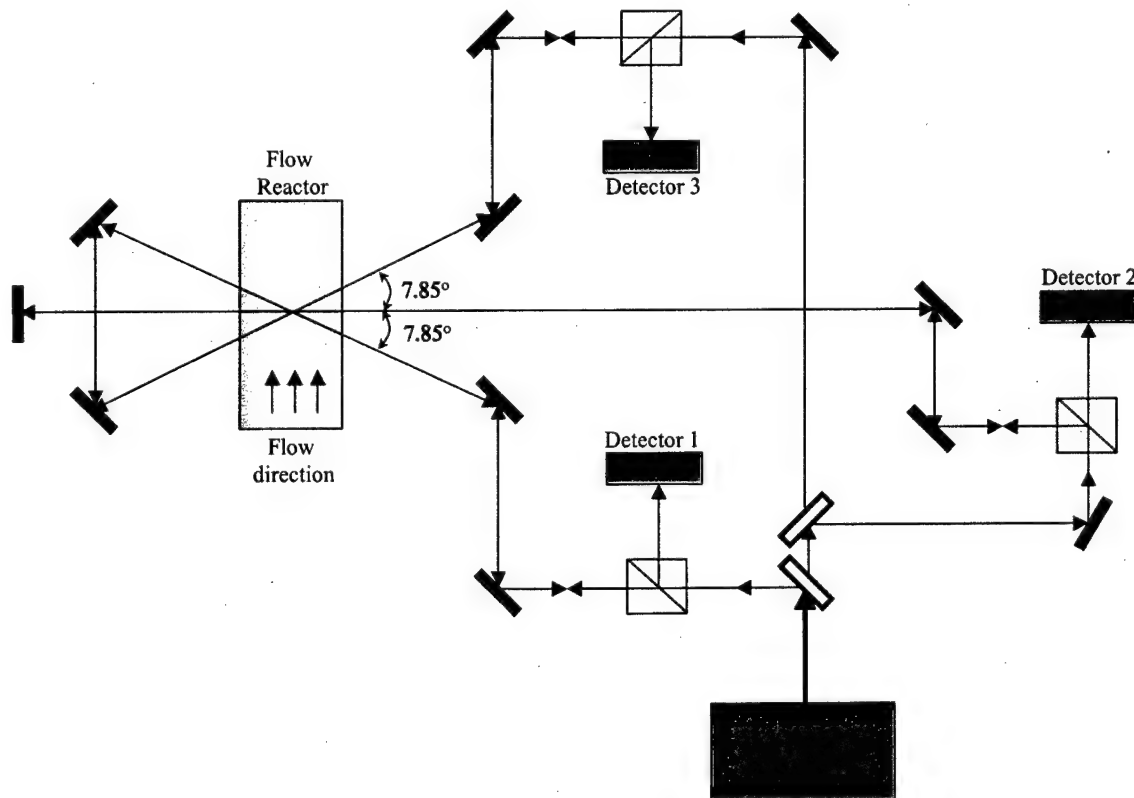


**Figure 3.13** Diagram of double pass Doppler velocity optical set-up.

cavity normal to the flow direction was compared to previous small signal gain measurements and served to verify flow sampling location.

The shift in the lineshape peak frequency is given by:

$$\nu = \nu_o \left[ 1 \pm \frac{V_y}{c} \right] \quad (3.9)$$

where  $\nu_o$  is the centerline frequency and  $V_y$  is the flow velocity component in the beam direction. The frequency difference between the peaks,  $\Delta\nu$ , is directly proportional to the flow velocity:

$$\frac{\Delta\nu}{2} = \frac{V_y}{c} \nu_o = \frac{V \sin \alpha}{\lambda} \quad (3.10)$$

where  $V$  is the flow velocity,  $\lambda$  is the transition wavelength and  $\alpha$  is the angle between the beam tube direction and a line perpendicular to the flow. The Mach number is given by

$$M = \frac{V}{a} = \frac{V}{\sqrt{\frac{\gamma \bar{R} T}{M W}}} \quad (3.11)$$

where  $a$  is the local speed of sound,  $\gamma$  is the ratio of specific heats,  $T$  is the local static temperature (as determined from the Gaussian line width) and  $MW$  is the molecular weight. Just as in the Pitot-static tube measurement, the unknown flow constituency creates uncertainty in the flow parameters, which introduces an error in the Mach number calculation. However, upper and lower bounds obtained by varying  $\gamma$  and  $MW$  showed less than a 1% effect on the calculated Mach number.

### 3.6 Power and Out-coupled Spectrum Measurements

Fundamental power was extracted from the laser using a simple two-mirror stable resonator. In this type of resonator one mirror has a maximum available reflectivity (Max R) at the wavelength of the lasing transition and the other mirror (the output coupler) has a somewhat reduced reflectivity. A standing wave develops between the mirrors in which the circulating intensity rapidly builds until a steady state condition is reached in which the round-trip loop-gain equals the cavity losses. Losses to the circulating radiation field intensity are caused by scattering, absorption and diffraction as well as by the power extracted from the cavity through the outcoupler. As the internal intensity increases, the population inversion, and therefore also the gain, within the system is reduced through stimulated emission by a process termed saturation. Saturation creates a balance between the pumping mechanisms, deactivation mechanisms, stimulated emission and optical losses within the cavity including useful outcoupled power.

Figure 3.14 shows typical curves of laser power as a function of output coupler transmissivity for resonators with and without cavity losses. Since, the absorbtivity of high quality optics is typically very low the transmittance,  $T$ , can be approximated as:

$$T=1-R$$

where  $R$  is the mirror reflectance. Changing the reflectance of the outcoupler ( $R_1$ ) while holding the Max R reflectance ( $R_2$ ) constant, changes the intensity of the recirculating radiation within the laser cavity resulting in a new saturation condition. These curves are therefore referred to as intensity saturation curves or I-Sat curves for short. The circulating intensity inside the laser cavity increases as the outcoupling reflectance

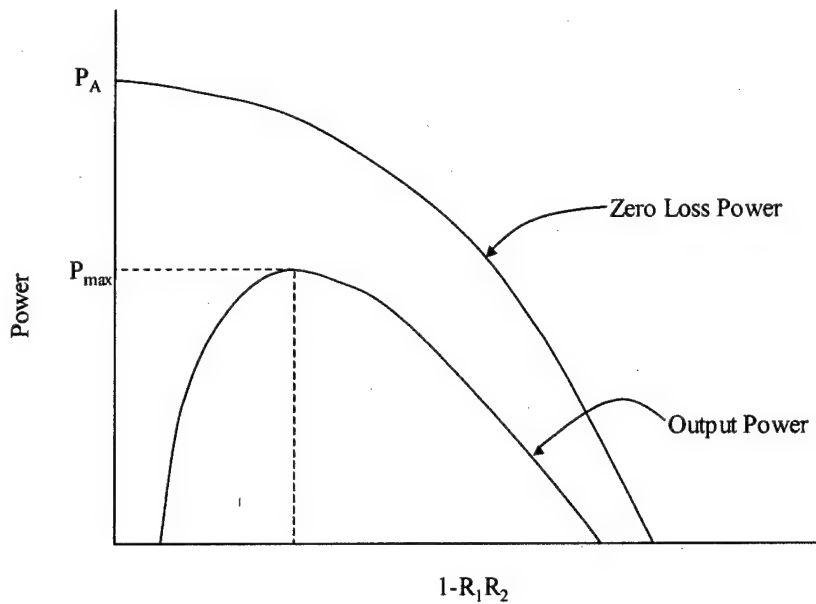


**Figure 3.14** Schematic representation of power versus outcoupling fraction.  $P_A$  represents the power available in the gain medium and  $P_{\max}$  represents the maximum power output from the resonator.  $R_1$  is the outcoupler reflectance and  $R_2$  is the Max R reflectance (i.e.,  $R_2 \approx 1$ )

increases and if no losses are present reaches a maximum for  $R_1=1$  ( $T=0$ ). The maximum internal intensity will extract the maximum amount of energy from the population inversion. Therefore, if no internal optical losses are present, the output power approaches the maximum power available from the gain medium as  $R_1$  approaches unity. However, all lasers have losses that dominate as the internal intensity increases thus causing the useful outcoupled power to decrease as  $R$  approaches unity as shown in Figure 3.14. This creates an optimal outcoupler reflectance to achieve maximum power output. Fundamental HF lasers are very high gain systems and assuming a low loss resonator, the outcoupler reflectance to achieve maximum power is typically very high (i.e.,  $R>90\%$ ).

### 3.6 Power and Out-coupled Spectrum Measurements

Fundamental power was extracted from the laser using a simple two-mirror stable resonator. In this type of resonator one mirror has a maximum available reflectivity (Max R) at the wavelength of the lasing transition and the other mirror (the output coupler) has a somewhat reduced reflectivity. A standing wave develops between the mirrors in which the circulating intensity rapidly builds until a steady state condition is reached in which the round-trip loop-gain equals the cavity losses. Losses to the circulating radiation field intensity are caused by scattering, absorption and diffraction as well as by the power extracted from the cavity through the outcoupler. As the internal intensity increases, the population inversion, and therefore also the gain, within the system is reduced through stimulated emission by a process termed saturation. Saturation creates a balance between the pumping mechanisms, deactivation mechanisms, stimulated emission and optical losses within the cavity including useful outcoupled power.

Figure 3.14 shows typical curves of laser power as a function of output coupler transmissivity for resonators with and without cavity losses. Since, the absorbtivity of high quality optics is typically very low the transmittance,  $T$ , can be approximated as:

$$T=1-R$$

where  $R$  is the mirror reflectance. Changing the reflectance of the outcoupler ( $R_1$ ) while holding the Max R reflectance ( $R_2$ ) constant, changes the intensity of the recirculating radiation within the laser cavity resulting in a new saturation condition. These curves are therefore referred to as intensity saturation curves or I-Sat curves for short. The circulating intensity inside the laser cavity increases

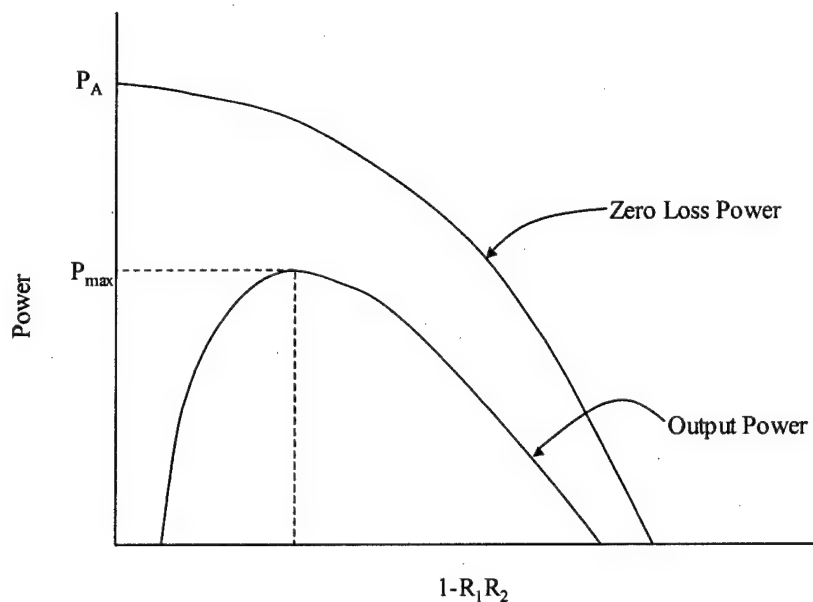


**Figure 3.14** Schematic representation of power versus outcoupling fraction.  $P_A$  represents the power available in the gain medium and  $P_{\max}$  represents the maximum power output from the resonator.  $R_1$  is the outcoupler reflectance and  $R_2$  is the Max R reflectance (i.e.,  $R_2 \approx 1$ )

as the outcoupling reflectance increases and if no losses are present reaches a maximum for  $R_1=1$  ( $T=0$ ). The maximum internal intensity will extract the maximum amount of energy from the population inversion. Therefore, if no internal optical losses are present, the output power approaches the maximum power available from the gain medium as  $R_1$  approaches unity. However, all lasers have losses that dominate as the internal intensity increases thus causing the useful outcoupled power to decrease as  $R$  approaches unity as shown in Figure 3.14. This creates an optimal outcoupler reflectance to achieve maximum power output. Fundamental HF lasers are very high gain systems and assuming a low loss resonator, the outcoupler reflectance to achieve maximum power is typically very high (i.e.,  $R>90\%$ ).

The round-trip loop gain equilibrium condition for a simple two mirror Fabry-Perot resonator, which is a good approximation for the resonator used in this investigation, gives (Hager et al. 1996):

$$\gamma \equiv \gamma_{th} + \mathcal{L} - \frac{\ln(1 - \delta)}{2L_g} \quad (3.12)$$

where  $\mathcal{L}$  is a distributed nonsaturable loss,  $\delta$  is the aperture diffraction loss and  $L_g$  is the gain length. The threshold gain,  $\gamma_{th}$ , is defined by:

$$\gamma_{th} \equiv \frac{-\ln(R_1 R_2)}{2L_g} \quad (3.13)$$

where  $R_1$  and  $R_2$  are the mirror reflectivities. When the outcoupling fraction,  $(R_1 R_2)$ , is small the laser will just barely flicker and the internal intensity of the radiation field will be small and have a minimal effect on the population inversion. Under these conditions the gain predicted from Equation (3.12) will equal the small signal gain. Neglecting the optical losses, which are typically small compared to the fundamental HF threshold gain, the small signal gain can be approximated as:

$$\gamma_o \approx \gamma_{th} = \frac{-\ln(R_1 R_2)}{2L_g} \quad (3.14)$$

Therefore an estimate of the small signal gain can be made by determining the outcoupler reflectivity at which the system barely lases.

The resonator in these experiments consisted of a 5.08 cm (2 in) diameter, concave (10 m radius of curvature) high reflector mirror (99.95% reflective at 2.5 – 3.1 mm) and a series of 5.08 cm (2 in) diameter flat outcoupler mirrors ranging in reflectance from 40% to 95%. The optics were mounted in the bellows mount assemblies on either side of the laser cavity giving a mirror separation of 65.75 cm. An aperture placed in the

bellows mount assembly limited the vertical height of the resonator aperture to 2.54 cm, which is slightly smaller than the vertical height of the laser cavity. The mirror retaining rings limited the horizontal length of the resonator aperture to  $\sim 4.5$  cm for a beam area of  $\sim 11.25 \text{ cm}^2$ .

A HeNe laser directed along the optical axis was used to align the resonator. The alignment procedure consisted of locating the optical axis at the desired downstream location, pulling the laser cavity under vacuum and then aligning the HeNe laser reflections from the inner and outer surfaces of the optics to a pinhole located at the source. Although this procedure worked quite well, small adjustments were often required while the laser was operating in order to maximize the output power. Power was measured with an Ophir model 5000W-LP thermal head power meter, whose output was recorded by the fluid supply system data acquisition computer. Figure 3.15 shows an example of the measured output power time trace along with the time trace of the fluorine flow rate. The power fluctuations are caused by vertical and horizontal alignment adjustments made during the hot fire to maximize power. The short delay between the fluorine flow rate activation and measured power is due to the thermal response of the power meter and time delay for the F atoms to reach the cavity from the flow control orifice about 15 m from the laser device.

HF lasers are multi-line lasers because they lase simultaneously on several different ro-vibrational transitions. In order to determine which transitions were lasing, the spectral content of the fundamental laser output was measured using an Acton Spectrapro 300i monochrometer and a Boston Electronics HgCdZnTe infrared

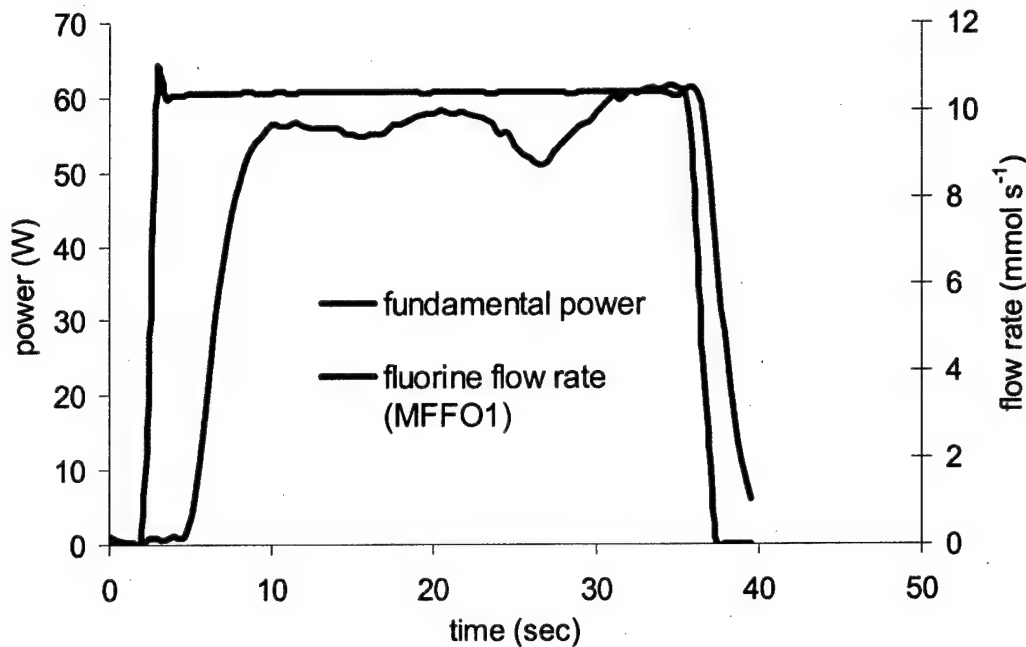


**Figure 3.15** Time traces of fundamental output power and fluorine flow rate for the ( $F_2=2$ ,  $H_2=10$ ) flow conditions taken 3.2 cm downstream of the NEP. Power fluctuations are caused by vertical and horizontal alignment adjustments made during the hot fire to maximize power.

detector as shown in Figure 3.16. The monochrometer used a  $2.0\text{ }\mu\text{m}$  grating with 300 lines  $\text{mm}^{-1}$  to split the incoming laser beam into its discrete spectrum. The spectrum was then scanned across the detector at the exit of the monochrometer producing a time trace that looked like a series of sharp peaks corresponding to the laser spectrum. The monochrometer was set to scan from  $2.5\text{ }\mu\text{m}$  to  $3.1\text{ }\mu\text{m}$  at a rate of  $2.0\text{ }\mu\text{m min}^{-1}$ , which covered all the  $v = 1$  to 0,  $v = 2$  to 1 and  $v = 3$  to 2 fundamental P branch transitions in about 18 s. The spectra show multiple lasing lines within each of these three vibrational bands.

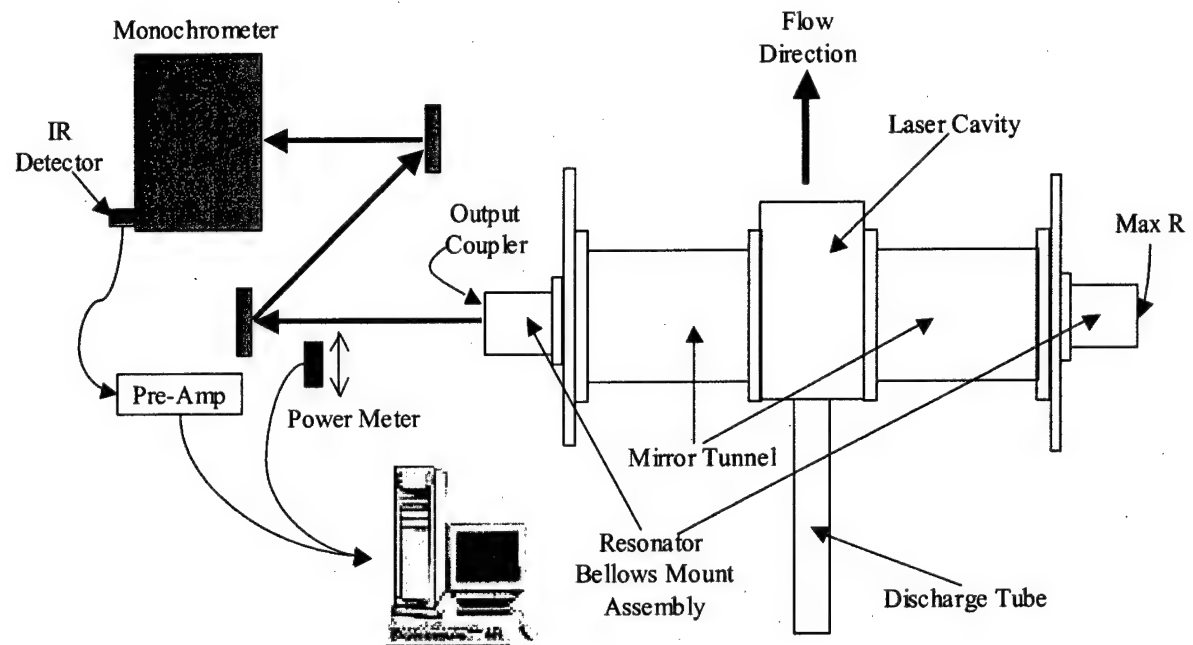


**Figure 3.16** Experimental set-up for power extraction and output laser beam spectrum measurements.

### 3.7 Saturated Gain Measurements

In Section 2.2.3 it was stated that the HF rotational relaxation rate constants were so fast that, to a very good approximation, the rotational levels within each vibrational band can be described by an equilibrium Boltzmann distribution. While this is undoubtedly the case under small signal conditions, questions remain on whether or not rotational equilibrium exists when the vibrational levels are saturated during lasing. If stimulated emission can remove energy from a ro-vibrational level faster than rotational relaxation can transfer energy between the rotational levels then the ro-vibrational levels will essentially act independent of each other. However, if rotational relaxation energy transfer is faster than stimulated emission, then the whole vibrational band will saturate as a unit. In order to investigate this, the overtone small signal gain of several different ro-vibrational transitions was measured while simultaneously lasing on the fundamental transitions. Since the gain measurements give a direct measure of the rotational distribution in the  $v = 2$  and  $v = 0$  levels simultaneously and because the laser saturates the  $v = 1$  to 0,  $v = 2$  to 1 and  $v = 3$  to 2 transitions, probing the  $v = 2$  to 0 transitions should give a direct representative measure of the degree of rotational relaxation and/or equilibrium (Manke et al. 2003).

The saturated overtone gain was measured by propagating the diode probe beam through the fundamental resonator optics at a slight angle as shown in Figure 3.17. The diode probe beam entered and exited the cavity at a  $3.5^\circ$  angle relative to the optical axis. At this small angle the probe beam remained within one beam diameter ( $\sim 2$  mm) of the optical axis over the entire 5 cm span of the active gain length. Because the resonator optics significantly attenuated the diode probe, only a single pass through the gain

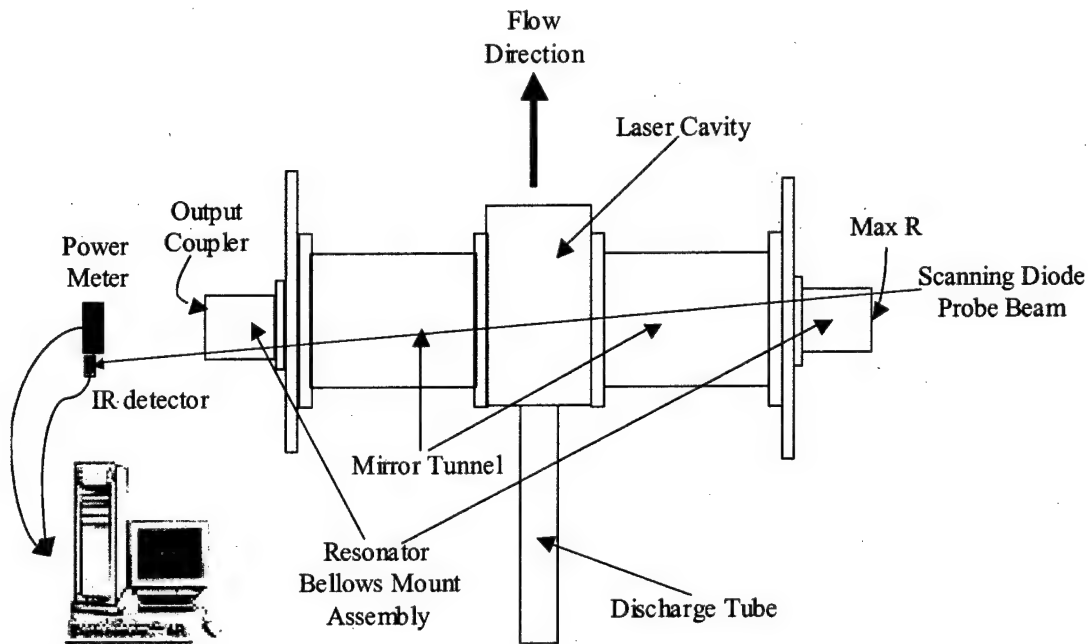


**Figure 3.17** Experimental set-up of overtone gain measurement while lasing on fundamental transitions.

medium was possible which greatly reduced the signal to noise ratio as compared to the double pass unsaturated gain measurements. Thus these gain measurements are restricted to the vertical region near the peak gain location.

These saturated gain measurements were taken for the P1, P2, P3, P4 and P5 overtone ( $\nu = 2$  to 0) transitions. The procedures for this test series entailed first aligning the fundamental resonator at a particular downstream location and then performing several hot fires to maximize the power. A short vertical gain profile for each transition was then performed to ensure all the transitions had the same vertical peak gain location. The laser power was monitored during these profiles to verify that saturation conditions did not change. This process was repeated for several different outcoupler reflectivities and several downstream locations for the ( $F_2=2$ ,  $H_2=10$ ) flow conditions.

## Chapter 4

### Modeling-Code Description

Due to the complexity of the interaction between the quantum mechanics, chemical kinetics and fluid mechanics within the laser flow field, interpretation of the trends within small signal gain data is very limited without the aid of a computer model. Numerical solutions of the three-dimensional (3-D) Navier-Stokes equations to model a laser cavity flow field for a Chemical Oxygen Iodine Laser (COIL) device have been obtained (Buggeln et al. 1994; Eppard et al. 2000; Madden 1997). These computer models are extremely complex requiring weeks of run time on large parallel processing computer systems to obtain converged solutions. In addition, modification of these codes to model the HF kinetics and geometry is nontrivial and beyond the scope of this experimental thesis. Instead, predictions were made with a two-dimensional (2-D) parabolic marching code that has been modified to model the HF laser chemistry (Crowell 2002). This code sacrifices fidelity in modeling the actual 3-D flow in favor of simplicity and short run times allowing the examination of a large parameter space.

The rationale for using a 2-D model is that the lateral spacing between injector holes is small enough such that the flow field will appear nearly two-dimensional at the nozzle exit/cavity entrance. Although the axial vorticity is not zero, as would be the case for a true 2-D flow field, it is not so large as to completely dominate the molecular diffusion mixing. That is, for the low angle injectors used in HF nozzle blades, the vorticity induced by the jets as they are turned parallel to the main flow should be small compared to that for normal (90°) injection. The low angle injection, combined with low pressure,

results in a situation where 2-D laminar mixing provides a reasonable estimate of the mixing rate. Because the code is only 2-D, it cannot capture the complexities of the mixing mechanisms, which are driven by flow turbulence intensity and are therefore inherently 3-D. The code instead bounds the problem by running in two separate modes. The *premix* mode assumes that the secondary He and H<sub>2</sub> flows are instantaneously mixed into the primary He and F atom flow and evenly distributed across the nozzle at a location just upstream of the base relief step. This is, of course, the best-case mixing scenario and will provide an upper bound on the laser performance. The *mixing* mode of the code provides a lower bound of performance. This mode uses simple geometrical considerations to predict the location of the secondary He and H<sub>2</sub> flow streams in the nozzle just upstream of the base relief step and assumes diffusional mixing from that point on.

Figure 3.3 shows the Cartesian coordinates of the nozzle where the streamwise, cross-stream and spanwise directions are defined by the x, y and z axes, respectively, with corresponding velocity components u, v and w. The 2-D assumption eliminates the spanwise (or transverse) momentum equation, all derivatives with respect to the z direction and the spanwise velocity component w from the Navier-Stokes equations. Parabolizing the Navier-Stokes equations entails neglecting the second derivative of the velocity components with respect to the flow direction (i.e.,  $\frac{\partial^2 u}{\partial x^2}$  and  $\frac{\partial^2 v}{\partial x^2}$ ) in the momentum equations (White 1991). This reduces the order of the momentum differential equations with respect to x, thus changing the system from a boundary value problem to an initial value problem and eliminating the need for a downstream boundary condition. The upstream flow field is therefore de-coupled from the downstream flow field, which is

a good assumption for supersonic flow. However, in the actual flow field, downstream influences can propagate upstream through the large subsonic base purge regions. These influences are not considered in this model nor is recirculation of the primary laser flow into the base purge region included.

The code uses the thin shear layer approximation to assume that the pressure varies only in the flow direction and not in the vertical (cross-stream) direction (White 1991). This allows the cross-stream momentum equation to be replaced by:

$$\frac{\partial p}{\partial y} = 0 \quad (4.1)$$

Chemical laser cavities are typically designed to minimize transverse pressure gradients. However, the large base purge step at the nozzle exit plane (NEP) of the HF nozzle being modeled here is likely to produce oblique shocks that will create transverse pressure gradients. The oblique shocks therefore cannot be resolved by this code.

The species mass conservation equations are given by:

$$\rho u \frac{\partial K_i}{\partial x} + \rho v \frac{\partial K_i}{\partial y} = - \frac{\partial}{\partial y} \left( \rho K_i \hat{v}_i - \frac{\mu_t}{S_t} \frac{\partial K_i}{\partial y} \right) + W_i + Z_i \quad (4.2)$$

where  $\rho$  is the local density,  $K_i$  is the mass fraction of the  $i^{\text{th}}$  species,  $\mu_t$  is the turbulent eddy viscosity,  $S_t$  is the turbulent Schmidt number,  $W_i$  is the species source term from chemical reactions,  $Z_i$  is the lasing source term and  $\hat{v}_i$  are the laminar diffusional velocities (Crowell 2002). The species source terms from chemical reactions are computed through detailed balance of the chemical reactions discussed in Section 2.2. Individual vibrational levels of the reactants and products are tracked as separate species requiring the code to compute 136 separate chemical reactions at each downstream location. The rotational levels of the reactants and products are handled by assuming a

Boltzmann distribution within individual vibrational levels. The lasing source term in Equation (4.2) is required because the extraction of laser energy from the flow field will change the population of the excited species. However, since this research has focused on understanding the small signal gain data trends, the code was not run with the lasing model activated.

The laminar diffusional velocities are expressed as:

$$K_i \hat{v}_i = S_{21} K_i - S_{31} \frac{\partial K_i}{\partial y} - \frac{D_i^T}{\rho T} \frac{\partial T}{\partial y} \quad (4.3)$$

The expressions for  $S_{21}$  and  $S_{31}$  are determined from an “effective” binary diffusion model based on the work of Ramshaw and Dukowicz (1979), which was modified to include the effects of pressure gradients on the diffusional velocities (Crowell 1987). The thermal diffusion coefficient,  $D_i^T$ , in Equation (4.3) represents the effect of temperature gradients on the diffusional velocities. Since the computation of  $D_i^T$  significantly increased the overall computation time and its effects on the diffusional velocity were minimal, an internal input flag was set to eliminate it from the computation.

The 2-D code cannot predict the actual 3-D turbulent flow field. However, the code includes a K- $\epsilon$  turbulence model, which tracks the transport and dissipation of turbulent kinetic energy, that can simulate some of the overall effects turbulence has on the flow. The Reynolds number for the flows of interest is of the order  $800 \text{ cm}^{-1}$  at the cavity entrance, which is sufficiently small that significant enhancement of the mixing rate due to turbulence would not be expected. Therefore the low Reynolds number Launder-Sharma (1974) turbulence model modifications, which are applicable to wall-bounded and free jet flows, have been included. A convenient input parameter flag was

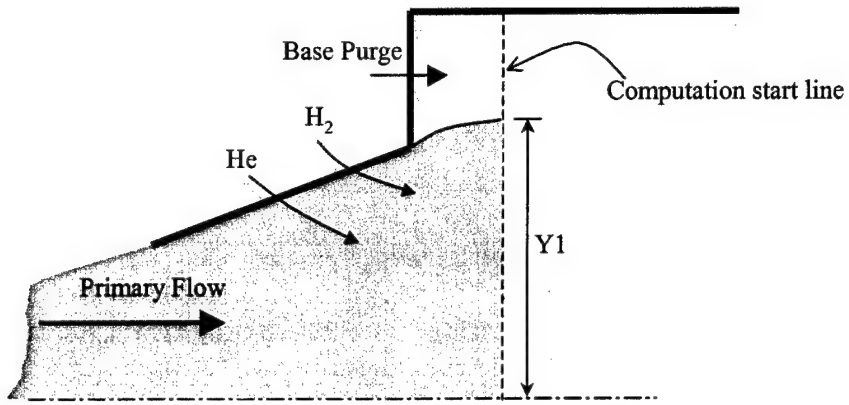
set-up to activate or disable the turbulence model in order to assess the significance of turbulence on the predicted flow field (see Section 5.4.2).

The computer model utilizes the flow field symmetry at the vertical centerline to reduce the computational domain to the upper plane bounded by the centerline and the upper cavity wall. The proper boundary condition at the cavity wall would, of course, be the no-slip condition. However, since the wall is so far from the reaction zone, conditions at the wall were thought to have little influence on the core flow field. A symmetry condition was used at the wall as well as at the centerline to reduce computation time. Attempts to verify the insensitivity of the small signal gain predictions to the wall boundary condition were complicated by numerical instabilities that prevented model convergence for the no-slip wall condition. For most flow conditions with the no-slip wall condition, the model marched several centimeters downstream before failing to converge. The small signal gain profiles upstream of the non-convergence location were nearly identical to profiles predicted with the symmetry boundary condition. The convergence problems appear to be caused by flow separation at the wall caused by an adverse pressure gradient. The effects of the improper wall boundary condition are apparent in comparisons between the measured and predicted small signal gain profiles near the wall more than 4 cm downstream of the NEP (see Section 5.4.4). However, the model appears to adequately predict the small signal gain profile within the core flow region, between  $\pm 5$  mm from the vertical centerline, at all downstream locations. In all the model prediction cases run for this research the cross-flow dimension was divided into 150 nodes, which were distributed to give more resolution in the region where the chemical reactions were assumed to take place and fewer nodes in the base purge region.

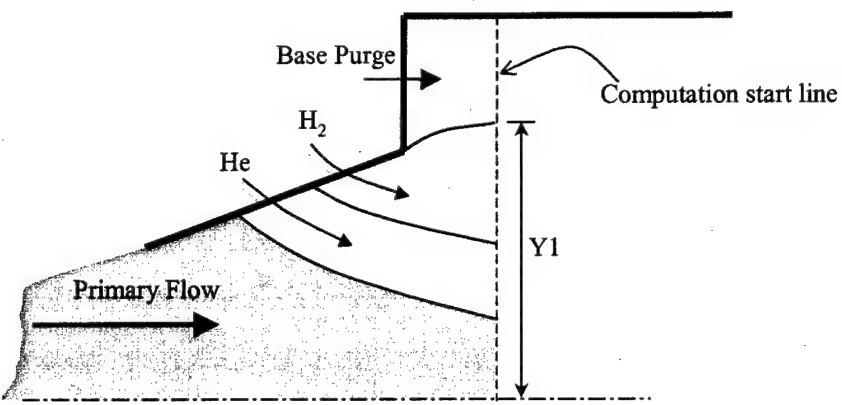
The required input parameters to the code were the nozzle geometry, species molar flow rates, cavity pressure, initial turbulence intensity of each flow stream, the total temperature and pressure upstream of the secondary He injection point and the Mach number of the injected flow streams. The calculations were started at the nozzle exit plane (NEP) and marched 10.0 cm downstream with a 0.025 cm step size.

#### 4.1 NEP Starting Conditions

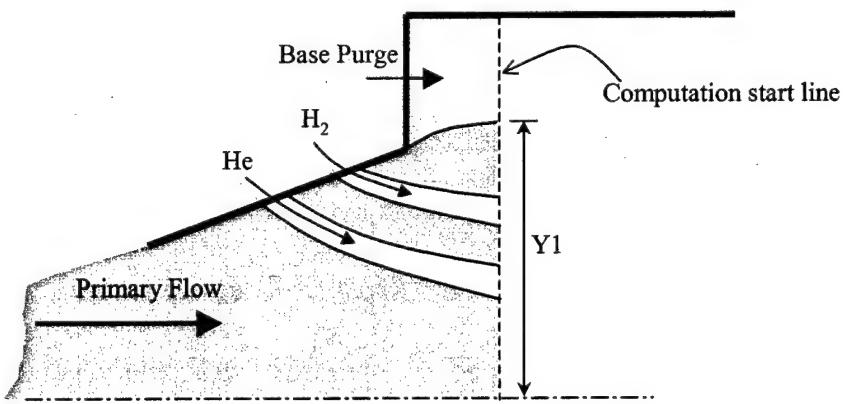
Since the parabolized Navier-Stokes marching calculations start at the NEP and the total pressure and temperature input parameters are specified just upstream of the secondary He injection point, an approximate representation of the injection process must be adopted to define the initial conditions at the NEP. Figure 4.1 shows the flow distribution an infinitesimal distance downstream of the NEP for the three injection scheme options available within the code. In setting the starting conditions for the premixed mode, the code instantaneously mixes the injected He and H<sub>2</sub> flow streams with the primary F atom flow and evenly distributes the flow at the NEP. Flow properties (temperature, pressure, Mach number, etc.) are calculated by conserving total mass, momentum and energy of the flow and not allowing chemical reactions to proceed. Because the thin shear layer assumption has been made, a pressure gradient cannot be sustained between the base purge flow and the nozzle flow. The code must therefore expand or contract the premixed nozzle and the base purge flows with a common pressure immediately downstream of the NEP. To do this the relative cross sectional areas occupied by the base purge and nozzle flows must first be determined. The under-expanded jets that issue from sonic orifices in the base purge flow region are assumed to pass through a normal shock. This shock takes the flow from a total pressure specified by the sonic conditions of the individual orifices to the measured cavity pressure and specifies the cross-sectional area occupied by the base purge flow. The cross-sectional area of the nozzle flow occupies the remaining area. The nozzle flow properties are then adjusted to fill the new area. This pressure equilibrium calculation happens within an



a) premix



b) imesh=2



c) imesh=3

**Figure 4.1** Flow distribution with mixing options a) premixed b) mixing with imesh=2 and c) mixing with imesh=3 injection schemes. The computational start line is an infinitesimal distance downstream of the NEP.

infinitesimal distance downstream of the NEP where the parabolic marching code takes over. The pressure equilibrium process in the actual flow will proceed through a series of oblique shocks and/or expansion fans that reflect off the shear layer between the nozzle flow and the base purge flow extending their influence down the length of the cavity. If the shocks or expansion fans are weak the vertical pressure gradients will be small and this method of computing the NEP starting conditions may produce good approximations for the relative size of the nozzle and purge flows.

Within the mixing mode of the code there are two separate options for setting-up the location of the H<sub>2</sub> and He injection jets at the NEP. For the imesh=2 mixing mode option shown in Figure 4.1b, the H<sub>2</sub> and He jets expand from their respective sonic orifices to fill the area between the primary flow and the wall. The trajectories, cross-sectional areas and properties of the jets are calculated from a modified Schetz (1966) trajectory model. For the imesh=3 mixing mode option shown in Figure 4.1c, the location and size of the injection jets at the NEP are user specified. Setting the input parameters so that the H<sub>2</sub> jet moves away from the nozzle wall automatically fills the region between the jet and nozzle wall with primary flow. This mode gives the user the flexibility to adjust the jet locations in an attempt to get predicted gain profiles to match measured gain profiles. For either mixing mode option, the code first performs a premix calculation to predict the cross-sectional area of the total nozzle flow. The injected jets are then located within that cross-sectional area. The jets in either mixing mode do not exchange mass, momentum or energy with the primary flow and the chemical reactions are not allowed to proceed until the flow reaches the NEP.

## 4.2 Comparison of Measured and Predicted Gain

The diagnostic probe beam diameter used to measure the small signal gain was approximately 2 mm, which is about 20% of the nozzle height at the NEP. The probe beam therefore averages the gain over a significant portion of the vertical flow field. A proper comparison between the predicted and measured gain distributions must take this averaging into account. The code accomplishes this by propagating a finite diameter probe beam in the z direction (perpendicular to the computational plane) through the predicted gain distribution.

The small signal gain,  $\gamma(v)$ , was defined by Beer's Law in Section 2.1.4 as:

$$\gamma(v) = \frac{1}{L} \ln \left[ \frac{I_e(v)}{I_o(v)} \right] \quad (4.4)$$

where  $I_e(v)$  and  $I_o(v)$  are the exit and input probe beam intensities, respectively, and L is the gain length. Solving for the exit beam intensity in terms of the input intensity and the small signal gain yields:

$$I_e(v) = I_o(v) e^{\gamma L} \quad (4.5)$$

for a beam of uniform intensity and a region of uniform gain,  $\gamma$ . The code predicts the gain distribution in the x-y plane and assumes the gain is constant in the z direction. The predicted gain lineshape, for a Doppler broadened gain medium, is then given by:

$$\bar{\gamma}(v, x, y) = \gamma_o(x, y) e^{-\hat{x}^2} \quad (4.6)$$

where the dimensionless frequency is:

$$\hat{x} = \frac{2(v - v_o) \sqrt{\ln 2}}{\Delta v_D} \quad (4.7)$$

where  $\gamma_o$  is the calculated line center (i.e.,  $v = v_o$ ) gain distribution over the x-y plane and the Doppler-broadened linewidth  $\Delta\nu_D$  is obtained from the predicted temperature over the x-y plane. To predict the gain lineshape of a finite diameter probe beam propagated through the computed gain medium, the input and exit beam intensities must be averaged over the beam cross section:

$$\gamma_p(v, x, y) = \frac{1}{L} \ln \left[ \frac{\int_0^{a/2} \int_0^{2\pi} I_o(r, \phi, v) e^{\bar{\gamma}L} r dr d\phi}{2\pi \int_0^{a/2} I_o(r, v) r dr} \right] \quad (4.8)$$

where  $a$  is the beam diameter. At line center  $\bar{\gamma}(x, y) = \gamma_o(x, y)$  and  $\gamma_p(x, y)$  is then the predicted line center gain averaged over the beam diameter that should approximate the measured line center gain. In order to perform the integration in Equation (4.8) the predicted gain lineshape, which is defined in terms of x-y coordinates, must be transformed into polar coordinates centered at the beam location. The integration requires knowledge of the gain distribution downstream of the probe beam center location forcing the calculation of  $\gamma_p(x, y)$  into a post process situation after the gain distribution had been determined for the entire flow field. However, over the span of the probe beam diameter the gradient of the gain is much larger in the vertical direction than in the downstream direction. Therefore for purposes of the integration in Equation (4.8), the gain was assumed to be symmetric about the vertical centerline of the probe beam diameter. This allowed  $\gamma_p(x, y)$  to be calculated as the gain was determined at each downstream x location. The static flow temperature can then be determined by fitting the gain lineshape,  $\gamma_p(v, x, y)$ , with a Gaussian profile in a manner similar to the way the measured gain lineshape fitting is performed. Because the temperature computed in this

manner is averaged over the beam cross-section, it will be different than the flow field temperature calculated by the code and a better representation of the measured static temperature.

## Chapter 5

### Results

The following sections detail the results of the experimental and theoretical investigations used to characterize the small-scale supersonic HF laser device described in Chapter 3. First described are the results of a titration experiment that characterized the performance of the discharge tube used to create the F atom oxidizer flow. The velocity and Mach number of the flow field are then described through a series of Doppler shift and Pitot-static tube measurements. The bulk of the experimental results reported here are vertical profiles of the HF overtone small signal gain and static flow temperature measured using a scanning diode laser system. A large section of this chapter is devoted to comparisons between the measured small signal gain and the small signal gain predict from a 2-D computer model of the laser system. The computer model is used to explain the trends of the data and determine the role of the important mechanisms in producing overtone gain. The final sections of this chapter discuss the results of fundamental power extraction from the laser cavity and how that power extraction affects the overtone small signal gain.

#### 5.1 Discharge Tube Characterization (F atom Titration)

Figure 5.1 shows measured absorbance for titrations carried out for initial fluorine molecule flow ( $F_2$ ) rates of 0.62, 1.0, 2.1 and 3.0  $\text{mmol s}^{-1}$ . The curves show the expected result of an initial linear increase in absorbance with HCl flow rate, which then plateaus to a constant value at higher HCl flow rates. Horizontal lines for each curve are

drawn through the average absorbance of the plateau region. The vertical lines for each curve are drawn through an estimate of the beginning of the plateau. The start of the plateau region is presumed to be the point where the HCl flow rate equals the F atom flow rate (Wisniewski et al. 2003c). For complete dissociation, the F atom flow rate in the laser cavity equals twice the molecular fluorine flow rate supplied to the discharge tube. The dissociation fraction is defined as:

$$\text{dissociation fraction} = \frac{(\text{F atom flow rate in cavity})}{2(\text{F}_2 \text{ flow rate supplied to discharge tube})} \quad (5.1)$$

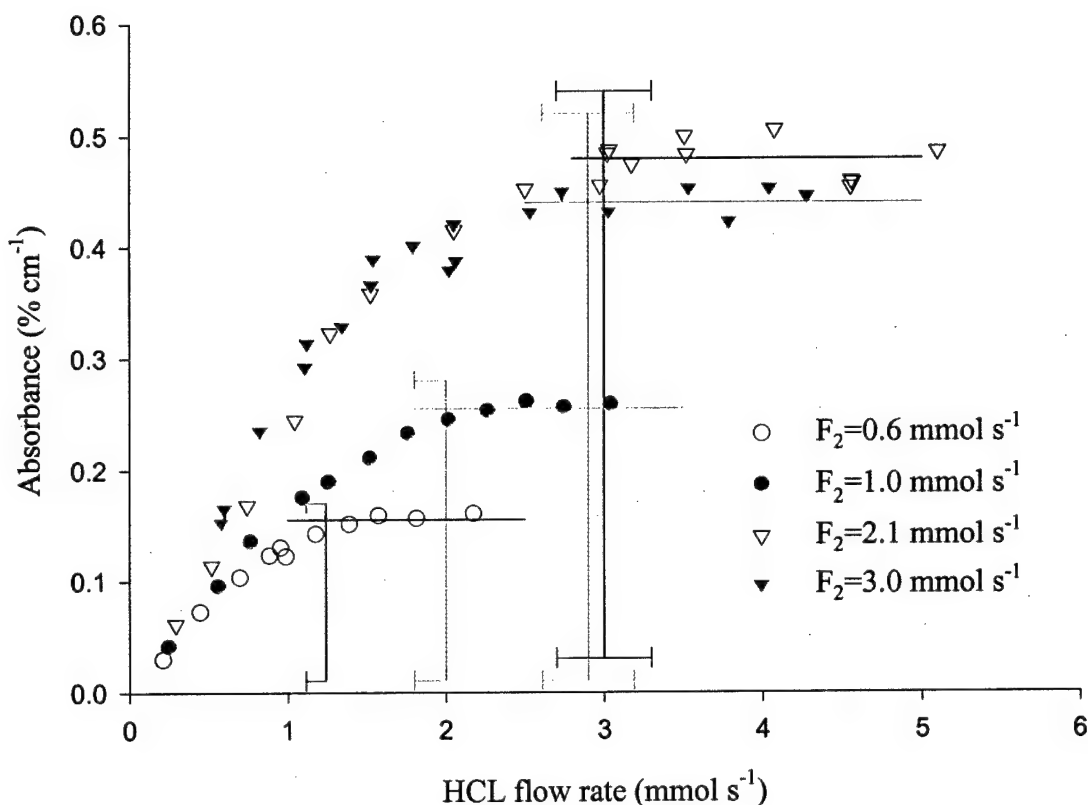


**Figure 5.1** F atom titration data using HCl. Horizontal lines for each curve are drawn through the average absorbance of the plateau region. The vertical lines for each curve are drawn at the point where the plateau region begins to indicate the point where the HCl flow rate equals the F atom flow rate. HCl flow rate error bars for the 2.1 and 3.0  $\text{mmol s}^{-1}$  cases are  $\pm 10\%$  and  $-10\%$  for the 0.62 and 1.0  $\text{mmol s}^{-1}$  cases. The 0.62 and 1.0  $\text{mmol s}^{-1}$  error bars are drawn only in the negative direction due to the nominal prediction of 100% dissociation.

Figure 5.2 shows the dissociation fraction as a function of  $F_2$  flow rate. The dissociation fraction is approximately 1 for  $F_2$  flow rates below  $1 \text{ mmol s}^{-1}$  and drops steadily as the  $F_2$  flow rate increases. For  $F_2$  flow rates of  $2.1$  and  $3.0 \text{ mmol s}^{-1}$  the dissociation fraction is approximately  $0.75$  and  $0.5$ , respectively. The resulting F atom flow rates for the four  $F_2$  flow rates are also plotted in Figure 5.2. The F atom flow rate initially increases with increasing  $F_2$  flow rate and then drops off as the dissociation fraction begins to drop. These dissociation fractions and F atom flow rates are reasonable and in relatively good agreement with other work (Herbelin et al. 1999; Manke et al. 2001).

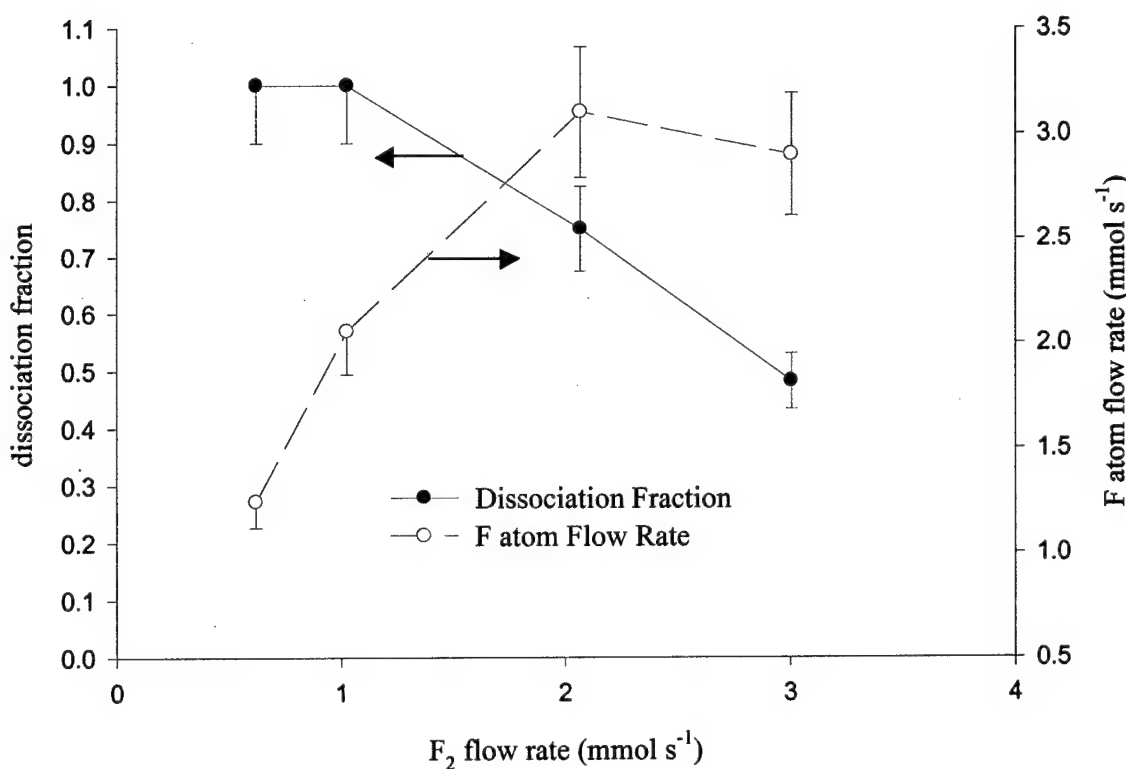


**Figure 5.2** Dissociation fraction and F atom flow rate for several different  $F_2$  flow rates. Dissociation fraction and corresponding F atom flow rate error bars for the  $2.1$  and  $3.0 \text{ mmol s}^{-1}$  cases are  $\pm 10\%$  and  $-10\%$  for the  $0.62$  and  $1.0 \text{ mmol s}^{-1}$  cases. The  $0.62$  and  $1.0 \text{ mmol s}^{-1}$  error bars are drawn only in the negative direction due to the nominal prediction of  $100\%$  dissociation.

Based on these titration measurements,  $F_2$  flow rates of 1.0, 2.0 and 3.0  $\text{mmol s}^{-1}$  were chosen to be used for cavity gain mapping. The highest  $F_2$  flow rate that produced complete dissociation was 1.0  $\text{mmol s}^{-1}$ . The cavity will therefore be free of fluorine molecules and the complexity of the hot reaction ( $\text{H} + \text{F}_2 \rightarrow \text{HF} + \text{F}$ ) will be eliminated from the cavity kinetics. An  $F_2$  flow rate of 2.0  $\text{mmol s}^{-1}$  will produce nearly the highest F atom flow rate, which will result in the highest gain and largest signal-to-noise ratio when making cavity gain measurements. An  $F_2$  flow rate of 3.0  $\text{mmol s}^{-1}$  produces nearly the same F atom flow rate as 2.0  $\text{mmol s}^{-1}$  but at a much lower dissociation fraction. This means that the  $F_2$  flow rate in the cavity will be much higher increasing the effect of the hot reaction.

## 5.2 Velocity and Mach Number Measurements

### 5.2.1 Horizontal Mach Number Profiles

Figure 5.3 shows horizontal Pitot-static tube Mach number profiles measured 2.0 cm, 4.5 cm, and 7.0 cm downstream of the NEP. For all of these profiles the Mach number is relatively constant over the region between  $\pm 25$  mm from the centerline. Further away from the centerline the Mach number increases due to the high speed bank blower flow. At the 2.0 cm downstream location, there was a small decrease in Mach number between the center and bank blower regions caused by remnants of the boundary layer that grew on the plate separating the bank blower nozzle block from the primary nozzle. This momentum deficit washes out quickly as the flow moves downstream. The Mach number in the center region drops from approximately 1.6 at 2.0 cm from the NEP, to 1.45 at 4.5 cm from the NEP, and then to 1.35 at 7.0 cm from the NEP. The Mach number in the bank blower region decreases from approximately 3.0 at 2.0 cm from the NEP, to 2.0 at 4.5 cm from the NEP, and then to 1.60 at 7.0 cm from the NEP. This dramatic decrease is likely caused by the interaction of the bank blower flow with the mirror tunnel purge flow which enters the laser cavity perpendicular to the primary flow and has to be accelerated by the bank blower flow.

The static pressure measured by the Pitot-static tube was nearly constant at 4.1  $\pm 0.5$  torr for all data taken during this test series. Since this is approximately 46% higher than the static pressure measured at the wall pressure ports for the same flow conditions when the Pitot-static tube was not in the laser cavity, this indicates significant channel blockage. The cross sectional area of the 3.175 mm (1/8 in) diameter tube is a little over 10% of that for the flow channel. The higher static pressure has the effect of lowering the

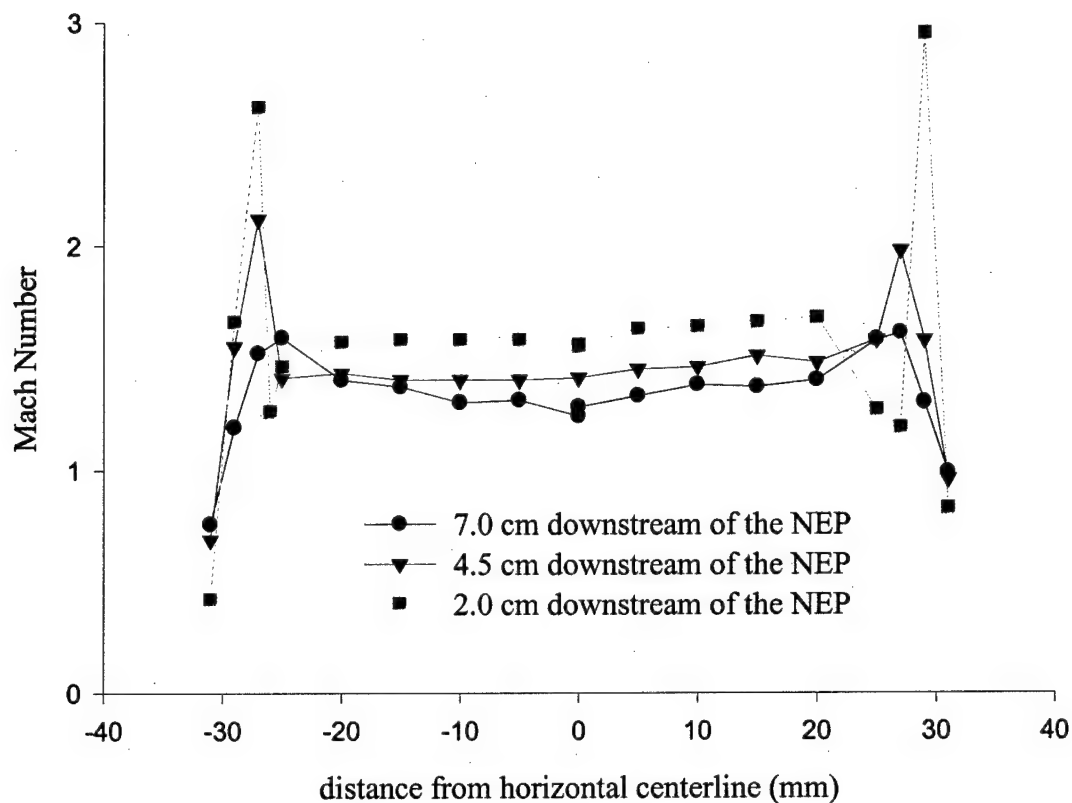


**Figure 5.3** Vertical Mach number profile at several downstream locations measured using a Pitot-static probe. The reagent flow rates used in these measurements were  $F_2=2.0$   $\text{mmol s}^{-1}$ ,  $H_2=10 \text{ mmol s}^{-1}$ , and He (bank blowers) =  $240 \text{ mmol s}^{-1}$ . The measurements were performed along the vertical centerline.

calculated Mach number. However, this error is the same for all Pitot-static tube locations so the relative Mach number profiles are a good representation of the momentum boundary between the primary and the bank blower flows. The bank blowers appear to confine the primary flow quite well with little lateral expansion or contraction as the flow moves downstream. Defining the point at which the Mach number begins to increase as the boundary between the primary and bank blower flows establishes the gain length of the active medium to be  $5.0 \pm 0.3$  cm (Wisniewski et al. 2003c).

### 5.2.2 Vertical Pitot Tube and Doppler Velocity Profiles

Figure 5.4 shows an example of the lineshapes from the three detectors in the “bow tie” optical setup shown in Figure 3.13 with measured parameters listed in Table 5.1. All measurements were performed for the P(3) ro-vibrational line of the first HF overtone ( $\nu'=2, J'=2 \nu=0, J=3$ ). Because the two Doppler shifted lineshapes have nearly the same peak gain, Gaussian widths and frequency shift with respect to the centerline beam, this is a good indication that the flow is symmetric about the horizontal centerline of the laser cavity (Wisniewski et al. 2003b).

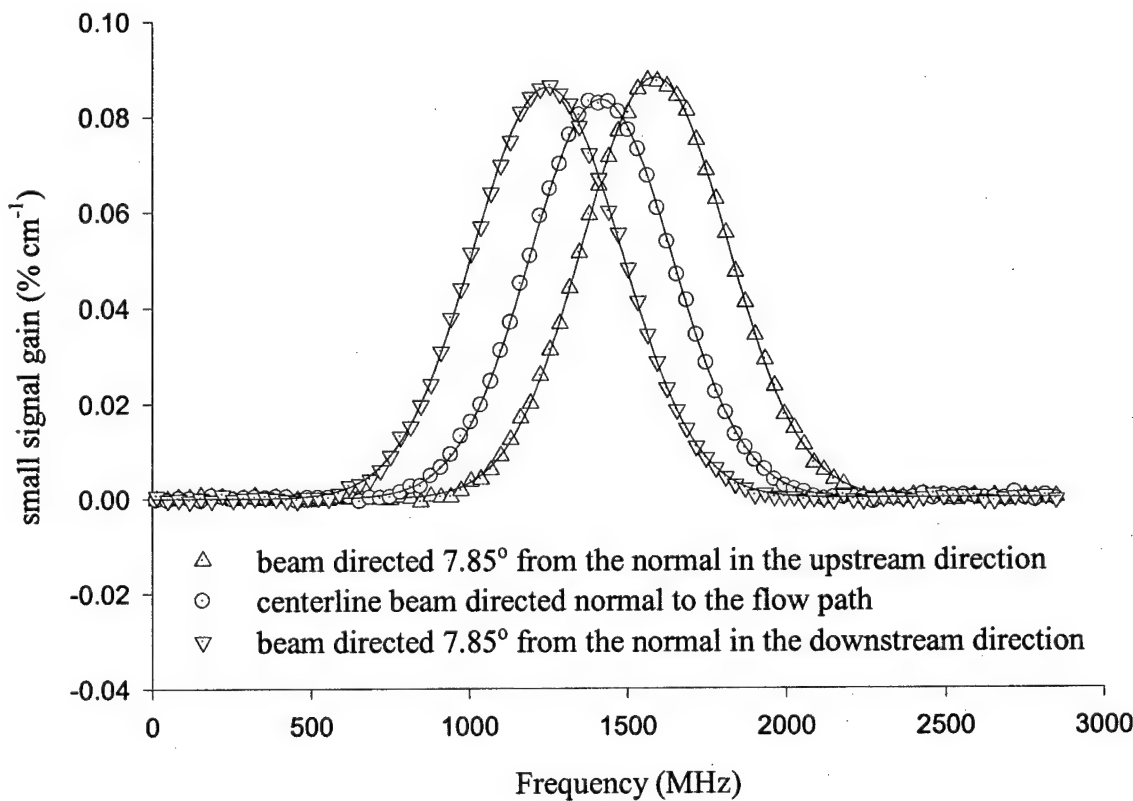


**Figure 5.4** Lineshapes from Doppler velocity measurement. The reagent flow rates used in these measurements were  $F_2=2.0 \text{ mmol s}^{-1}$ ,  $H_2=10 \text{ mmol s}^{-1}$ , He (bank blowers) =  $240 \text{ mmol s}^{-1}$ , and He (base purge) =  $15 \text{ mmol s}^{-1}$ . The measurements were performed along the vertical centerline and 4 cm downstream from the NEP.

**Table 5.1.** Doppler velocity measurement parameters taken 4 cm downstream of the NEP on the vertical centerline. Note that the Doppler shift frequency is relative to the transition frequency of the P(3) ro-vibrational line of the first HF overtone ( $v'=2, J'=2$ ,  $v=0, J=3$ ).

Detector	Peak gain (% cm <sup>-1</sup> )	Doppler Shift Frequency (MHz)	Gaussian Width (MHz)	Temperature (K)
1	0.081	-174.5±5	530.3	210.1
2	0.076	0	524.0	205.2
3	0.079	172.5±5	529.6	209.7

The 5 MHz uncertainty in the Doppler shift frequency and 5% uncertainty in the probe beam angle lead to an uncertainty in the computed velocity of approximately 100 m s<sup>-1</sup> which is about 6% of the velocity measured at the vertical centerline 4 cm downstream of the NEP. The subsequent Mach number calculation includes uncertainties in velocity, static temperature and flow properties. As mentioned in Section 3.5.2, the high dilution of the reactant flow streams makes the uncertainty in the flow properties negligible. The 100 m s<sup>-1</sup> uncertainty in the velocity and estimated 15 K uncertainty in the temperature produces a Mach number uncertainty of 0.17 which is approximately 9% of the calculated Mach number at the vertical centerline 4 cm downstream of the NEP.

Figures 5.5 through 5.11 show vertical Mach number and/or velocity profiles at downstream locations from  $x=2$  cm to 8 cm. Pitot-static measurements were made at  $x=2, 4, 6$  and 8 cm. Doppler measurements were made at the same locations except at 2 cm where the angled beams were clipped by the window tunnel purge hardware. The static pressures measured with the Pitot-static tube inserted from the top were nearly identical with the static pressures measured at the wall pressure taps when the Pitot-static tube was removed. The vertical profiles from Pitot-static tube measurements therefore

don't appear to have the same channel blockage problem that was seen in the horizontal measurements because a much smaller length of the tube was actually in the flow.

The Doppler measurements at 4 cm downstream of the NEP (Figure 5.6) show a peak velocity of about  $1650 \text{ m s}^{-1}$  on the vertical centerline with velocity decreasing to approximately  $1450 \text{ m s}^{-1}$  at 4 mm above or below the vertical centerline. This decrease is due to the interaction of the primary flow with the subsonic base purge flow. The Mach number profile is very similar; the peak value at the center is  $M=2.0$  and Mach number decreases to 1.67 at 4mm from the centerline. The Pitot-static tube measurements at this downstream location have a similar profile but differ significantly in magnitude with a peak Mach number at the centerline of 1.73. The difference may be

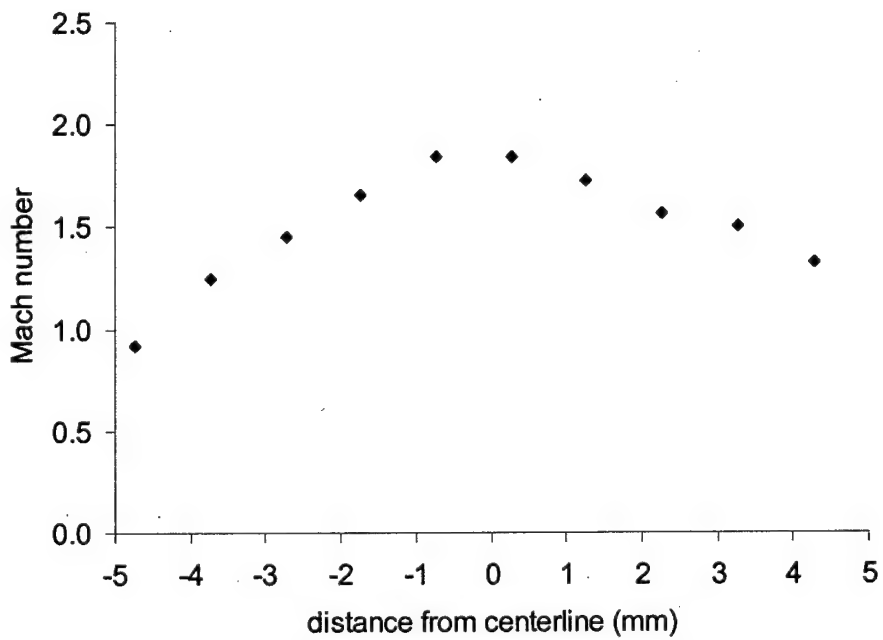


**Figure 5.5** Vertical Pitot-static tube Mach number profile taken 2 cm downstream of the NEP.

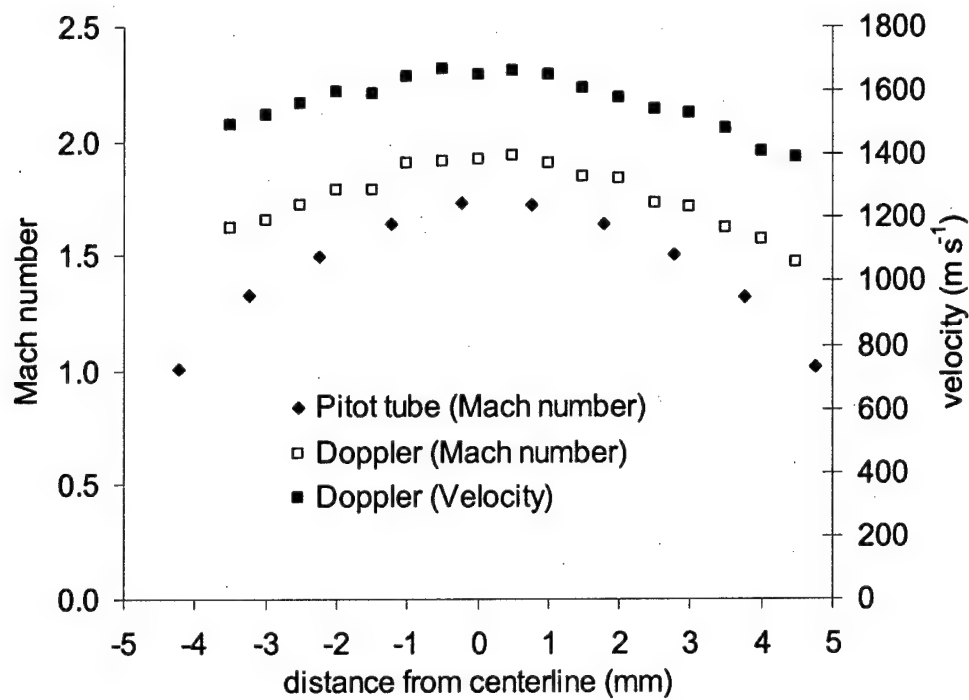


**Figure 5.6** Vertical Mach number and velocity profiles taken 4 cm downstream of the NEP.

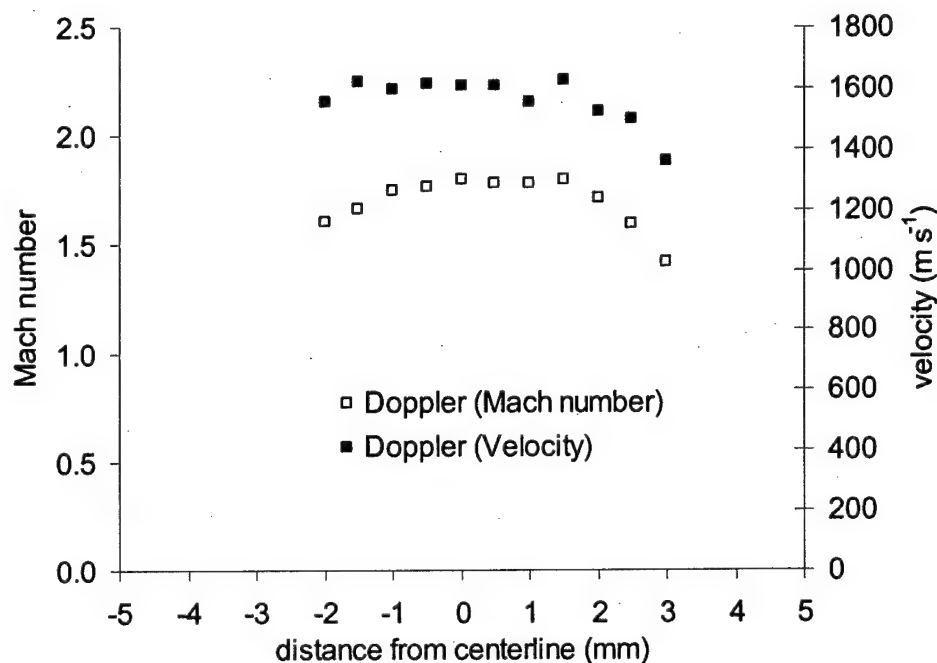


**Figure 5.7** Vertical Mach number and velocity profiles taken 4.5 cm downstream of the NEP.

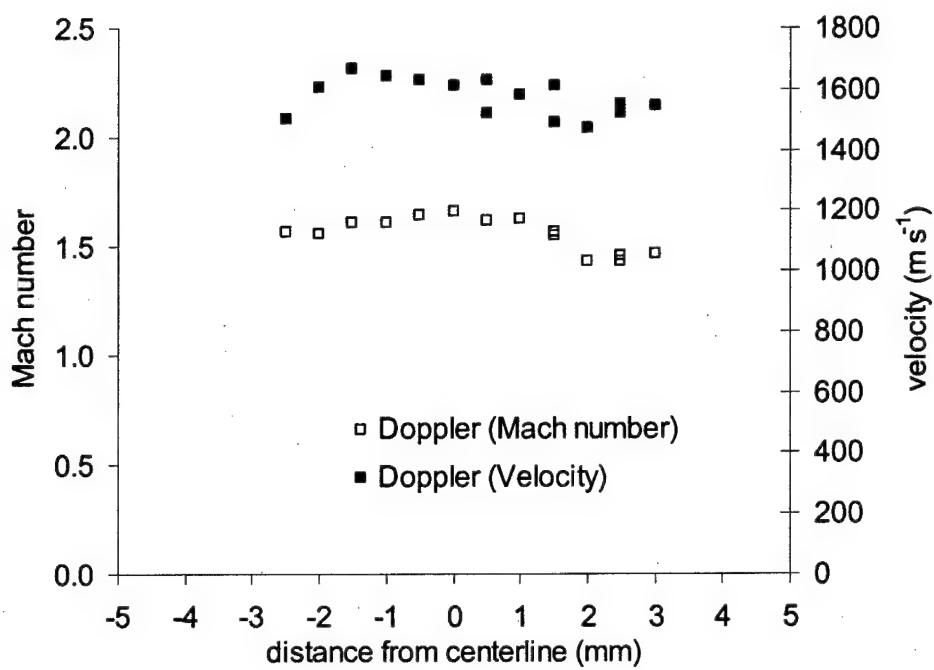


**Figure 5.8** Vertical Mach number and velocity profiles taken 5 cm downstream of the NEP.

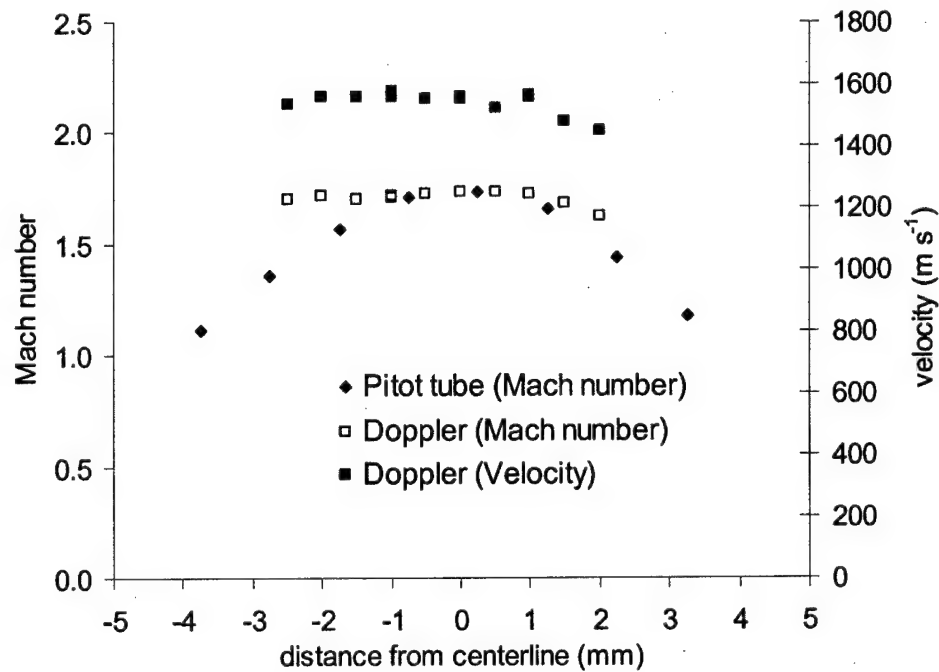


**Figure 5.9** Vertical Mach number and velocity profiles taken 6 cm downstream of the NEP.

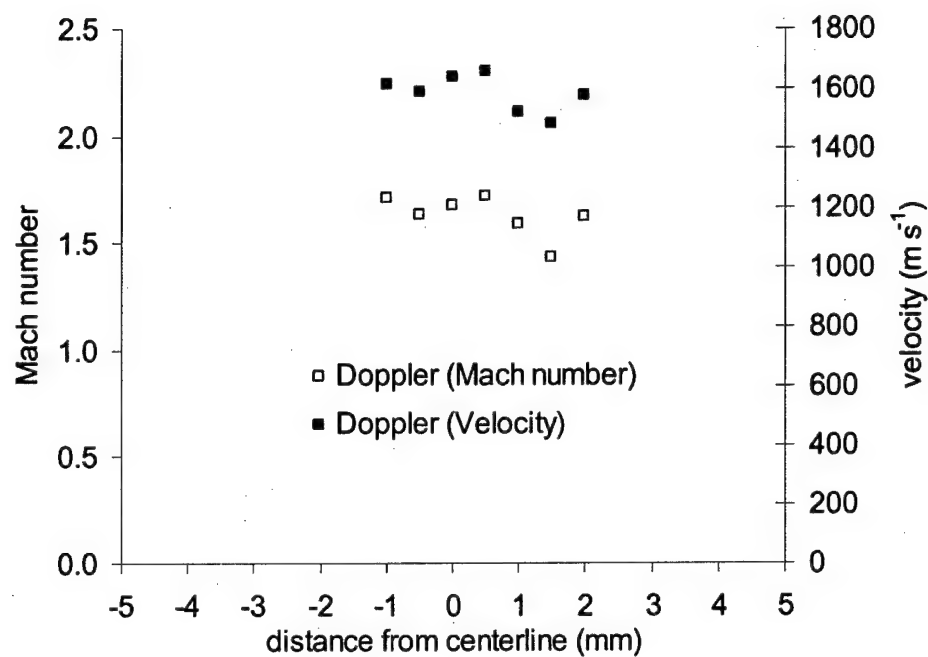


**Figure 5.10** Vertical Mach number and velocity profiles taken 7 cm downstream of the NEP.

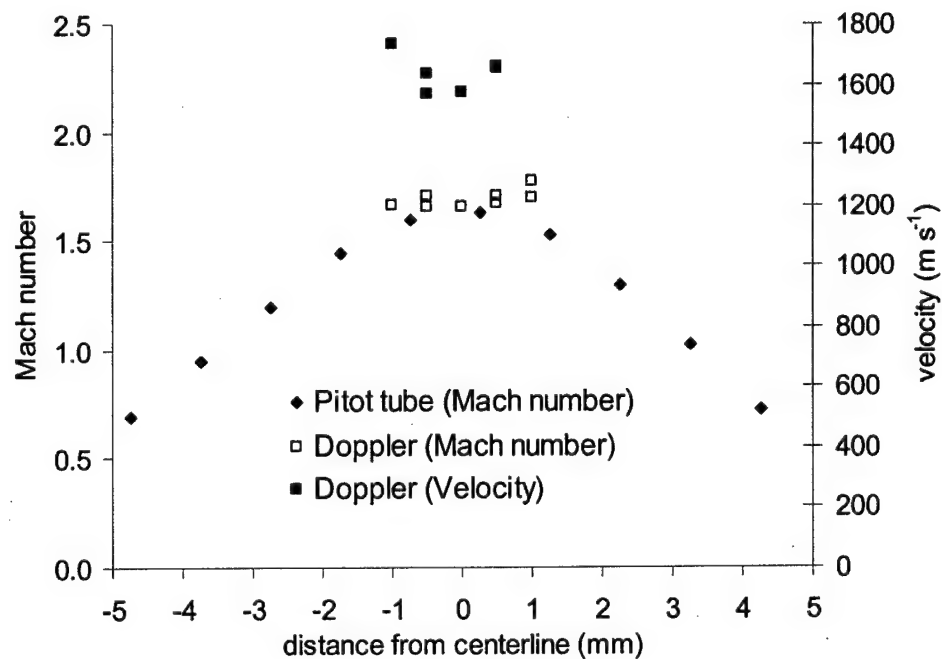


**Figure 5.11** Vertical Mach number and velocity profiles taken 8 cm downstream of the NEP.

partly explained by the low temperature measured during the Doppler test series at this location. These temperatures are about 30 K lower than the temperature measured during the small signal gain test series at the same location. The lower temperature means a lower speed of sound, which would correspond to a higher Mach number for the same velocity. The reason for the temperature discrepancy is unknown but could be explained by a mis-calibration of the frequency axis while taking the Doppler data. This explanation is somewhat suspect because other data taken on the same test day did not have this problem. In addition, the mis-calibration of the frequency axis would likely cause a shift in the peak separation that would affect the calculated velocity. However, the velocity at this location seems to be in good agreement with the velocity at other locations.

The Doppler Mach number profiles are similar at the other locations, with the peak on or about the centerline. The region over which Doppler measurements can be made decreases in the downstream direction because the small signal gain is decreasing. As the gain decreases, the signal-to-noise ratio drops and it becomes more difficult to resolve the difference in the peaks. Therefore the profile at the 8 cm downstream location is restricted to a region very close to the centerline. Figure 5.12 shows centerline Doppler and Pitot-static tube Mach number measurements as well as the centerline Doppler velocity data. The centerline flow velocity decreases slightly in the downstream direction going from  $1650 \text{ m s}^{-1}$  at 4 cm from the NEP to  $1575 \text{ m s}^{-1}$  at 8 cm from the NEP. The centerline Doppler and Pitot-static tube Mach numbers are nearly identical at the 6 and 8 cm locations but differ by approximately 15% at the 4 cm location. This

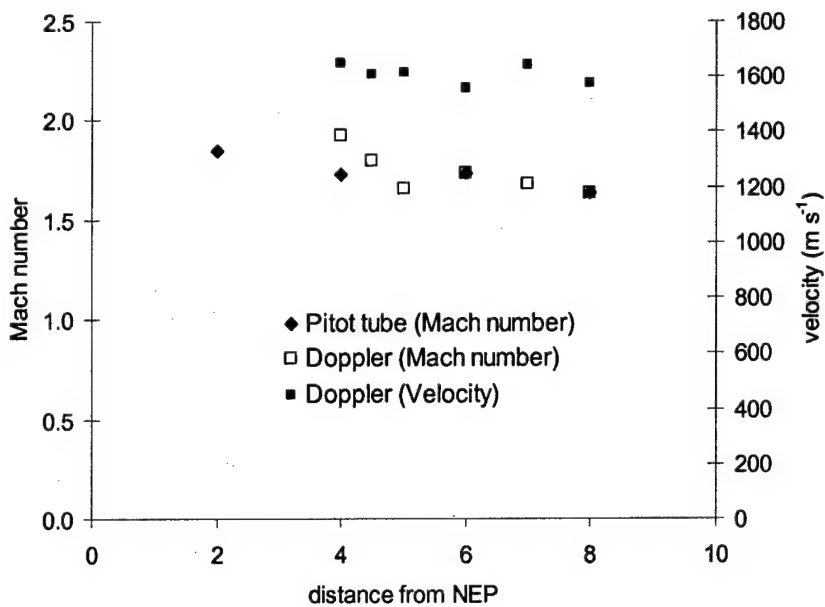


**Figure 5.12** Centerline Doppler velocity and Mach number measurements along with Pitot-static tube Mach number measurements taken on the vertical centerline at various downstream locations.

difference can be decreased to about 10% by using the temperature measured during the small signal gain test series instead of the temperature measured in this test series.

The Doppler velocity measurements show that the centerline flow velocity remains nearly constant at  $1600 \pm 50 \text{ m s}^{-1}$  while the Mach number decreases from about 2.0 to 1.6 as the flow moves from 4 to 8 cm downstream of the NEP. The Mach number decrease is largely due to the 100 K increase in the static temperature of the flow over this distance. The vertical profiles of Mach number from Pitot-static tube measurements are in good agreement with the Doppler measurements under these conditions. However, for higher power laser systems, with higher concentrations of reactants and higher Mach numbers, more sophisticated Pitot-static tubes (i.e., thin wedged leading edges, liquid cooled) would probably be required. Doppler measurement may be a better technique under these conditions because it is non-intrusive and avoids the inherent problems of

traditional flow measuring devices in small channels. This technique can be applied to other types of flow systems provided an appropriate chromophore and resonant sub-Doppler tunable laser source is available.

### 5.3 Vertical Gain and Temperature Mapping

Vertical gain and temperature mapping of the laser cavity was performed for the four cases described by the nominal flow conditions listed in Table 5.2 (Wisniewski et al. 2003a). The primary differences between these cases are the  $H_2$  and  $F_2$  flow rates. The four cases are referred to by their respective nominal  $F_2$  and  $H_2$  flow rates in  $mmol\ s^{-1}$ . For the ( $F_2=1$ ,  $H_2=5$ ) flow case the dissociation fraction, as measured by the titration experiments, is 1.0 resulting in an F atom flow rate of  $2.2\ mmol\ s^{-1}$ . The ( $F_2=2$ ,  $H_2=10$ ) flow case doubles the  $F_2$  flow rate but because the dissociation fraction decreases to 0.75 the resulting F atom flow rate in the nozzle only increases by 40% to  $3.1\ mmol\ s^{-1}$ . Further increases in  $F_2$  flow rate do not produce higher F atom flow rates due to the decrease in dissociation fraction. The ( $F_2=3$ ,  $H_2=10$ ) flow case therefore has the same F atom flow rate as the ( $F_2=2$ ,  $H_2=10$ ) case but with an increased amount of undissociated  $F_2$  in the nozzle. The stoichiometric required  $H_2$  to F atom ratio is 1.0 for the  $H_2 + F \rightarrow HF + H$  reaction. The ( $F_2=1$ ,  $H_2=5$ ), ( $F_2=2$ ,  $H_2=10$ ), ( $F_2=3$ ,  $H_2=10$ ) flow cases have  $H_2$  to F atom ratios of 2.4, 3.3 and 3.3, respectively. These fuel rich mixtures are typical for HF lasers and are an attempt to increase the cold pumping rate of reaction. The ( $F_2=2$ ,  $H_2=27$ ) flow case increases this ratio to 8.7.

Table 5.3 lists the resulting cavity and plenum pressures for the four flow cases, with the description and location of each transducer given in Table 3.2. The total primary He diluent flow rate was adjusted for each flow case to maintain a plenum pressure of approximately 27 torr. The ( $F_2=1$ ,  $H_2=5$ ) flow case therefore has a higher primary flow rate resulting in a significantly lower F atom concentration. Likewise, the ( $F_2=3$ ,  $H_2=10$ ) flow case has the lowest primary He diluent flow rate and the highest F atom

**Table 5.2** Nominal flow rates (mmol s<sup>-1</sup>) for gain and temperature mapping flow conditions. Full description of flow designations are given in Table 3.1 of Section 3.1.1.

Flow Designation	Flow Name	F <sub>2</sub> =1 H <sub>2</sub> =5	F <sub>2</sub> =2 H <sub>2</sub> =10	F <sub>2</sub> =2 H <sub>2</sub> =27	F <sub>2</sub> =3 H <sub>2</sub> =10
MFHE1	Cathode He	15.3	15.3	15.1	15.4
MFHE2	F <sub>2</sub> Diluent	5.4	5.3	5.0	8.6
MFHE3	Primary He Diluent	71.1	55.5	56.0	36.7
MFFO1 (80% He 20% F <sub>2</sub> )	F <sub>2</sub>	5.6	10.2	10.2	15.4
	F <sub>2</sub> at discharge tube inlet	1.1	2.0	2.0	3.1
	Total Primary He	96.2	84.2	84.4	73.0
	F atoms in Plenum	2.2	3.1	3.1	3.1
	F <sub>2</sub> in Plenum	0.0	0.5	0.5	1.5
MFH21	H <sub>2</sub>	5.2	10.2	27.0	10.3
MFHE4	Secondary He Injection	10.4	10.2	10.1	10.3
MFHE5	H <sub>2</sub> Diluent	30.7	24.3	0.0	24.2
MFSRD	Base Purge Flow	15.4	15.2	15.1	15.2
MFCUR	Curtain Flow	240.6	240.4	239.8	240.3
MFTUN	Tunnel Purge	10.4	10.3	10.2	10.2

concentration. The H<sub>2</sub> diluent flow rate was also adjusted to maintain the total momentum of the flow through the H<sub>2</sub> injection holes. The (F<sub>2</sub>=2, H<sub>2</sub>= 27) flow case has no H<sub>2</sub> diluent and therefore the highest H<sub>2</sub> concentration in the injected flow stream while the (F<sub>2</sub>=1, H<sub>2</sub>= 5) flow case has the highest H<sub>2</sub> diluent flow and the lowest H<sub>2</sub> concentration in the injected flow stream. By holding the plenum and cavity pressures constant between the different flow cases, the flow velocity in the cavity is held relatively

**Table 5.3** Nominal pressures (torr) for flow conditions listed in Table 5.2. Location and description of transducers are given in Table 3.2 of Section 3.1.2.

Transducer Designation	F <sub>2</sub> =1 H <sub>2</sub> =5	F <sub>2</sub> =2 H <sub>2</sub> =10	F <sub>2</sub> =2 H <sub>2</sub> =27	F <sub>2</sub> =3 H <sub>2</sub> =10
PVCA1	2.7	3.0	2.9	3.5
PVCA2	2.7	2.9	2.9	3.6
PVCA3	2.6	3.0	3.1	3.6
PVCA4	2.6	2.8	2.7	3.3
PVCA5	2.5	2.9	2.9	3.5
PVCA6	2.4	2.5	2.6	2.9
PVCA7	25.2	27.6	27.6	27.0

constant. This is important because the velocity significantly affects the gain distribution in the streamwise direction.

The primary source of bias uncertainty in the small signal gain measurement comes from uncertainty in the gain length, which was estimated from the Pitot-static probe measurements in Section 5.2.1 to be  $\pm 6\%$ . The only other bias errors in the gain measurement stem from uncertainties in the probe beam intensity measurement caused by the data acquisition system and fluctuations in the laser diode, all of which are significantly smaller than the uncertainty in the gain length and can therefore be ignored. The precision uncertainty of the small signal gain was estimated by determining the standard deviation of measurements made at the same location and flow conditions. Several lineshapes from each sampled laser hot fire were analyzed to increase the statistical sample size. Table 5.4 shows the results of this analysis, which was performed at two different locations having very different average gains. At a location with an average small signal gain of  $0.14\% \text{ cm}^{-1}$  the resulting standard deviation,  $\sigma_g$ , was  $0.002\% \text{ cm}^{-1}$  corresponding to a precision uncertainty,  $2\sigma_g$ , of  $3.0\%$  of the average measured gain. Because the standard deviation of the gain was the same at a location where the

**Table 5.4** Results of small signal gain and temperature precision uncertainty analysis.

Average Gain (% cm <sup>-1</sup> )	Gain Standard Deviation ( $\sigma_g$ ) (% cm <sup>-1</sup> )	Gain Precision Uncertainty ( $2 \sigma_g$ )	Temperature Standard Deviation ( $\sigma_T$ ) (K)	Temperature Precision Uncertainty ( $2 \sigma_T$ )
0.14	0.002	3.0 %	5	4.5%
0.02	0.002	20 %	25	18%

average small signal gain dropped to 0.02 % cm<sup>-1</sup>, the corresponding precision uncertainty increased to 20% of the average measured gain.

The static temperature was determined from Equation (2.58) in which all the variables are known to very high accuracy except the measured Gaussian linewidth. The primary source of bias uncertainty is therefore caused by mechanisms that broaden the lineshape but do not add to the Gaussian linewidth. However, the excellent curve fits attained by fitting the measured lineshapes with Gaussian profiles (as shown in Figure 3.10) indicate that these effects are insignificant and that the lineshapes are dominated by Doppler broadening. The precision uncertainty was estimated in the same manner as that for the small signal gain and is also listed in Table 5.4. At the location where the average gain was 0.14 % cm<sup>-1</sup> the standard deviation of the temperature,  $\sigma_T$ , was 5 K with a corresponding precision uncertainty,  $2 \sigma_T$ , of 4.5 % of the average measured temperature. Since  $\sigma_T$  increases to 25 K at the location where the average gain is 0.02 % cm<sup>-1</sup>, the corresponding precision uncertainty is 18 % of the average measured temperature. The increase in the precision uncertainty is indicative of the difficulties in fitting the lineshape with poor signal-to-noise ratio for the lower average gain case.

Before discussing the vertical gain profiles a few definitions are in order. The term “peak gain” refers to the maximum gain within a vertical profile at a specified

streamwise location. The term "maximum peak gain" refers to the maximum gain at any streamwise location for a particular flow condition. Vertical gain profiles were made every 0.5 cm starting at 0.5 cm downstream of the NEP going out to 5.5 cm downstream of the NEP for the ( $F_2=1$ ,  $H_2=5$ ), ( $F_2=2$ ,  $H_2=27$ ) and ( $F_2=3$ ,  $H_2=10$ ) cases and out to 9.0 cm downstream of the NEP for the ( $F_2=2$ ,  $H_2=10$ ) case. Figures 5.13 through 5.16 show vertical gain profiles for the four flow cases at distances of 0.5, 2.0, 3.5 and 5.5 cm downstream of the nozzle exit plane (NEP), respectively. The gain shown in these figures is for the P3 [ $(v'=2, J'=2)$  to  $(v=0, J=3)$ ] overtone transition. In these figures, the solid black lines at  $\pm 4.778$  mm from the centerline represent the vertical height of the nozzle at the NEP. Since, the  $H_2$  flow is injected at nearly this vertical location at a  $15^\circ$  angle toward the centerline, the bulk of the reactants lie in the region between these lines. Outside of this region the flow is dominated by the He base purge flow. The reactants/products of the cold pumping reaction and the base purge flow will obviously diffuse across these imaginary nozzle extension lines but they can be used as useful reference lines. The height of the cavity downstream of the NEP is 2.85 cm, or  $\pm 14.2$  mm from the centerline.

At the 0.5 cm location all the flow cases have a distinctive double humped gain profile with nearly zero gain at the vertical centerline and peak gains about halfway between the centerline and nozzle extension lines. The lack of gain at the centerline indicates that the  $H_2$  flow stream has not penetrated to the vertical centerline and therefore  $HF(v)$  cannot be produced there. The ( $F_2=2$ ,  $H_2=10$ ), ( $F_2=2$ ,  $H_2=27$ ) and ( $F_2=3$ ,  $H_2=10$ ) flow cases all have generally the same gain profile shape with very similar peak gain that is significantly higher than the ( $F_2=1$ ,  $H_2=5$ ) flow case. The smaller peak

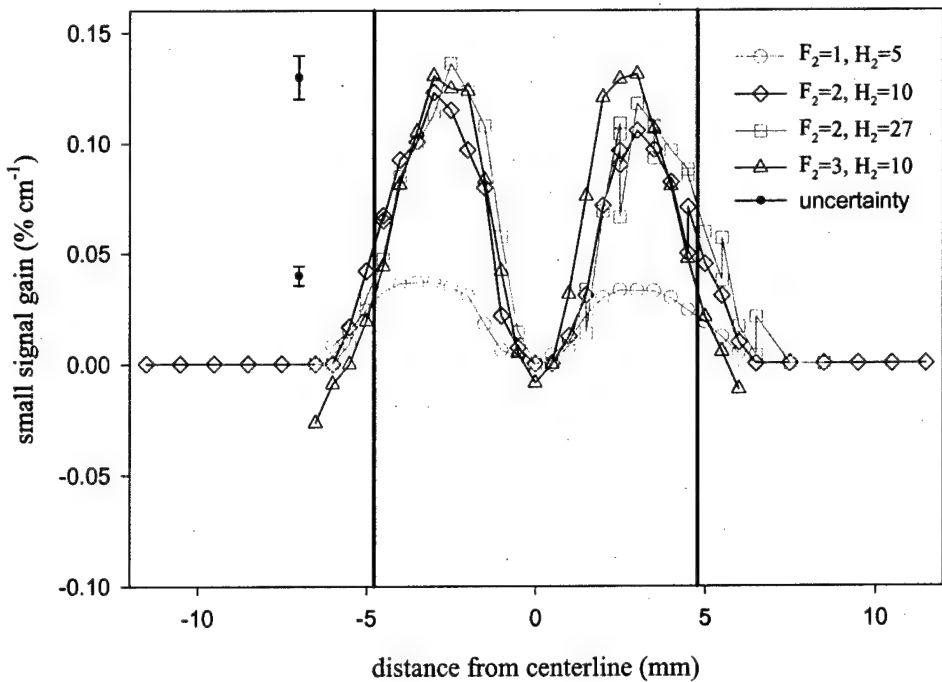


**Figure 5.13** Vertical P3 overtone small signal gain profiles 0.5 cm downstream of NEP. Solid black lines indicate the vertical height of the nozzle at the NEP. Error bars represent 6% bias and 0.002 % cm<sup>-1</sup> precision uncertainties.

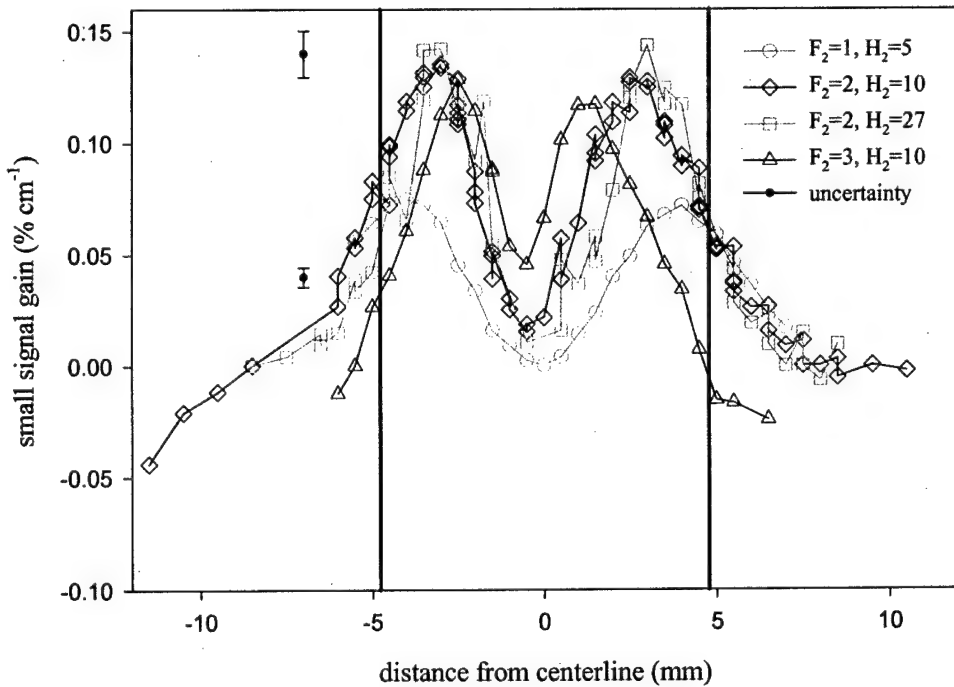


**Figure 5.14** Vertical P3 overtone small signal gain profiles 2.0 cm downstream of NEP. Solid black lines indicate the vertical height of the nozzle at the NEP. Error bars represent 6% bias and 0.002 % cm<sup>-1</sup> precision uncertainties.

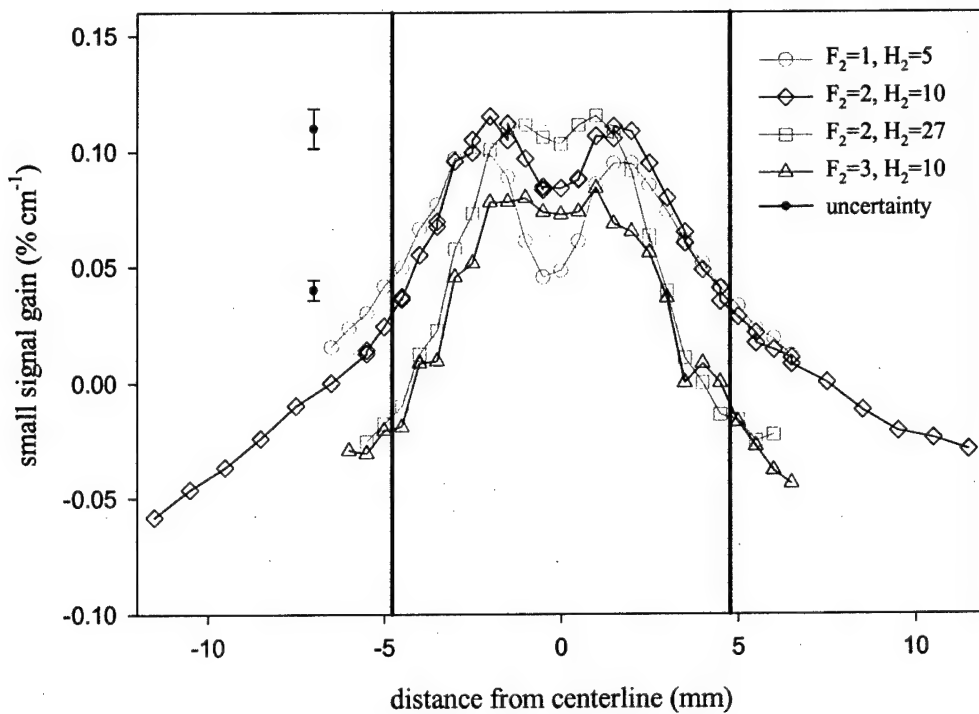


**Figure 5.15** Vertical P3 overtone small signal gain profiles 3.5 cm downstream of NEP. Solid black lines indicate the vertical height of the nozzle at the NEP. Error bars represent 6% bias and 0.002 % cm<sup>-1</sup> precision uncertainties.

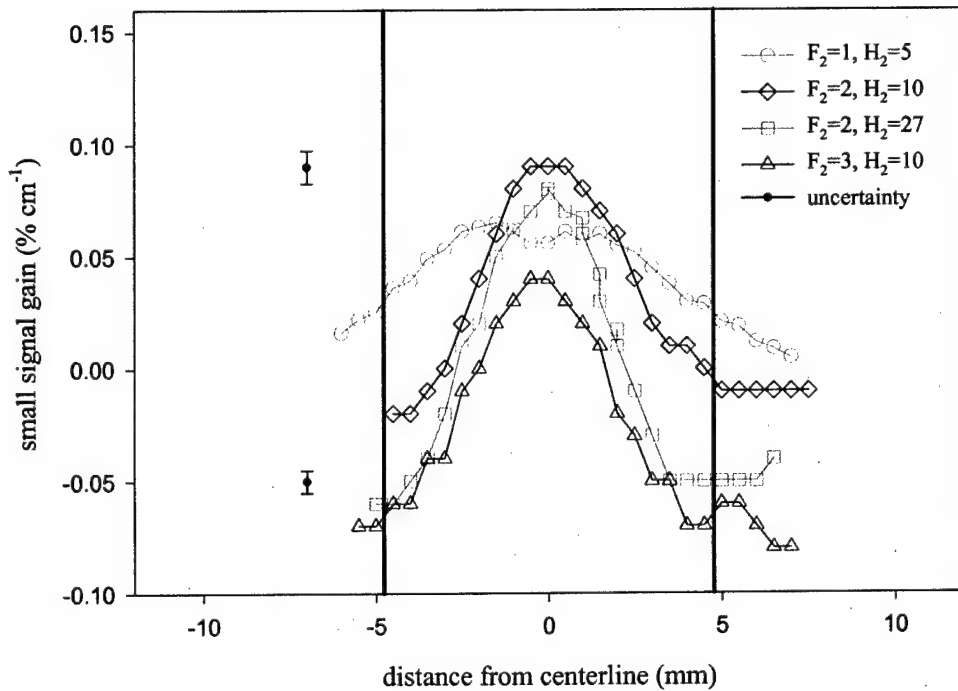


**Figure 5.16** Vertical P3 overtone small signal gain profiles 5.5 cm downstream of NEP. Solid black lines indicate the vertical height of the nozzle at the NEP. Error bars represent 6% bias and 0.002 % cm<sup>-1</sup> precision uncertainties.

gain for the ( $F_2=1$ ,  $H_2=5$ ) flow conditions is due to the significantly reduced F atom and  $H_2$  concentrations caused by higher diluent flows.

At the 2.0 cm location the ( $F_2=3$ ,  $H_2=10$ ) gain profile has become noticeably narrower with higher centerline gain than any other case. The vertical location of the peak gain for the ( $F_2=3$ ,  $H_2=10$ ) flow case also occurs closer to the vertical centerline than it does for the other flow cases at this downstream location while the peak gain location for the ( $F_2=1$ ,  $H_2=5$ ) case occurs further away from the centerline than for the other flow cases. The shift in the peak gain location may result from the flow exiting the nozzle being deflected by oblique shocks and /or expansion fans that result from over/under expansion of the nozzle flow. This could also account for the narrower gain profile of the ( $F_2=3$ ,  $H_2=10$ ) flow case. Unfortunately measurements were not made that would determine the strength or location of the shocks/expansion fans. An analysis of the effects the shocks/expansion fans have on the flow field is made with the help of the 2-D computer model in Section 5.4.5.

At the 3.5 cm location the peak gain of the ( $F_2=1$ ,  $H_2=5$ ) flow case has surpassed the peak for the ( $F_2=3$ ,  $H_2=10$ ) flow case and is only slightly lower than the other two cases. The centerline gain has increased significantly for all the flow cases while the location of the peak gain has moved closer to the vertical centerline. At this downstream location the ( $F_2=2$ ,  $H_2=10$ ) flow case shows significant levels of absorption (i.e., negative gain) in the region outside of the nozzle extension lines. For the ( $F_2=3$ ,  $H_2=10$ ) and ( $F_2=2$ ,  $H_2=27$ ) flow cases the absorption extends within the nozzle extension lines.

At 5.5 cm downstream of the NEP the ( $F_2=2$ ,  $H_2=10$ ), ( $F_2=2$ ,  $H_2=27$ ) and ( $F_2=3$ ,  $H_2=10$ ) flow cases all show peak gain at the vertical centerline while the ( $F_2=1$ ,  $H_2=5$ )

case still has a slight dip in gain at the centerline. The gain region for the ( $F_2=2, H_2=10$ ), ( $F_2=2, H_2=27$ ) and ( $F_2=3, H_2=10$ ) flow cases is restricted to the region between  $\pm 2.5$  mm from the vertical centerline and the peak is greatly reduced for the ( $F_2=3, H_2=10$ ) flow case.

These data trends may also be illustrated by separately plotting the peak gain and centerline gain as functions of distance downstream of the NEP. These results for the four flow cases are shown in Figures 5.17 and 5.18, respectively. Note that locations for the peak within each gain profile shown in Figure 5.17 are presented in Figure 5.19. The maximum peak gain for the ( $F_2=2, H_2=10$ ), ( $F_2=2, H_2=27$ ) and ( $F_2=3, H_2=10$ ) flow cases occurs at 1.0 cm downstream of the NEP. The higher  $H_2$  flow rate for the ( $F_2=2, H_2=27$ ) flow case creates a slightly higher maximum peak ( $0.17\% \text{ cm}^{-1}$ ) than the ( $F_2=2, H_2=10$ ) and ( $F_2=3, H_2=10$ ) cases, each of which has a maximum peak gain of about  $0.15\% \text{ cm}^{-1}$ . The downstream decrease in peak gain is about the same for the ( $F_2=2, H_2=10$ ) and ( $F_2=2, H_2=27$ ) cases, while the ( $F_2=3, H_2=10$ ) decrease is noticeably steeper. The peak gain values for the ( $F_2=1, H_2=5$ ) flow case start low and increase gradually until reaching a maximum about 3.5 cm downstream of the NEP and then gradually decreasing. The ( $F_2=2, H_2=10$ ) and ( $F_2=2, H_2=27$ ) flow cases show a large increase in centerline gain by 2.5 cm while the jump in centerline gain for ( $F_2=3, H_2=10$ ) flow case happens by 2.0 cm. The ( $F_2=1, H_2=5$ ) flow case does not have a sudden increase in centerline gain but instead shows a gradual rise starting at about 2.0 cm downstream of the NEP. This is likely the result of the lower F atom and  $H_2$  concentrations for this flow case due to the higher diluent ratio.

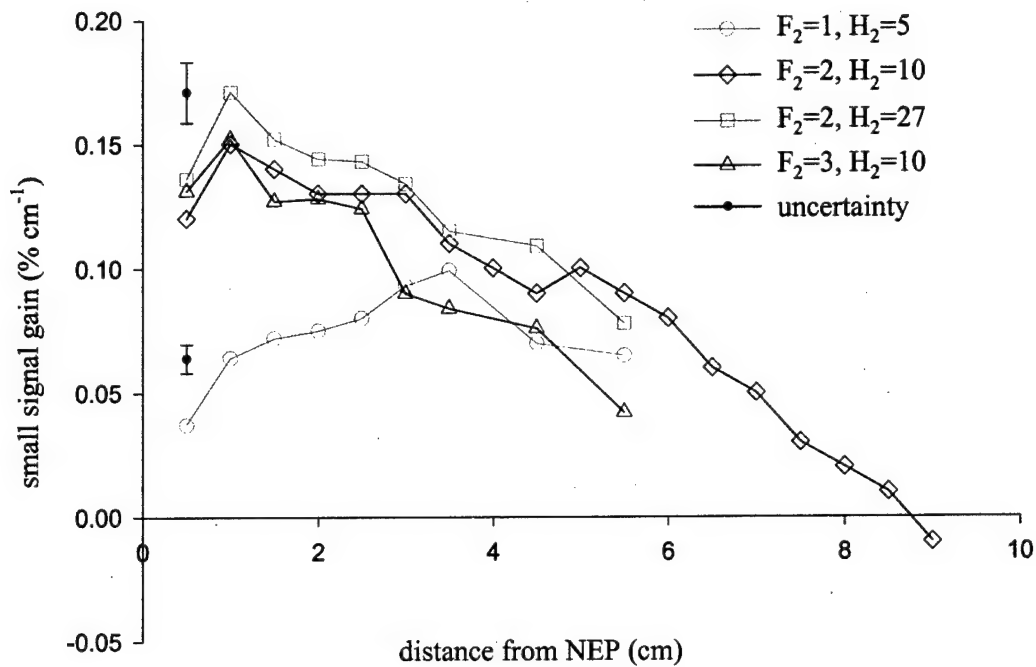


**Figure 5.17** P3 overtone small signal gain measured at the peak gain location. Peak gain refers to the maximum gain within a vertical profile at each streamwise measurement location. Error bars represent 6% bias and  $0.002\text{ \% cm}^{-1}$  precision uncertainties.

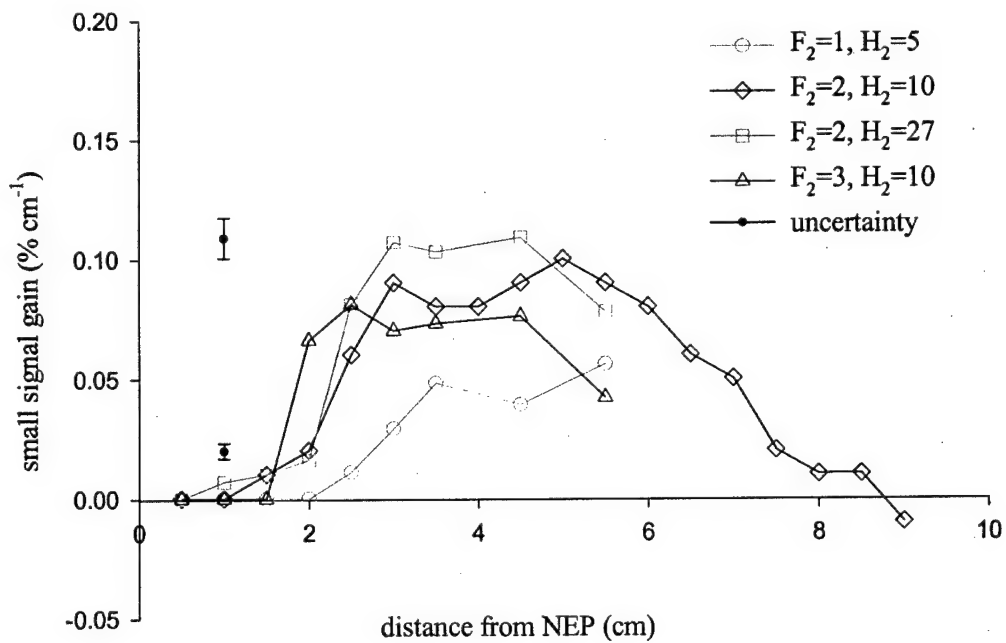


**Figure 5.18** P3 overtone small signal gain measured at the vertical centerline. Error bars represent 6% bias and  $0.002\text{ \% cm}^{-1}$  precision uncertainties.

Figure 5.19 shows the vertical location of the peak within each gain profile for the four flow cases versus distance downstream of the NEP. The peak gain for all flow cases occurs between 2.5 and 3.5 mm from the vertical centerline at 0.5 cm downstream of the NEP (as seen in Figure 5.13). Peak gain for the ( $F_2=2$ ,  $H_2=10$ ) and ( $F_2=2$ ,  $H_2=27$ ) cases occurs between 2.5 and 3.0 mm from the vertical centerline through about 2.0 cm downstream of the NEP after which the peaks move toward the centerline. Peak gain for the ( $F_2=2$ ,  $H_2=27$ ) occurs at the centerline by 3 cm downstream of the NEP while in the ( $F_2=2$ ,  $H_2=10$ ) case peak gain does not occur at the centerline until 5 cm downstream of the NEP. The higher  $H_2$  concentration in the ( $F_2=2$ ,  $H_2=27$ ) flow case creates a higher diffusion velocity allowing the  $H_2$  to reach the centerline sooner. The location of peak gain for the ( $F_2=3$ ,  $H_2=10$ ) flow case moves toward the center line most quickly among all flow cases, moving from 3.5 to 1.5 mm from the vertical centerline over the first 2.0

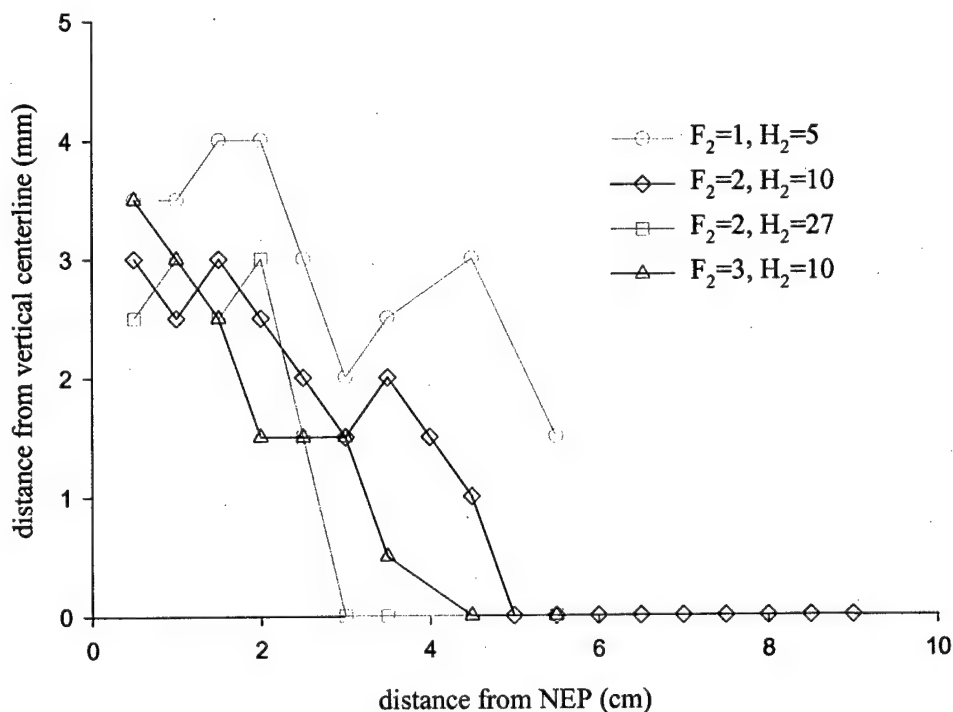


**Figure 5.19** Vertical location of the peak gain shown in Figure 5.17.

cm. The location of peak gain remains at that vertical location through 3.0 cm after which it moves steadily toward the centerline, reaching the centerline by 4.5 cm downstream of the NEP. The location of peak gain for the ( $F_2=1$ ,  $H_2=5$ ) case initially moves slightly away from the centerline then moves toward it and away again. The peak gain occurs 1.5 mm from the centerline at 5.5 cm downstream of the NEP because diffusion of  $H_2$  is so slow. As stated previously, the location of peak gain may be influenced by oblique shock and expansion fan patterns created by the over/under expansion of the primary nozzle flow.

The centerline and peak gain values have been used to describe the streamwise gain distribution of the four flow conditions. Although useful comparisons can be made in this way, these distributions cannot include the vertical profiles of gain. To properly compare the total gain produced by the different flow conditions versus downstream location the gain must be averaged over the vertical height of the profiles. This is of particular interest in assessing laser output power performance. When producing laser output power, energy is extracted from the flow field across the full vertical and horizontal (streamwise) aperture of the resonator. The resonator effectively integrates the gain profiles in both directions. Therefore it is not just the peak or centerline gain that is of importance for laser performance but the total gain. Since variations in gain are much larger in the vertical direction than in the streamwise direction, vertical averaging of the gain profiles is sufficient to compare the overall performance of the four flow conditions. Figure 5.20 shows the vertically-averaged gain as a function of streamwise location for the four flow cases. The gain has been averaged over the vertical profile between  $\pm 5$  mm from the vertical centerline because that is the region with reliable data. Moreover the

resonator aperture height is 1 cm. The lower average gain for the ( $F_2=1, H_2=5$ ) flow condition is consistent with the lower F atom concentration which reduces the cold pumping rate of reaction and stretches the gain in the downstream direction. The maximum values of vertically-averaged gain for the other three case are nearly the same. The shift of the maximum peak gain closer to the NEP for the ( $F_2=2, H_2=27$ ) and ( $F_2=3, H_2=10$ ) cases is probably due to increases in the cold pumping rate of reaction for these flow conditions. The cold pumping rate of reaction increases for the ( $F_2=2, H_2=27$ ) case because of the higher  $H_2$  concentration and for the ( $F_2=3, H_2=10$ ) case because of the higher cavity pressure.

Figures 5.21 through 5.24 show vertical temperature profiles for the four flow cases at distances of 0.5, 2.0, 3.5 and 5.5 cm downstream of the nozzle exit plane (NEP), respectively. Temperature can only be determined in regions where the gain is high

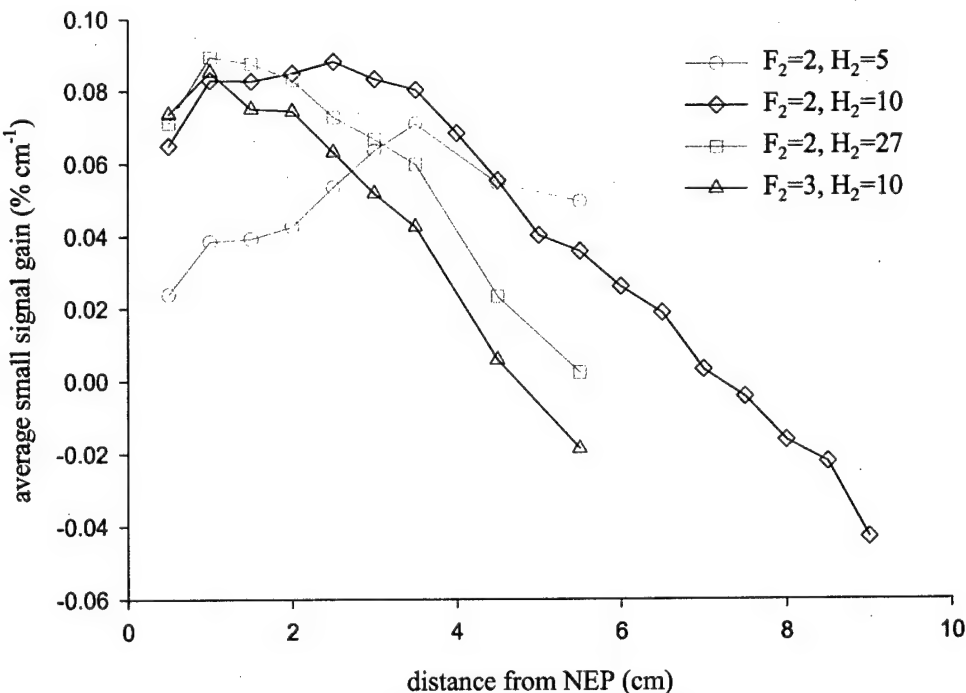


**Figure 5.20** Measured P3 overtone small signal gain averaged over the vertical profile between  $\pm 5$  mm from the vertical centerline.

enough to resolve the transition lineshape. There is significantly more scatter in the temperature data for the ( $F_2=3$ ,  $H_2=10$ ) flow case at all streamwise locations. The cause of this is not immediately evident. In regions where the gain is small, the signal-to-noise ratio will decrease making it more difficult to fit the lineshape and increase the certainty of the temperature measurement. At the 0.5 cm location shown in Figure 5.21 each temperature profile has minima at locations that correspond roughly to the vertical locations of the peak gain. One may think that the temperature at the peak gain location should be high due to heat release from the cold pumping reaction. However, the peak gain location also corresponds to high  $H_2$  concentration. The total temperature of the  $H_2$  jet is basically ambient, or 300 K, while the primary nozzle flow was heated by the discharge tube to 400 to 500 K before entering the nozzle.

At the 2.0 cm location temperature profiles shown in Figure 5.22 for the ( $F_2=1$ ,  $H_2=5$ ), ( $F_2=2$ ,  $H_2=10$ ) and ( $F_2=2$ ,  $H_2=27$ ) flow cases have minima near the vertical centerline with temperature increasing by 50 to 75 K at the nozzle extension lines. These profiles are influenced by the vertical velocity profile, which peaks at the vertical centerline and decreases to the nozzle extension lines where the supersonic primary nozzle flow interacts with the subsonic base purge flow. The cause of the temperature peak at the vertical centerline of the ( $F_2=3$ ,  $H_2=10$ ) flow case is unknown. Perhaps the significantly narrower gain distribution at this downstream location shown in Figure 5.14 means that the reaction zone is smaller and the heat from the cold pumping reaction is being released in a more confined region. At the 3.5 cm and 5.5 cm downstream locations the temperature profiles (shown in Figures 5.23 and 5.24) are flatter probably

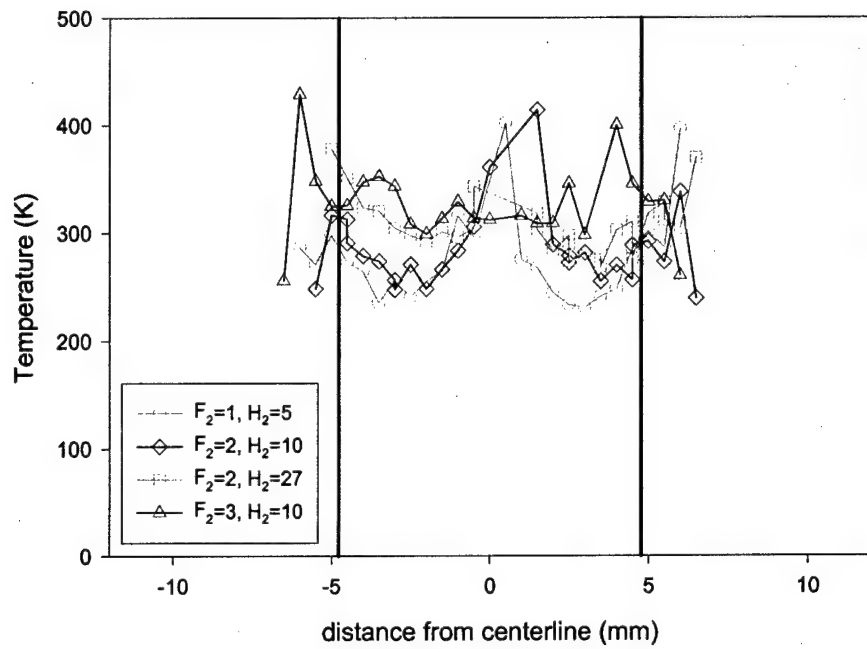


**Figure 5.21** Vertical static temperature profiles 0.5 cm downstream of NEP. Temperature is determined from Gaussian curve fit of the P3 overtone small signal gain transition lineshape. Solid black lines indicate the vertical height of the nozzle at the NEP.

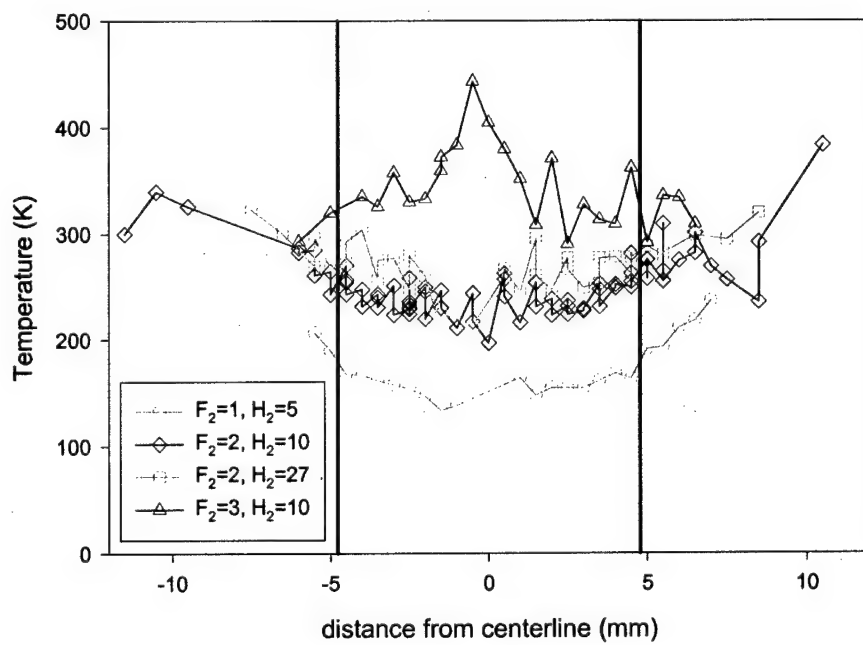


**Figure 5.22** Vertical static temperature profiles 2.0 cm downstream of NEP. Temperature is determined from Gaussian curve fit of the P3 overtone small signal gain transition lineshape. Solid black lines indicate the vertical height of the nozzle at the NEP.

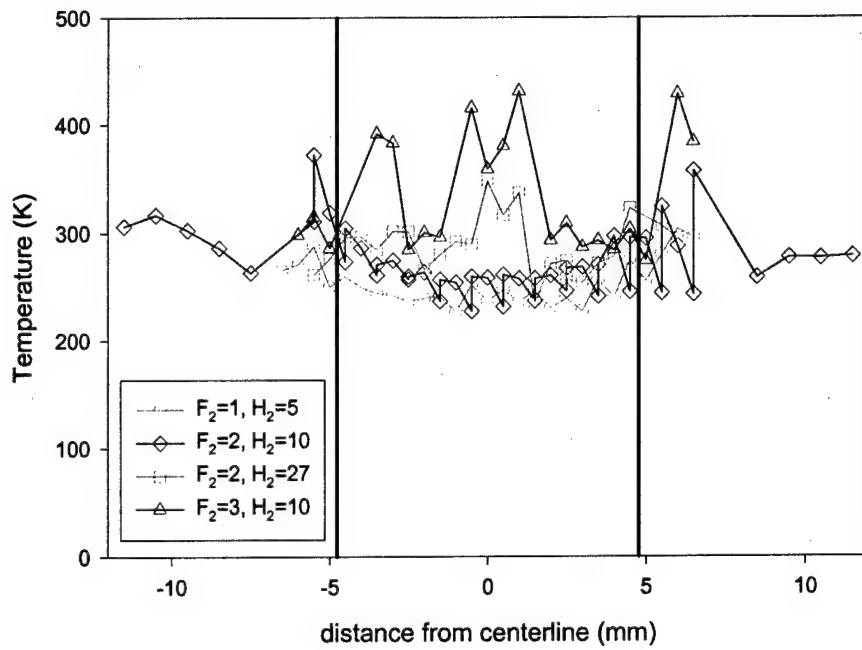


**Figure 5.23.** Vertical static temperature profiles 3.5 cm downstream of NEP. Temperature is determined from Gaussian curve fit of the P3 overtone small signal gain transition lineshape. Solid black lines indicate the vertical height of the nozzle at the NEP.

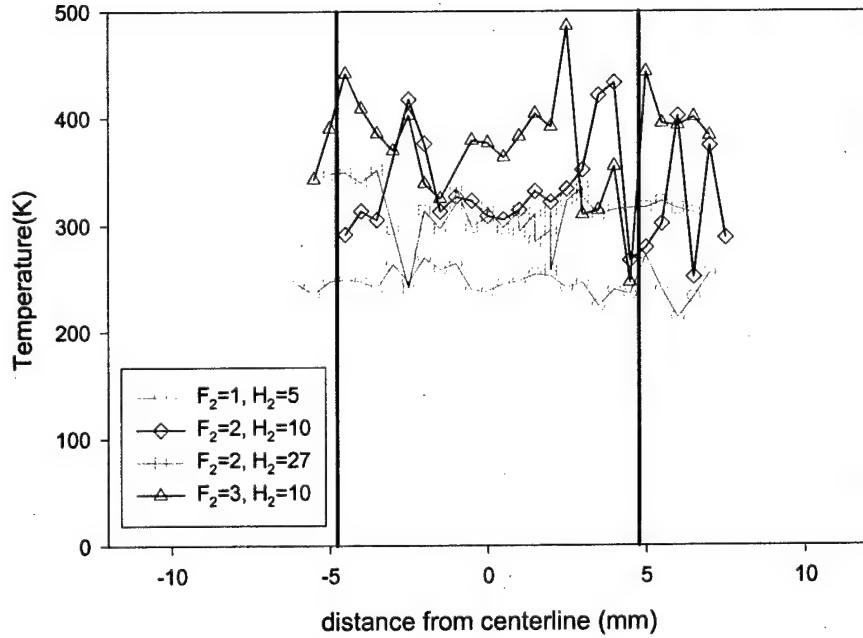


**Figure 5.24** Vertical static temperature profiles 5.5 cm downstream of NEP. Temperature is determined from Gaussian curve fit of the P3 overtone small signal gain transition lineshape. Solid black lines indicate the vertical height of the nozzle at the NEP.

due to a flatter velocity profile. There is a significant increase in scatter at vertical locations far from the peak gain near the centerline.

Figure 5.25 shows the streamwise distribution of temperature at the vertical location of the peak gain for the four flow cases given in Figure 5.19. It should be noted that these measurements were not taken at the same vertical locations. This is a necessary consequence of the temperature measurement, which requires an adequate gain signal in order to resolve the transition lineshape. The ( $F_2=2, H_2=10$ ), ( $F_2=2, H_2=27$ ) and ( $F_2=3, H_2=10$ ) flow conditions show streamwise temperature oscillations of about 50 to 100 K (peak to valley). The peaks are separated by about 2 cm in the downstream direction and occur at about the same downstream location for these three flow conditions. The temperature oscillations for the ( $F_2=1, H_2=5$ ) flow condition are somewhat less pronounced than for the other flow conditions. The difference in temperature level between these four flow cases is likely due to the different He diluent flow rates. The higher the diluent flow rate the lower the overall temperature. Each profile shows a general increase in temperature in the streamwise direction, which is separate from the temperature oscillations. This is expected due to the heat release of the cold pumping reaction.

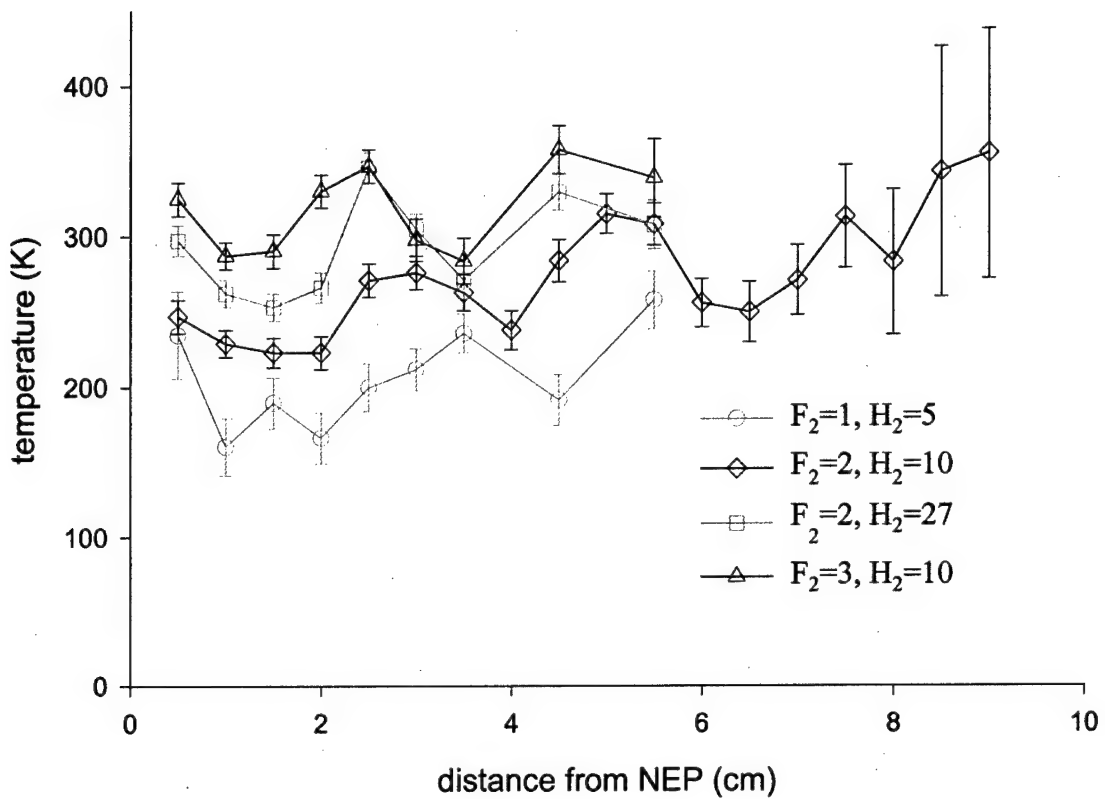


**Figure 5.25** Static temperature measured at the peak gain locations of Figure 5.19. Temperature is determined from Gaussian curve fit of the P3 overtone small signal gain transition lineshape. Error bars represent the precision uncertainty of temperature measurement, which increases as gain decreases.

## 5.4 Data and Model Comparison

### 5.4.1 Premix Model Sensitivity to Kinetics

Figure 5.26 shows predicted P3 overtone ( $\nu=2$  to  $\nu=0$ ) small signal gain as a function of downstream location for a series of premix cases in which only selected chemical reactions are allowed to proceed. By running the model in premix mode, the effects of the chemical kinetics can be seen without the complication of reactant mixing; this allows the dominant chemical reactions to be identified. Table 5.5 lists the nine cases that were run. Each case adds a new reaction or set of reactions to the previous case. It is important to note that each new case adds both the forward and reverse reactions listed in Table 5.5. In all cases, the ( $F_2=2$ ,  $H_2=10$ ) flow conditions listed in Table 5.2 were used.

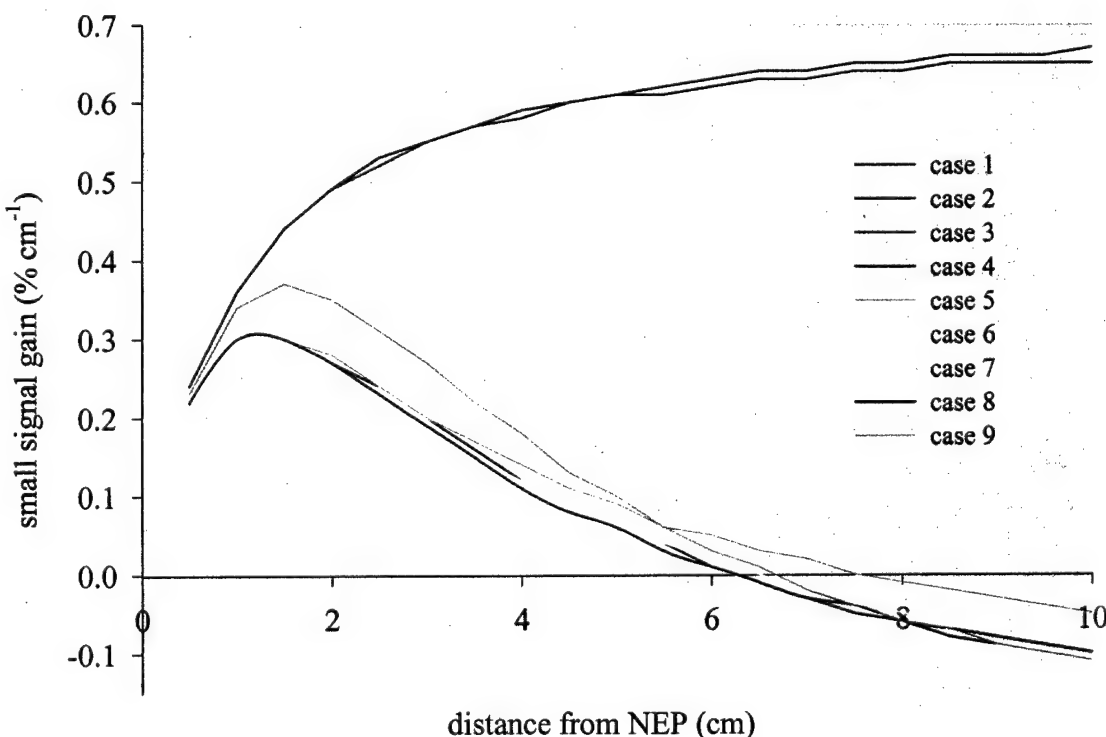


**Figure 5.26** Predicted small signal gain for premixed ( $F_2=2$ ,  $H_2=10$ ) flow conditions for kinetics cases specified in Table 5.5.

**Table 5.5** Premix kinetics cases. Each case adds the forward and reverse chemical reaction listed to those in the previous case with all other rates set to zero.

Case number		
1	Cold Pumping Reaction	$F + H_2 \rightarrow HF(v) + H$
2	Hot Pumping Reaction	$F_2 + H \rightarrow HF(v) + F$
3	V-V energy transfer with HF	$HF(v) + HF(v') \rightarrow HF(v+1) + HF(v'-1)$
4	V-V energy transfer with $H_2$	$HF(v) + H_2(v') \rightarrow HF(v-1) + H_2(v'+1)$
5	Reactive Quenching	$HF(v \geq 4) + H \rightarrow H_2 + F$
6	V-T Self Deactivation	$HF(v) + HF(0) \rightarrow HF(v-1) + HF(0)$
7	V-T Energy Transfer with $M = H_2, F, He$ and $F_2$	$HF(v) + M \rightarrow HF(v-1) + M$
8	Fluorine Dissociation and Recombination $M = H_2, F, He$ and $F_2$	$F + F + M \rightarrow F_2 + M$
9	V-T energy transfer with H atoms	$HF(v) + H \rightarrow HF(v-1) + H$

Case 1 is the most basic reaction set. It includes only HF generation via the cold pumping reaction with no deactivation. Hence, the predicted gain increases until all the F atoms are consumed and a maximum gain of nearly  $0.7\% \text{ cm}^{-1}$  is achieved. Case 2 shows that adding the hot pumping reaction only slightly decreases the predicted maximum overall gain. Since the dissociation fraction is  $\sim 75\%$  for the flow conditions selected here, there is a significant amount of  $F_2$  in the flow and one would expect the hot reaction to enhance the gain. However, the combination of a small rate constant and the diffuse vibrational distribution of product HF produced by the hot reaction greatly reduces this effect. The reverse hot pumping reaction, which consumes both vibrationally excited HF and F atoms, is the most likely cause of the observed gain decrease.

Case 3 adds the V-V energy transfer reactions between excited HF molecules. These reactions have a dramatic effect on the predicted maximum gain, lowering it by almost 60% to 0.3 % cm<sup>-1</sup>. The kinetics become dominated by these reactions very quickly to change the gain from increasing asymptotically in the streamwise direction for the cold pumping reaction (case 1) to decreasing asymptotically in the streamwise direction within 2 cm of the NEP. It will be shown in Section 5.4.4 that the rather large uncertainty in the rate constants for these reactions presents a significant obstacle in trying to predict laser system gain.

Case 4 adds V-V energy transfer between excited HF and H<sub>2</sub> molecules and has a negligible effect on the gain. Case 5 adds reactive quenching for HF( $\nu \geq 4$ ). The reverse cold pumping reaction already includes reactive quenching for HF( $\nu \leq 3$ ). These reactions have no effect on the predicted maximum gain but do increase the gain further downstream compared to case 4 by converting the higher ( $\nu \geq 4$ ) vibrationally excited HF molecules into F atoms that can be used to create more HF( $\nu=2$ ). However, this downstream gain increase is taken away in case 6 by adding V-T self deactivation. Cases 7 and 8 add all other V-T energy transfers and the three-body fluorine recombination/dissociation reactions, respectively. Each has negligible effect on the predicted maximum gain and gain distribution in the flow direction.

The V-T deactivation of HF( $\nu$ ) by H atoms was saved for case 9 because of a disagreement in the literature concerning this reaction mechanism. As stated in Section 2.2.5 the rate for HF( $\nu \geq 3$ ) deactivation by H atoms is much faster than the rate for HF( $\nu=2$ ) deactivation. This creates a “bottleneck” in the deactivation path toward equilibrium that takes all the higher vibrational energy and puts it into  $\nu=2$ . Figure 5.26

shows that these reactions correspondingly increase the predicted peak gain by ~25% as compared to case 8. The dramatic gain increase caused by these deactivation reactions raises some skepticism as to their legitimacy. In light of this, we have decided to follow the recommendation of Bartoszek et al. (1978) and remove them from the kinetics package. Removing these rates may be considered somewhat controversial due to the fact that some form of this deactivation mechanism is included in most HF laser kinetics models. However, by following the last available published opinion on the subject, we feel justified in this action. Since the model, in both premix and mixing modes, consistently overpredicts the measured gain, removing these reactions improves agreement with the data. Clearly an experimental investigation is needed to resolve this issue.

The significant result from this premix analysis is that, to a very good approximation, the chemical kinetic system of this HF laser is defined by the cold pumping reaction and V-V energy transfer between excited HF molecules (case 3). The much slower V-T energy transfer, hot pumping, reactive quenching and three-body recombination reactions each has a small effect on the predicted gain. However, since computation time is not a significant factor, these reactions were kept (except for  $\text{HF}(v) + \text{H} \rightarrow \text{HF}(v-1) + \text{H}$  added in case 9) and all subsequent predictions were made with a kinetics package represented by case 8.

#### 5.4.2 Model Turbulence Effect

As stated in Chapter 4.0, the 2-D code cannot predict the actual 3-D turbulent flow field. However, the turbulence model within the 2-D code can simulate the overall effect

turbulence has on the flow. In particular, we would like to know the degree of mixing enhancement between the F atom and H<sub>2</sub> flow streams that can be attributed to turbulence. This section compares predictions with the turbulence model turned on and turned off. All these code runs were performed with the (F<sub>2</sub>=2, H<sub>2</sub>=10) flow conditions and a kinetics package represented by case 8 as described in Section 5.4.1. The flow distribution at the nozzle exit plane (NEP) was set so that the injected H<sub>2</sub> flow filled the area between the primary F atom flow and the nozzle wall (i.e., input parameter imesh=2). To run the turbulence model, the turbulence intensity in each of the primary, H<sub>2</sub>, He injection, and base purge flow streams must be specified at the NEP. Three cases were chosen with initial turbulence intensity (for all streams) of 0.5%, 1% and 2%, respectively, and the output was analyzed with respect to the change in reactant mixing.

Figures 5.27, 5.28, 5.29 and 5.30 show H<sub>2</sub>, F atom and HF(v=2) vertical concentration profiles for laminar and turbulent (with 1% initial turbulence intensity) cases at distances of 0.025 cm, 2 cm, 4 cm, and 6 cm from the NEP, respectively. At 0.025 cm the laminar and turbulent profiles lie on top of each other and show the initial distributions of the primary and injected flows specified by the model injection scheme. The gap between the F atom and H<sub>2</sub> flows at around 4 mm from the centerline is the secondary He injection flow. At 2.0 cm downstream of the NEP, the HF(v=2) concentration has grown in the region where the F atom and H<sub>2</sub> concentrations overlap. This overlap region defines the reaction zone of the cold pumping reaction. By the time the flow reaches 4 cm downstream of the NEP, the F atom concentration at the vertical centerline has decreased significantly more for the turbulent case than for the laminar case. The decrease in F atom concentration corresponds to an increase in HF(v=2)

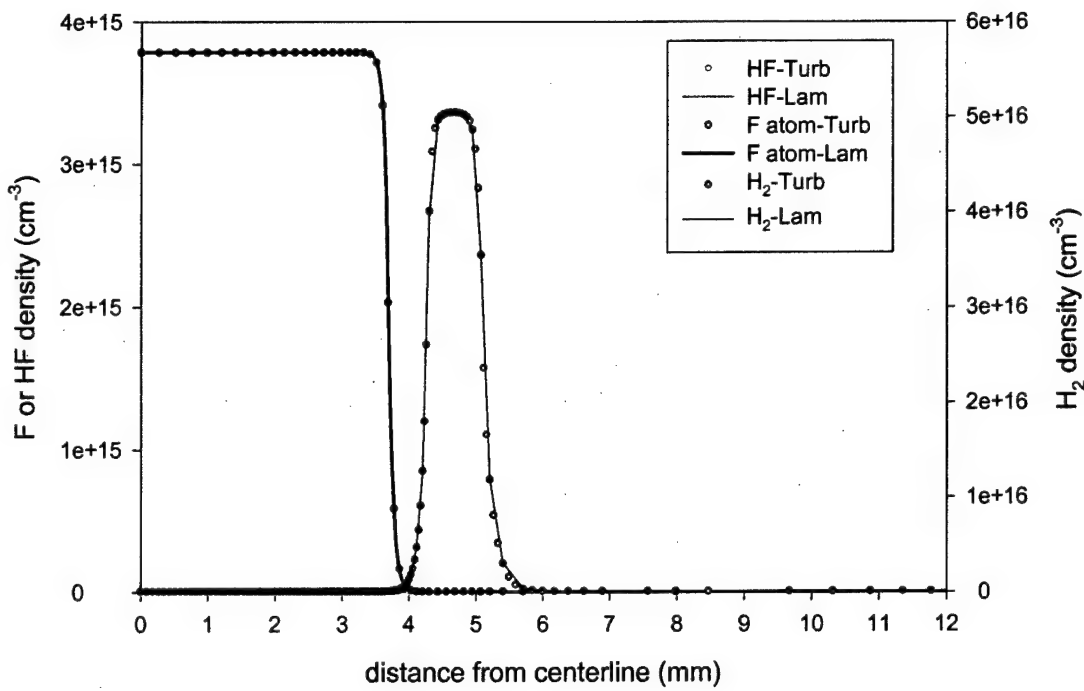


**Figure 5.27** Predicted vertical concentration profiles 0.025 cm downstream of the NEP for the ( $F_2=2$ ,  $H_2=10$ ) flow conditions. Turbulent modeling case has 1% initial turbulence intensity.

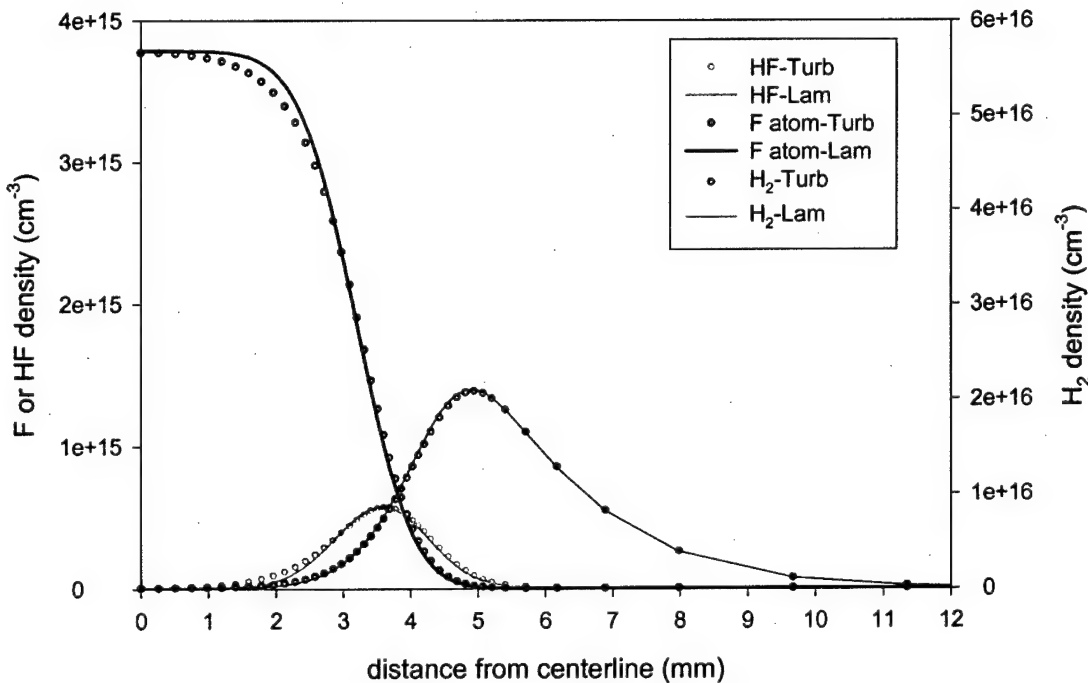


**Figure 5.28** Predicted vertical concentration profiles 2.0 cm downstream of the NEP for the ( $F_2=2$ ,  $H_2=10$ ) flow conditions. Turbulent modeling case has 1% initial turbulence intensity.

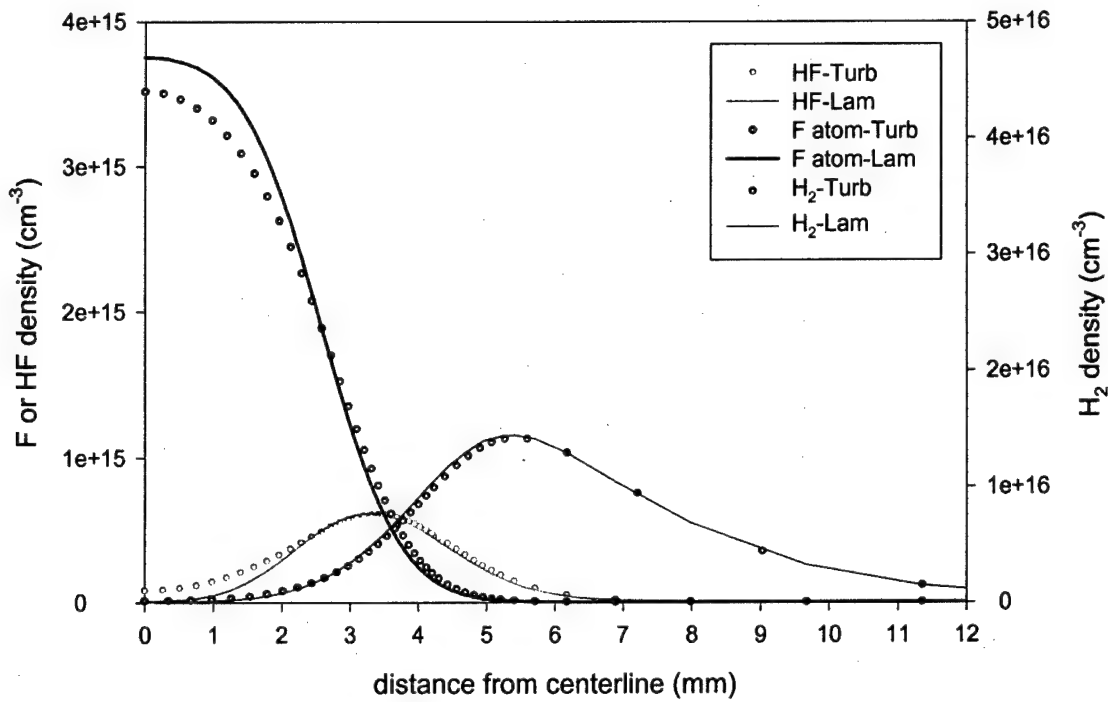


**Figure 5.29** Predicted vertical concentration profiles 4.0 cm downstream of the NEP for the ( $F_2=2$ ,  $H_2=10$ ) flow conditions. Turbulent modeling case has 1% initial turbulence intensity.

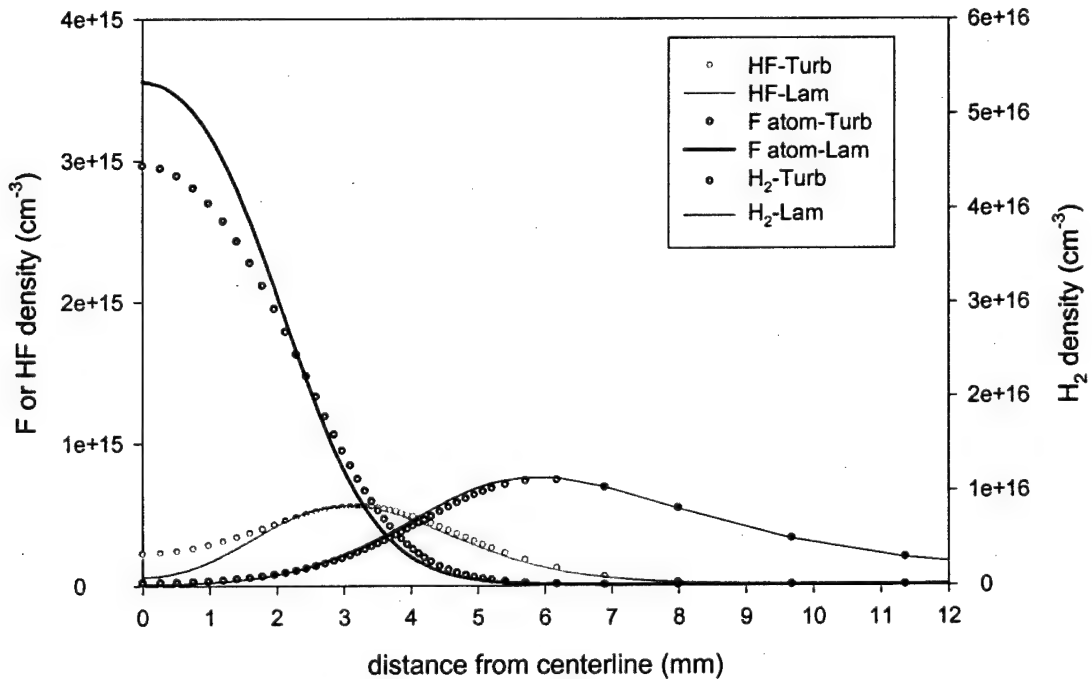


**Figure 5.30** Predicted vertical concentration profiles 6.0 cm downstream of the NEP for the ( $F_2=2$ ,  $H_2=10$ ) flow conditions. Turbulent modeling case has 1% initial turbulence intensity.

concentration at the vertical centerline. The difference between turbulent and laminar centerline F atom and HF( $v=2$ ) concentrations continues to grow as the flow moves downstream. Interestingly enough, the peak HF( $v=2$ ) concentration at each streamwise location is nearly identical for these two modeling cases. This indicates that the mixing enhancement provided by the flow turbulence widens the reaction zone but does not reduce the concentration at the peak.

Figures 5.31 and 5.32 show the P3 overtone ( $v=2$  to  $v=0$ ) gain at the peak and vertical centerline locations, respectively, for the turbulent and laminar predictions. The premix predictions and measurements are included for comparison. The mixing enhancement created by the turbulence allows the reaction zone and therefore also the gain to reach the centerline closer to the NEP. The peak gain also moves closer to the NEP and increases in magnitude due to the greater F atom utilization. The peak gain for the turbulent flow case is just slightly higher than for the laminar flow cases. This again illustrates that the mixing enhancement due to turbulence stretches the reaction zone in the vertical direction without reducing the gain at the peak location and thus turbulence has a much greater effect on centerline gain than on peak gain.

Figures 5.31 and 5.32 also show the peak and centerline gains, respectively, for the experimental data and the premix predictions. The premix case represents the limit of infinitely fast mixing and has a nearly uniform gain across the vertical profiles, being only slightly affected by the interaction between the primary flow and the base purge flow. For the premixed case, the gain reaches a maximum 1.5 cm downstream of the NEP and then falls off sharply as V-V energy transfer begins to dominate the kinetics.

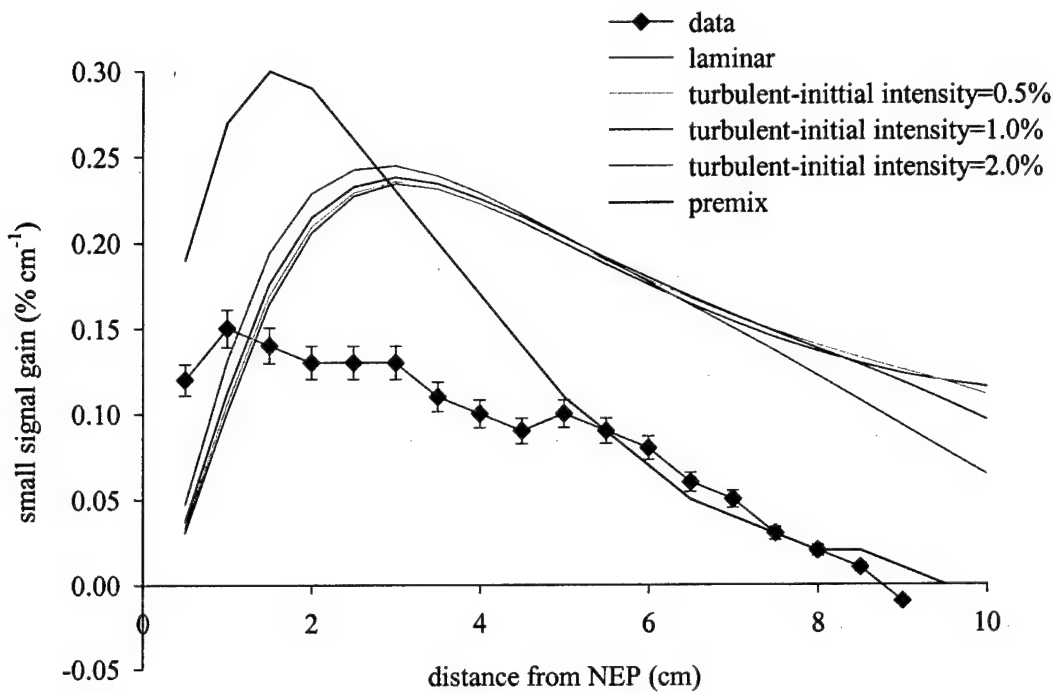


**Figure 5.31** Measured and predicted peak gain for ( $F_2=2$ ,  $H_2=10$ ) flow conditions.

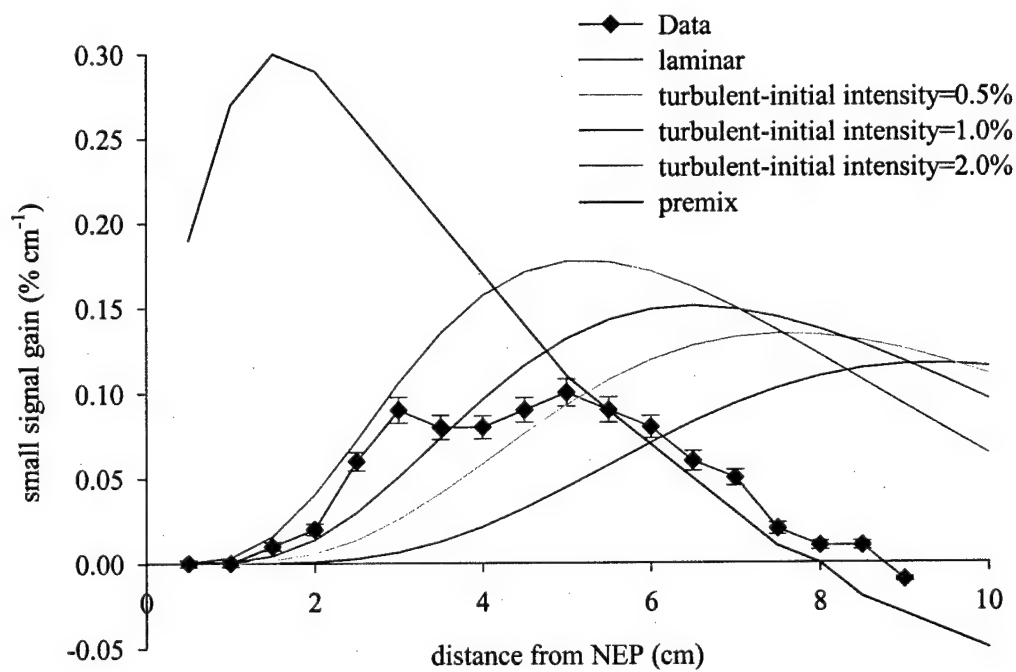


**Figure 5.32** Measured and predicted centerline gain for ( $F_2=2$ ,  $H_2=10$ ) flow conditions.

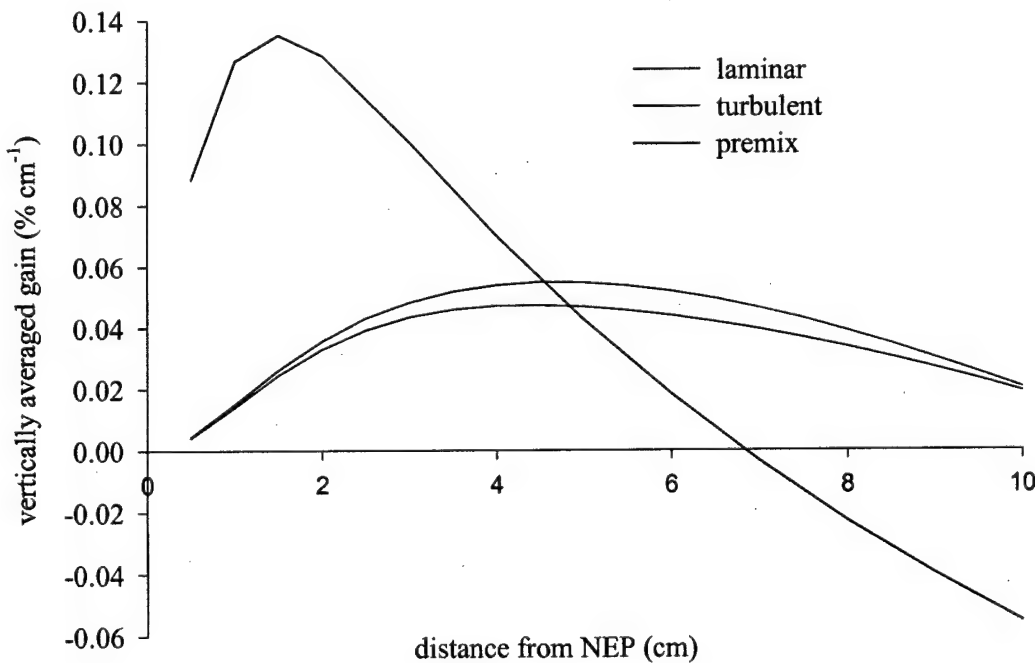
By increasing the initial turbulence intensity up to 2%, the turbulent mixing predictions are only slightly closer to the premix predictions of peak gain. Ignoring for now the difference in magnitude between the measured gain and the turbulent predictions, we see some interesting trends in the shape of the curves. The predictions for 2% initial turbulent intensity case agree quite well with the measured onset of gain at the vertical centerline. The location where the centerline gain begins to decrease ( $\sim 5$  cm from the NEP) and the slope of the decrease also agree well. However, as shown in Figure 5.31, the initial peak gain and the downstream location of the maximum peak gain are significantly different in the measurements and the turbulent predictions. At 0.5 cm downstream of the NEP the model substantially underpredicts the measured peak gain but the predictions quickly surpass the measurement by 1.5 cm downstream of the NEP, reaching a maximum about 3.0 cm downstream of the NEP. Increases in the initial turbulence intensity have a much smaller effect on the peak gain than on the centerline gain. Further increasing the initial turbulence intensity beyond 2% will decrease the agreement between the predicted and measured gain at the centerline with only a marginal improvement in the agreement in the predicted and measured peak gain. It does not appear that turbulent mixing of the flow field can account for the differences between the shapes of the measured and predicted gain curves. Some other mixing mechanism not accounted for in the 2-D turbulence model must have a strong influence on the flow field.

Figure 5.33 shows the vertically-averaged gain for the premix, laminar, and turbulent (with 1% initial turbulence intensity) predictions as a function of downstream location. The maximum average gains for the premix, turbulent and laminar modeling

cases are 0.135, 0.054 and 0.047 % cm<sup>-1</sup>, respectively. The difference in average gain between the three different modeling cases may be explained by the utilization of F atoms, which is illustrated in Figure 5.34. F atom utilization,  $U_{F\ atom}$ , is defined as:

$$U_{F\ atom} = 1 - \frac{\text{F atom flow rate}}{\text{initial F atom flow rate}} \quad (5.1)$$

At the location of maximum average gain the turbulent and laminar modeling cases predict F atom utilizations of 39 and 34%, respectively, as indicated by the arrows. Therefore, a modest 5% increase in F atom utilization created by turbulent mixing produces a significant 16% increase in maximum vertically-averaged gain. As expected the premix case has the best F atom utilization with a value of 63% at the maximum vertically-averaged gain location (~ 1.5 cm from the NEP), which produces a maximum



**Figure 5.33** Predicted vertically-average gain for (F<sub>2</sub>=2, H<sub>2</sub>=10) flow conditions.

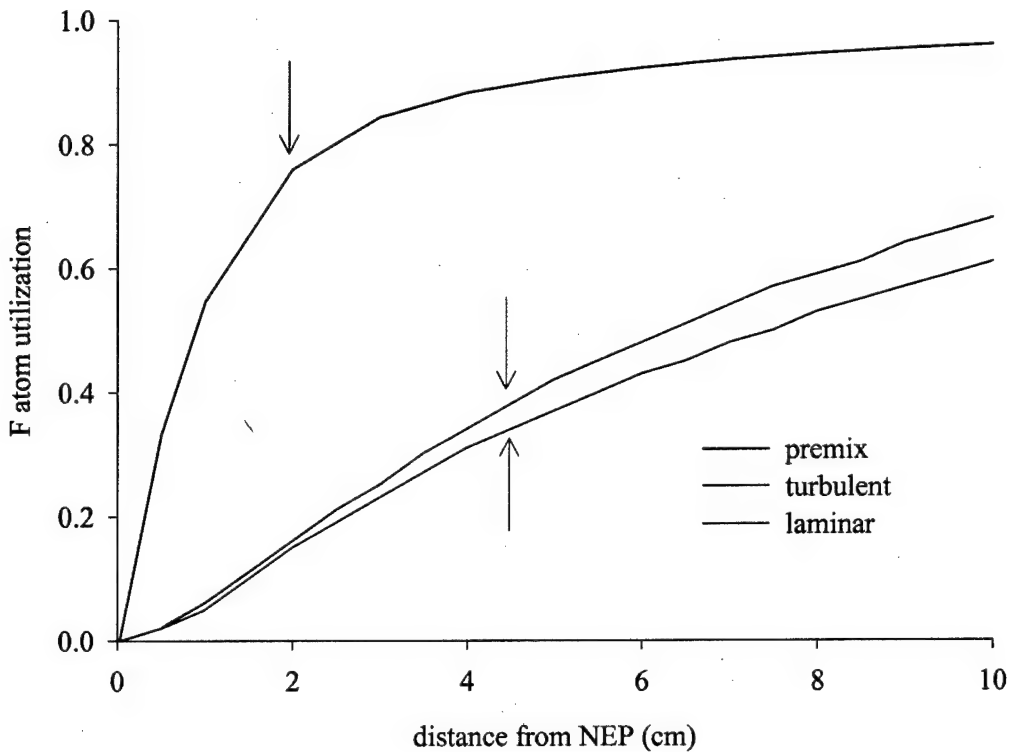


**Figure 5.34** Predicted F atom utilization for ( $F_2=2$ ,  $H_2=10$ ) flow conditions. Arrows are at the locations of maximum vertically-averaged gain in Figure 5.33

vertically-averaged gain almost 200% greater than the maximum for the laminar modeling case. Therefore with the possibility of huge improvements in laser power for small increases in mixing performance, the importance of mixing inside the laser cannot be overemphasized.

#### 5.4.3 Model Injection Scheme Effect

The imesh=2 injection scheme used in the previous section to investigate the effects of turbulence on the flow field uses a conservation of momentum argument to fix the size and location of the injected flow streams at the nozzle exit plane (NEP). This method ignores completely the large-scale vortex structures that are created by shear stresses between the injected and primary flows. One of the dominant vortex structures

that develops is the counter-rotating streamwise-oriented vortex pair discussed in Section 2.3.1. These structures cause part of the primary flow to be entrained into the injected flow jet and circulated around from the upstream side to the downstream side of the jet. Vorticity is a complex 3-dimensional flow phenomenon that is further complicated in this situation by the interaction of the secondary He injector jets and impingement of jets from adjacent injection holes. The net effect of these vortex structures is to transfer some portion of the primary flow from the center region to the area between the H<sub>2</sub> injection flow and the nozzle wall. Since the shear stresses are largest at the point of injection and diminish as the jets are turned parallel to the primary flow, the bulk of the vorticity is likely to be generated by the time the flow reaches the NEP.

Setting the computer model input parameter imesh=3 allows the location and relative size of the H<sub>2</sub> and secondary He injection jets to be specified at the NEP. Placing the H<sub>2</sub> jet away from the nozzle wall automatically fills in the region between the jet and the wall with a portion of the primary flow. The imesh=3 injection scheme can therefore, to a very crude approximation, simulate some of the counter-rotating vortex pair effects. Again it must be emphasized that the 2-dimensional code has, by definition, zero axial vorticity and this is merely an attempt to model, as best we can, the zeroth-order effects of the jet injection. Additionally, unlike the turbulence model, which propagates an initial assumed turbulence intensity downstream, this injection scheme only attempts to represent the effect of the large-scale vorticity structures at a single downstream location in the flow field. However, despite the crudeness of this attempt, the results of this computer experiment say some interesting things about the mixing inside HF laser nozzles.

All of the modeling predictions presented in this section are for the ( $F_2=2$ ,  $H_2=10$ ) flow conditions listed in Table 5.2. Figures 5.35, 5.36, 5.37 and 5.38 show the vertical  $H_2$ , F atom and HF( $v=2$ ) concentration profiles for the imesh=2 and imesh=3 modeling cases at 0.025 cm, 0.5 cm, 2.0 cm and 4 cm downstream of the NEP, respectively. Both cases were run with the turbulence model active and 1% initial turbulence intensity for all streams. The imesh=2 case is identical to the turbulent mixing case of Section 5.4.2. The jet location and size input parameters required for the imesh=3 case were determined by iteration to obtain approximate agreement between the measured and predicted gain profiles 0.5 cm downstream of the NEP. The 0.025 cm concentration profiles for the imesh=3 case in Figure 5.35 show the  $H_2$  jet centered 3.2 mm from the vertical centerline with flow of F atoms on either side. The dip in the F atom concentration 2.3 mm from the centerline is caused by the secondary He injection jet. This simulation shows one benefit of the large-scale vortex structures is to give additional surface area contact between the  $H_2$  and F atom flows. In fact, in three dimensions the  $H_2$  jet would be surrounded and entrained with the primary flow. At 0.5 cm downstream of the NEP, the HF( $v=2$ ) concentration in Figure 5.36 has grown on each side of the  $H_2$  jet and the F atom flow between the  $H_2$  jet (centered at 3.2 mm) and the upper surface of the laser cavity is greatly reduced.

By 2.0 cm downstream of the NEP in Figure 5.37, the F atom flow between the  $H_2$  jet and the upper cavity surface is nearly depleted and a small amount of HF( $v=2$ ) has reached the centerline. This shows that the reaction zone has expanded in the vertical direction with a corresponding increase in F atom utilization. By 4.0 cm downstream of the NEP in Figure 5.38 there is more HF( $v=2$ ) at the centerline for the imesh=3 case and

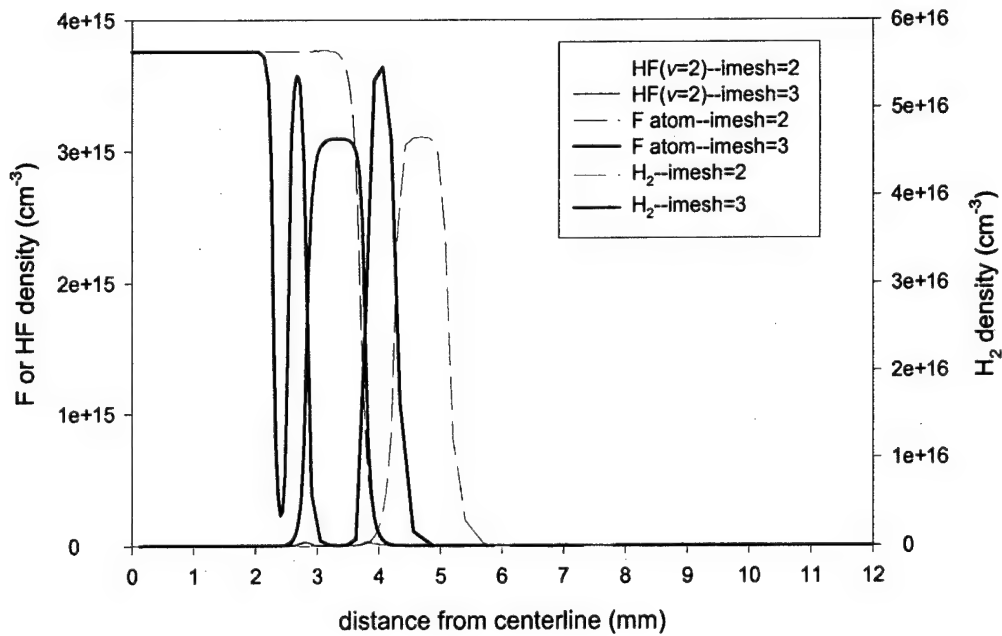


**Figure 5.35** Predicted imesh=2 and imesh=3 concentration profiles 0.025 cm downstream of the NEP for the ( $F_2=2$ ,  $H_2=10$ ) flow conditions with 1% initial turbulence intensity.

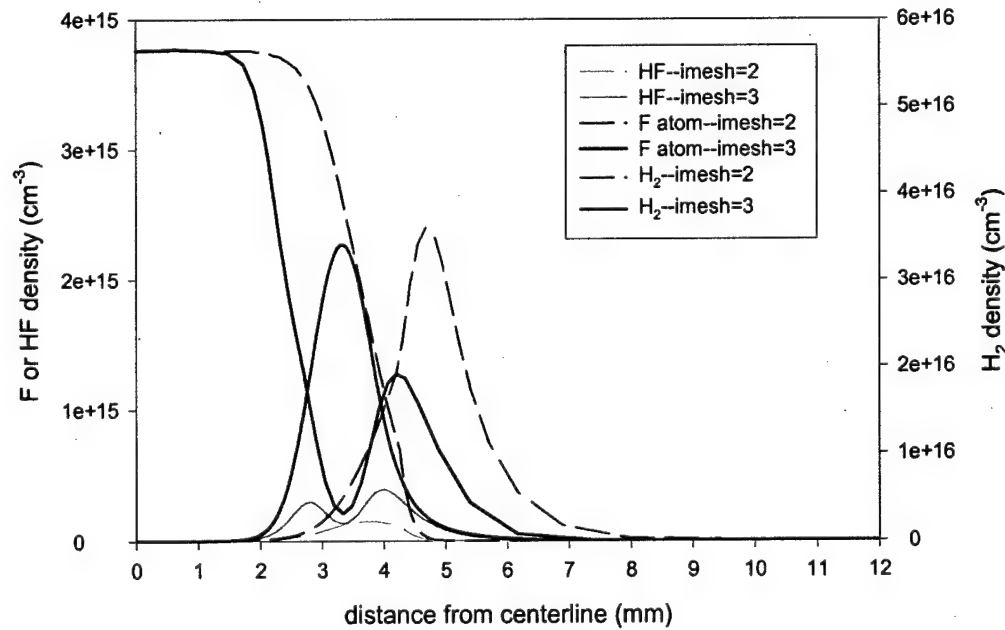


**Figure 5.36** Predicted imesh=2 and imesh=3 concentration profiles 0.5 cm downstream of the NEP for the ( $F_2=2$ ,  $H_2=10$ ) flow conditions with 1% initial turbulence intensity.

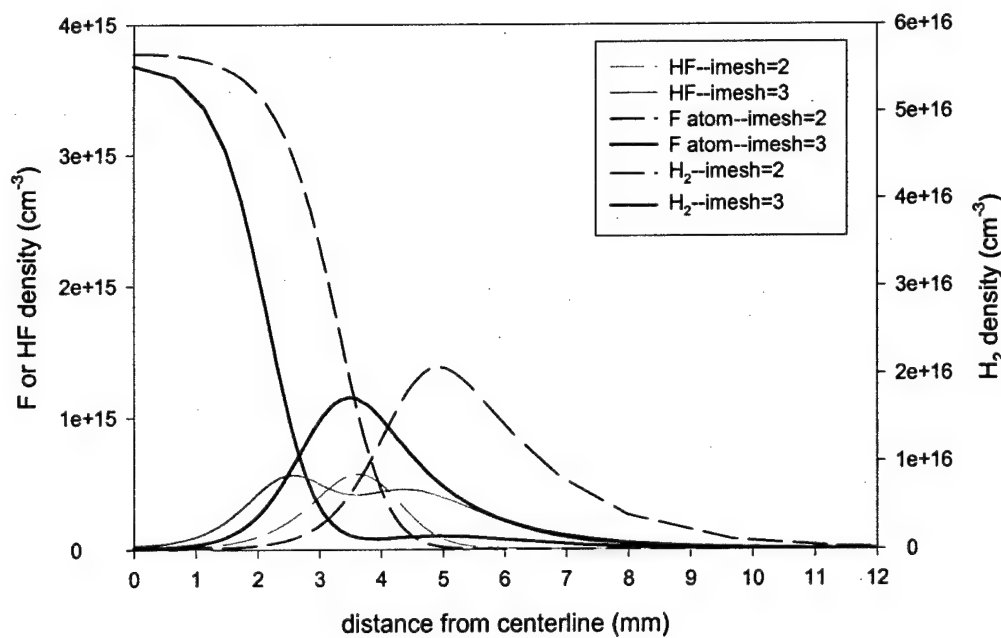


**Figure 5.37** Predicted imesh=2 and imesh=3 concentration profiles 2.0 cm downstream of the NEP for the ( $F_2=2$ ,  $H_2=10$ ) flow conditions with 1% initial turbulence intensity.

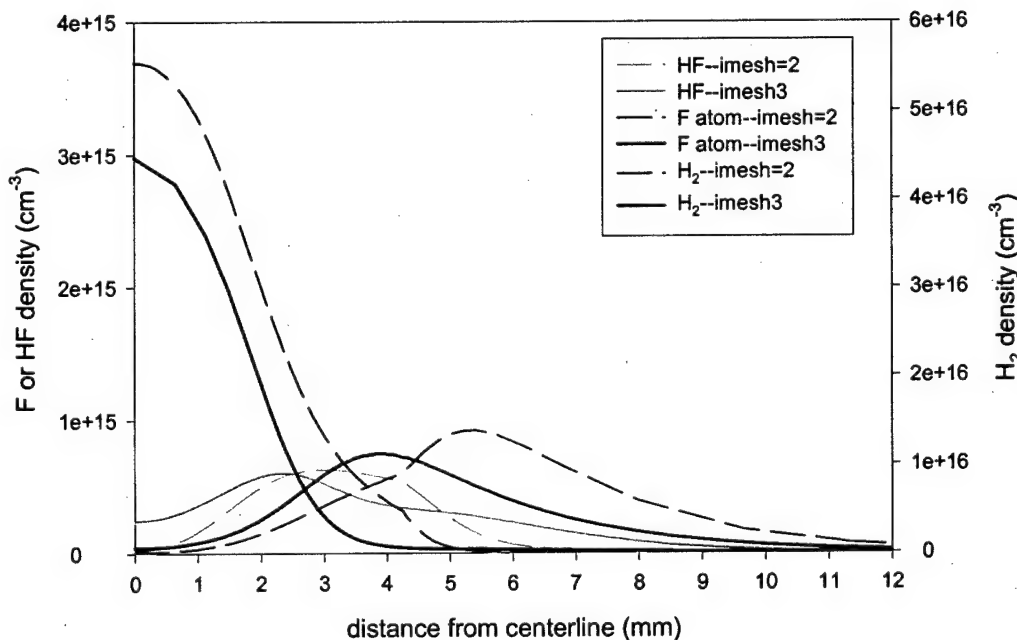


**Figure 5.38** Predicted imesh=2 and imesh=3 concentration profiles 4.0 cm downstream of the NEP for the ( $F_2=2$ ,  $H_2=10$ ) flow conditions with 1% initial turbulence intensity.

the peak HF( $\nu=2$ ) location is slightly closer to the centerline than for the imesh=2 case. Just like in the comparison between the laminar and turbulent predictions, the maximum HF( $\nu=2$ ) concentrations at a given downstream location for the two imesh cases are nearly identical. So again we see that mixing enhancement has a much greater effect on the width of the reaction zone than on the peak concentration.

Figures 5.39, 5.40 and 5.41 show the P3 ( $\nu=2$  to  $\nu=0$ ) overtone gain profiles for the measurement and for the imesh=2 and imesh=3 predictions at 0.5 cm, 2 cm, and 4 cm downstream of the NEP, respectively. The imesh=3 input parameters were chosen to attain good agreement between the shape of the predicted and measured gain profiles at 0.5 cm downstream of NEP as shown in Figure 5.39 where the dual reaction zones have effectively widened the gain region in the vertical direction. For the imesh=2 case, the H<sub>2</sub> has to diffuse through the secondary He jet located at  $\pm 3$  mm from the vertical centerline to reach the F atoms resulting in a narrow gain region and substantially reduced peak gain. At 2.0 cm downstream of the NEP in Figure 5.40 the imesh=2 peak gain is only slightly lower than the imesh=3 peak gain with both predictions significantly higher than the measured peak gain. The predicted vertical gain profile for the imesh=2 case is still significantly narrower than the measurements whereas for the imesh=3 case the predicted width of the gain region agrees with the data somewhat better. The shape of the predicted gain for the imesh=3 case also matches the measured profile much better with a steeper slope on the side of the peak toward the centerline and a more rounded contour away from the centerline. At 4.0 cm downstream of the NEP in Figure 5.41 the imesh=2 peak gain is now slightly higher than the imesh=3 peak gain with both

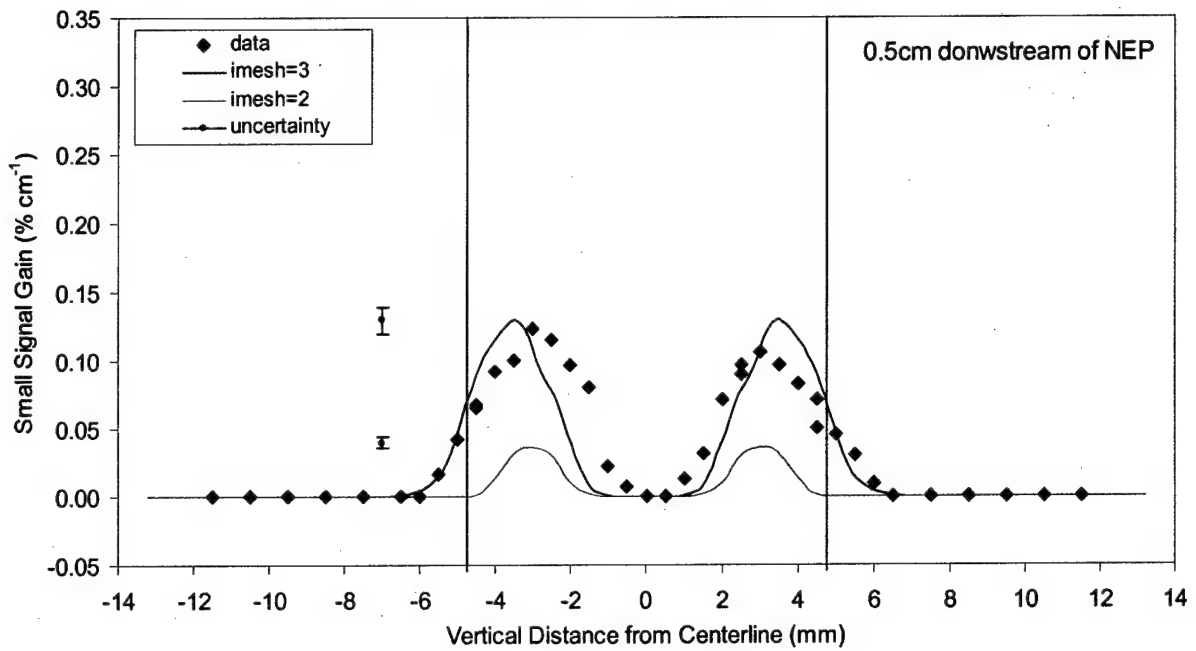


**Figure 5.39** Measured and predicted gain profiles 0.5 cm downstream of the NEP for the ( $F_2=2$ ,  $H_2=10$ ) flow conditions. Solid black vertical lines indicate the vertical height of the nozzle at the NEP. Error bars represent 6% bias and  $0.002 \text{ \% cm}^{-1}$  precision uncertainties.

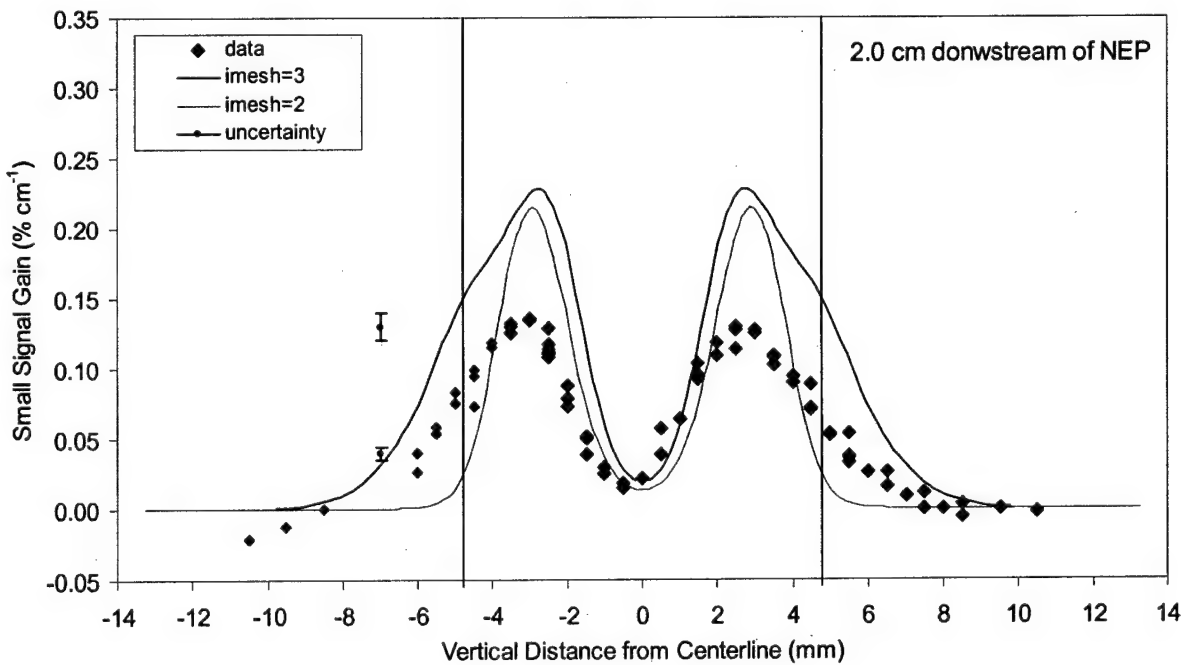


**Figure 5.40** Measured and predicted gain profiles 2.0 cm downstream of the NEP for the ( $F_2=2$ ,  $H_2=10$ ) flow conditions. Solid black vertical lines indicate the vertical height of the nozzle at the NEP. Error bars represent 6% bias and  $0.002 \text{ \% cm}^{-1}$  precision uncertainties.

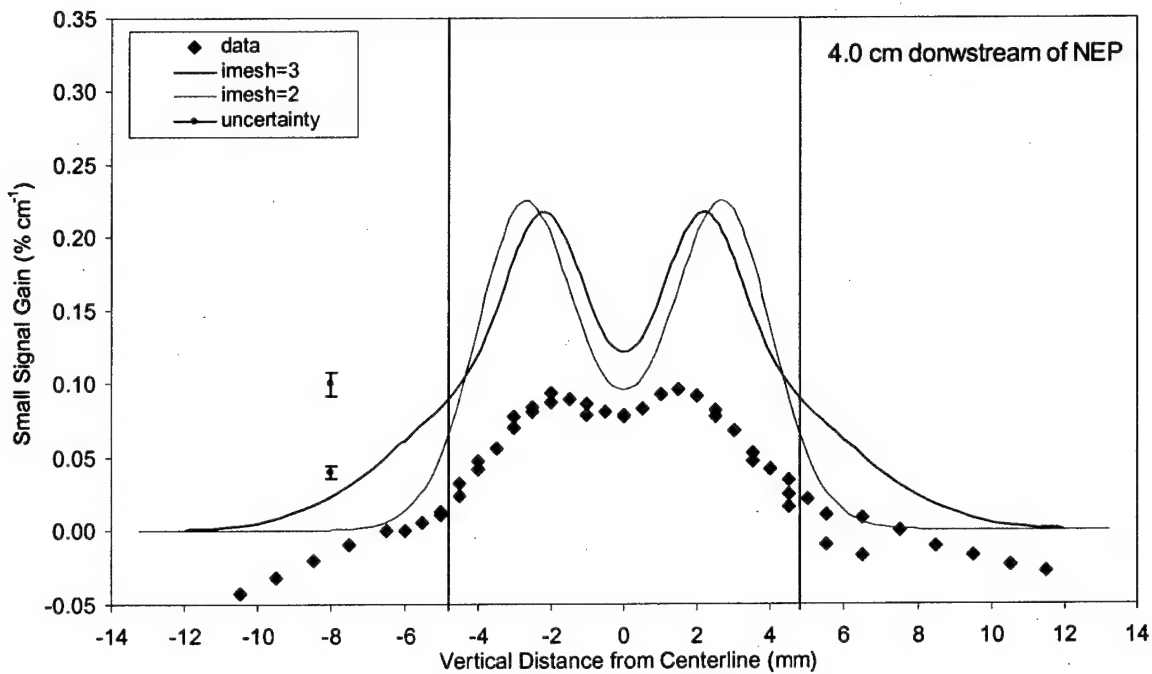


**Figure 5.41** Measured and predicted gain profiles 4.0 cm downstream of the NEP for the ( $F_2=2$ ,  $H_2=10$ ) flow conditions. Solid black vertical lines indicate the vertical height of the nozzle at the NEP. Error bars represent 6% bias and  $0.002\text{ \% cm}^{-1}$  precision uncertainties.

predictions still significantly higher than the measured peak gain. The major difference between the predictions at 4.0 cm downstream of the NEP is in the region more than 5 mm from the centerline. The imesh=2 case predicts zero gain over almost this entire region while the predicted gain for the imesh=3 case decreases gradually to zero over this region in good agreement with the slope of the data. Little gain is predicted in this region for the imesh=2 case because there is little F atom flow between the  $H_2$  jet and the nozzle wall as shown in Figure 5.38.

Figures 5.42, 5.43 and 5.44 show the peak gain, centerline gain, and vertical location of the peak gain for the two imesh modeling cases and the data. The result of switching from the imesh=2 to imesh=3 injection scheme is an increase in the peak gain 0.5 cm downstream of the NEP without an increase in the maximum peak gain as shown

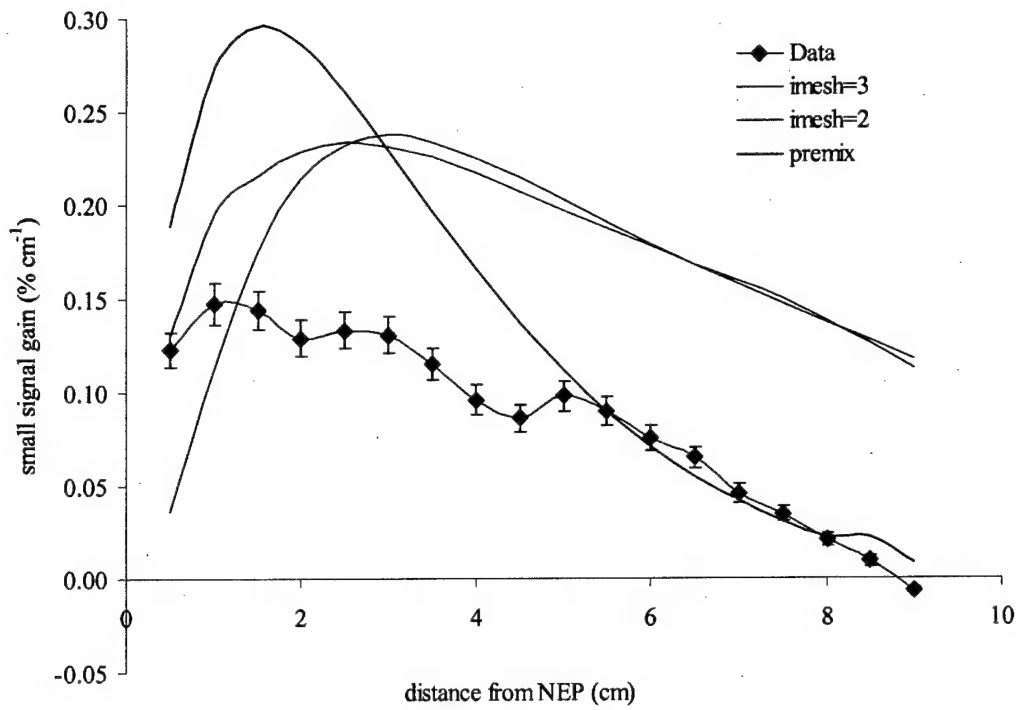


**Figure 5.42** Measured and predicted peak gain for the ( $F_2=2$ ,  $H_2=10$ ) flow conditions. Error bars represent 6% bias and  $0.002\% \text{ cm}^{-1}$  precision uncertainties.

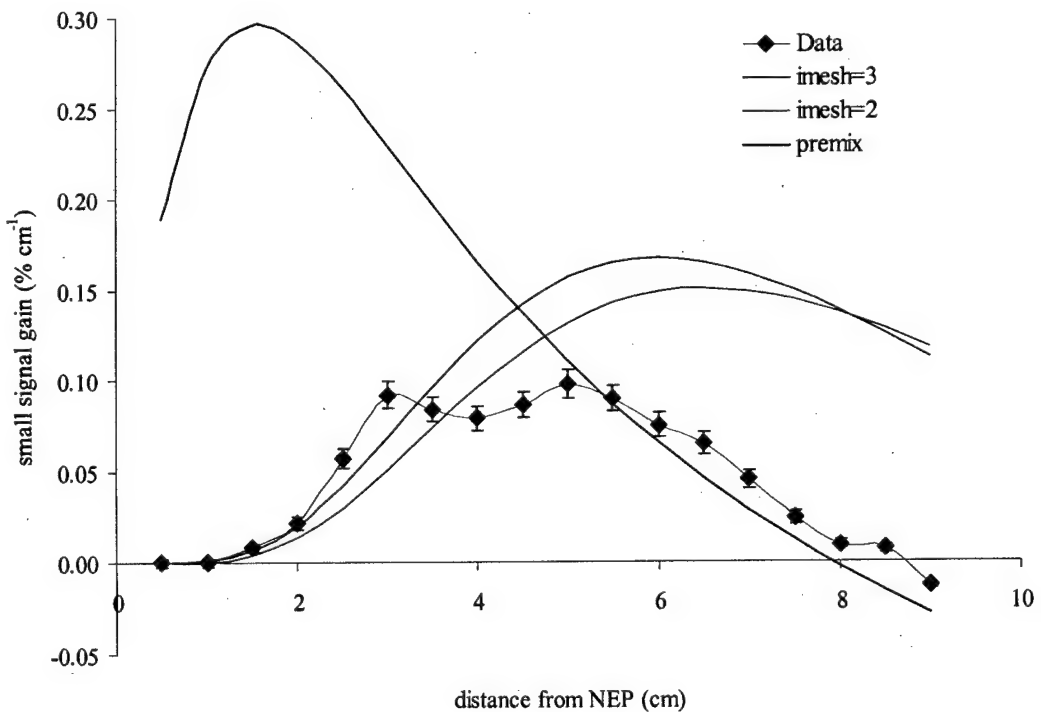


**Figure 5.43** Measured and predicted centerline gain for the ( $F_2=2$ ,  $H_2=10$ ) flow conditions. Error bars represent 6% bias and  $0.002\% \text{ cm}^{-1}$  precision uncertainties.

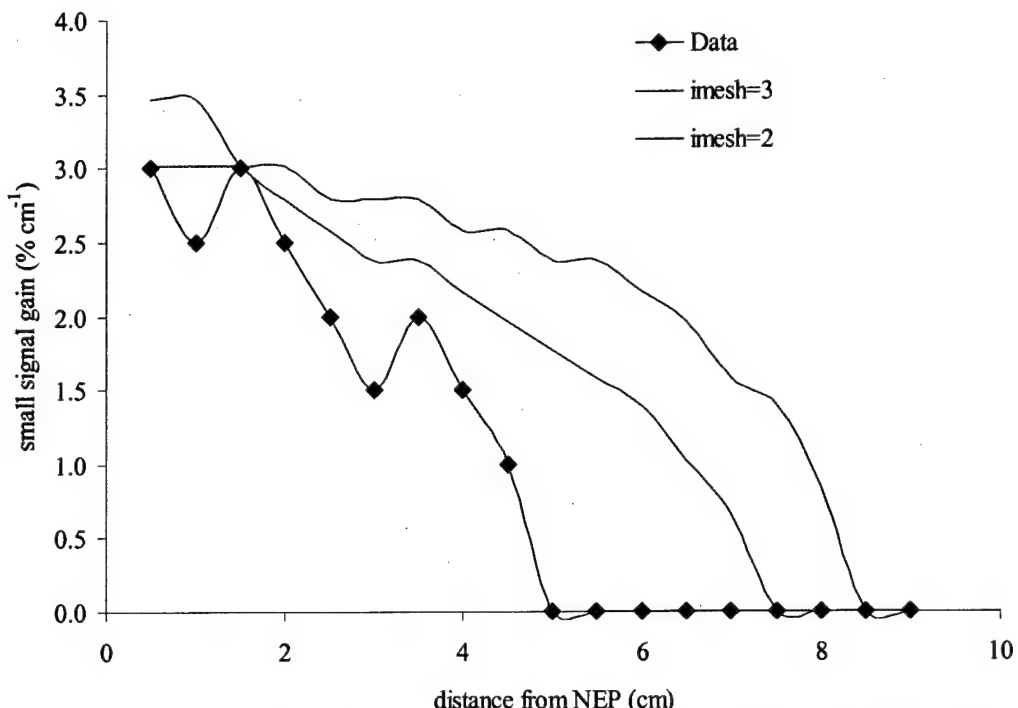


**Figure 5.44** Measured and predicted locations of peak gain shown in Figure 5.42 for the ( $F_2=2$ ,  $H_2=10$ ) flow conditions.

in Figure 5.42. The location of the maximum peak gain is also shifted slightly closer to the NEP. Changing from the  $\text{imesh}=2$  to  $\text{imesh}=3$  injection scheme also moves the maximum centerline gain closer to the NEP and shifts the location of the peak gain closer to the vertical centerline for 2 cm beyond the NEP. All of these changes improve the agreement of measured gain and that predicted by the model.

Figures 5.45 and 5.46 show vertically-averaged gain and F atom utilization, respectively, for the two  $\text{imesh}$  modeling cases, the premix case and an “optimized” injection case. The optimized injection case will be discussed below. The averaging in Figure 5.45 was performed over the entire vertical height of the laser cavity (i.e.,  $\pm 1.4$  cm from the vertical centerline). Since this averaging includes the base purge region which the predictions show has little or no excited HF, the predicted average gain is significantly lower than the predicted peak gain. As expected the  $\text{imesh}=3$  case shows an

increase in F atom utilization and average gain over the imesh=2 case. The increased mixing provided by the imesh=3 injection scheme moves the location of the maximum average gain closer to the NEP. At their respective maximum average gain locations as indicated by the arrows on Figure 5.46, the imesh=2 and imesh=3 cases have F atom utilizations of 39% and 44%, respectively, resulting in a 28% increase in maximum average gain from the imesh=2 to imesh=3 case. The higher rate of F atom utilization appears to occur within 2.0 cm of the NEP. This is because the small region of F atom flow between the H<sub>2</sub> jet and the upper surface of laser cavity is consumed very quickly. This leads to the conclusion that further increases in F atom utilization and average gain are possible by changing the injection scheme to include more F atoms between the H<sub>2</sub> jet and the upper surface of the laser cavity. Figure 5.47 shows initial concentration of F atom, H<sub>2</sub> and HF( $\nu=2$ ) for an “optimized” injection scheme that places the H<sub>2</sub> jet at the center of the nozzle half plane with equal F atom flows on either side of the jet. The resulting F atom utilization and averaged gain for this optimized injection scheme are included in Figures 5.45 and 5.46. The maximum average gain increases 28% over the imesh=3 case to 0.089% cm<sup>-1</sup> while the F atom utilization, also at the respective maximum average gain location, increases from 44% to 65%. Increasing the injection angle of the H<sub>2</sub> jet with respect to the nozzle wall might attain an injection scheme such as this. This would have a dual effect of increasing the amount of axial vorticity while directing the jet closer to the vertical centerline.

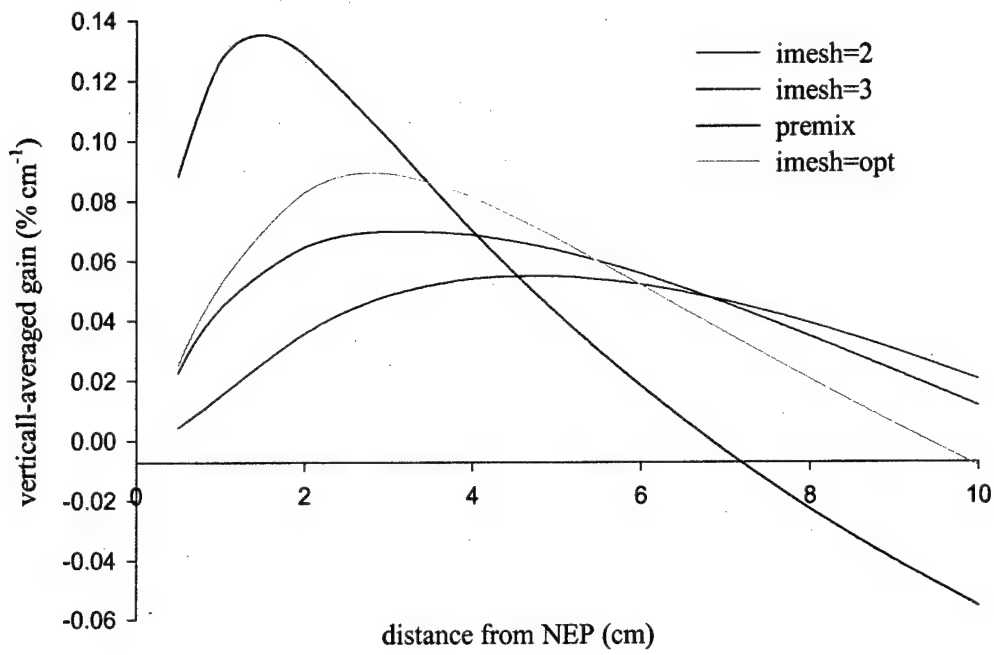


**Figure 5.45** Predicted gain averaged over the entire vertical height of the laser cavity at each streamwise location for the ( $F_2=2$ ,  $H_2=10$ ) flow conditions.

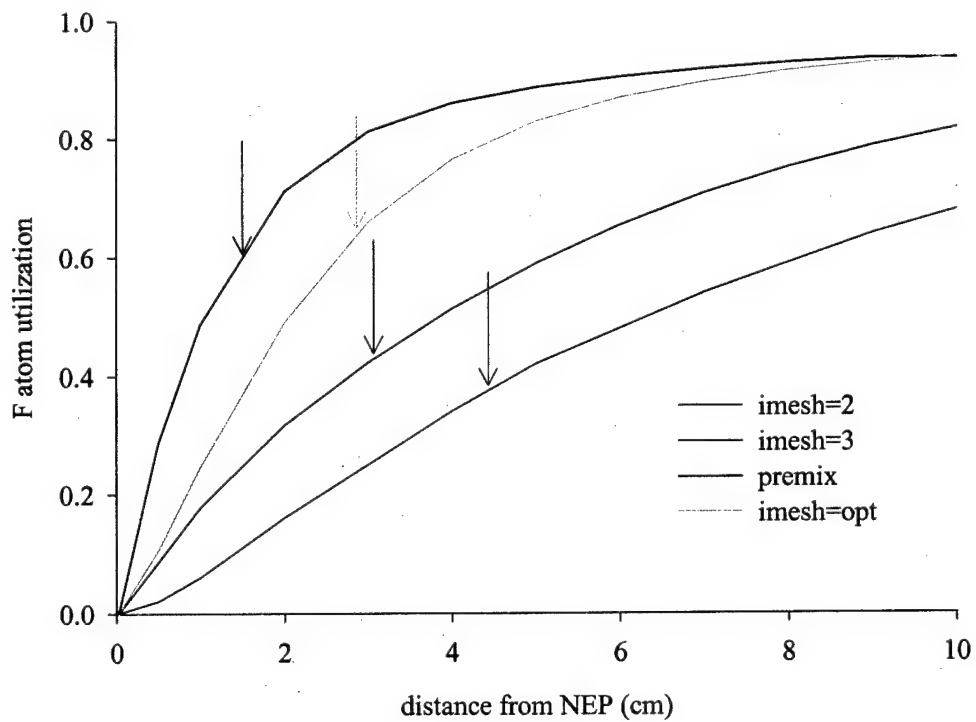


**Figure 5.46** Predicted F atom utilization for the ( $F_2=2$ ,  $H_2=10$ ) flow conditions. Arrows are at the locations of maximum vertically-averaged gain in Figure 5.45.

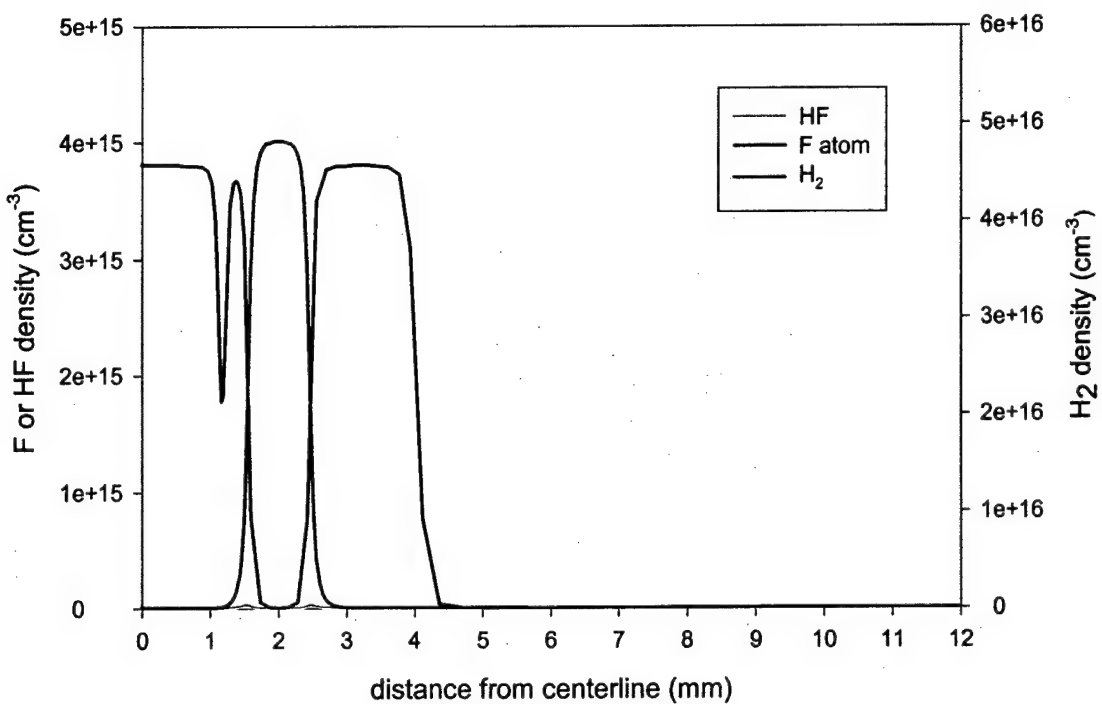


**Figure 5.47** Predicted optimized injection scheme concentration profiles 0.025 cm downstream of NEP for ( $F_2=2$ ,  $H_2=10$ ) flow conditions.

#### 5.4.4 Mixing Model Sensitivity to Kinetics

The peak gain for the imesh=3 predictions follow the trends of the data fairly well as shown in Figure 5.43. However, the maximum predicted gain is 58% larger than the measured value. 2-D turbulence and large scale vortex structure modeling were shown in Sections 5.4.2 and 5.4.3 to be effective at spreading the gain in the vertical direction resulting in increases in average gain but to have relatively small effects on the maximum peak gain. Changing the mixing parameters within the model will not significantly lower the predicted peak gain without drastically changing the vertical gain profiles so that they no longer match the data. The insensitivity of the peak gain to the flow field hydrodynamics indicates that it must instead be dominated by chemical kinetics. To

resolve the discrepancies between measured and predicted peak gain the uncertainties in the rates of reaction must be addressed.

The results of Section 5.4.1 indicate that the kinetics of the HF laser system, under the conditions investigated here, are dominated by the cold pumping reaction and V-V energy transfer between vibrationally-excited HF molecules. The rate of reaction for these second-order reactions was defined in Section 2.2 as:

$$R = -\frac{d[A]}{dt} = -\frac{d[B]}{dt} = \frac{d[C]}{dt} = \frac{d[D]}{dt} = k[A][B]$$

Under ideal gas assumptions, the species concentrations can be defined in terms of flow properties to give the rate of reaction as:

$$R = k[A][B] = k(T)\dot{n}_A\dot{n}_B \left( \frac{P A_V}{R T \dot{n}_{tot}} \right)^2 \quad (5.2)$$

where  $\dot{n}_A$ ,  $\dot{n}_B$  and  $\dot{n}_{tot}$  are the molar flow rates of species A and B and the total molar flow rate, respectively.  $P$  and  $T$  are the local static pressure and temperature and  $A_V$  is Avogadro's number. The rate of reaction is therefore susceptible to errors in pressure, temperature, molar flow rate and reaction rate constant. The following sections investigate the effects of changing these four input parameters in the model in an effort to isolate the main contributors to the disagreement between predictions and data. In some instances the parameters are intentionally varied beyond the recommended error bands in order to exaggerate the influence on the model predictions. Unless otherwise noted, the following predictions were made for the ( $F_2=2$ ,  $H_2=10$ ) flow conditions, the turbulence model active with 1% initial turbulence intensity for all flow streams and the same  $imesh=3$  injection scheme used in Section 5.4.3.

**a. Pressure and Temperature** Because of the dependence of the rate of reaction on the square of pressure and inverse of the square of temperature in Equation (5.2), small changes in pressure and temperature can have large effects on the rate of reaction. Transducers at pressure taps in the laser cavity wall directly measure the pressure with an error of  $<1\%$ . However, if the nozzle is not perfectly expanded, oblique shocks and expansion fans will form and create regions in the flow that are not at the ambient wall pressure. Lowering the pressure for a given molar flow decreases the reactant concentrations thereby lowering the rate of reaction. This spreads the gain over a larger area in the downstream direction and lowers the maximum peak gain. Decreasing the pressure also increases the flow velocity, which further spreads the gain in the downstream direction. Figures 5.48 and 5.49 show the centerline gain and peak gain, respectively, for cavity pressures of 2.5 torr, 2.0 torr and 1.5 torr. The nominal cavity pressure measured 2.0 cm downstream of the NEP for these flow conditions was 2.5 torr. A substantial error ( $\sim 40\%$ ) in cavity pressure could lower the predicted peak and centerline gains down to the level of the measurements but not without drastically changing the streamwise gain distribution. Therefore, an error in cavity pressure is not likely to be the major cause of the discrepancy between the predicted and measured gain.

Raising the temperature will affect the species concentrations and flow velocity in the same manner as lowering the pressure with similar results on the maximum peak gain. The temperature dependence of the reaction rate constants adds an additional effect. The  $e^{-1/T}$  temperature dependence means that the cold pumping reaction rate constant will increase as the temperature increases. The rate constant for the V-V energy transfer between HF molecules varies as  $T^{-1}$  and therefore decreases with increasing

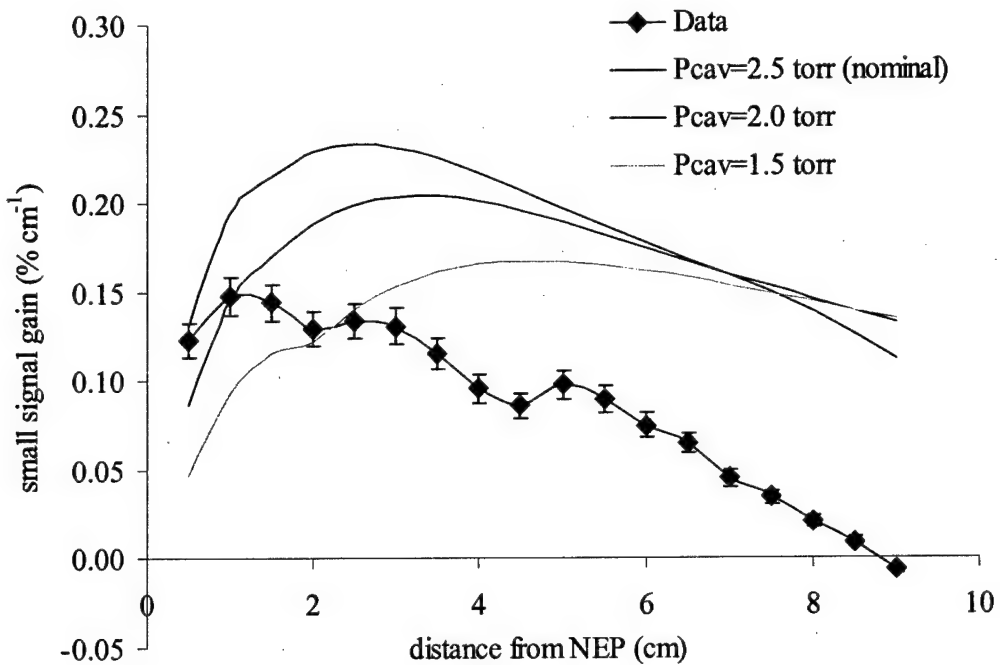


**Figure 5.48** Measured and predicted peak gain at different cavity pressures for the ( $F_2=2$ ,  $H_2=10$ ) flow conditions. Error bars represent 6% bias and  $0.002\% \text{ cm}^{-1}$  precision uncertainties.

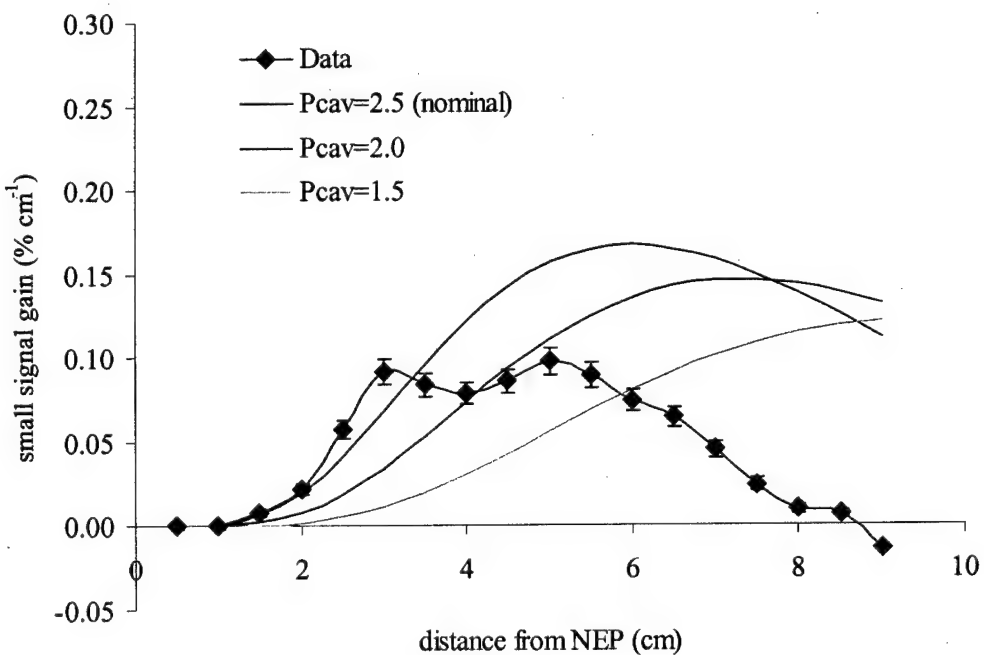


**Figure 5.49** Measured and predicted centerline gain at different cavity pressures for the ( $F_2=2$ ,  $H_2=10$ ) flow conditions. Error bars represent 6% bias and  $0.002\% \text{ cm}^{-1}$  precision uncertainties.

temperature. Therefore by increasing the flow temperature the cold pumping reaction rate increases and the V-V energy transfer rate slows, thus improving the performance of the laser system. The temperature is determined from the lineshape of the probe gain measurement with an estimated uncertainty of  $\pm 50$  K. The only adjustable temperature input parameter in the code is the total temperature at the injection point inside the nozzle. Figures 5.50 and 5.51 show the effect on the predicted peak and centerline gain, respectively, of raising and lowering this temperature by  $\pm 20\%$ . Changing the temperature input to the code has a larger effect on the flow velocity than on the cavity temperature. Lowering the temperature input increases the velocity spreading the gain in the downstream direction and lowers the maximum peak gain.

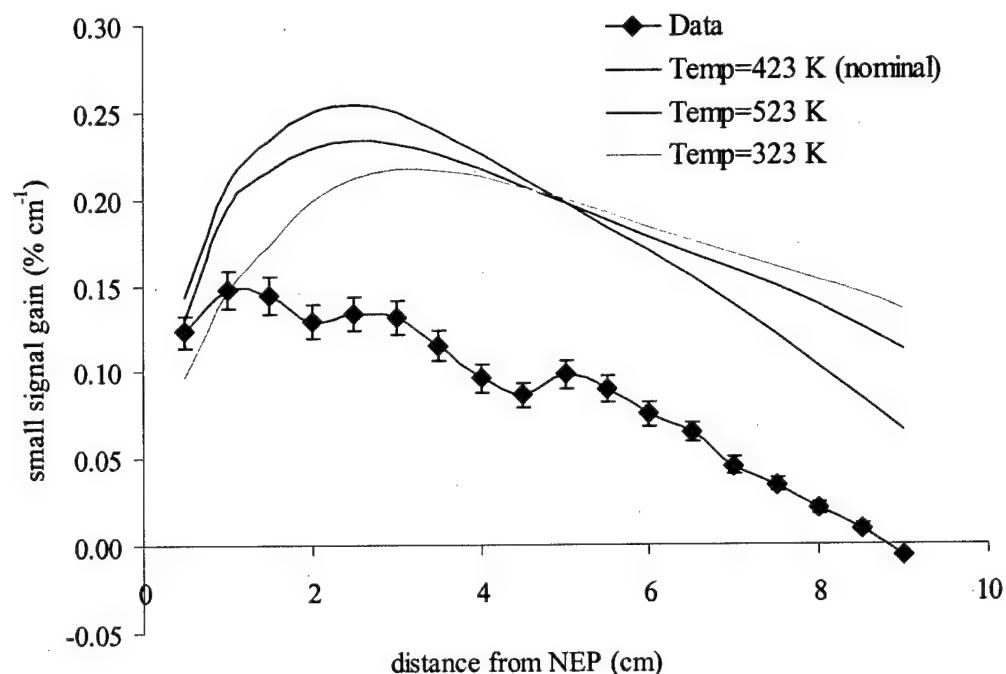


**Figure 5.50** Measured and predicted peak gain at different cavity temperatures for the ( $F_2=2$ ,  $H_2=10$ ) flow conditions. Error bars represent 6% bias and  $0.002\text{ % cm}^{-1}$  precision uncertainties.

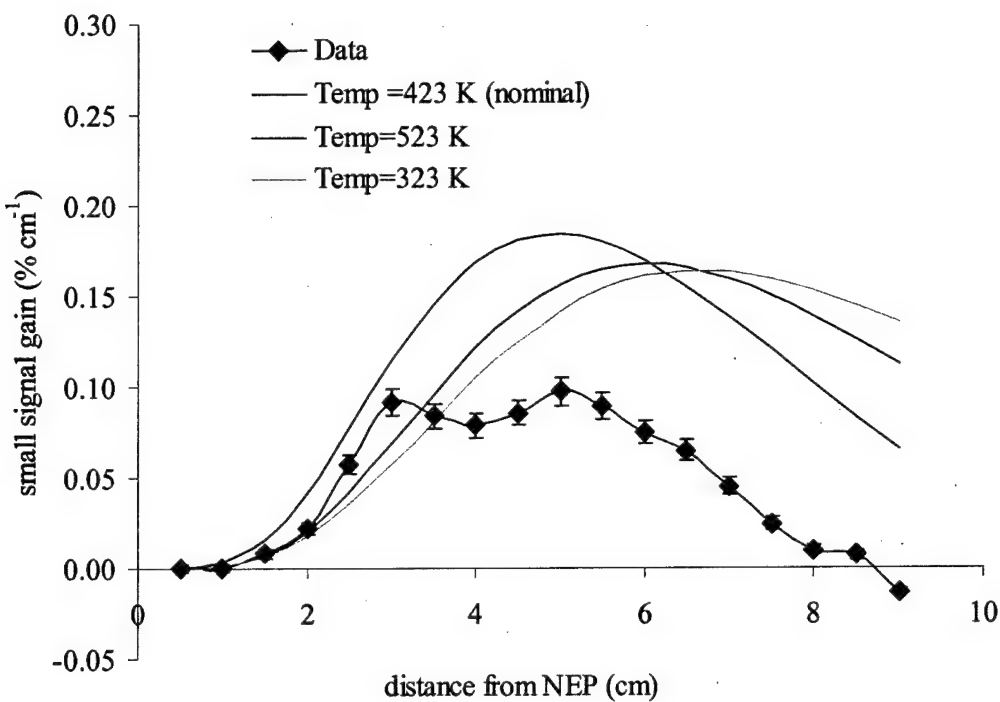


**Figure 5.51** Measured and predicted centerline gain at different cavity temperatures for the ( $F_2=2$ ,  $H_2=10$ ) flow conditions. Error bars represent 6% bias and  $0.002\text{ % cm}^{-1}$  precision uncertainties.

Raising the temperature input decreases the velocity, compresses the gain in the downstream direction, and raises the maximum peak gain. Since the temperature input to the code would have to be reduced several hundred degrees below the measured temperature to bring the magnitude of predicted and measured gain into agreement, it is not likely this is a significant contributor to the gain discrepancy.

**b. Cold Pumping Rate Constant** The cold pumping reaction is one of the most studied chemical reactions both theoretically and experimentally. As a result the error bands on the rate constant are relatively small, varying between  $\pm 15\%$  to  $\pm 30\%$  over

the temperature range from 200K to 700K. Figures 5.52 and 5.53 show the effect of a reduced cold pumping reaction rate constant on the peak gain and centerline gain, respectively, for the ( $F_2=2$ ,  $H_2=10$ ) flow conditions. Decreasing the cold pumping reaction rate lowers the maximum peak gain and the peak gain near the NEP. This also pushes the locations of the maximum peak gain and the onset of gain at the vertical centerline further downstream. Lowering the maximum peak gain is the only of these trends that improves agreement with the data. This agreement, however, comes by stretching the gain in the downstream, which degrades the agreement between the shape of the predicted and measured peak and centerline gain curves. Increasing the rate constant will obviously increase the maximum peak gain making the disagreement between the predictions and measurement larger.

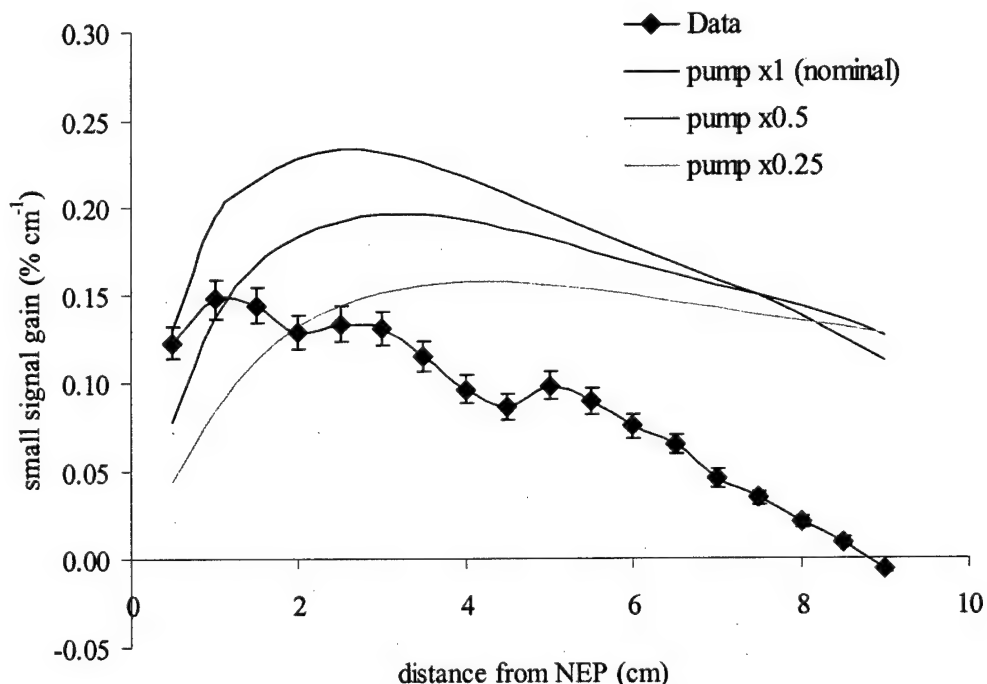


**Figure 5.52** Measured and predicted peak gain at different cold pumping reaction rate constants for the ( $F_2=2$ ,  $H_2=10$ ) flow conditions. Error bars represent 6% bias and 0.002  $\% \text{ cm}^{-1}$  precision uncertainties.

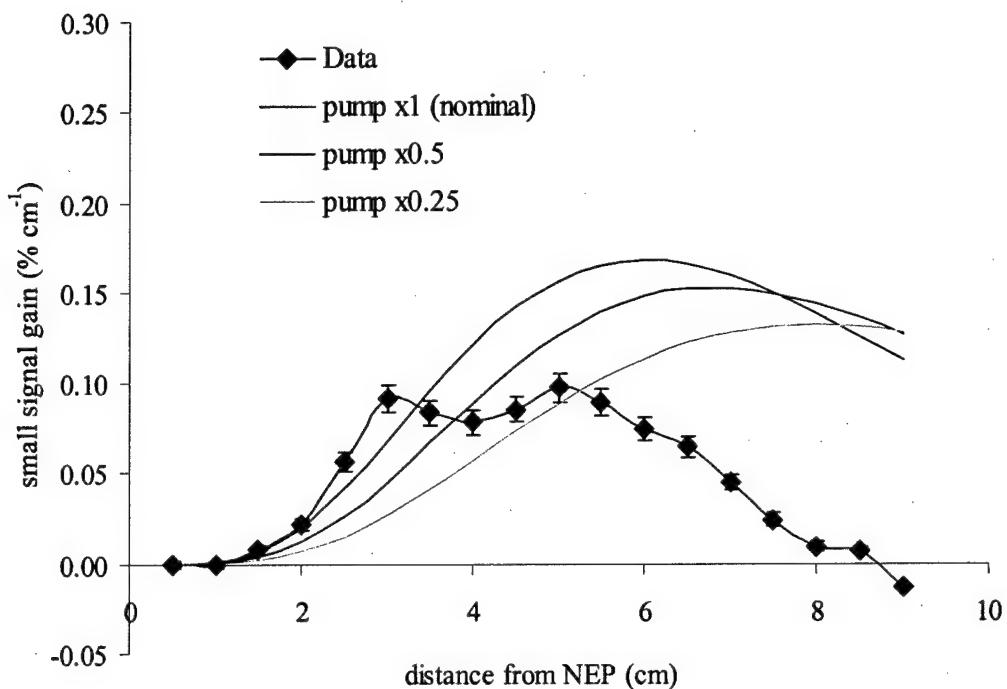


**Figure 5.53** Measured and predicted centerline gain at different cold pumping reaction rate constants for the ( $F_2=2$ ,  $H_2=10$ ) flow conditions. Error bars represent 6% bias and  $0.002\text{ % cm}^{-1}$  precision uncertainties.

**c. Molar Flow Rates** The predicted gain will be most sensitive to errors in F atom flow rate. The F atom flow rate was measured by a titration experiment (described in Section 5.1) with an uncertainty of  $\pm 20\%$ . Figures 5.54 and 5.55 show the effect of lowering the F atom flow rate on the peak and centerline gain, respectively. Reducing the F atom flow rate has the same effect as lowering the cold pumping rate constant. The rate of reaction decreases lowering the maximum peak gain by spreading the gain in the downstream direction. Clearly this is not the trend to bring the model into better agreement with the data.

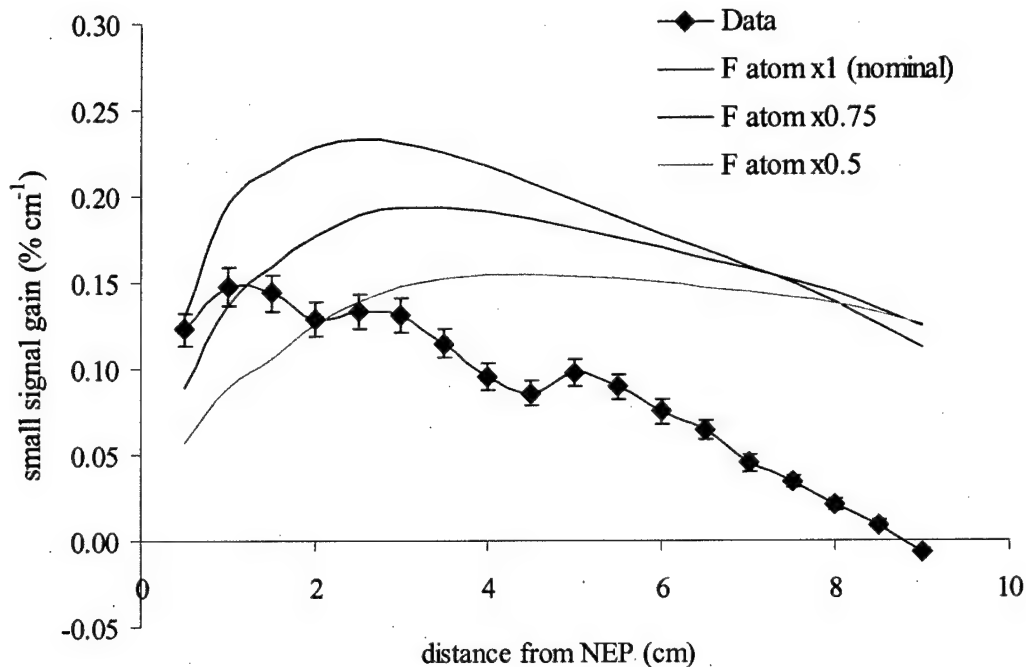


**Figure 5.54** Measured and predicted peak gain at different F atom flow rates for the ( $F_2=2$ ,  $H_2=10$ ) flow conditions. Error bars represent 6% bias and  $0.002\% \text{ cm}^{-1}$  precision uncertainties.

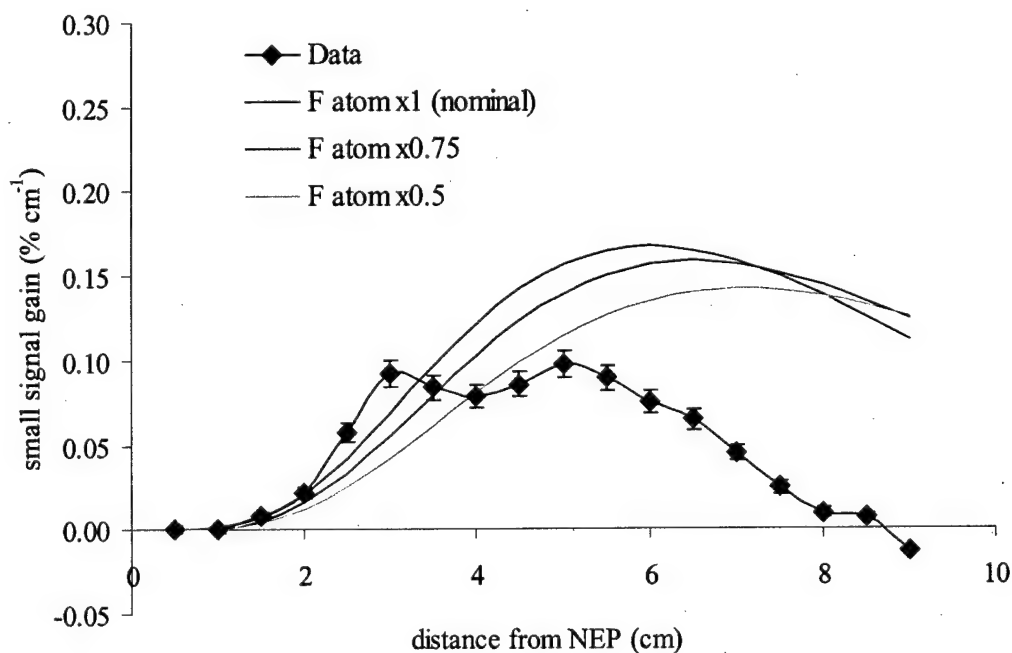
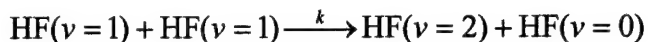


**Figure 5.55** Measured and predicted centerline gain at different F atom flow rates for the ( $F_2=2$ ,  $H_2=10$ ) flow conditions. Error bars represent 6% bias and  $0.002\% \text{ cm}^{-1}$  precision uncertainties.

**d. V-V Energy Transfer** The only rate constant measured for V-V energy transfer between vibrationally excited HF molecules is for:



The rate constants between other vibrational states are then established through theoretical interpolation. The resulting rate constants are reported in the literature without corresponding error bands indicating a high level of uncertainty. Figures 5.56 and 5.56 show the effects of increasing these V-V energy transfer rate constants on the peak and centerline gain, respectively. The rate constants for all V-V reactions were changed by the same factor. Increasing these rates lowers the maximum peak gain and moves the location of the peak gain closer to the NEP in better agreement with the data.

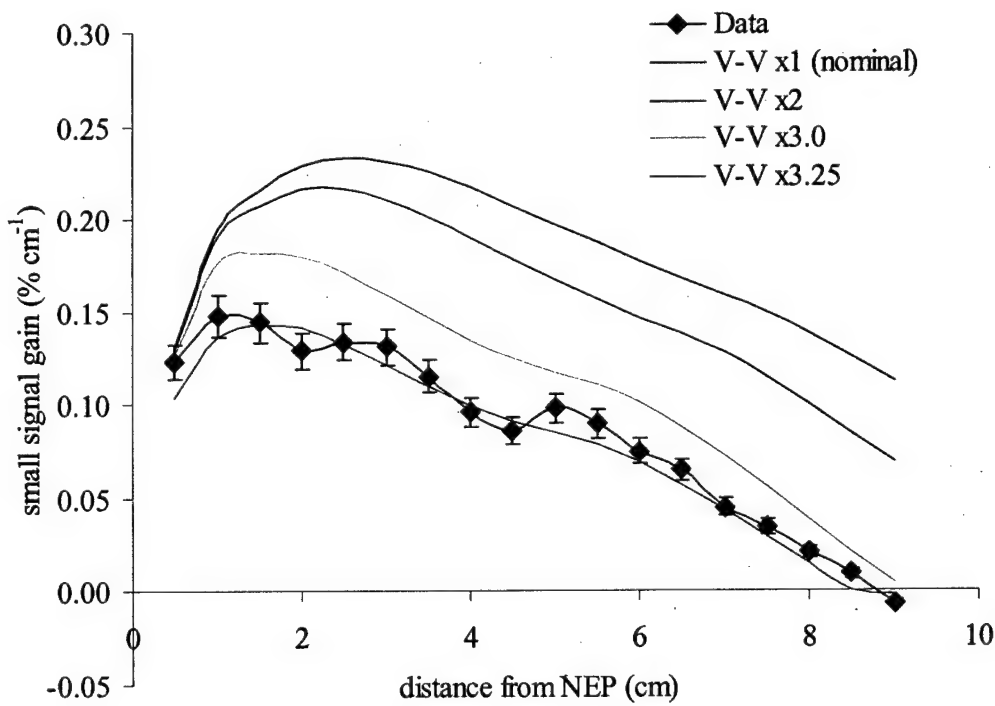


**Figure 5.56** Measured and predicted peak gain for different HF V-V rate constants for the ( $F_2=2$ ,  $H_2=10$ ) flow conditions. Error bars represent 6% bias and  $0.002\text{ % cm}^{-1}$  precision uncertainties.

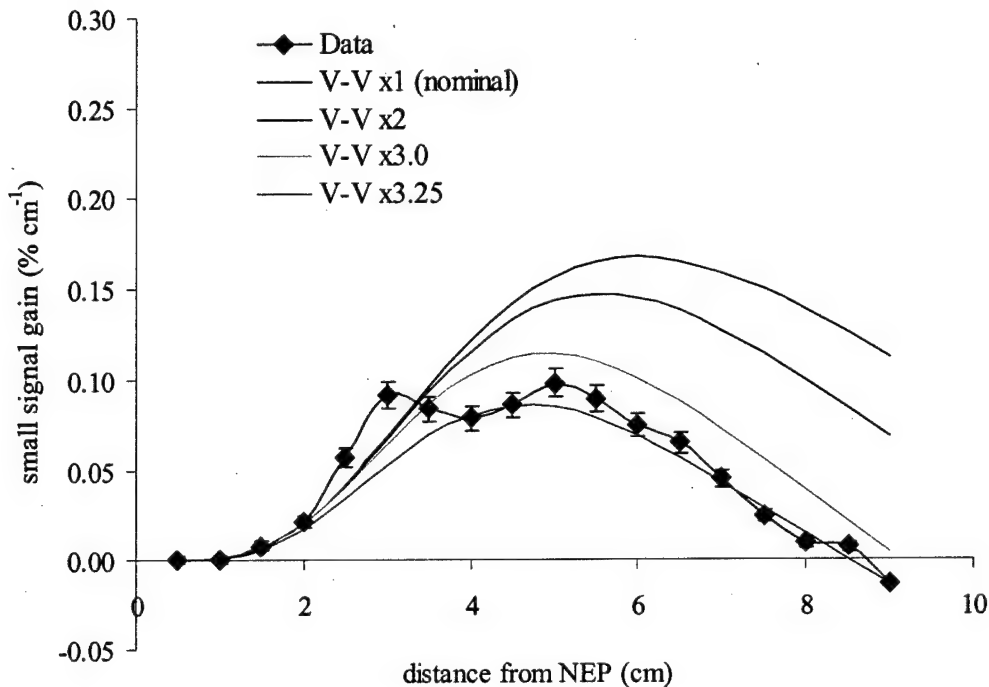


**Figure 5.57** Measured and predicted centerline gain for different HF V-V rate constants for the ( $F_2=2$ ,  $H_2=10$ ) flow conditions. Error bars represent 6% bias and  $0.002\text{ % cm}^{-1}$  precision uncertainties.

The location of the onset of gain at the vertical centerline remains unchanged while the peak centerline gain is reduced and moved closer to the NEP. All of these trends are in the direction to improve agreement between the predictions and the measured gain.

Figures 5.58, 5.59, 5.60 and 5.61 show vertical gain profiles for the ( $F_2=2$ ,  $H_2=10$ ) flow conditions at 0.5, 2.0, 4.0 and 6.0 cm downstream of the NEP, respectively. The predictions were made with the HF V-V energy transfer rates multiplied by a factor of 3.25, which gives excellent agreement at the peak and centerline locations. At the 0.5 cm and 2.0 cm downstream locations the increased V-V deactivation has brought the peak gain into very good agreement with the data. The centerline region, within  $\pm 3$  mm of the vertical centerline, is also in excellent agreement with the data for the 4 cm and 6 cm

downstream locations. However, these two predicted vertical profiles diverge from the data in the region closer to the wall. Starting at about 5 mm from the vertical centerline and moving toward the wall, the predicted gain increases while the measured gain decreases. This discrepancy is likely due to a coding deficiency that restricts the code from running with the proper boundary condition at the wall. Instead of the appropriate no-slip condition, a symmetry condition must be set in order to avoid numerical instabilities that cause the code to crash. This allows a higher velocity in the region near the wall allowing the  $HF(v)$  to travel further downstream before deactivation occurs. The absence of a wall in the computer model also eliminates the possibility of wall deactivation.

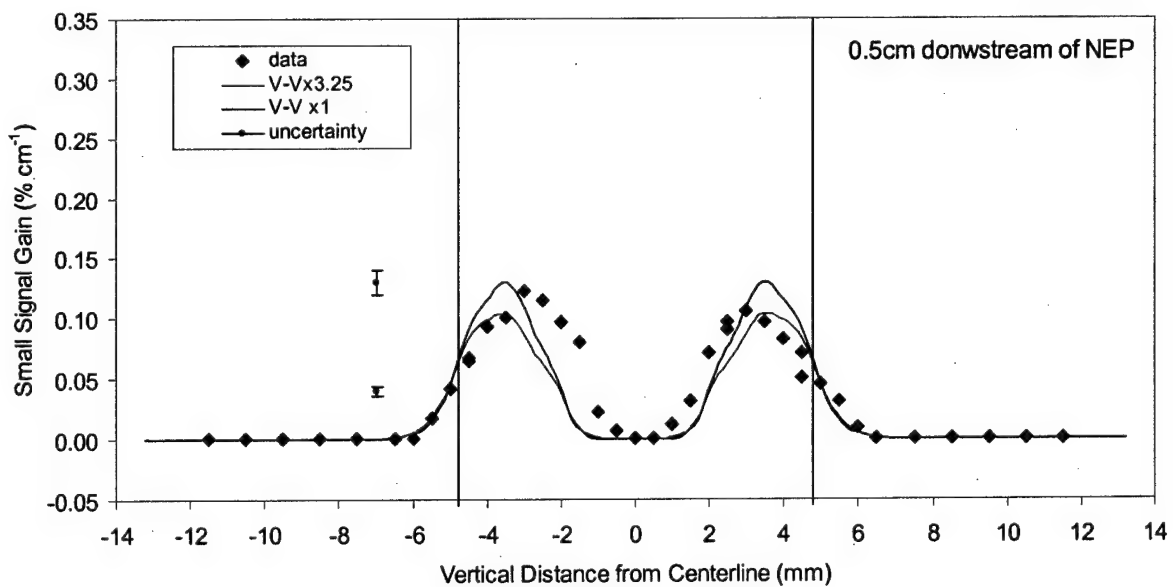


**Figure 5.58** Measured and predicted vertical gain profiles 0.5 cm downstream of NEP for the ( $F_2=2$ ,  $H_2=10$ ) flow conditions. Solid black vertical lines indicate the vertical height of the nozzle at the NEP. Error bars represent 6% bias and  $0.002\text{ % cm}^{-1}$  precision uncertainties.

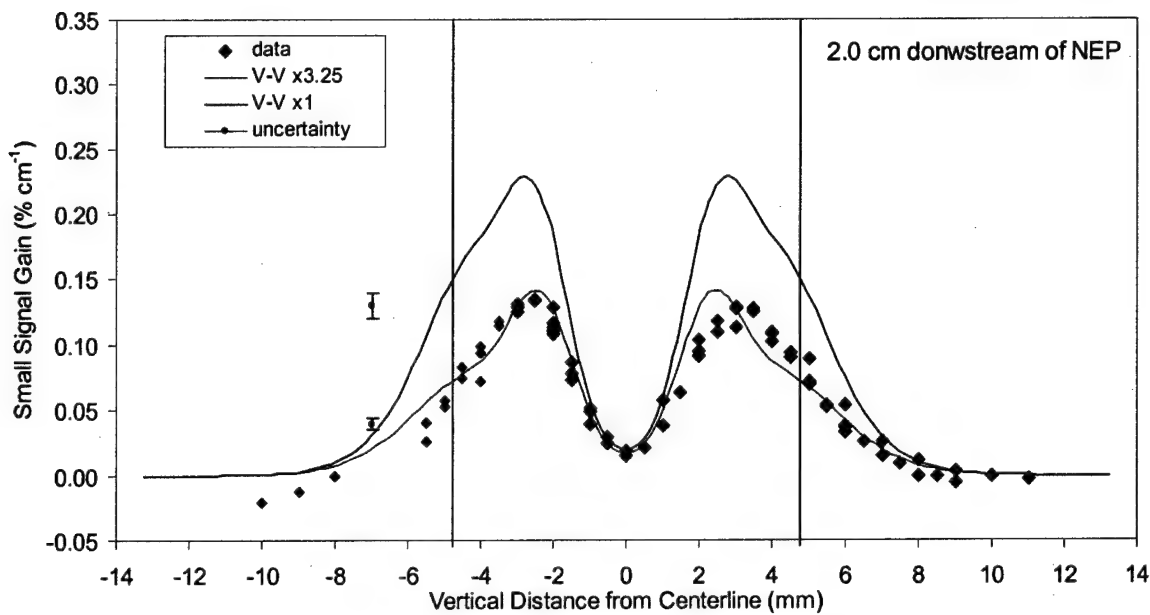


**Figure 5.59** Measured and predicted vertical gain profiles 2.0 cm downstream of NEP for the ( $F_2=2$ ,  $H_2=10$ ) flow conditions. Solid black vertical lines indicate the vertical height of the nozzle at the NEP. Error bars represent 6% bias and  $0.002 \text{ \% cm}^{-1}$  precision uncertainties.

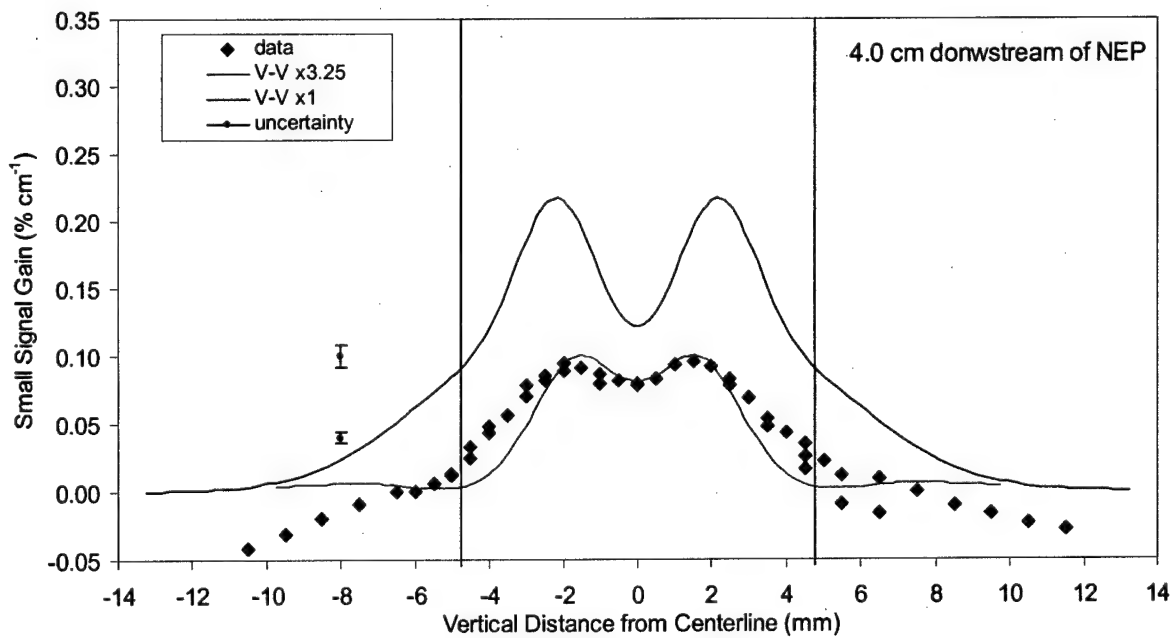


**Figure 5.60** Measured and predicted vertical gain profiles 4.0 cm downstream of NEP for the ( $F_2=2$ ,  $H_2=10$ ) flow conditions. Solid black vertical lines indicate the vertical height of the nozzle at the NEP. Error bars represent 6% bias and  $0.002 \text{ \% cm}^{-1}$  precision uncertainties.

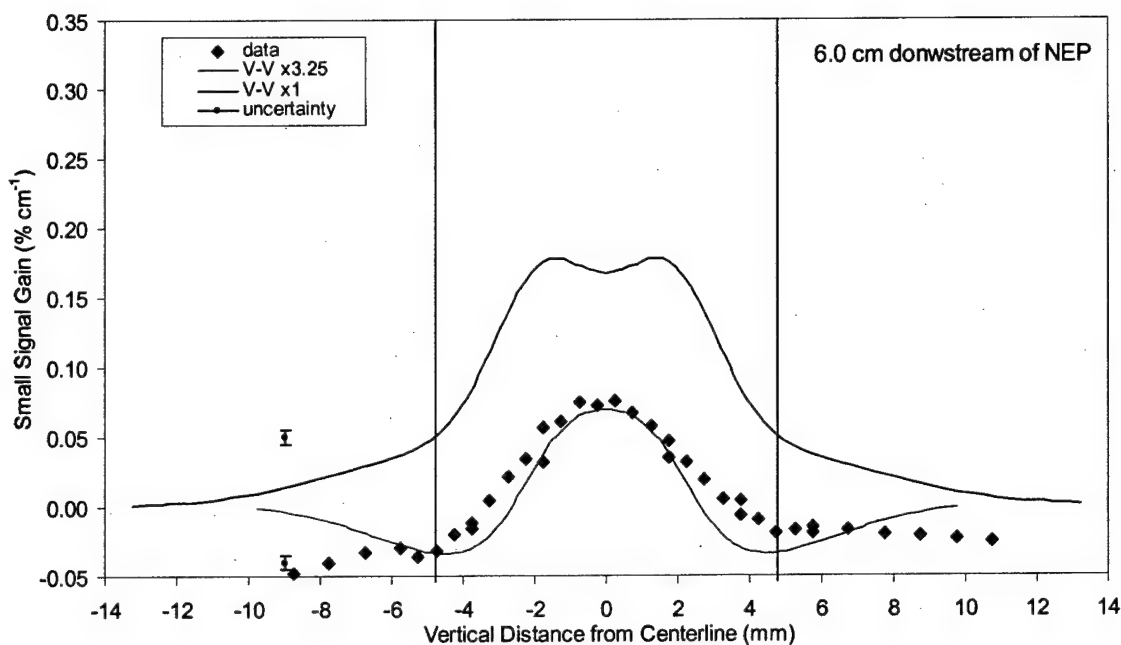


**Figure 5.61** Measured and predicted vertical gain profiles 6.0 cm downstream of NEP for the ( $F_2=2$ ,  $H_2=10$ ) flow conditions. Solid black vertical lines indicate the vertical height of the nozzle at the NEP. Error bars represent 6% bias and  $0.002\text{ \% cm}^{-1}$  precision uncertainties.

Figures 5.62, 5.63, 5.64 and 5.65 show vertical temperature profiles for the ( $F_2=2$ ,  $H_2=10$ ) flow conditions at 0.5, 2.0, 4.0 and 6.0 cm downstream of the NEP, respectively. The predictions in these figures were made with identical input parameters as the gain profiles shown in Figures 5.58 - 5.61. The model predicts the magnitude and shape of the temperature profiles very well at the 2.0, 4.0 and 6.0 cm downstream locations. At the 0.5 cm downstream location the model predicts the shape of the temperature very well but under predicts the magnitude of the temperature by about 50 K. The V-V energy transfer rate adjustment has only a minor effect on the predicted magnitude and shape of the temperature profiles.

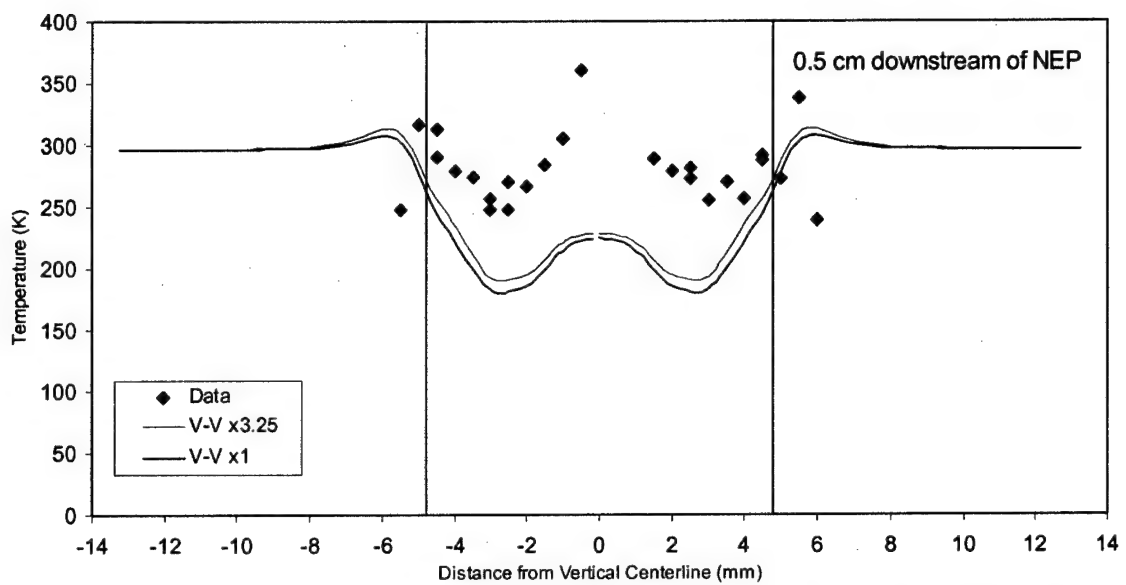


**Figure 5.62** Measured and predicted vertical temperature profiles 0.5 cm downstream of NEP for the ( $F_2=2$ ,  $H_2=10$ ) flow conditions. Solid black vertical lines indicate the vertical height of the nozzle at the NEP.

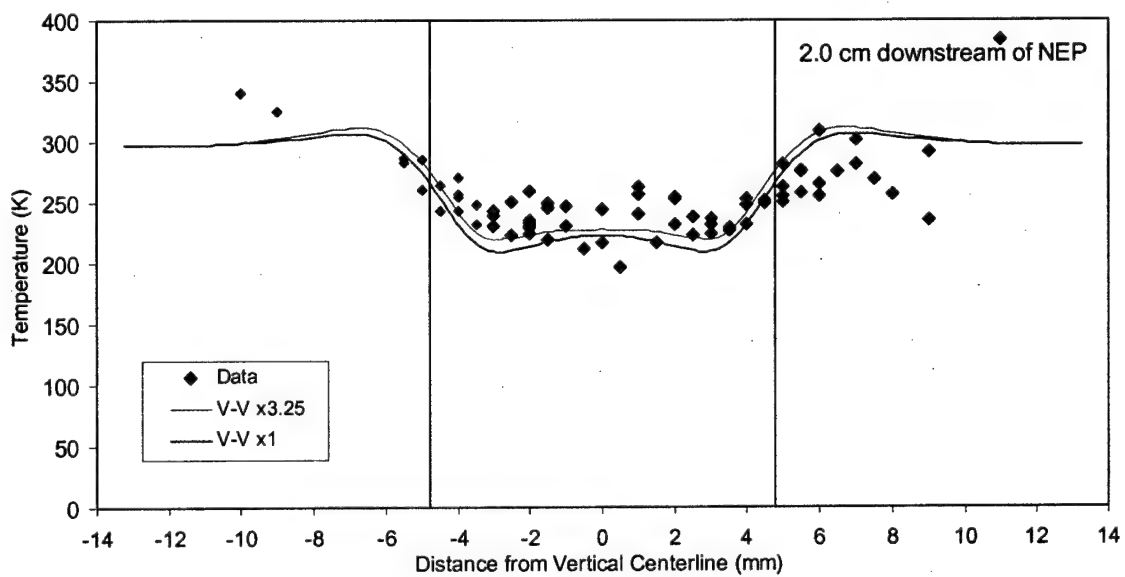


**Figure 5.63** Measured and predicted vertical temperature profiles 2.0 cm downstream of NEP for the ( $F_2=2$ ,  $H_2=10$ ) flow conditions. Solid black vertical lines indicate the vertical height of the nozzle at the NEP.

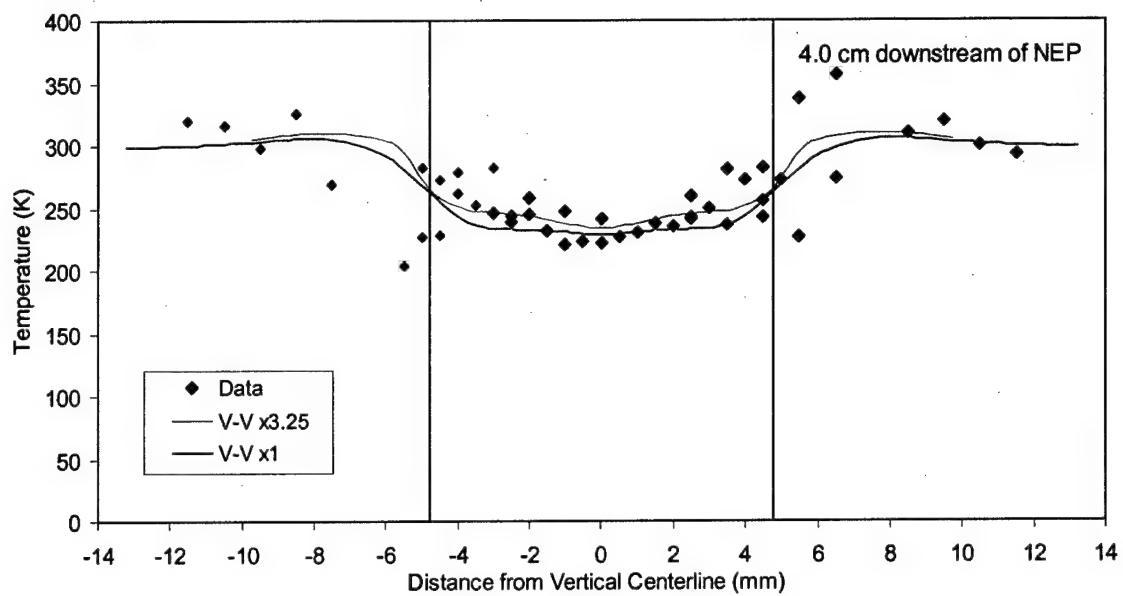


**Figure 5.64** Measured and predicted vertical temperature profiles 4.0 cm downstream of NEP for the ( $F_2=2$ ,  $H_2=10$ ) flow conditions. Solid black vertical lines indicate the vertical height of the nozzle at the NEP.

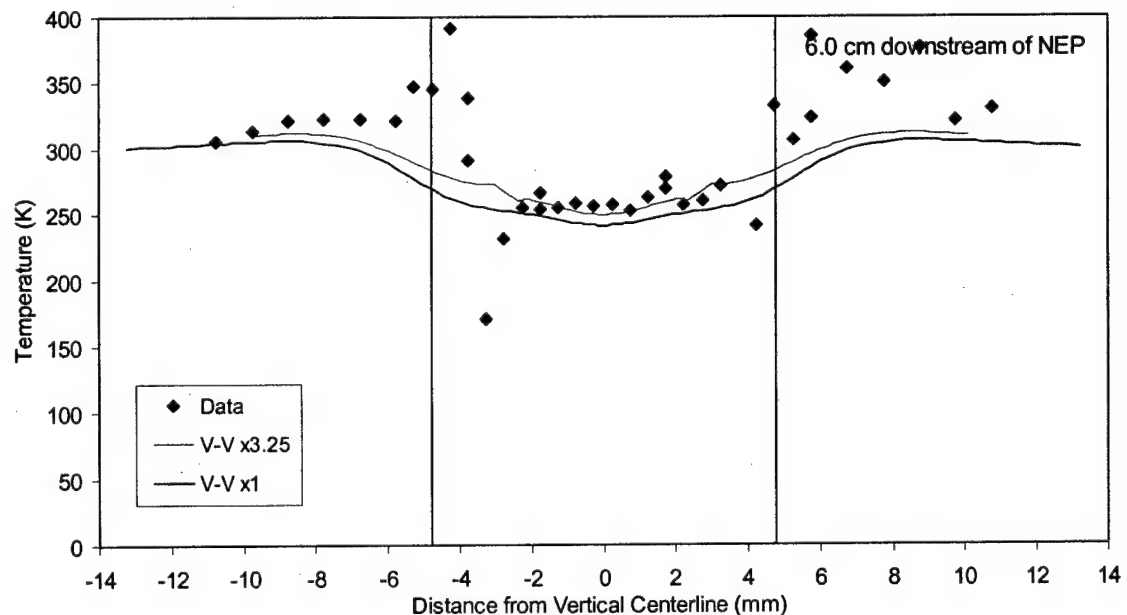


**Figure 5.65** Measured and predicted vertical temperature profiles 6.0 cm downstream of NEP for the ( $F_2=2$ ,  $H_2=10$ ) flow conditions. Solid black vertical lines indicate the vertical height of the nozzle at the NEP.

Figure 5.66 shows measured and predicted streamwise temperatures at their respective peak gain locations shown in Figure 5.67. As the flow moves downstream, the location of the peak gain moves toward the centerline for these flow conditions so the streamwise profiles shown in Figure 5.66 are not at a fixed vertical location. The model does however predict the location of the peak gain very well as shown in Figure 5.67. The measured and predicted temperatures in Figure 5.66 are therefore at the nearly the same vertical location at each downstream location. The model predicts the general streamwise trend of the temperature data, which increases by about 75 K from 0.5 to 9.0 cm downstream of the NEP, but it does not predict the large  $\pm 50$  K streamwise temperature oscillations. The overall temperature increase is presumably caused by heat release from the cold pumping reaction and heat transfer between the  $H_2$  and primary

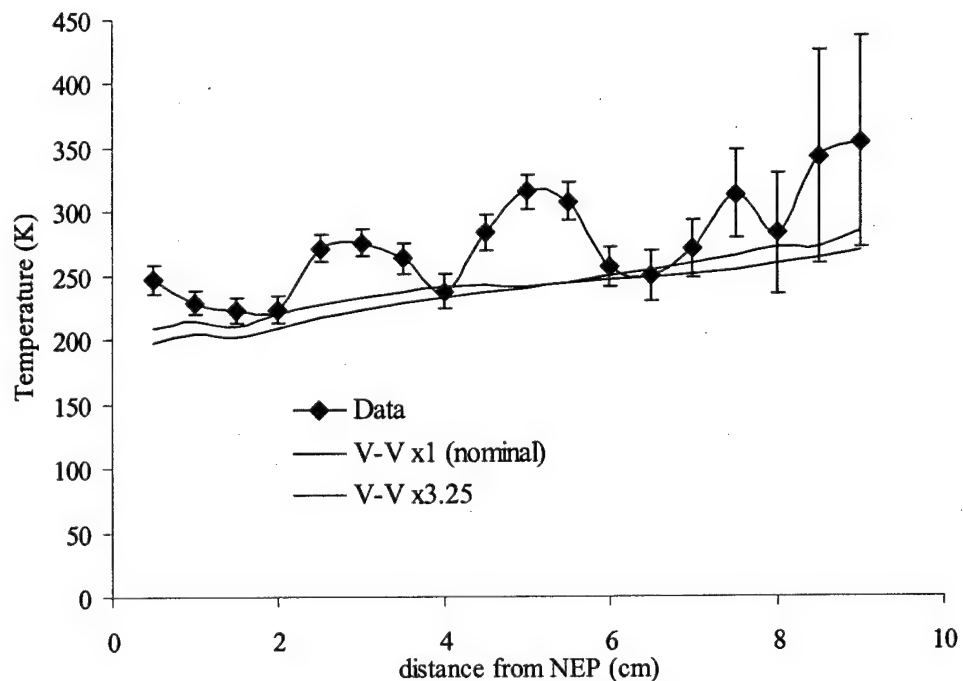


**Figure 5.66** Measured and predicted temperatures at peak gain locations for ( $F_2=2$ ,  $H_2=10$ ) flow conditions. Error bars represent the precision uncertainty of temperature measurement, which increases as gain decreases.

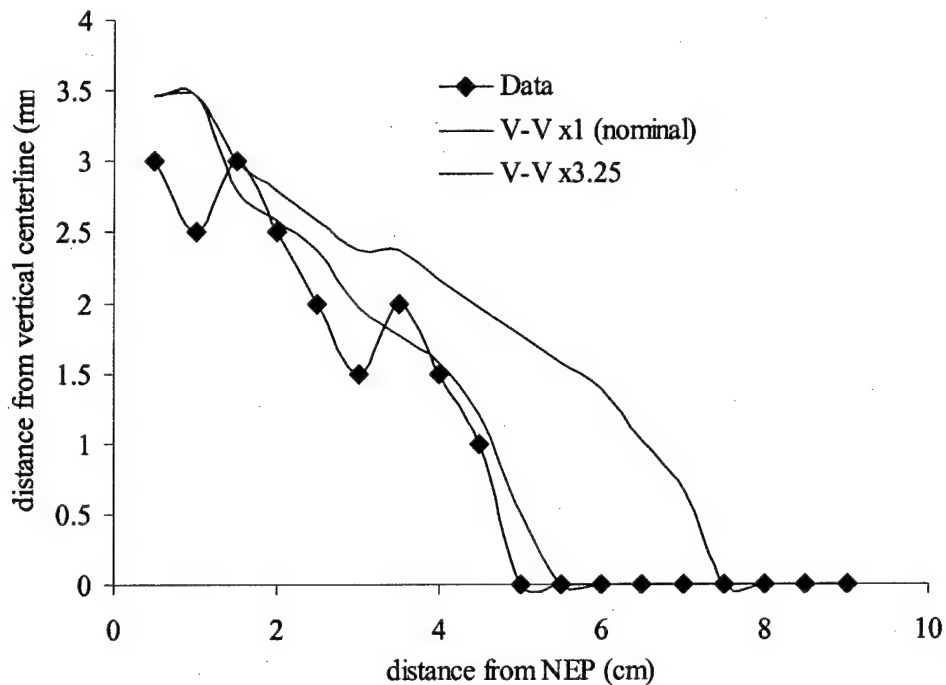


**Figure 5.67** Measured and predicted vertical locations of peak gain of Figure 5.56 for the ( $F_2=2$ ,  $H_2=10$ ) flow conditions.

flow streams. The cause of the temperature oscillations will be addressed in a subsequent section.

Figures 5.68 through 5.73 show the centerline gain and peak gain for the other three flow conditions listed in Table 5.2. These figures show very good agreement between predictions and measurements. The predictions were made with the same HF V-V energy transfer rate constant adjustment (V-V x3.25) used to attained good agreement between predictions and data for the ( $F_2=2$ ,  $H_2=10$ ) flow conditions and the same imesh=3 input parameters. The pressure measured at the first downstream wall pressure port for each flow condition was used as the cavity pressure input parameter. The total pressure and temperature at the injection point inside the nozzle were determined by running the code in the INOZ=1 mode for each flow condition. Description of the INOZ=1 computer option will be given in the following section.

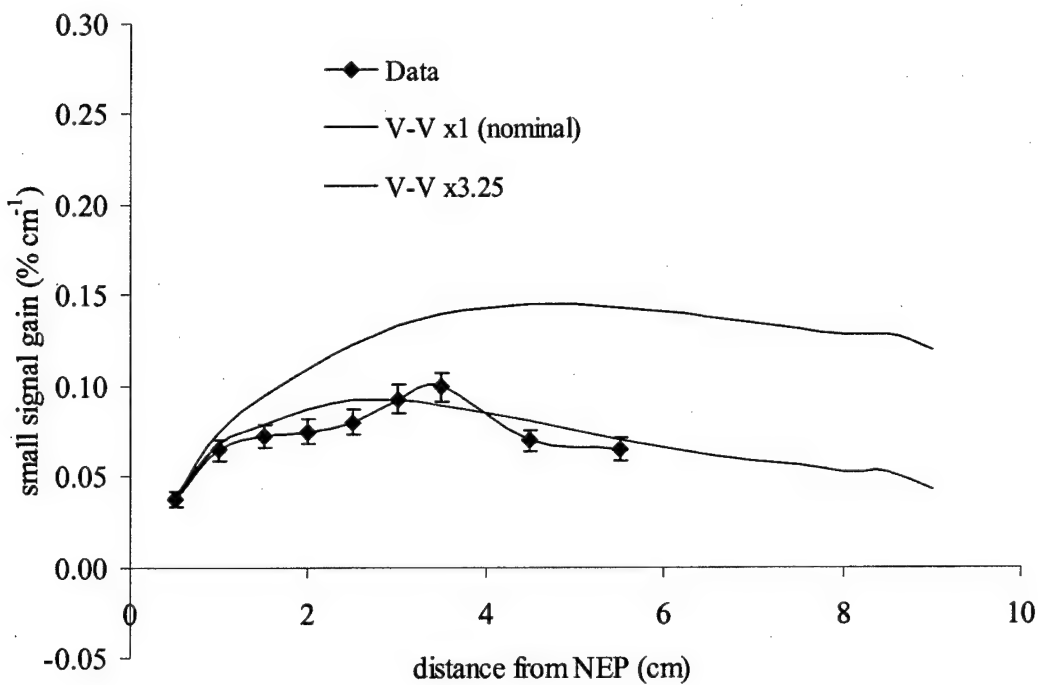


**Figure 5.68** Measured and predicted peak gain with V-V rate constant adjustment for the ( $F_2=1$ ,  $H_2=5$ ) flow conditions. Error bars represent 6% bias and  $0.002\text{ % cm}^{-1}$  precision uncertainties.

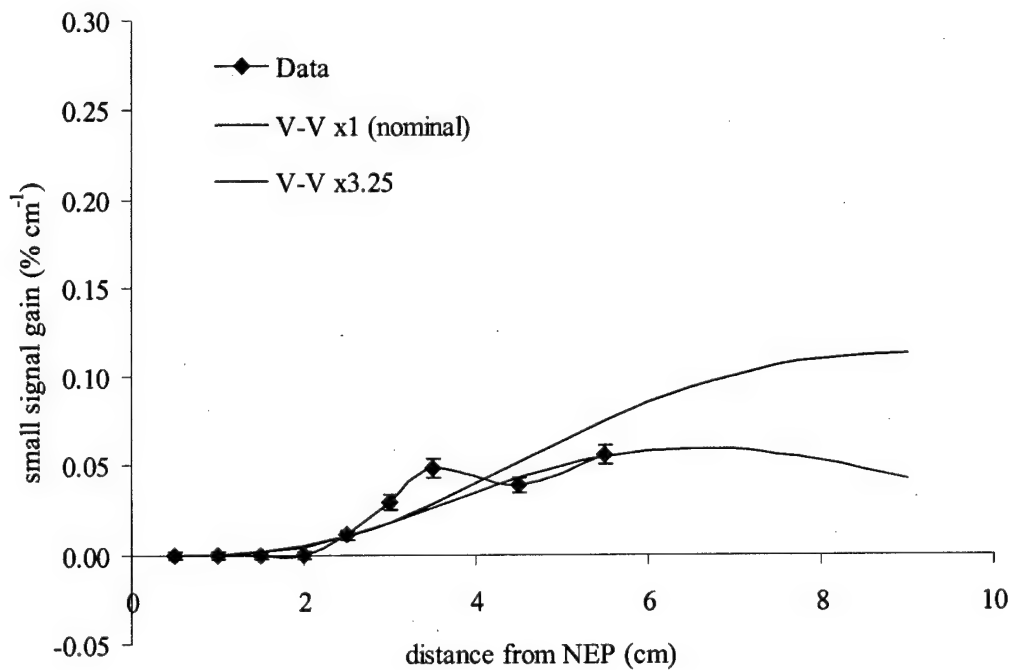


**Figure 5.69** Measured and predicted centerline gain with V-V rate constant adjustment for the ( $F_2=1$ ,  $H_2=5$ ) flow conditions. Error bars represent 6% bias and  $0.002\text{ % cm}^{-1}$  precision uncertainties.

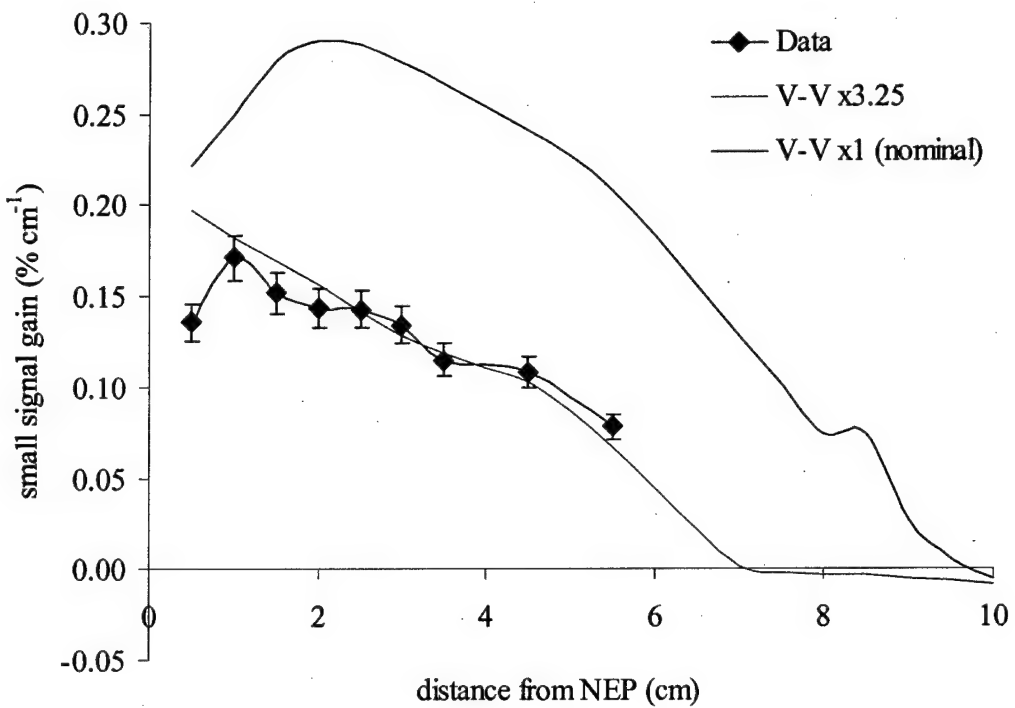


**Figure 5.70** Measured and predicted peak gain with V-V rate constant adjustment for the ( $F_2=2$ ,  $H_2=27$ ) flow conditions. Error bars represent 6% bias and  $0.002\text{ % cm}^{-1}$  precision uncertainties.

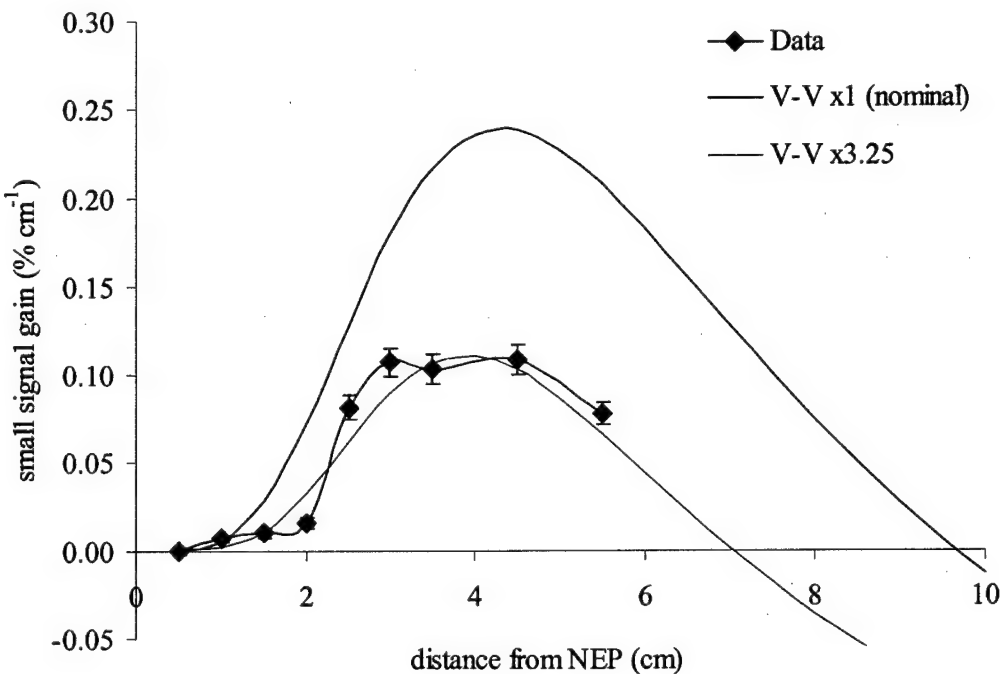


**Figure 5.71** Measured and predicted centerline gain with V-V rate constant adjustment for the ( $F_2=2$ ,  $H_2=27$ ) flow conditions. Error bars represent 6% bias and  $0.002\text{ % cm}^{-1}$  precision uncertainties.

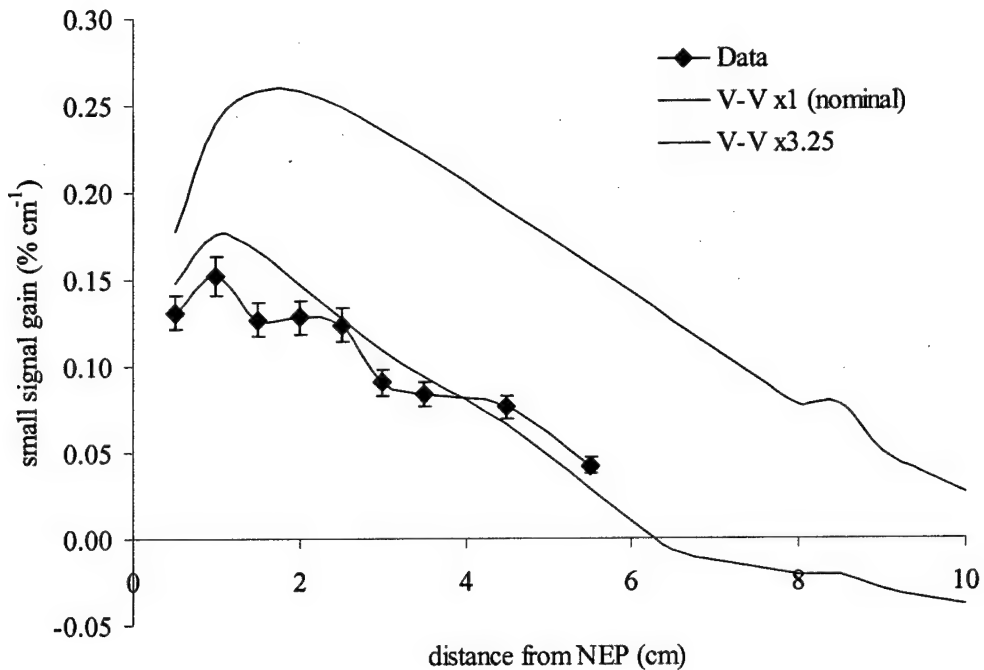


Figure 5.72 Measured and predicted peak gain with V-V rate constant adjustment for the ( $F_2=3$ ,  $H_2=10$ ) flow conditions. Error bars represent 6% bias and  $0.002\text{ % cm}^{-1}$  precision uncertainties.

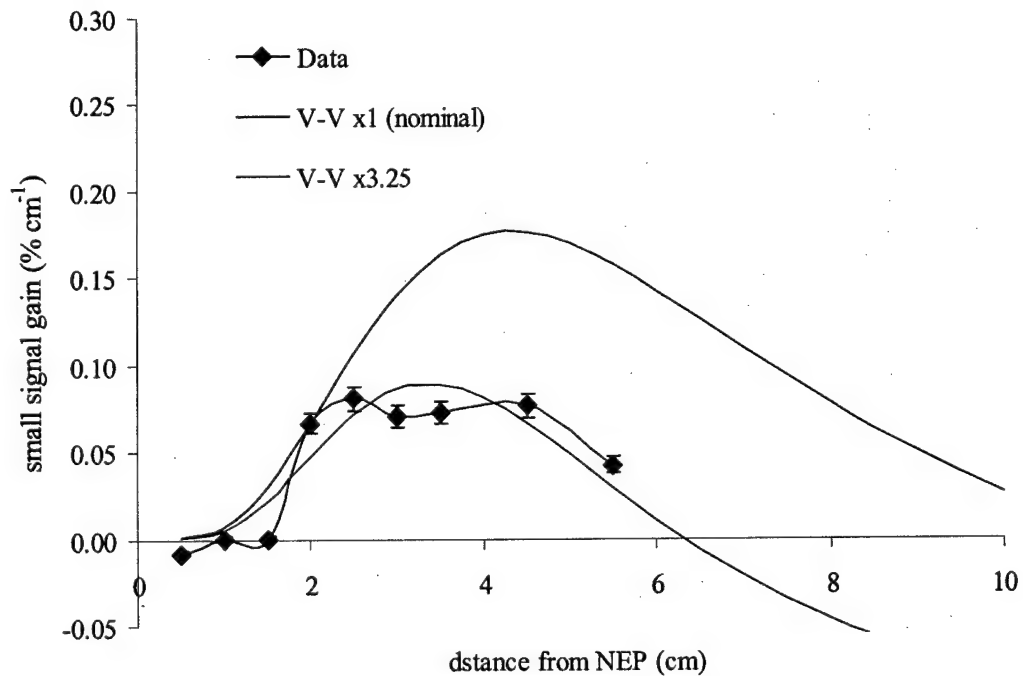
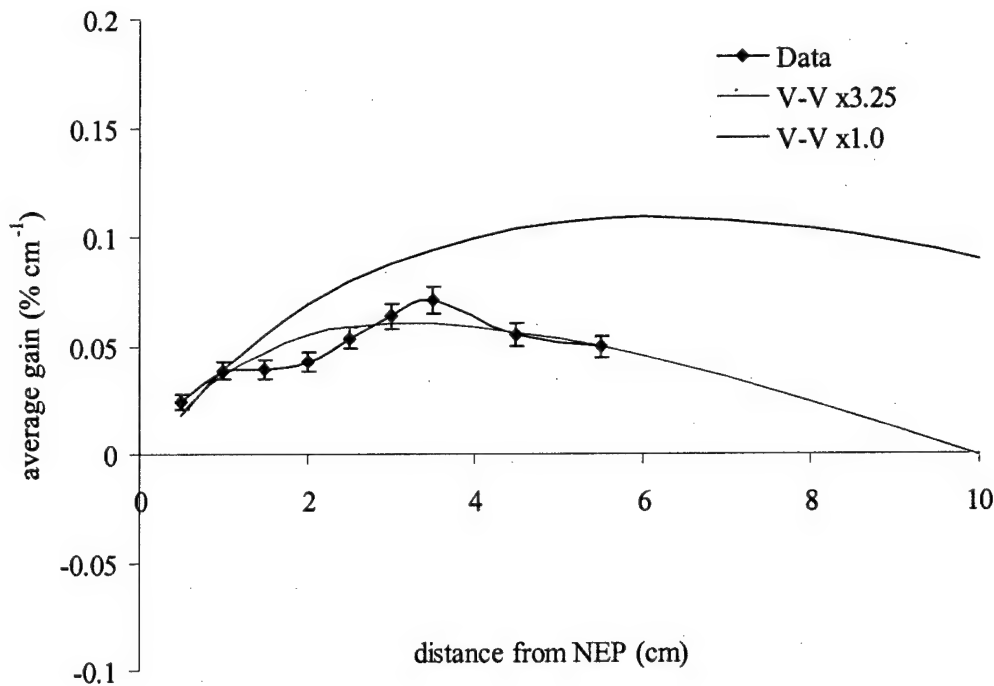


Figure 5.73 Measured and predicted centerline gain with V-V rate constant adjustment for the ( $F_2=3$ ,  $H_2=10$ ) flow conditions. Error bars represent 6% bias and  $0.002\text{ % cm}^{-1}$  precision uncertainties.

Figures 5.74 through 5.77 show the vertically-average vertical gain for the predictions and the measurements for the four flow conditions. The gain has been averaged over the vertical profile  $\pm 5$  mm from the vertical centerline because that is the region with reliable data. These figures also show good agreement between predictions and measurements indicating that not only do the peak and centerline gains match the data but also the vertical width of the gain profiles. Table 5.6 compares the key parameters of the average gain distributions for the data and predictions. Interestingly enough, these three flow cases have nearly the same predicted F atom utilization at their respective maximum average gain locations. These three flow conditions should have very similar mixing characteristics but have different kinetics due to slightly different cavity pressures and reactant species concentrations. This suggests that F atom utilization is more a function of mixing and less of a function of kinetics. Improving the mixing behavior could therefore have a big impact on laser performance.

**Table 5.6** Comparison of measured and predicted maximum average gain.

Flow Condition ( $\text{mmol s}^{-1}$ )	Maximum Average Gain (% $\text{cm}^{-1}$ )		Location of Maximum Average Gain (cm from NEP)		F atom Utilization at Maximum Gain Location Prediction
	Data	Prediction	Data	Prediction	
( $\text{F}_2=1, \text{H}_2=5$ )	0.061	0.056	3.7	2.4	0.21
( $\text{F}_2=2, \text{H}_2=10$ )	0.088	0.092	2.1	1.9	0.30
( $\text{F}_2=2, \text{H}_2=27$ )	0.088	0.097	1.4	1.1	0.32
( $\text{F}_2=3, \text{H}_2=10$ )	0.083	0.107	1.0	1.4	0.31



**Figure 5.74** Measured and predicted average gain with and without V-V rate constant adjustment for the ( $F_2=1$ ,  $H_2=5$ ) flow conditions. The gain is averaged over a region  $\pm 5$  mm from the vertical centerline.

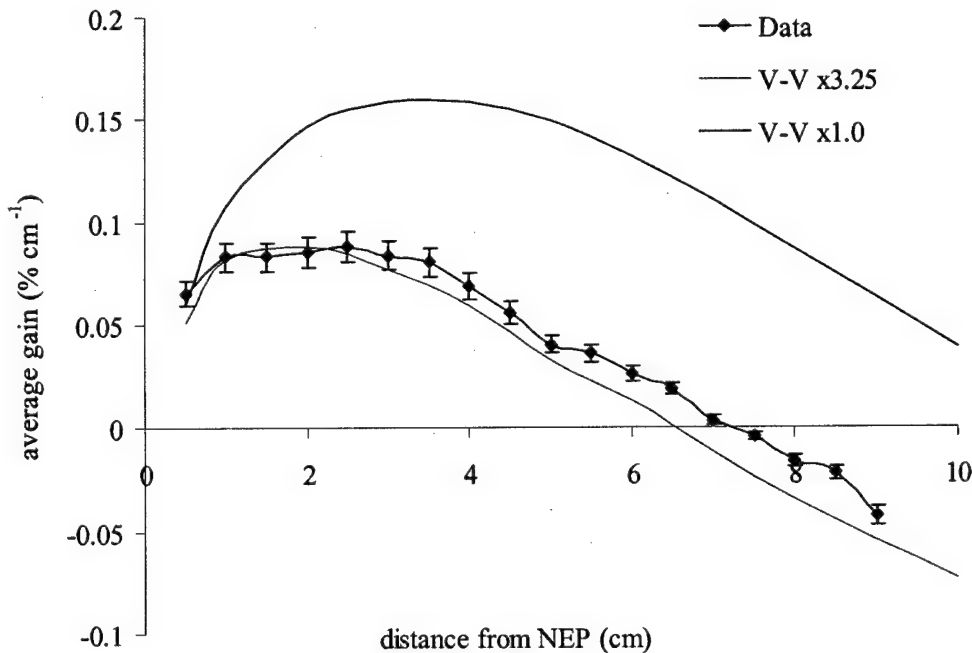


**Figure 5.75** Measured and predicted average gain with and without V-V rate constant adjustment for the ( $F_2=2$ ,  $H_2=10$ ) flow conditions. The gain is averaged over a region  $\pm 5$  mm from the vertical centerline.

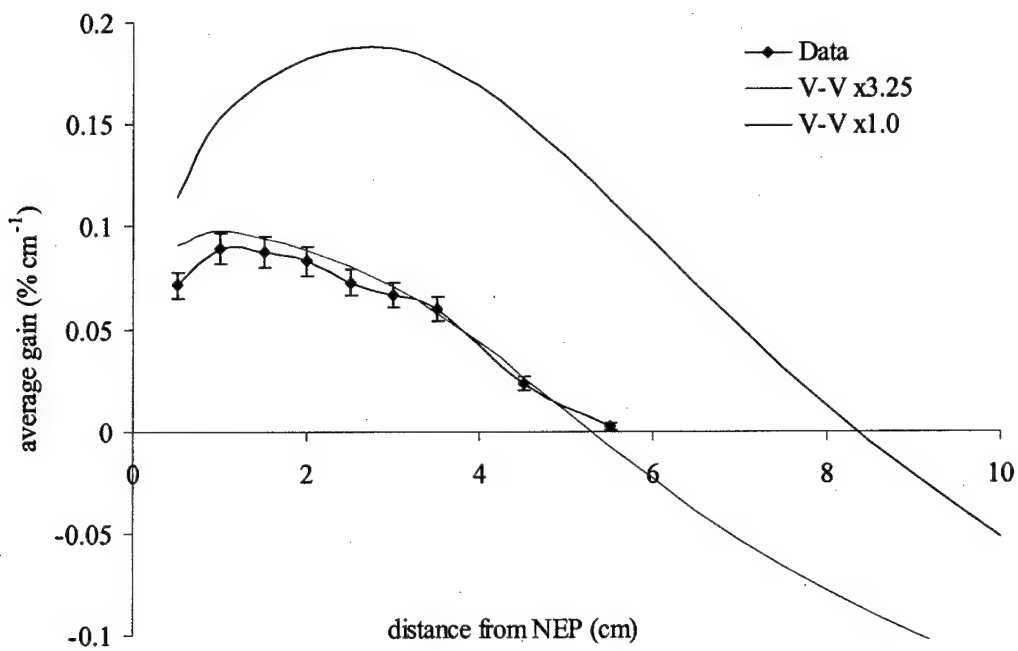


**Figure 5.76** Measured and predicted average gain with and without V-V rate constant adjustment for the ( $F_2=2$ ,  $H_2=27$ ) flow conditions. The gain is averaged over a region  $\pm 5$  mm from the vertical centerline.

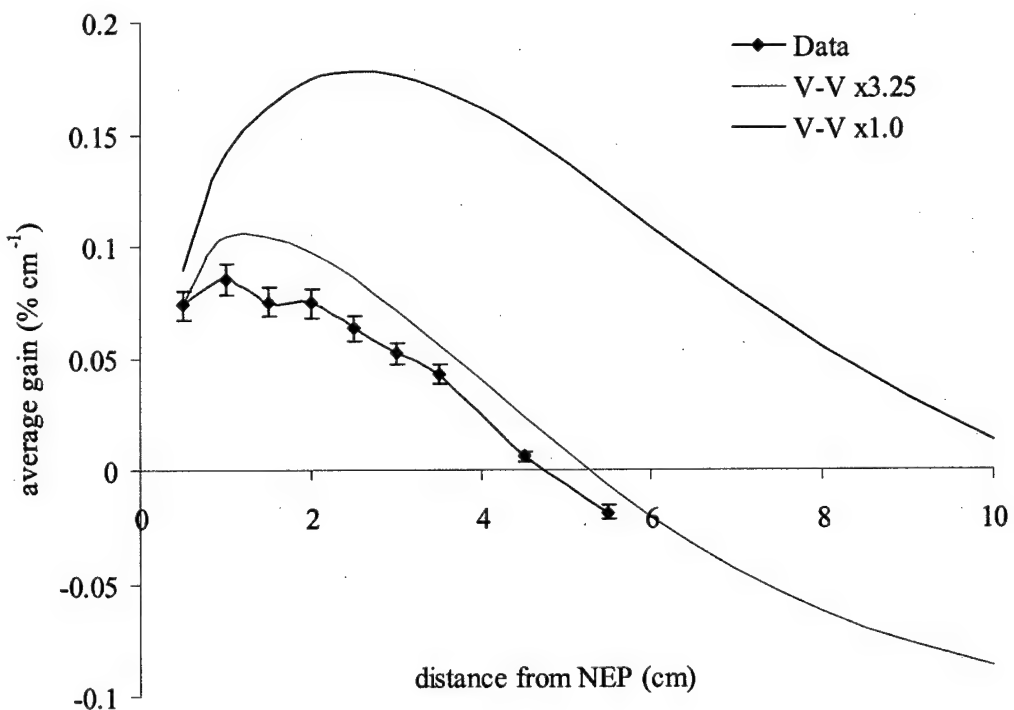


**Figure 5.77** Measured and predicted average gain with and without V-V rate constant adjustment for the ( $F_2=3$ ,  $H_2=10$ ) flow conditions. The gain is averaged over a region  $\pm 5$  mm from the vertical centerline.

In the preceding text the magnitude of the "adjustments" to the code input parameters have been de-emphasized in favor of focusing on the resulting trends caused by the "adjustments". This is because the code is not intended to be used as a multi-parameter fitting routine in an attempt to deduce the actual physical parameters of the experiment. The code is instead used to investigate trends in the predicted gain distribution. The resulting analysis shows that an increase in the HF V-V energy transfer rate constants is the only input parameter that lowers the predicted gain to the level of the data while maintaining the trends in the streamwise distribution of the measured gain. This, along with the fact that a single "adjustment" is all that is necessary to attain good agreement between the predictions and the data for several different flow conditions, is an indication that the HF V-V energy transfer rate constants may actually be significantly larger than reported in the literature. However, due to the complexity of the hydrodynamic and chemical kinetic interactions in the experiment and relative crudeness of the 2-D code, assessing the magnitude of this increase is not possible.

In terms of the peak gain, the computer model is only as good as the rate constants for the primary chemical reactions. This would mean that even true 3-dimensional modeling of the flow field would not bring the magnitude of the predicted gain into agreement with the data. 3-D modeling will resolve more of the fine structure of the flow field with better modeling of the mixing mechanisms inside the laser cavity that will result in better predictions of vertical gain distribution. 3-D modeling will also better resolve the pressure, temperature and velocity fields which have been shown to affect the streamwise gain distribution and could have significant impact on predicting the maximum peak gain of the system. However, from the analysis in this and the

previous sections, it is not likely that this increase in modeling sophistication would be enough to bring the magnitude of the predicted gain into agreement with the measurements. In order to make better predictions of gain magnitude, an independent measurement of the HF V-V energy transfer rate constants is needed.

#### 5.4.5 Model Velocity and Mach Number Predictions

The distribution of gain in the streamwise direction depends strongly on the streamwise velocity. Therefore in order to properly predict the gain distributions the computer model must first be able to predict the velocity. To predict the velocity at the nozzle exit plane (NEP), the computer model needs inputs of total pressure and temperature. The large area ratio between the plenum and the nozzle throat means the Mach number in the plenum is low and the static pressure measured at the wall pressure taps is a good representation of the total pressure. However, the thermal response of the thermocouple in the plenum is too slow to accurately measure the plenum total temperature that changes rapidly during a laser hot fire. The total temperature in the plenum can instead be calculated from the sonic orifice equation (Perry and Green 1997):

$$\dot{n} = PAC_d \Gamma \sqrt{\frac{\gamma}{M_w \bar{R} T}} \quad (5.3)$$

where  $\dot{n}$  is the total molar flow through the nozzle,  $P$  and  $T$  are the total pressure and temperature upstream of the nozzle,  $A$  is the nozzle throat area,  $C_d$  is the discharge coefficient,  $\gamma$  is the ratio of specific heats,  $M_w$  is the average molecular weight of the flow,  $\bar{R}$  is the universal gas constant and  $\Gamma$  is defined by:

$$\Gamma = \left[ \frac{2}{\gamma + 1} \right]^{\frac{\gamma + 1}{2(\gamma - 1)}}$$

Equation (5.3) is valid when the upstream Mach number  $\leq 0.2$  and sonic conditions exist at the nozzle throat. The low upstream Mach number means that the static and total flow properties are nearly the same. The discharge coefficient is first determined during cold flow conditions. Then by knowing the pressure and molar flow rate during the hot fire, the temperature in the plenum can be determined from the sonic orifice equation.

As the flow expands through the nozzle, heat transfer to the walls and boundary layer growth will reduce the total pressure and temperature. These non-isentropic losses can be estimated by running the 2-D code in the INOZ=1 mode. In this mode the computations start at the nozzle throat and run up to the location of the secondary He injectors. Table 5.7 lists the plenum total properties as well as the predicted total properties at the secondary He injector location. The losses are most significant for the ( $F_2=3$ ,  $H_2=10$ ) flow case, which has a plenum total temperature more than 100 K higher than the other flow cases. The higher temperature is caused by the lower diluent flows in the plenum required to achieve the same plenum pressure as the other flow cases and maintain discharge tube performance. The total properties at the secondary He injection point are then used as input parameters when running the code in the normal mode starting at the NEP. In the normal mode the code calculates the velocity and Mach number at the NEP from the total properties, the momentum of the injection jets and the cavity pressure.

Figures 5.78 and 5.79 show the vertical velocity and Mach number profiles, respectively, from the Doppler measurements and the model predictions at 4 cm

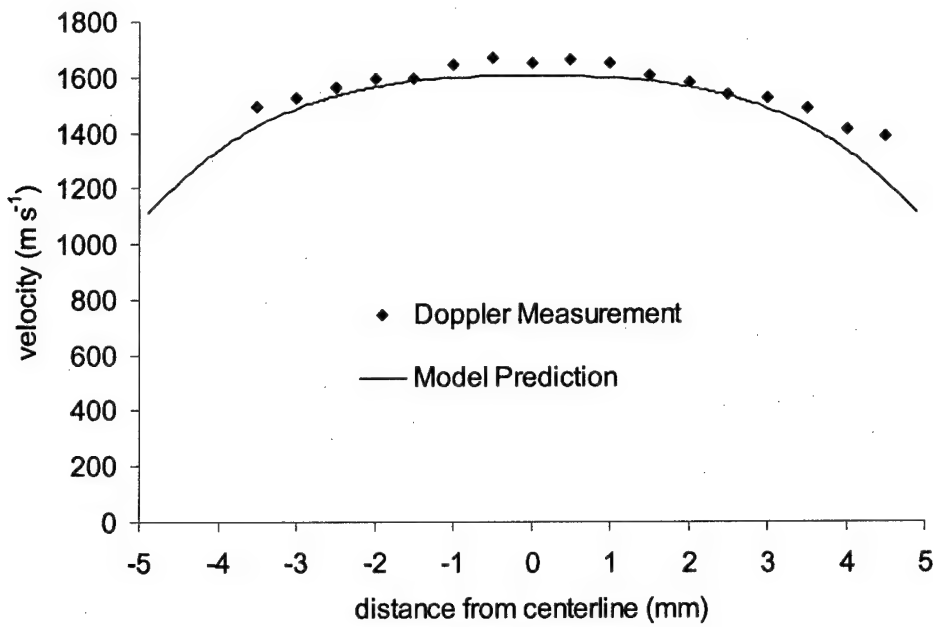


**Figure 5.78** Vertical velocity profile 4 cm downstream of the NEP for the ( $F_2=2$ ,  $H_2=10$ ) flow conditions. Measurements were made with the Doppler technique described in Section 3.5.2 and the model predictions were made with the same input parameters used to attain excellent agreement between the vertical gain profiles.

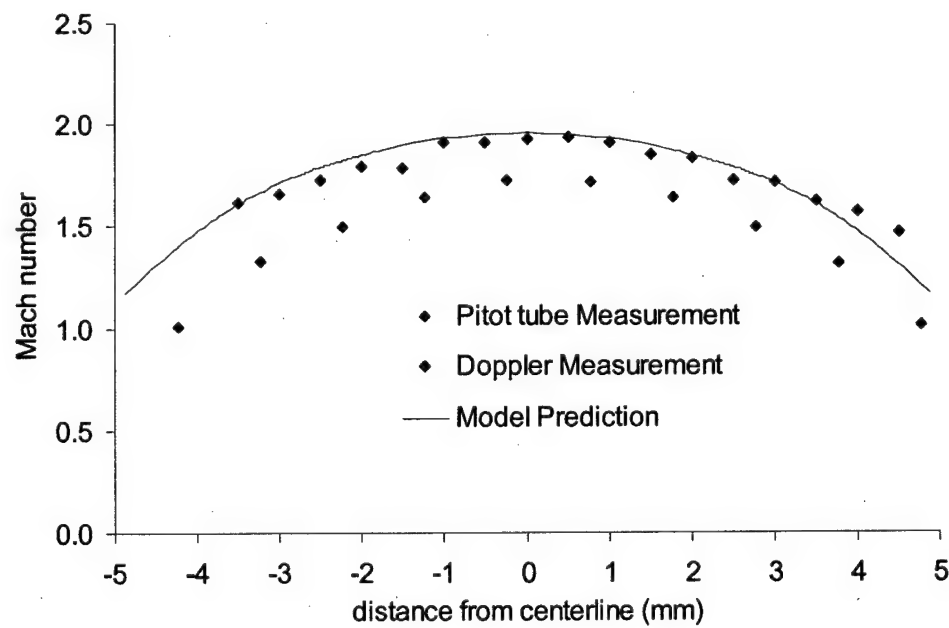


**Figure 5.79** Vertical Mach number profile 4 cm downstream of the NEP for the ( $F_2=2$ ,  $H_2=10$ ) flow conditions. Measurements were made with the Doppler technique described in Section 3.5.2 and the model predictions were made with the same input parameters used to attain excellent agreement between the vertical gain profiles.

downstream of the NEP for the ( $F_2=2$ ,  $H_2=10$ ) flow conditions. The Pitot-static tube Mach number measurements are also included in Figure 5.79. The predictions are in excellent agreement with the magnitude and shape of the measurements. The model input parameters used in this comparison are the same as those used in Section 5.4.4 that attained agreement between the measured and predicted gain profiles. Figures 5.80 and 5.81 show the streamwise variation of the measured and predicted velocity and Mach number, respectively, at the vertical centerline for the ( $F_2=2$ ,  $H_2=10$ ) flow conditions. The predicted velocity is in excellent agreement with the measurement. The centerline velocity decreases slightly in the streamwise direction. The model overpredicts the centerline Mach number at most locations by about 10%. With the excellent agreement in the velocity, the Mach number disagreement is probably due to the disagreement

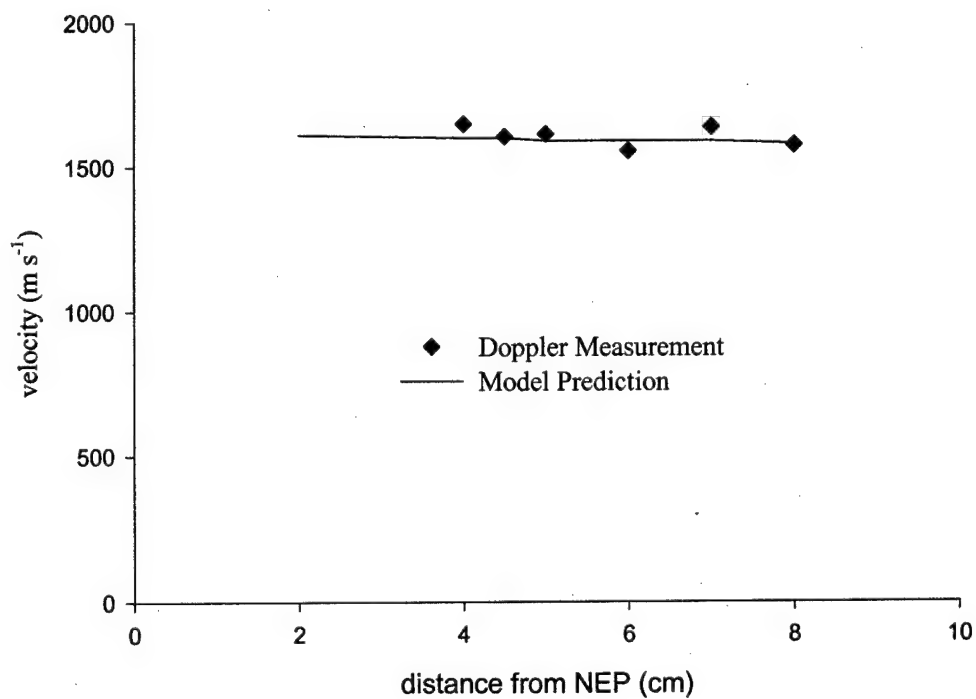


**Figure 5.80** Streamwise velocity at the vertical centerline for the ( $F_2=2$ ,  $H_2=10$ ) flow conditions.

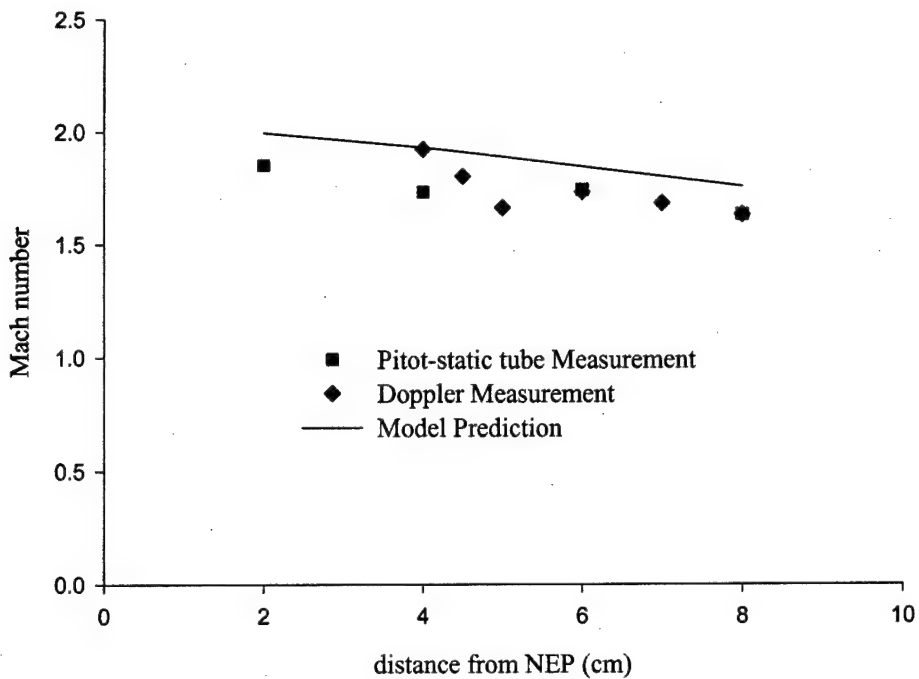


**Figure 5.81** Streamwise Mach number at the vertical centerline for the ( $F_2=2$ ,  $H_2=10$ ) flow conditions.

between the measured and predicted temperature at the vertical centerline that would affect the calculation of the speed of sound.

Table 5.7 lists the predicted centerline velocity and Mach number at the NEP for the four flow conditions. The ( $F_2=3$ ,  $H_2=10$ ) flow case has a significantly lower velocity and Mach number than the other three flow conditions. This is due to the greater total pressure loss in the nozzle and slightly higher cavity pressure. The lower velocity for this flow case will move the location of the maximum peak gain and the onset of gain at the vertical centerline closer to the NEP. The lower velocity will also shift the location where the V-V energy transfer reactions start to dominate over the cold pumping reaction closer to the NEP. All these trends are consistent with the comparisons between the ( $F_2=2$ ,  $H_2=10$ ) and ( $F_2=3$ ,  $H_2=10$ ) peak, centerline and average gain plots in Figures 5.17, 5.18 and 5.20.

**Table 5.7** Flow parameters for various flow cases. Total pressure is measured in the plenum. Total temperature is calculated from the sonic orifice equation. All other listed parameters are predicted from computer model.

	<b>F<sub>2</sub>=1 H<sub>2</sub>=5</b>	<b>F<sub>2</sub>=2 H<sub>2</sub>=10</b>	<b>F<sub>2</sub>=2 H<sub>2</sub>=27</b>	<b>F<sub>2</sub>=3 H<sub>2</sub>=10</b>
Total pressure in Plenum (torr)	25.2	27.6	27.6	27.0
Total Pressure at He Injector (torr)	21.2	20.9	20.9	18.6
Total Temperature in Plenum (K)	393	433	433	549
Total Temperature at He Injection (K)	385	423	423	526
Mach Number at He Injection	2.45	2.53	2.53	2.54
Centerline Velocity at NEP (m s <sup>-1</sup> )	1686	1742	1772	1305
Centerline Mach Number at NEP	2.2	2.1	2.0	1.85

#### 5.4.6 Cavity Shock and Expansion Fans

If flow through the nozzle is not perfectly expanded, the pressure at the NEP will not match the cavity pressure. Since a pressure difference cannot be sustained across the free boundary between the primary nozzle flow and the base purge flow a series of oblique shocks or expansion fans will form. If the pressure just inside the nozzle is less than the ambient cavity pressure, the nozzle is considered over-expanded and oblique shock waves form to raise the pressure to match the cavity pressure. If the pressure inside the nozzle is higher than the cavity pressure, the nozzle is under-expanded and expansion fans form to lower the pressure to match the cavity pressure. Examples of over-expanded and under-expanded nozzles are shown in Figures 5.82 and 5.83, respectively. The oblique shock A in the over-expanded nozzle deflects the flow toward the centerline and raises the pressure to ambient,  $P_2=P_{\text{amb}}$ . Since the flow cannot cross

the centerline due to symmetry constraints, another oblique shock (or reflected shock) B forms to turn the flow back parallel to the centerline symmetry axis. Pressure also increases across the second oblique shock creating a region of pressure higher than the ambient cavity pressure,  $P_3 > P_{\text{amb}}$ . The flow must then expand across an expansion fan C to equalize the pressure to  $P_4 = P_{\text{amb}}$ . The expansion fan deflects the flow away from the centerline. Another expansion fan D then forms to turn the flow back parallel to the axis. This expansion fan however, creates a region whose pressure is lower than the ambient pressure,  $P_5 < P_{\text{amb}}$ . If this pressure is low enough, another oblique shock E will form to equalize the pressure and the whole cycle starts all over again. Over-expanded flow in a nozzle is the same except the first set of oblique shocks is eliminated and the flow is first turned away from the axis by a set of expansion fans that lower the pressure to match ambient pressure.

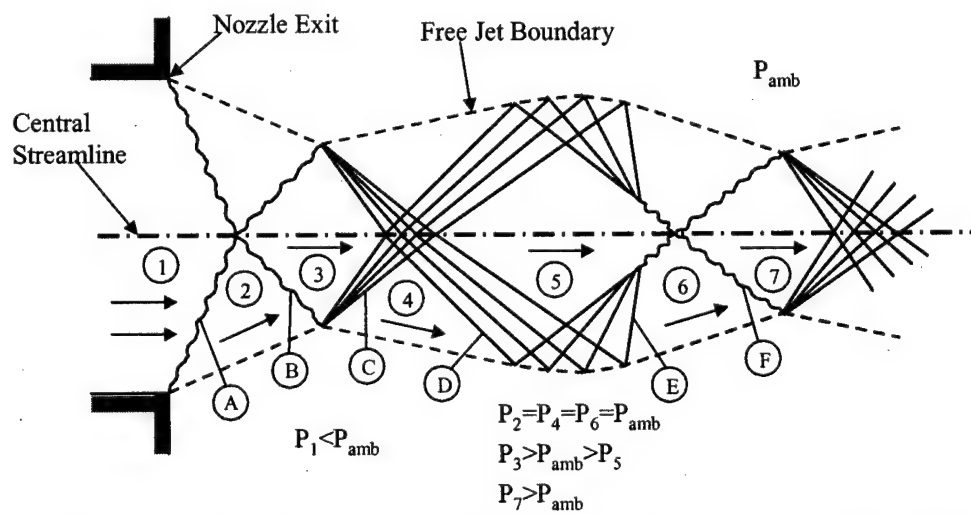


**Figure 5.82** Example of over-expanded oblique shock and expansion fan pattern.

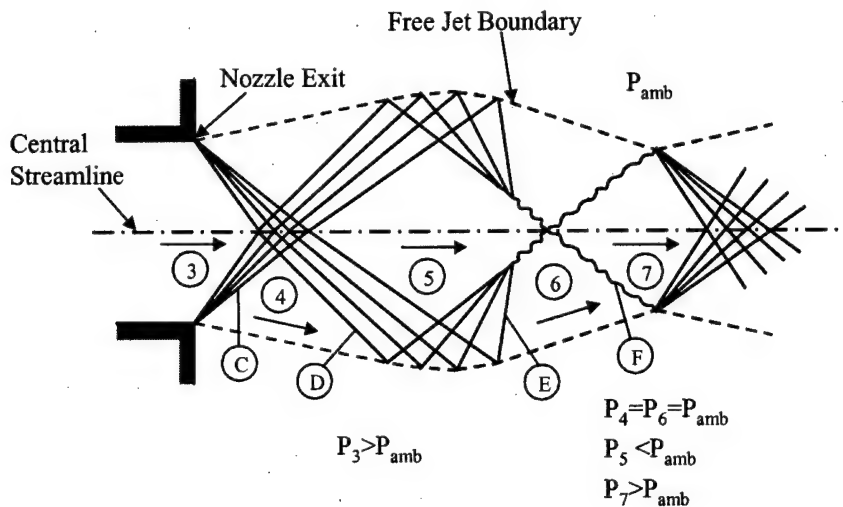


**Figure 5.83** Example of under-expanded oblique shock and expansion fan pattern.

The computer model cannot predict oblique shocks or expansion fans because of the thin shear layer approximation used in the code to simplify the cross-stream momentum equation. Instead it expands or contracts the primary nozzle flow to fill the region between the base purge flow and the centerline so that the pressure matches the input ambient cavity pressure. This pressure equalization computation occurs immediately downstream of the NEP. If the shocks or expansion fans that actually occur are weak, the errors in this method will be small. An estimate of the oblique shock strength and deflection angle was made using the calculated pressure and Mach number at the secondary He injection point and the measured ambient cavity pressure. This analysis ignores completely the injected flow streams, which are likely to have a very large effect on the shock/expansion formation, and the large heat addition to the flow from the chemical reaction. Nevertheless a qualitative assessment of the shock/expansion structure can be made.

The results of the over-expanded flow analysis, illustrated in Figure 5.84, show that all four flow conditions are over-expanded with similar shock structures. The ( $F_2=2$ ,  $H_2=10$ ) and ( $F_2=2$ ,  $H_2= 27$ ) have the same primary flow rates and cavity pressure so their shock and deflection angles calculated from this analysis are the same. Table 5.8 lists the shock and deflection angles of the initial oblique shock measured relative to the horizontal. Flow deflection caused by the oblique shocks will drive the reactants toward the centerline. The higher deflection angle of the ( $F_2=3$ ,  $H_2=10$ ) flow case may explain the narrower gain profile at the 2 cm downstream location (Figure 5.14) for this flow rate. The deflection angle will also work to drive the location of the peak gain toward the centerline, which is shown in Figure 5.19. For the ( $F_2=2$ ,  $H_2=10$ ) and ( $F_2=2$ ,  $H_2= 27$ ) flow cases, which should have similar shock angles from this analysis, the peak gain locations are about the same through about 2.5 cm downstream of the NEP. From 0.5 cm to 2.0 cm downstream of the NEP, the location of the peak gain for the ( $F_2=3$ ,  $H_2=10$ ) flow case moves from 3.5 mm to 1.5 mm from the vertical centerline while the ( $F_2=2$ ,  $H_2=10$ ) and ( $F_2=2$ ,  $H_2= 27$ ) flow cases remain between 2.5 and 3.0 mm from the vertical centerline. The location of the peak gain for the ( $F_2=1$ ,  $H_2= 5$ ) flow case moves away from the centerline through the first 2 cm downstream of the NEP. The width of the gain profile for the ( $F_2=1$ ,  $H_2= 5$ ) flow case also appears to be slightly greater than for the other flow cases at 2 cm downstream of the NEP. This could be an indication that this flow case is actually under-expanded with an initial deflection angle away from the centerline. This analysis shows that relatively small differences in ambient cavity

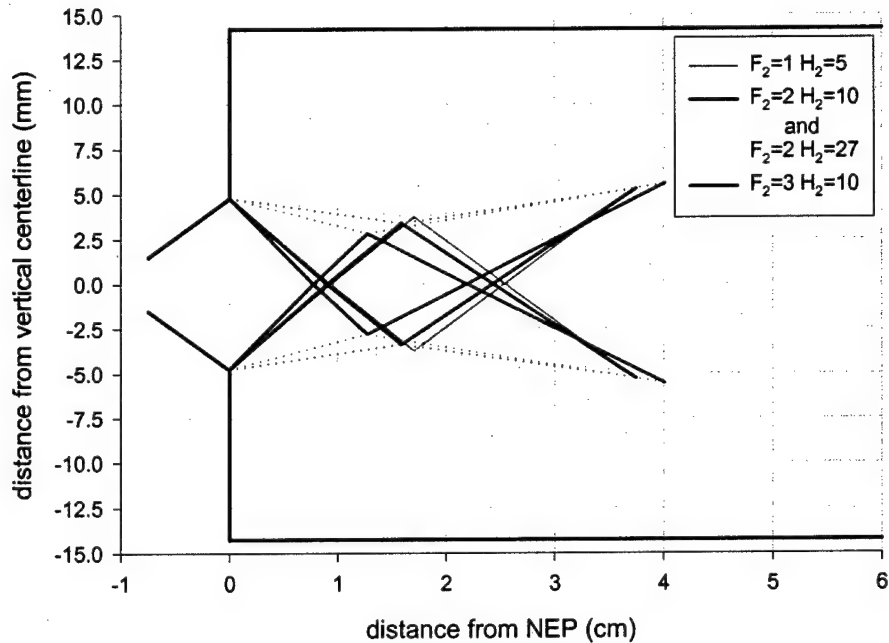


**Figure 5.84** Oblique shock and expansion fan pattern for each of the four flow conditions based on computer model prediction of total properties at the secondary He nozzle injection point and the measured cavity pressure. The ( $F_2=2, H_2=10$ ) and ( $F_2=2, H_2=27$ ) have very similar flow conditions and are therefore represented by the same curve.

**Table 5.8** Parameters predicted by oblique shock/expansion fan system shown in Figure 5.84.

	$F_2=1, H_2=5$	$F_2=2 H_2=10$	$F_2=2 H_2=10$	$F_2=3 H_2=10$
Initial Shock Angle (deg)	27	28	28	32
Initial Deflection Angle (deg)	3	5	5	9
Static Temperature Rise Across Initial Shock (K)	14	28	28	51

pressure and total pressure loss in the nozzle can have significant effects on the cavity shock structure and may explain some of the vertical gain profile trends.

Static temperature increases across oblique shocks and decreases across expansion fans. Table 5.8 also lists the static temperature increase across the initial oblique shock calculated from this analysis for the four flow conditions. Since the deflection angles are relatively shallow, the reflected shocks have about the same angle as the initial shock and therefore also have about the same temperature rise. The temperature drop across the expansion fans is likewise about the same as the temperature rise across the initial oblique shock. Therefore, in the streamwise direction the flow will experience abrupt temperature increases while passing through the initial and reflected oblique shocks followed by two abrupt temperature decreases while passing through the expansion fans.

It is difficult to say whether or not the measured temperature oscillations at the peak gain location shown in Figure 5.25 are caused by such a shock/expansion pattern. The magnitude of the temperature oscillations (peak to valley) for the ( $F_2=2, H_2=10$ ), ( $F_2=2, H_2=27$ ) and ( $F_2=3, H_2=10$ ) flow conditions is between 50 and 100 K which is in good agreement with the magnitude of the predicted temperature changes. The temperature oscillations for the ( $F_2=1, H_2=5$ ) flow conditions are much less pronounced indicating weaker shock/expansion structures, which is also in good agreement with the predictions. The location of the initial temperature increase for the ( $F_2=2, H_2=10$ ), ( $F_2=2, H_2=27$ ) and ( $F_2=3, H_2=10$ ) flow conditions is about 1 to 1.5 cm downstream of the NEP, which corresponds fairly well to the location of the second oblique shock. The temperature increase for these three flow conditions is followed very quickly by a

decrease in measured temperature. At these downstream locations the peak gain occurs about 2 mm from the vertical centerline, which is where the temperature measurement is being made (Figure 5.19). This is very close to the location where the second oblique shock reflects off the free boundary between the base purge and nozzle flow. Thus the temperature decrease associated with the first expansion fan should occur just downstream of the temperature increase caused by the second oblique shock (Figure 5.84). By the time the flow reaches 3 cm downstream of the NEP, the peak gain occurs about 1.5 mm from the vertical centerline for the ( $F_2=2, H_2=10$ ), ( $F_2=2, H_2=27$ ) and ( $F_2=3, H_2=10$ ) flow conditions and should have crossed the second expansion fan where the temperature would drop again. Up until about 3 cm downstream of the NEP, the shock/expansion fan pattern predicted by this analysis appears to explain the streamwise temperature oscillations at the vertical peak location rather well. However, this shock/expansion fan pattern does not appear to explain the sudden temperature increase that occurs 3.5-4 cm downstream of the NEP for these three flow conditions (Figure 5.25). This temperature rise would not be expected until after the second expansion fan reflects from the free boundary, coalesces into an oblique shock and crosses the vertical centerline, which would not occur until 5 to 6 cm downstream of the NEP.

This analysis has shown that small changes in cavity pressure can influence the shock/expansion fan pattern in the laser cavity and may have significant effects on the cavity gain distribution. This suggests that resolving the shock/expansion fan pattern through 3-D modeling of the flow field could significantly improve predictions. Locating the oblique shocks and expansion fans through experimental investigation could also be very enlightening.

## 5.5 Fundamental Power and Spectra

The fundamental output power and spectra were measured with the optical axis at several different streamwise positions with outcoupler reflectivities ranging from 40% to 95%. In all cases the Max R reflectivity was 99.95% and the optical aperture was limited to 2.54 cm in the vertical direction by a copper insert and 4.5 cm in the streamwise direction by the mirror retaining rings. Figure 5.85 shows the measured fundamental output power as a function of downstream location for the ( $F_2=1, H_2=5$ ), ( $F_2=2, H_2=10$ ) and ( $F_2=3, H_2=15$ ) flow conditions. All of these power measurements were made with a maximum available outcoupler (OC) reflectivity of 95%. The maximum output power was 32 W, 63 W and 68 W, respectively, for the ( $F_2=1, H_2=5$ ), ( $F_2=2, H_2=10$ ) and ( $F_2=3, H_2=15$ ) flow conditions. The maximum power for the ( $F_2=2, H_2=10$ ) and ( $F_2=3, H_2=10$ ) flow conditions occurred 2.7 cm downstream of the NEP and the power decreased as the optical axis was moved further downstream. The steeper decrease in fundamental power in the streamwise direction for the ( $F_2=3, H_2=10$ ) flow conditions than for the ( $F_2=2, H_2=10$ ) flow conditions is consistent with the steeper streamwise decrease of the average overtone small signal gain shown in Figure 5.20. The slight increase in maximum power for the ( $F_2=3, H_2=10$ ) case over the ( $F_2=2, H_2=10$ ) flow case may be caused by its narrower vertical gain profile (Figures 5.14 and 5.15). The 2.54 cm vertical resonator aperture includes a significant portion of the base purge region, which may contain more absorbing molecules for the wider ( $F_2=2, H_2=10$ ) gain profile. The maximum power for the ( $F_2=1, H_2=5$ ) flow conditions occurs with the optical axis 2.0 cm further downstream of the NEP than the other two flow conditions. The streamwise power profile is also much flatter than for the other flow conditions remaining within 20% of the maximum

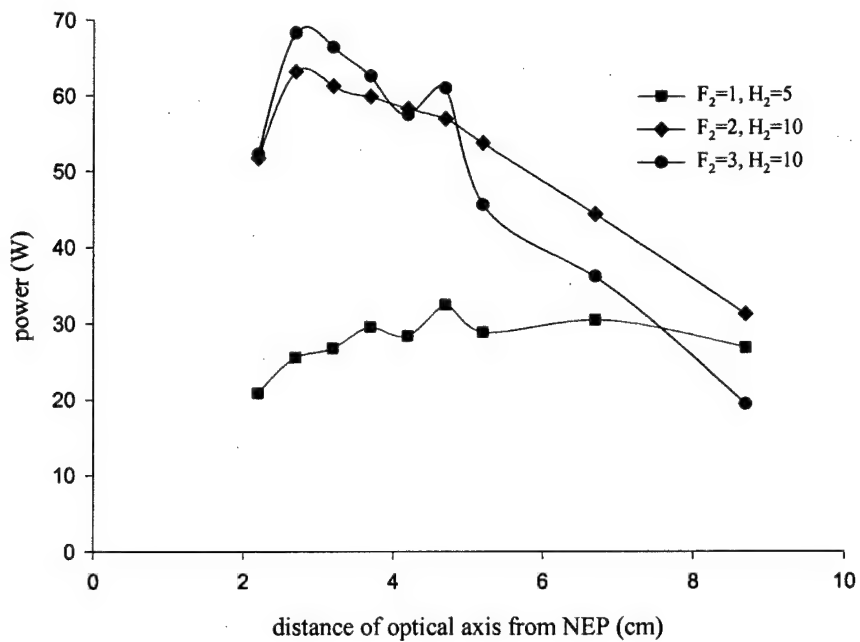


**Figure 5.85** Fundamental power as a function of downstream location for the ( $F_2=1$ ,  $H_2=5$ ), ( $F_2=2$ ,  $H_2=10$ ) and ( $F_2=3$ ,  $H_2=10$ ) flow conditions. All data were taken with a resonator consisting of a Max R (99.95% reflectivity) and 95% reflectivity outcoupler.

power for all measured optical axis locations except at the 2.2 cm downstream location. Both of these trends are consistent with the overtone small signal gain trends in comparisons between the different flow conditions.

Figures 5.86, 5.87 and 5.88 show the multi-line lasing spectra of the outcoupled fundamental beam with the optical axis positioned 2.7 cm, 4.7 cm and 8.7 cm downstream of the NEP for the ( $F_2=1$ ,  $H_2=5$ ), ( $F_2=2$ ,  $H_2=10$ ) and ( $F_2=3$ ,  $H_2=10$ ) flow conditions, respectively. These spectra were all collected with the maximum available OC reflectivity of 95% and correspond to the power measurements shown in Figure 5.85. The intensity of the transitions within a particular spectra are scaled relative to the intensity of the largest peak within that spectra. Since, the output power changes with flow conditions and downstream location the relative intensities of the transition peaks from panel to panel in these figures cannot be compared. All of these spectra show

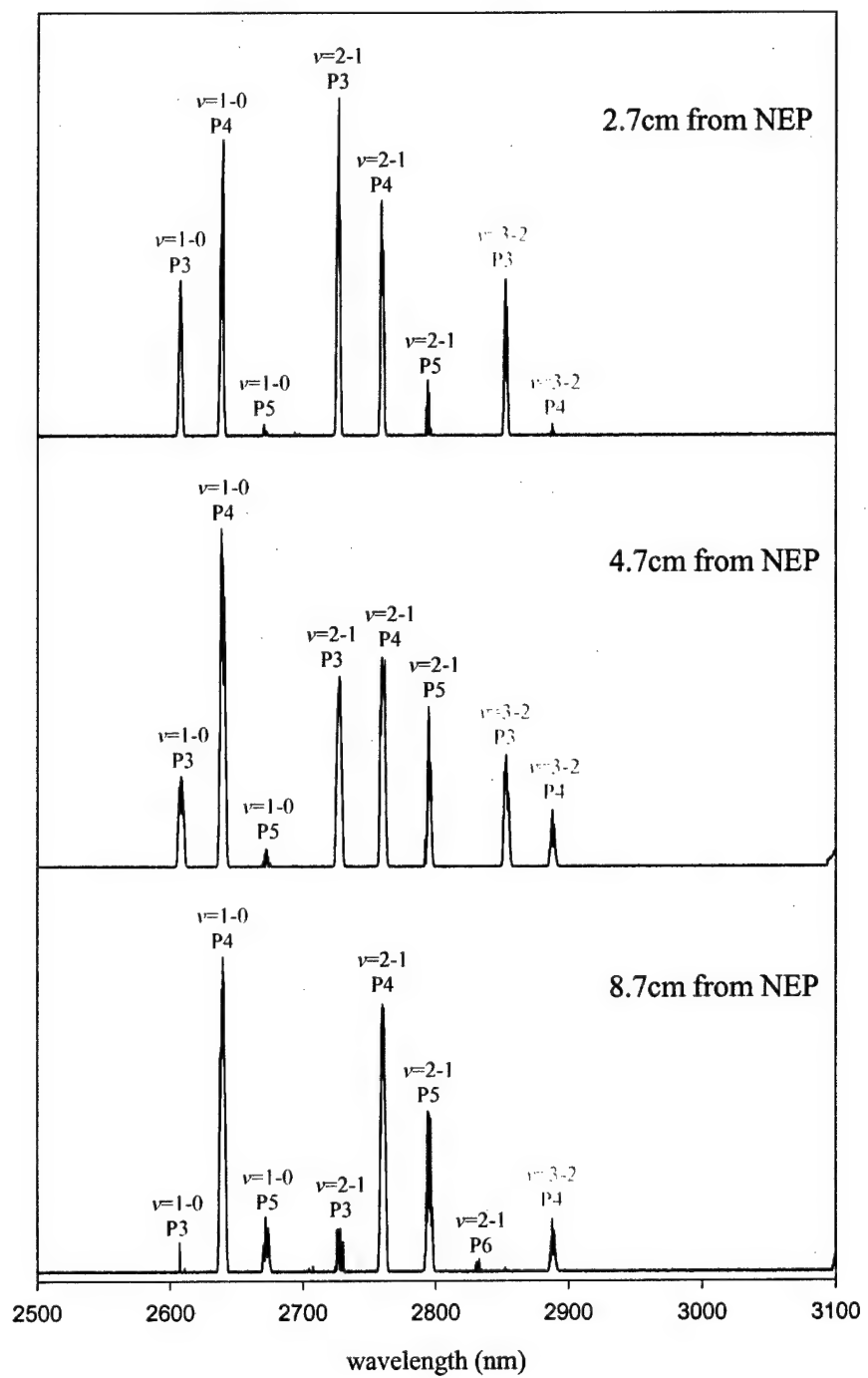


**Figure 5.86** Fundamental multi-lasing spectra for the ( $F_2=1$ ,  $H_2=5$ ) flow conditions at optical axis positions of 2.7, 4.7 and 8.7 cm downstream of the NEP. All spectra were taken with Max R and 95% outcoupler reflectivity resonator. The intensity of each lasing line is scaled relative to the most intense line at each downstream location.

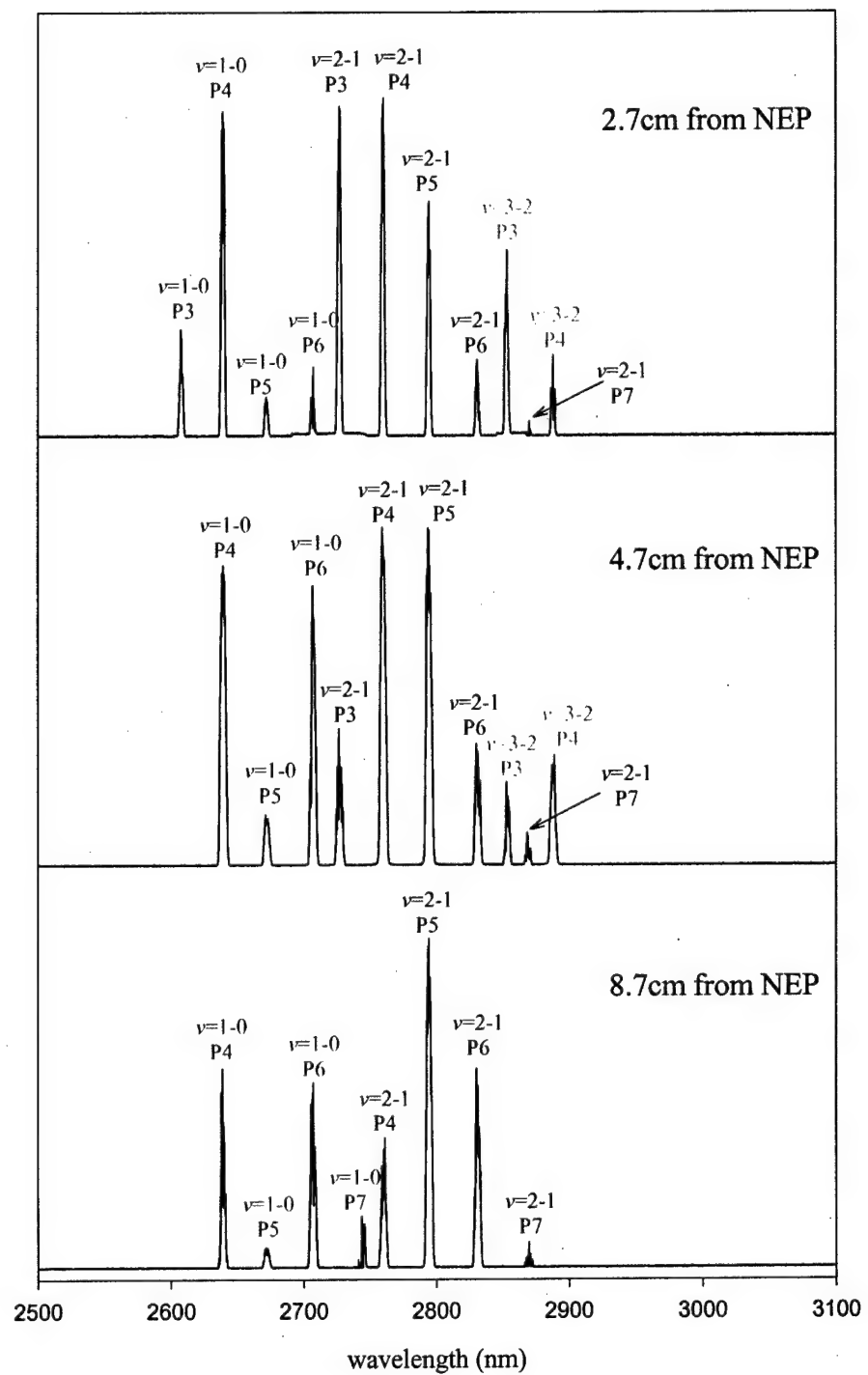


**Figure 5.87** Fundamental multi-lasing spectra for the ( $F_2=2$ ,  $H_2=10$ ) flow conditions at optical axis positions of 2.7, 4.7 and 8.7 cm downstream of the NEP. All spectra were taken with Max R and 95% outcoupler reflectivity resonator. The intensity of each lasing line is scaled relative to the most intense line at each downstream location.

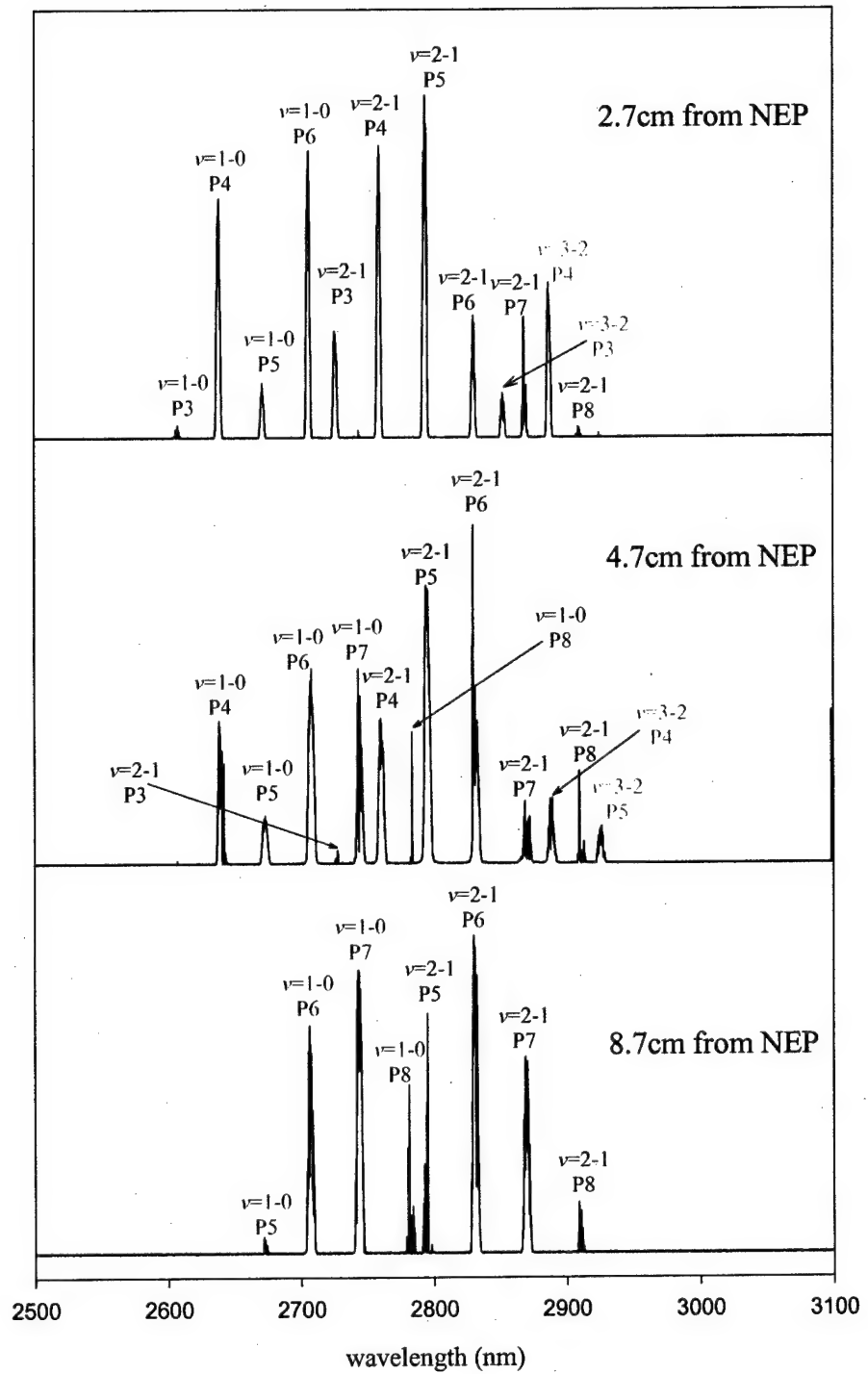


**Figure 5.88** Fundamental multi-lasing spectra for the ( $F_2=3$ ,  $H_2=10$ ) flow conditions at optical axis positions of 2.7, 4.7 and 8.7 cm downstream of the NEP. All spectra were taken with Max R and 95% outcoupler reflectivity resonator. The intensity of each lasing line is scaled relative to the most intense line at each downstream location.

multiple lasing lines with as many as six separate ro-vibrational lines lasing within a single vibrational band (( $F_2=3$ ,  $H_2=10$ ) flow conditions 2.7 cm downstream of the NEP).

At the 2.7 cm location on Figure 5.86, the spectra for the ( $F_2=1$ ,  $H_2=5$ ) flow conditions shows lasing lines of P3, P4 and P5 within the  $v=1-0$  vibrational band transition, P3, P4 and P5 within the  $v=2-1$  vibrational band transition and P3 and P4 within the  $v=3-2$  vibrational band transition. The ( $F_2=2$ ,  $H_2=10$ ) flow conditions add lines at P6 within the  $v=1-0$  vibrational band transition and P6 and P7 within the  $v=2-1$  vibrational band transition. The ( $F_2=3$ ,  $H_2=10$ ) flow conditions add the P8  $v=2-1$  lasing line to the ( $F_2=2$ ,  $H_2=10$ ) spectrum. The addition of the higher P branch lasing lines for the ( $F_2=2$ ,  $H_2=10$ ) and ( $F_2=3$ ,  $H_2=10$ ) flow conditions is consistent with the higher temperature for these flow conditions that shifts the rotational Boltzman distribution within the vibrational bands to higher J levels.

The shift to the higher P branch lasing lines can also be seen in comparisons between the spectra at different downstream locations for a particular flow condition. For instance, the relative height of the P5  $v=1-0$  transition line increases for the ( $F_2=1$ ,  $H_2=5$ ) flow conditions as the optical axis is moved downstream while the relative height of the P3  $v=1-0$  transition line decreases. Similarly the relative intensity of the P5  $v=2-1$  transition line increases while the relative intensity for the P3  $v=2-1$  decreases. Similar streamwise trends are also evident for the other flow conditions. This is presumably the result of the rotational Bolztmann re-distribution within the vibrational levels caused by the streamwise temperature rise.

Figures 5.89, 5.90 and 5.91 show the intensity saturation (I-Sat) curves for the ( $F_2=1$ ,  $H_2=5$ ), ( $F_2=2$ ,  $H_2=10$ ) and ( $F_2=3$ ,  $H_2=10$ ) flow conditions, respectively, at several

different downstream locations. For all three flow conditions and at all downstream locations the maximum power was achieved with the maximum available outcoupler reflectivity of 95% (i.e., 5% outcoupler transmittance). Further increases in outcoupler reflectivity would have likely increased the output power. The high outcoupler reflectivity required to achieve maximum power is an indication that the optical losses are small compared to the small signal gain. Neglecting optical losses, the fundamental small signal gain is estimated by the threshold gain:

$$\gamma_o \approx \gamma_{th} = \frac{-\ln(R_1 R_2)}{2L_g} \quad (5.4)$$

where  $R_2$  is the reflectivity of the Max R and  $R_1$  is the reflectivity of the OC mirror at

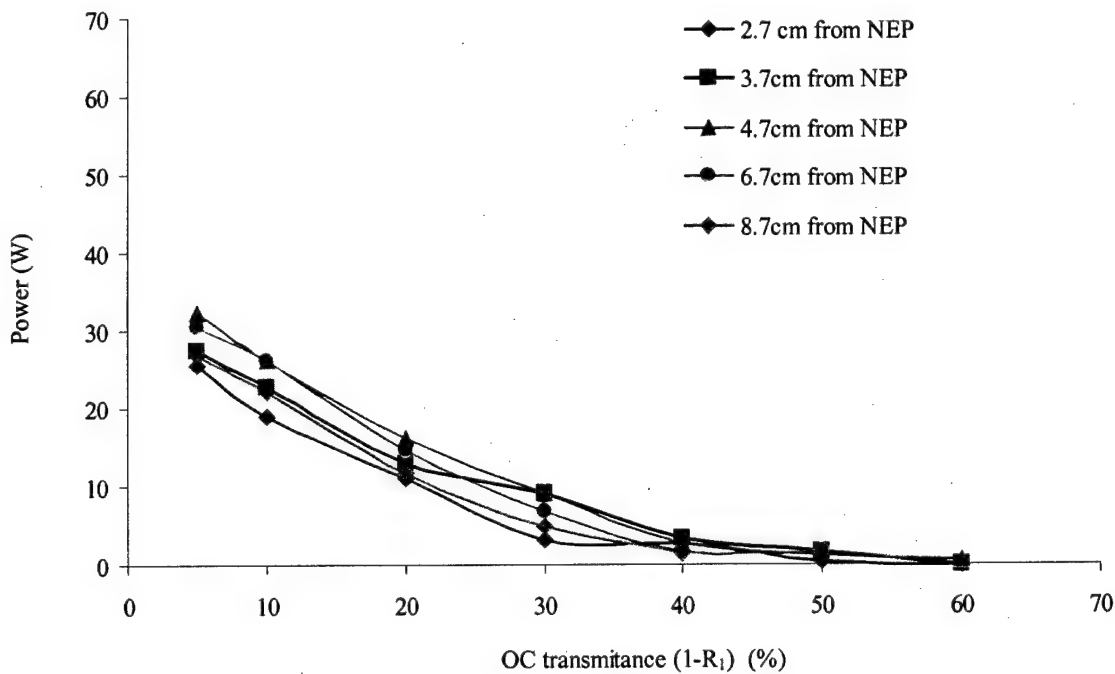


**Figure 5.89** Intensity saturation curve at several downstream locations for the ( $F_2=1$ ,  $H_2=5$ ) flow conditions.

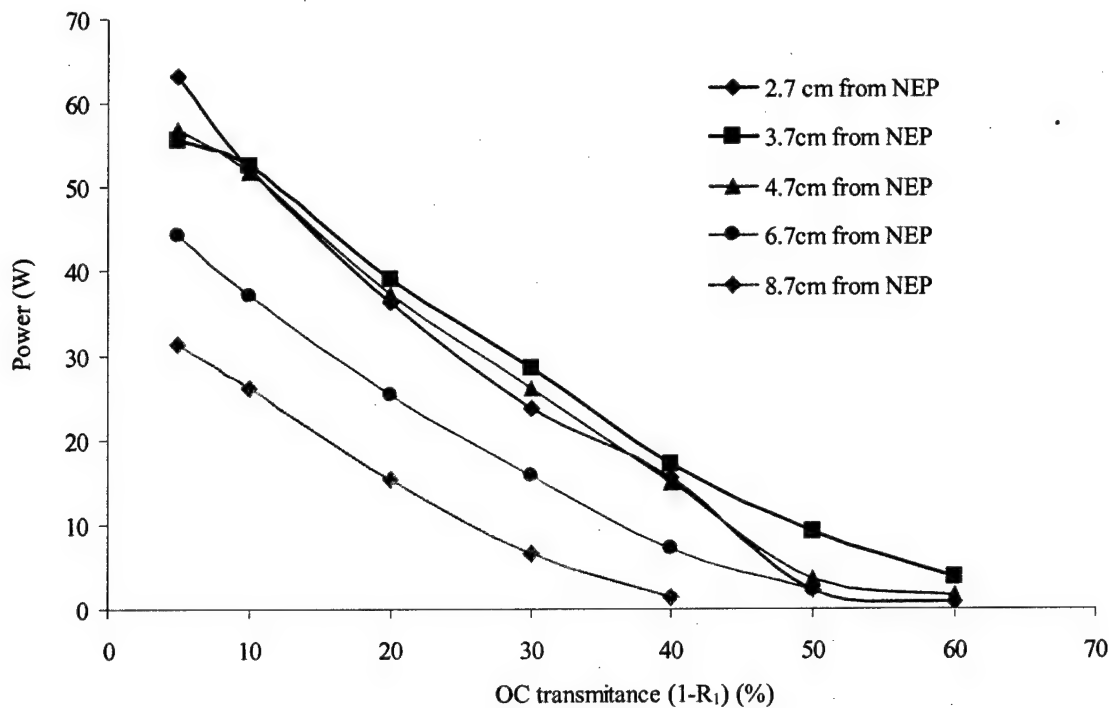


**Figure 5.90** Intensity saturation curve at several downstream locations for the ( $F_2=2$ ,  $H_2=10$ ) flow conditions.

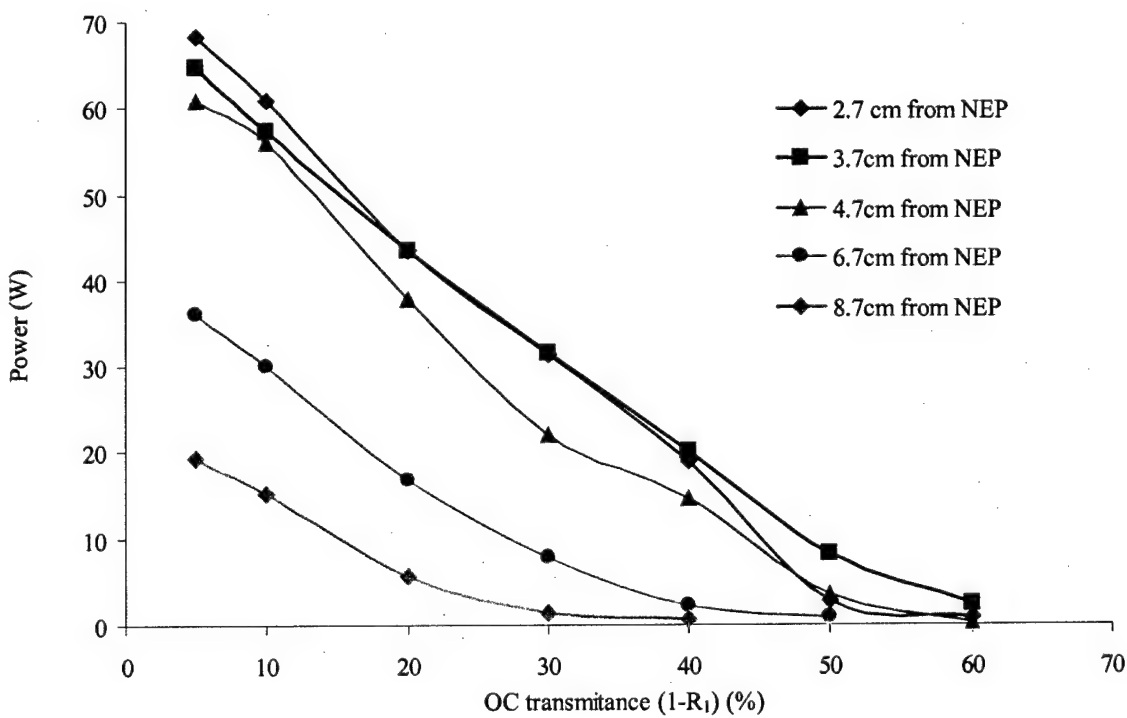


**Figure 5.91** Intensity saturation curve at several downstream locations for the ( $F_2=3$ ,  $H_2=10$ ) flow conditions.

which the system just barely lases.  $R_1$  was estimated from Figures 5.89, 5.90 and 5.91 for each set of flow conditions at each downstream location to within  $\pm 5\%$  of the actual threshold OC reflectivity. The spectra of the fundamental outcoupled beam were taken at each OC reflectivity and downstream location for all three flow conditions in order to determine which of the many different transitions that lase when operating at full power is associated with the small signal gain measured at threshold.

Figures 5.92, 5.93 and 5.94 show examples of the outcoupled fundamental spectra for the  $(F_2=1, H_2=5)$ ,  $(F_2=2, H_2=10)$  and  $(F_2=3, H_2=10)$  flow conditions, respectively, taken with the optical axis 4.7 cm downstream of the NEP for three different OC reflectivities. The lower panel in these three figures represents the spectra taken with the lowest OC reflectivity that lased for each flow condition. Therefore near threshold the dominant transition is P3  $\nu=2-1$  for the  $(F_2=1, H_2=5)$  and  $(F_2=2, H_2=10)$  flow conditions and P4  $\nu=2-1$  for the  $(F_2=3, H_2=10)$  flow conditions at the 4.7 cm downstream location. The streamwise temperature rise for all the flow conditions does not appear to be great enough to alter the dominant transition so all the small signal gains estimated from the I-Sat curves at the different streamwise locations in Figures 5.89, 5.90 and 5.91 are associated with the same transitions determined at the 4.7 cm downstream location from Figures 5.92, 5.93 and 5.94.

One may notice that the transition that dominates at threshold is not the same transition that dominates at the full power conditions (i.e.,  $R_1=95\%$ ). For example the P4  $\nu=1-0$  transition dominates the full power spectrum of the  $(F_2=1, H_2=5)$  flow conditions for  $R_1=95\%$  (Figure 5.92) compared to the P3  $\nu=2-1$  transition that dominates at threshold for  $R_1=50\%$ . This could be caused by the complex interaction that occurs

between the stimulating radiation field and the populations of the various ro-vibrational energy levels under heavily saturated conditions. For instance, lasing on the P3  $v=2-1$  transition will add to the population of the  $v=1 J=3$  energy level thus increasing the gain of the P4  $v=1-0$  transition created by the cold pumping reaction. Subsequent redistribution of rotational levels within the vibrational bands through collisional processes may also play a role in determining the dominant lasing transition under saturated conditions.

Figure 5.95 shows the fundamental small signal gain for the dominant threshold transition as a function of streamwise location for the ( $F_2=1, H_2=5$ ), ( $F_2=2, H_2=10$ ) and ( $F_2=3, H_2=10$ ) flow conditions. The maximum small signal gain for the ( $F_2=2, H_2=10$ ) and ( $F_2=3, H_2=10$ ) flow conditions is approximately  $12\% \text{ cm}^{-1}$  and occurs  $3.7 \text{ cm}$  downstream of the NEP. It should be noted that although these two flow conditions have the same maximum small signal gain they have different dominant threshold transitions. The maximum gain for the ( $F_2=1, H_2=5$ ) flow conditions is approximately  $9\% \text{ cm}^{-1}$  and occurs  $4.7 \text{ cm}$  downstream of the NEP. These measurements are in good agreement with previous small signal gain measurements from similar devices (Sentman et al. 1999a; Sentman et al. 1999b). As expected these fundamental gains are about a factor of 100 greater than the measured overtone small signal gains. The general trends in the streamwise distribution of the fundamental gains between these three flow conditions compare well with the trends of the overtone gains shown in Figures 5.17 and 5.18. However, it is difficult to determine from these figures whether the fundamental gain should be compared to the peak or centerline overtone gain.

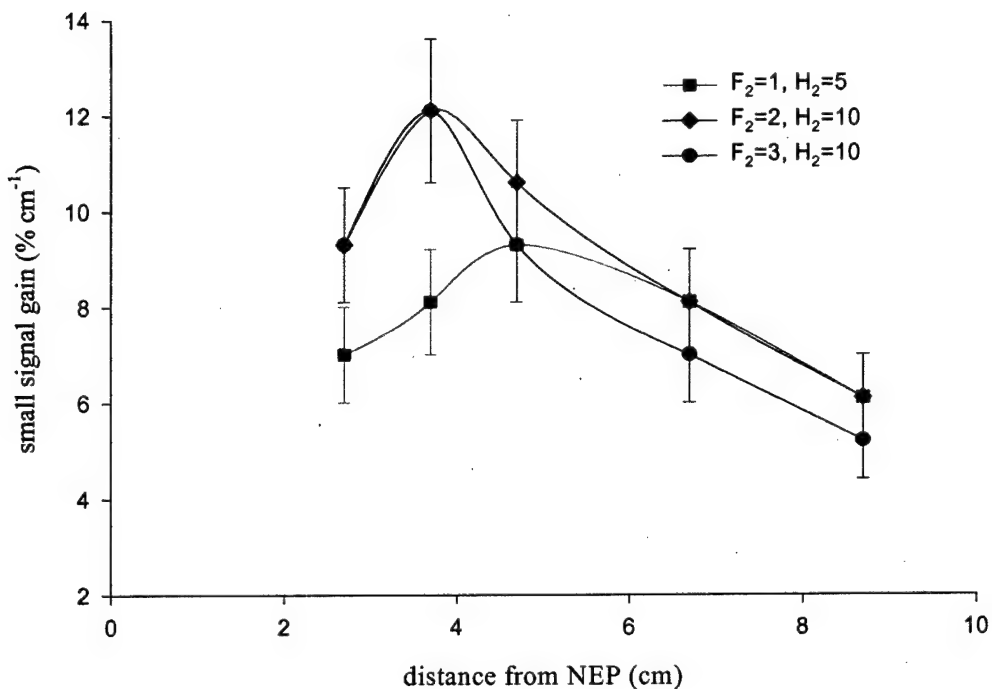


**Figure 5.95** Fundamental small signal gain determined from the I-Sat curves shown in Figures 5.89, 5.90 and 5.91 for the dominate threshold transition of the ( $F_2=1, H_2=5$ ), ( $F_2=2, H_2=10$ ) and ( $F_2=3, H_2=10$ ) flow conditions shown in Figures 5.92, 5.93 and 5.94. The dominant threshold transition is  $P3 \nu=2-1$  for the ( $F_2=1, H_2=5$ ) and ( $F_2=2, H_2=10$ ) flow conditions and  $P4 \nu=2-1$  for the ( $F_2=3, H_2=10$ ) flow conditions. Error bars represent a  $\pm 5\%$  uncertainty in the threshold outcoupler reflectivity.

A spatially uniform gain medium would lase on the lowest order spatial mode at threshold, which for a Gaussian beam is designated as  $TEM_{00}$  and lies along the optical axis (Verdeyen 1995). Under these conditions the small signal gain determined by the I-Sat curves would correspond to the gain at the vertical center and at the downstream location of the optical axis. However, the gain medium in this case is not uniform and the spatial mode that lases at threshold instead corresponds to the mode with the largest gain to loss ratio. This spatial mode is likely to include the region near the vertical peak gain. The gain determined from the I-Sat curves then corresponds to the average gain over this spatial mode. Figures 5.96, 5.97 and 5.98 show the measured fundamental small signal

gain for the  $(F_2=1, H_2=5)$ ,  $(F_2=2, H_2=10)$  and  $(F_2=3, H_2=10)$  flow conditions, respectively, along with the corresponding predicted centerline and peak small signal gain. Close to NEP, before the predicted peak gain reaches the vertical centerline, the measured gain in general for all three flow conditions lies between the predicted peak and centerline gains. The streamwise gain distribution downstream of the maximum measured gain also agrees well with the predictions for all three flow conditions. This suggests that the measured fundamental gain represents an average gain over a region that includes the peak and centerline gains upstream of the location where the peak gain reaches the centerline. Downstream of this location the measured fundamental small signal gain appears to approximate the centerline gain fairly well.

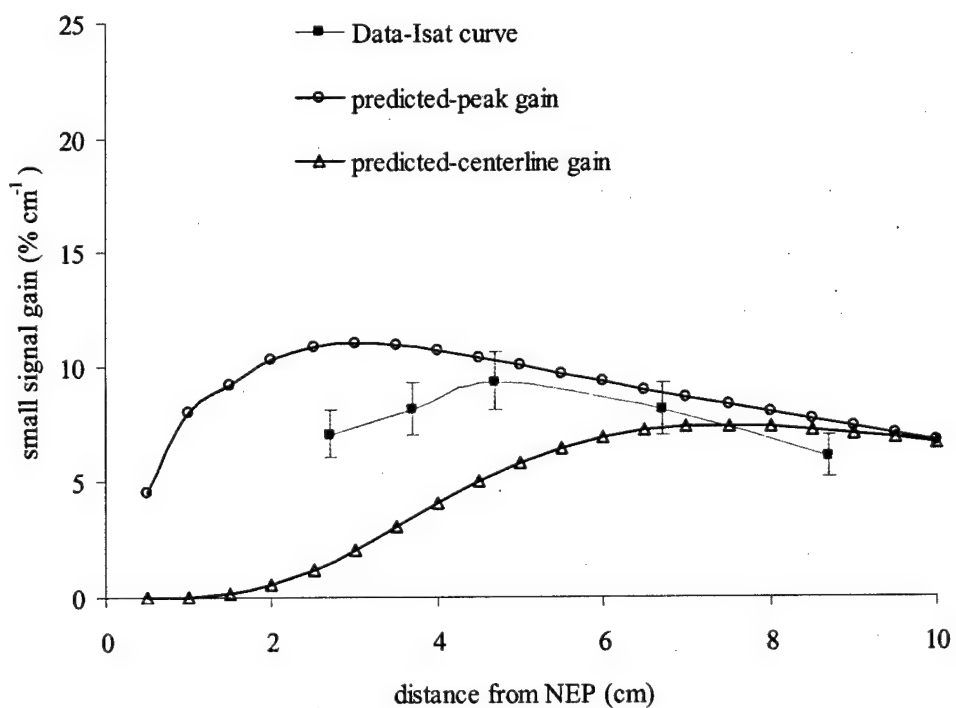


**Figure 5.96** Measured and predicted P3  $\nu=2-1$  fundamental small signal gain as a function of streamwise location for the  $(F_2=1, H_2=5)$  flow conditions.

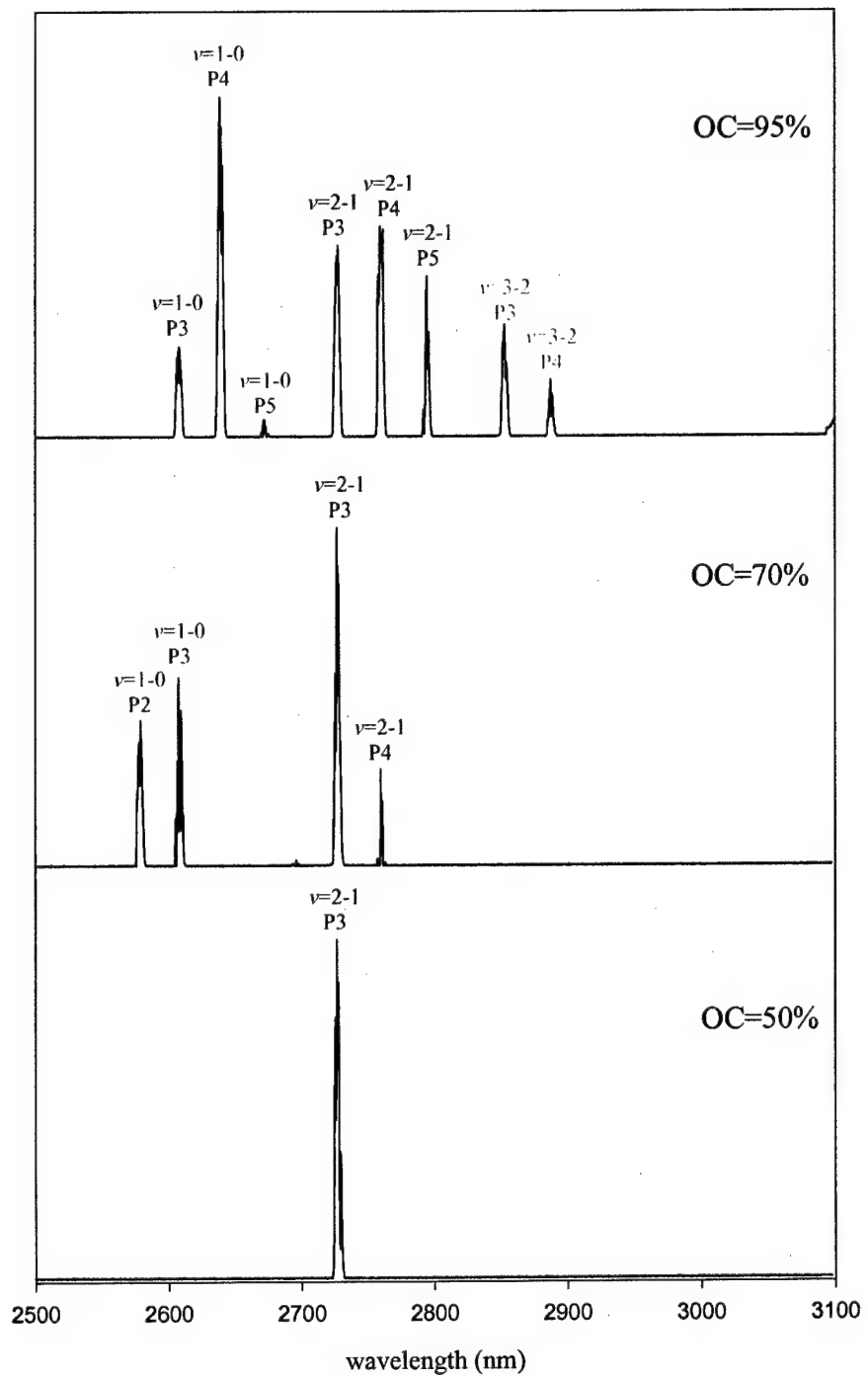


**Figure 5.92** Fundamental multi-lasing spectra for the ( $F_2=1$ ,  $H_2=5$ ) flow conditions at optical axis positions 4.7 cm downstream of the NEP for OC reflectivities of 95%, 70% and 50%. The intensity of each lasing line is scaled relative to the most intense line at each downstream location

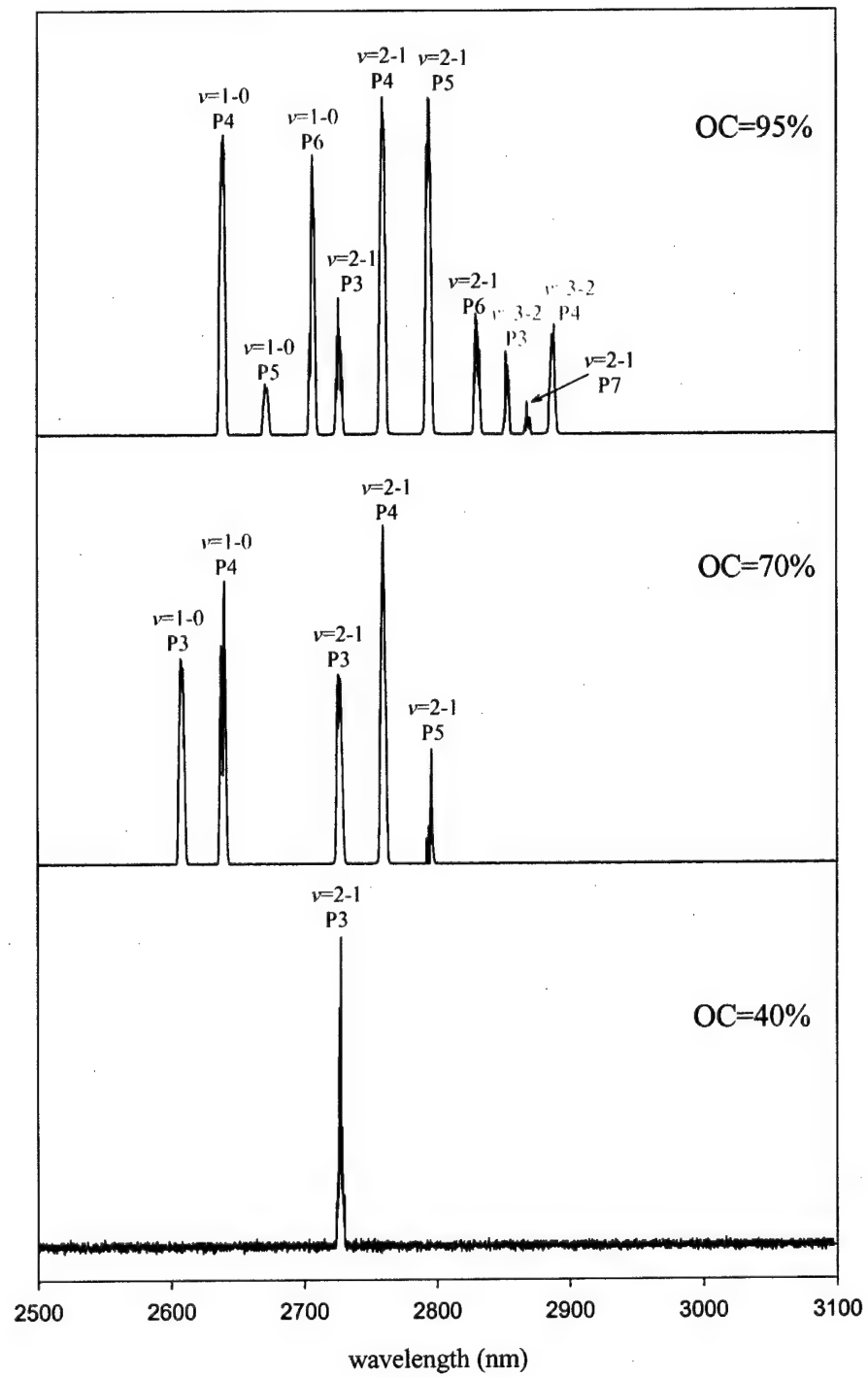


**Figure 5.93** Fundamental multi-lasing spectra for the ( $F_2=2$ ,  $H_2=10$ ) flow conditions at optical axis positions 4.7 cm downstream of the NEP for OC reflectivities of 95%, 70% and 50%. The intensity of each lasing line is scaled relative to the most intense line at each downstream location

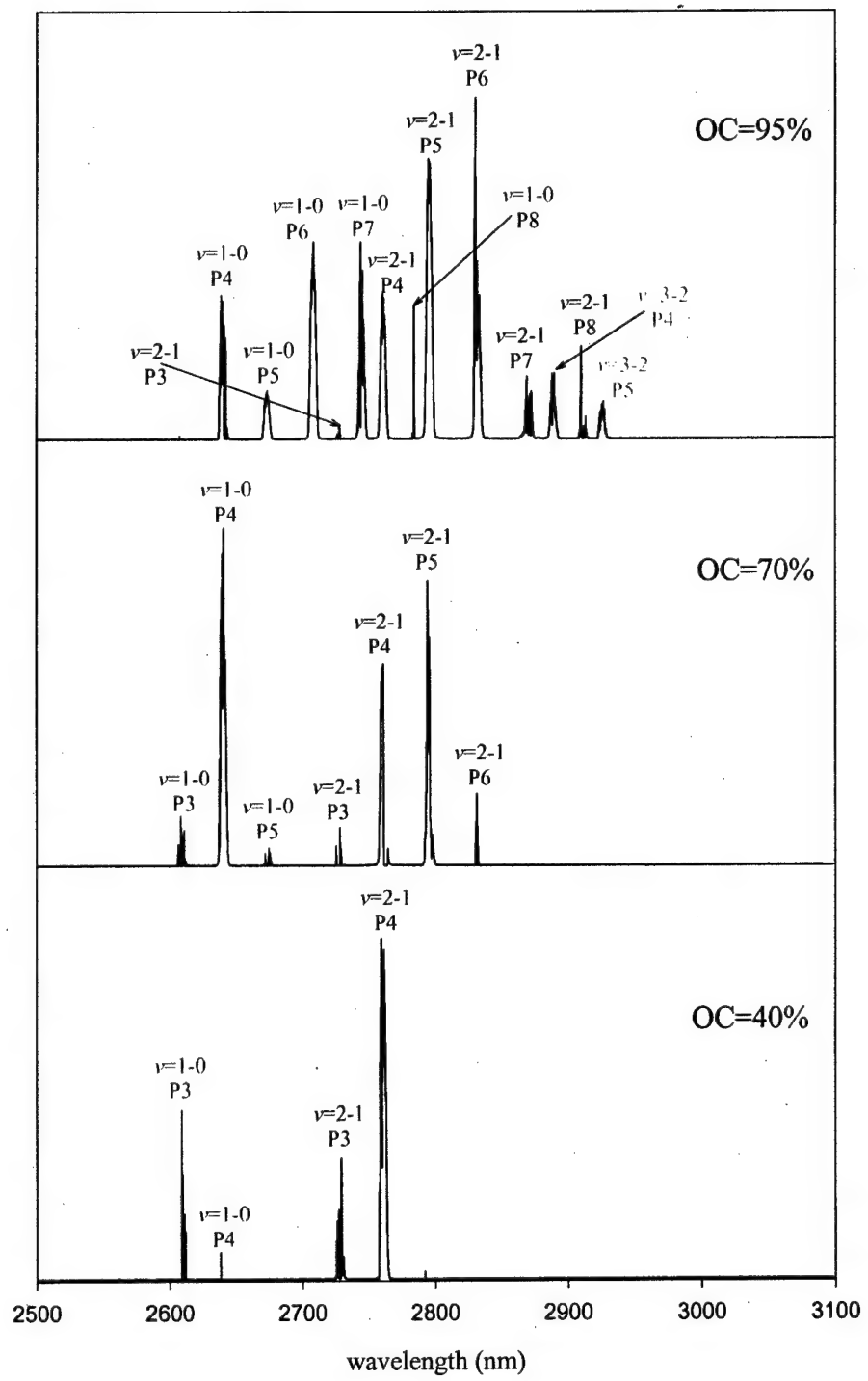


**Figure 5.94** Fundamental multi-lasing spectra for the ( $F_2=3$ ,  $H_2=10$ ) flow conditions at optical axis positions 4.7 cm downstream of the NEP for OC reflectivities of 95%, 70% and 50%. The intensity of each lasing line is scaled relative to the most intense line at each downstream location

conditions for  $R_1=95\%$  (Figure 5.92) compared to the P3  $\nu=2-1$  transition that dominates at threshold for  $R_1=50\%$ . This could be caused by the complex interaction that occurs between the stimulating radiation field and the populations of the various ro-vibrational energy levels under heavily saturated conditions. For instance, lasing on the P3  $\nu=2-1$  transition will add to the population of the  $\nu=1 J=3$  energy level thus increasing the gain of the P4  $\nu=1-0$  transition created by the cold pumping reaction. Subsequent redistribution of rotational levels within the vibrational bands through collisional processes may also play a role in determining the dominant lasing transition under saturated conditions.

Figure 5.95 shows the fundamental small signal gain for the dominant threshold transition as a function of streamwise location for the  $(F_2=1, H_2=5)$ ,  $(F_2=2, H_2=10)$  and  $(F_2=3, H_2=10)$  flow conditions. The maximum small signal gain for the  $(F_2=2, H_2=10)$  and  $(F_2=3, H_2=10)$  flow conditions is approximately  $12\% \text{ cm}^{-1}$  and occurs  $3.7 \text{ cm}$  downstream of the NEP. It should be noted that although these two flow conditions have the same maximum small signal gain they have different dominant threshold transitions. The maximum gain for the  $(F_2=1, H_2=5)$  flow conditions is approximately  $9\% \text{ cm}^{-1}$  and occurs  $4.7 \text{ cm}$  downstream of the NEP. These measurements are in good agreement with previous small signal gain measurements from similar devices (Sentman et al. 1999a; Sentman et al. 1999b). As expected these fundamental gains are about a factor of 100 greater than the measured overtone small signal gains. The general trends in the streamwise distribution of the fundamental gains between these three flow conditions compare well with the trends of the overtone gains shown in Figures 5.17 and 5.18.

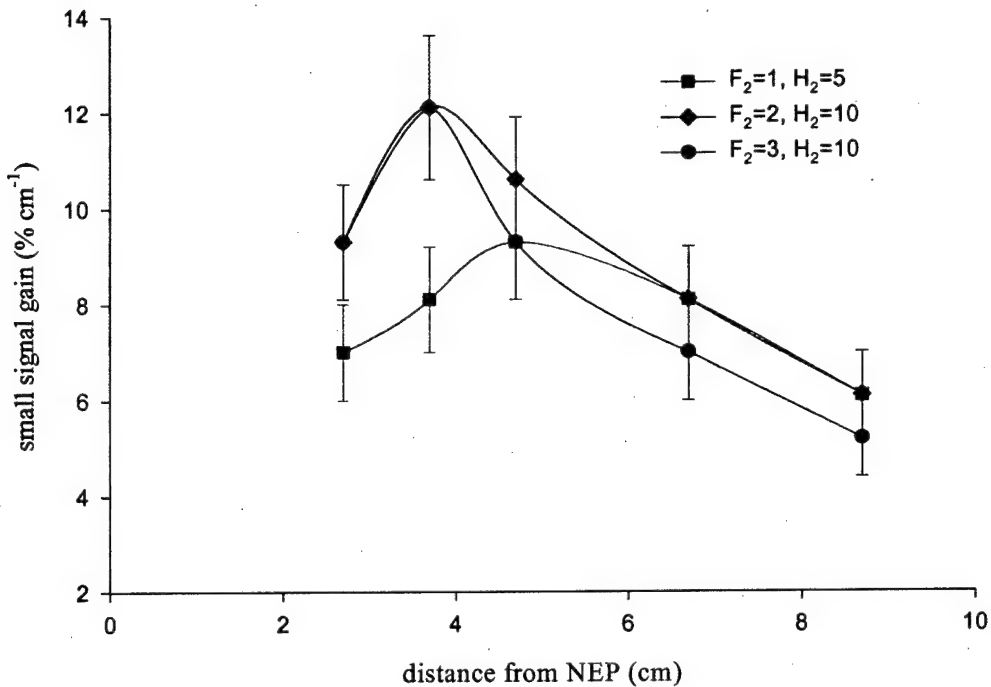


**Figure 5.95** Fundamental small signal gain determined from the I-Sat curves shown in Figures 5.89, 5.90 and 5.91 for the dominate threshold transition of the ( $F_2=1, H_2=5$ ), ( $F_2=2, H_2=10$ ) and ( $F_2=3, H_2=10$ ) flow conditions shown in Figures 5.92, 5.93 and 5.94. The dominant threshold transition is  $P3 \nu=2-1$  for the ( $F_2=1, H_2=5$ ) and ( $F_2=2, H_2=10$ ) flow conditions and  $P4 \nu=2-1$  for the ( $F_2=3, H_2=10$ ) flow conditions. Error bars represent a  $\pm 5\%$  uncertainty in the threshold outcoupler reflectivity.

However, it is difficult to determine from these figures whether the fundamental gain should be compared to the peak or centerline overtone gain.

A spatially uniform gain medium would lase on the lowest order spatial mode at threshold, which for a Gaussian beam is designated as  $TEM_{00}$  and lies along the optical axis (Verdeyen 1995). Under these conditions the small signal gain determined by the I-Sat curves would correspond to the gain at the vertical center and at the downstream location of the optical axis. However, the gain medium in this case is not uniform and the spatial mode that lases at threshold instead corresponds to the mode with the largest gain to loss ratio. This spatial mode is likely to include the region near the vertical peak gain.

The gain determined from the I-Sat curves then corresponds to the average gain over this spatial mode. Figures 5.96, 5.97 and 5.98 show the measured fundamental small signal gain for the ( $F_2=1$ ,  $H_2=5$ ), ( $F_2=2$ ,  $H_2=10$ ) and ( $F_2=3$ ,  $H_2=10$ ) flow conditions, respectively, along with the corresponding predicted centerline and peak small signal gain. Close to NEP, before the predicted peak gain reaches the vertical centerline, the measured gain in general for all three flow conditions lies between the predicted peak and centerline gains. The streamwise gain distribution downstream of the maximum measured gain also agrees well with the predictions for all three flow conditions. This suggests that the measured fundamental gain represents an average gain over a region that includes the peak and centerline gains upstream of the location where the peak gain reaches the centerline. Downstream of this location the measured fundamental small signal gain appears to approximate the centerline gain fairly well.

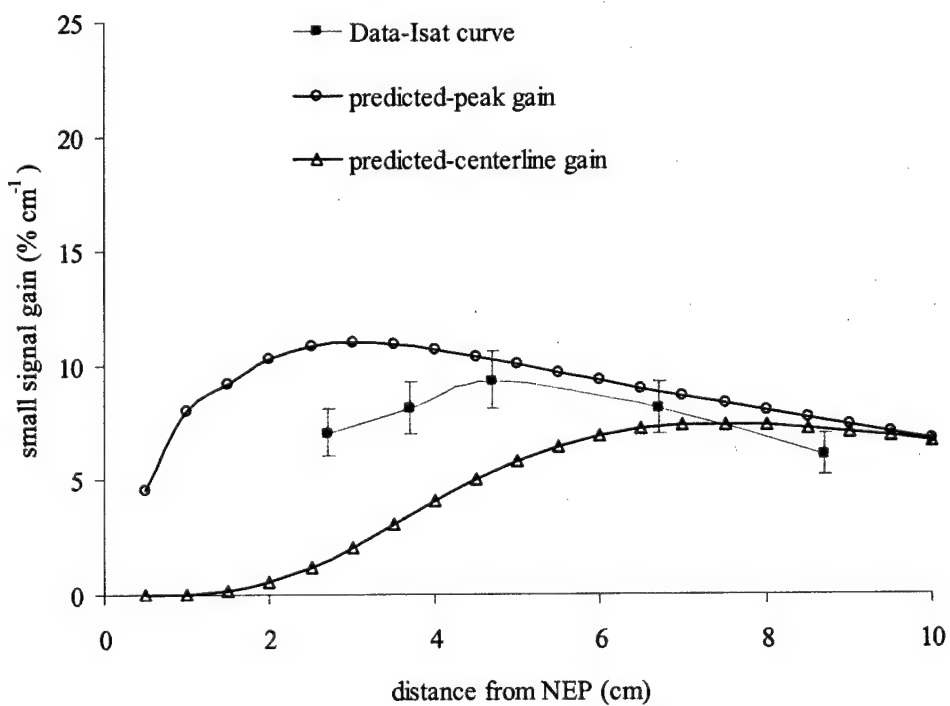


**Figure 5.96** Measured and predicted P3  $\nu=2-1$  fundamental small signal gain as a function of streamwise location for the ( $F_2=1$ ,  $H_2=5$ ) flow conditions.

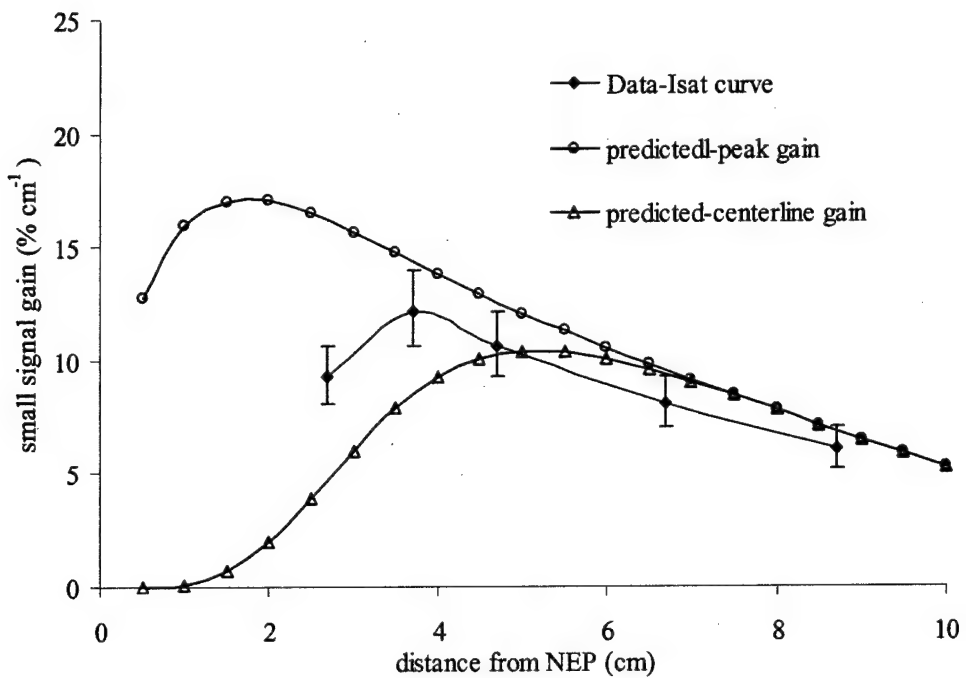


**Figure 5.97** Measured and predicted P3  $\nu=2-1$  fundamental small signal gain as a function of streamwise location for the ( $F_2=2$ ,  $H_2=10$ ) flow conditions.

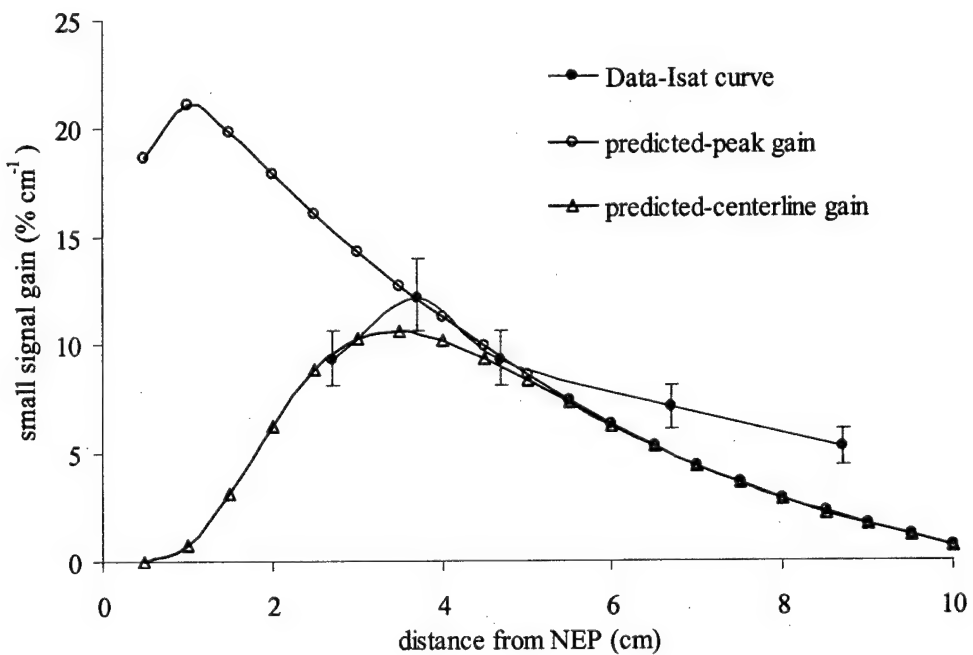


**Figure 5.98** Measured and predicted P4  $\nu=2-1$  fundamental small signal gain as a function of streamwise location for the ( $F_2=3$ ,  $H_2=10$ ) flow conditions.

Figures 5.99 and 5.100 show the predicted fundamental ( $P_3 \nu=2-1$ ) and overtone ( $P_3 \nu=2-0$ ) peak gain and centerline gain, respectively, for the ( $F_2=2$ ,  $H_2=10$ ) flow conditions. In these figures, each gain curve is normalized by its maximum. The computer code input parameters are the same as those used to achieve good agreement between the predicted overtone gain profiles in Section 5.4.4. The streamwise locations at which the maximum fundamental and overtone peak gains occur in Figure 5.99 are quite similar. The streamwise locations at which the maximum centerline gain occurs in Figure 5.100 are also quite similar. The streamwise distributions of the peak gain and centerline gain upstream of their maximum locations are also nearly identical. However, the gain distribution downstream of the maximum gain locations decreases significantly faster for the overtone gain than for the fundamental gain.

Downstream of the maximum gain location the V-V deactivation reactions begin to dominate the kinetics and work to redistribute the vibrational energy into a monotonically decreasing distribution according to Boltzmann statistics. Even at the extremely high vibrational temperatures ( $T_{vib} \sim 10,000$  K) created by the cold pumping reaction, the Boltzmann distribution places most of the HF population in the vibrational ground state ( $\nu=0$ ). This has a much more detrimental effect on the overtone ( $\nu=2-0$ ) population inversion than on the fundamental ( $\nu=2-1$ ) population inversion. Therefore, the difficulties encountered when attempting to extract optical energy from the gain medium using the fundamental transitions will be compounded when attempting to use the overtone transitions. HF lasers designed specifically to operate on the overtone transitions must take this into account. Particular consideration must be placed on mixing,

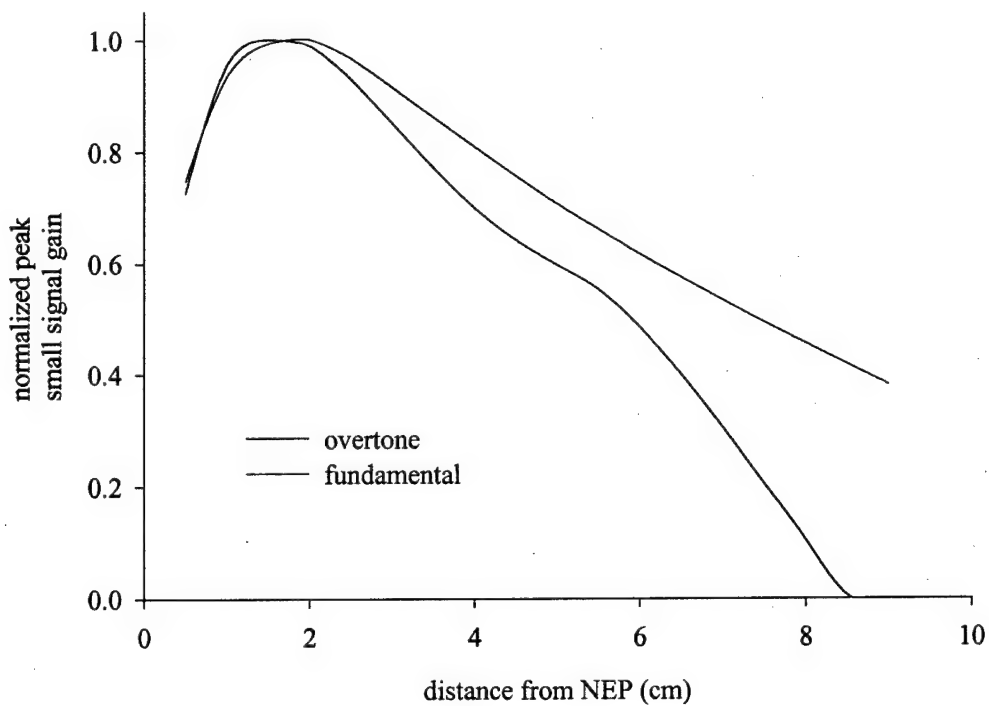


**Figure 5.99** Streamwise distribution of the predicted overtone (P3  $\nu=2-0$ ) and fundamental (P3  $\nu=2-1$ ) peak gain for the ( $F_2=2$ ,  $H_2=10$ ) flow conditions. Gains are normalized to their respective maximum peak values.

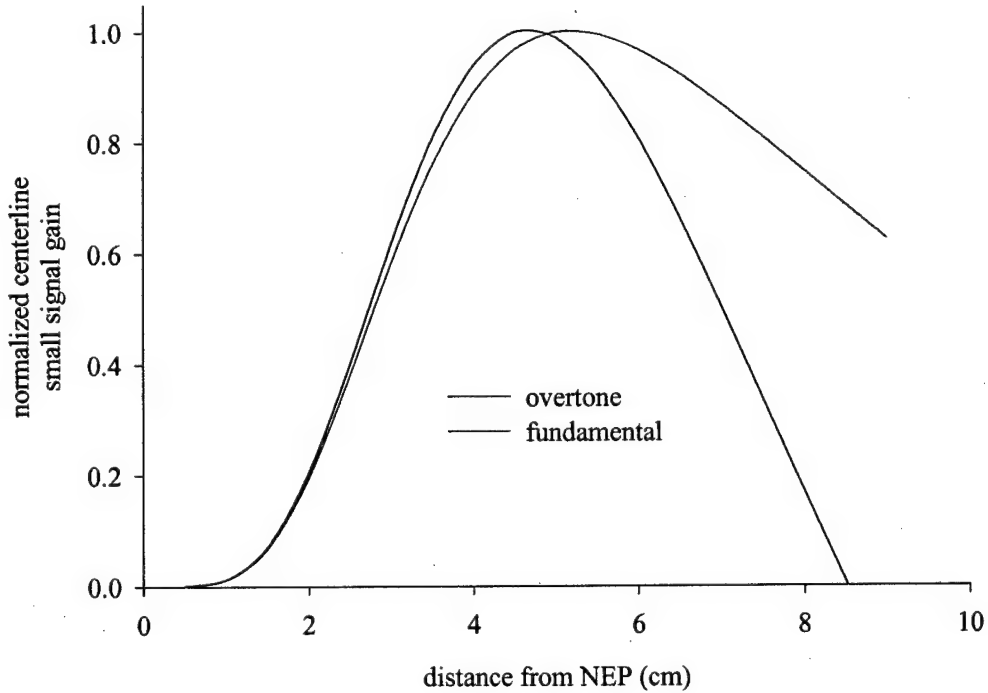


**Figure 5.100** Streamwise distribution of the predicted overtone (P3  $\nu=2-0$ ) and fundamental (P3  $\nu=2-1$ ) centerline gain for the ( $F_2=2$ ,  $H_2=10$ ) flow conditions. Gains are normalized to their respective maximum centerline values.

which is even more critical in the HF overtone laser than in the HF fundamental laser due to the shorter streamwise gain distribution. The faster deactivation of the overtone population inversion is also likely to drive the overtone laser designs to high Mach numbers and lower cavity pressures.

## 5.6 Saturated Gain

Throughout this thesis the assumption of rotational equilibrium has been made based on the recommendation of Manke and Hager's (2001) HF kinetics review that showed the rotational relaxation rate constants were orders of magnitude faster than the vibrational deactivation rate constants. The extremely fast rotational relaxation reactions enforce a Boltzmann distribution on the rotational levels within a given vibrational band maintaining equilibrium between the rotational and translational degrees of freedom. While this is undoubtedly the case under small signal gain conditions, questions remain about whether or not the rotational equilibrium assumption holds under saturated lasing conditions. In fact numerous reports over the years of HF laser research have grappled with this issue (Cohen et al. 1986; Kwok et al. 1985; Manke and Hager 2001; Mirels 1988). The Manke and Hager kinetics review did not consider HF rotational relaxation in an active chemical laser medium, where the stimulated emission processes could conceivably lead to a nonequilibrium rotational distribution, particularly if the stimulated emission lifetime is significantly shorter than the rotational relaxation lifetime.

The observation of multi-line lasing in a cw HF laser, as shown in Section 5.5, is the principal evidence that supports the presence of rotational nonequilibrium. Laser theory predicts that a spatially homogeneous gain medium with a simple Fabry-Perot resonator can only produce a single lasing line per inverted vibrational energy band if the rotational levels remain in a Boltzmann distribution while saturated (Verdeyen 1995). However, according to a well-documented review of the rotational nonequilibrium phenomenon by Cohen et al (1986), several factors could account for the observation of multiline lasing. For example, it has been postulated that if the spatial optical modes of

the laser do not fill the entire gain volume or if the HF laser medium is inhomogeneous (i.e., the laser has a non-uniform flow field), multi-line output could result. However, according to the HF laser modeling community, only models that include rotational nonequilibrium are able to reproduce multiline lasing (Cohen et al. 1986; Sentman 1975; Sentman et al. 1989a; Sentman et al. 1984; Skifstad and Chao 1975). In addition, models that allow rotational nonequilibrium are more successful at predicting HF laser performance than those that assume rotational equilibrium (Cohen et al. 1986; Sentman 1975).

Unfortunately, the models used to reach these conclusions include some important caveats and limitations that reduce their ability to decisively demonstrate the presence (or absence) of rotational nonequilibrium. For example, Sentman and co-workers (1975; 1977) have published computational results which (though state of the art at the time) claimed that rotational nonequilibrium is the only way to reproduce multiline lasing in a CFD model. Additional theoretical and experimental work from Sentman's laboratory examines the role of time dependent oscillations in a cw HF laser that uses an unstable resonator (Sentman 1978; Sentman et al. 1985). Again, they found that the incorporation of rotational nonequilibrium was essential to predict and model the oscillations they observed in their chemical laser flows. Notably, they showed that "the amplitude of the fluctuation was determined by the fraction of the resonator filled by the saturated gain zone of the oscillating line and the frequency of the oscillation was determined by the resonator magnification." (Sentman 1978; Sentman et al. 1989a; Sentman et al. 1985) However, many of these models assumed a constant temperature, premixed flow. Obviously, these approximations deviate significantly from the characteristics of real HF

lasers. In addition, some of the calculations used a Fabry-Perot resonator model to extract the laser energy. In the work reported here a stable resonator is used that couples all regions of the flow in the optical cavity through the symmetry axis that is coincident with the optical axis. The coupled regions may have significant variations in local density and temperature. In fact the measurements of Section 5.3 show conclusively that an HF laser flow field may be highly inhomogeneous in the vertical and streamwise directions. The magnitude and location of gain was determined by mixing and local temperature variations on the order of 50 – 100 K were found in the flow. Even larger temperature and density gradients may exist in larger scale, high Mach number, combustion driven HF lasers. It is not clear that the conclusions and predictions of previous modeling work that assume a constant temperature, premixed flow are applicable to real HF laser experiments where the flow is anything but homogeneous. It is also unclear that the conclusions and predictions based on Fabry-Perot and confocal unstable resonator designs are applicable to our stable resonator laser.

Finally, all of the previous modeling work has been performed with kinetic models that include erroneous or out-of-date rate constants for many important processes. Most important to the present case are the values used for the state-to-state rotational relaxation rate constants. In lieu of actual measurements (which were published between 1981 – 1989, 5 – 15 years after some of the initial work on this subject (Copeland and Crim 1983; Copeland and Crim 1984; Copeland et al. 1981; Haugen et al. 1984; Taatjes and Leone 1988; Taatjes and Leone 1991) investigators have made various approximations in an effort to estimate the multitude of state-to-state rotational relaxation rate constants necessary to produce and support a rotational nonequilibrium model that

tracks each HF(v,J) state independently (Hough and Kerber 1975; Sentman 1975; Sentman 1977; Skifstad and Chao 1975). In all cases, the approximation is essentially a variation of the exponential energy gap model developed by Polanyi and Woodall (Polanyi and Sloan 1972). Crim, Leone, and others, however, have shown that the scaling laws that rely solely on energy gap arguments underestimate the rotational relaxation rate constants for high J levels by more than 2 orders of magnitude (Copeland and Crim 1984; Haugen et al. 1984) in some applications. Improved predictions of rotational relaxation rate constants generally require scaling relations that are based on the energy corrected sudden approximation (DePristo et al. 1979; DePristo and Rabitz 1979) or other methods which include effects related to scattering theory. At least one theoretical treatment of Crim's and Leone's rotational relaxation data predicts very large rate constants ( $k \geq 10^{-10} \text{ cm}^3 \text{ molecule}^{-1} \text{ s}^{-1}$ ), even for  $v = 2, J = 20$  (Bollati et al. 1985; Bollati et al. 1988). Additional updates to the HF laser kinetics model that post-date most modeling work have been described in detail elsewhere (Manke and Hager 2001).

Figure 5.101 shows the P1, P2, P3, P4 and P5  $v=2-0$  overtone gain under small signal conditions and while lasing on the fundamental transitions with an outcoupler mirror reflectance,  $R_1=80\%$  (Manke et al. 2003). All of this data was collected with the probe beam directed at a slight angle along the optical axis 2.7 cm downstream of the NEP and approximately 3.0 mm above the vertical centerline for the ( $F_2=2, H_2=10$ ) flow conditions. With  $R_1=80\%$  and the optical axis 2.7 cm downstream of the NEP the laser produced 36 W of power with the fundamental multi-line spectrum shown in Figure 5.102. Outcoupling fundamental power lowered the gain on the P3 transition from a

small signal value of  $0.14\% \text{ cm}^{-1}$  to  $0.026\% \text{ cm}^{-1}$ . This 80% drop in gain indicates a high level of saturation

and represents a significant change to the populations of the  $v=2$  and  $v=0$  energy levels.

The gain of an individual ro-vibrational transition,  $\gamma(v)$  is defined as:

$$\gamma_{u \rightarrow l}(v_o) = \sigma_{u \rightarrow l}(v_o) \left[ P_{Ju} N_u - \frac{g_u}{g_l} P_{Jl} N_l \right] \quad (5.5)$$

where  $\sigma(v)$  is the stimulated emission cross section,  $g_u$  and  $g_l$  are the degeneracies of the upper and lower energy states,  $N_u$  and  $N_l$  are the populations of the upper and lower vibrational states and  $P_{Ju}$  and  $P_{Jl}$  are fractional populations of individual ro-vibrational

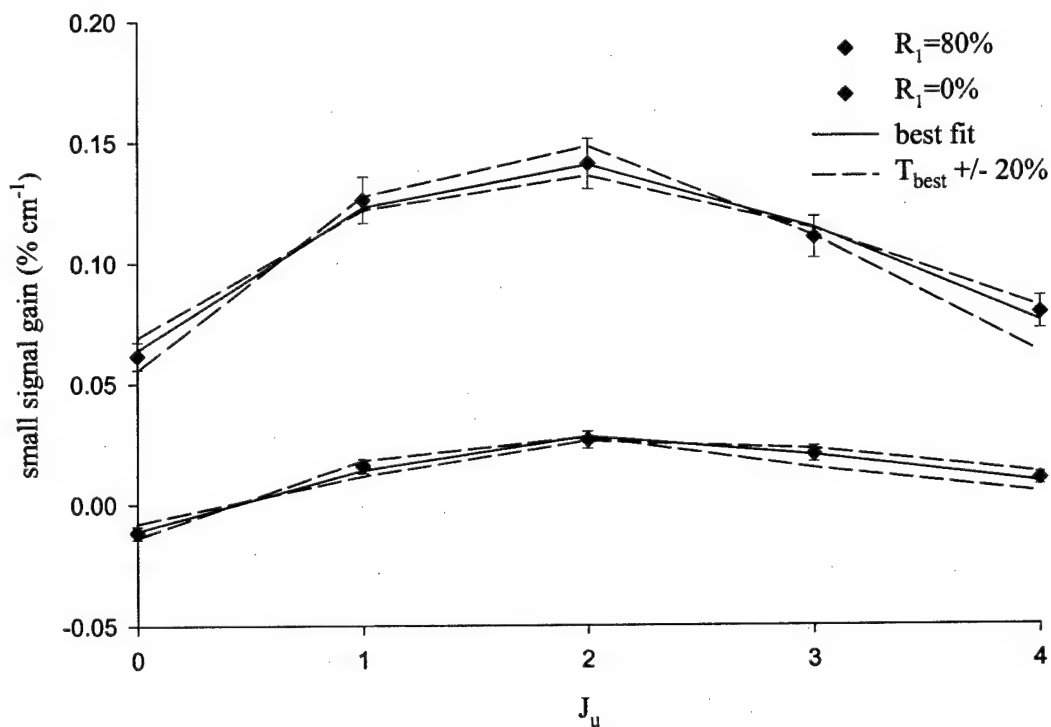


**Figure 5.101** P1, P2, P3, P4 and P5  $v=2-0$  overtone gain distribution under small signal gain conditions ( $R_1=0\%$ ) and saturated conditions ( $R_1=80\%$ ). Data was taken 2.7 cm downstream of the NEP and 3.0 mm above the vertical centerline for the ( $F_2=2$ ,  $H_2=10$ ) flow conditions. The solid curves represent a least squares curve fit to a rotational equilibrium gain distribution with corresponding temperatures of 277 K and 164 K for  $R_1=0$  and 80%, respectively. The dashed lines represent curve fits while holding the temperature fixed at  $\pm 20\%$  of the temperature determined from the least squares fit.

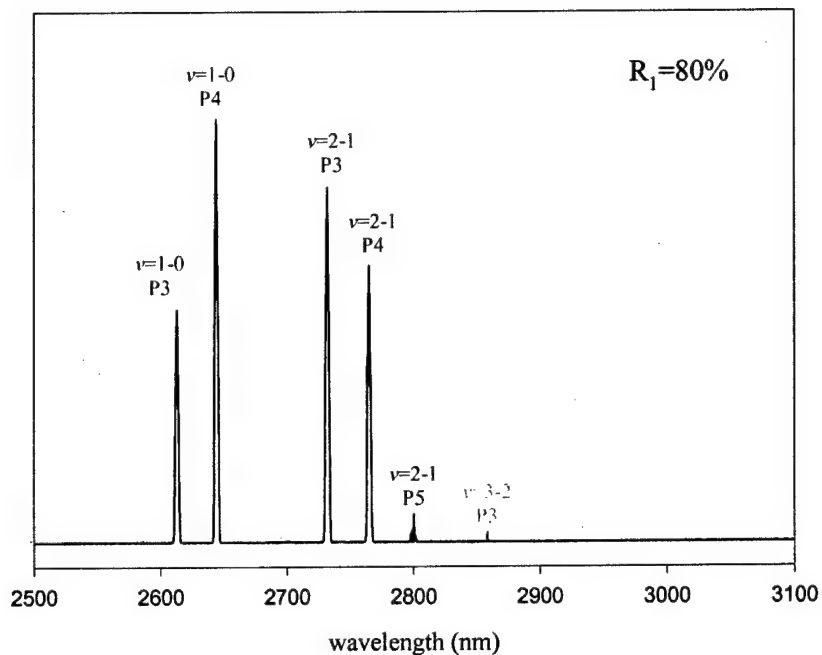


**Figure 5.102** Fundamental output beam spectrum for the ( $F_2=2$ ,  $H_2=10$ ) flow conditions with optical axis positioned 2.7 cm downstream of the NEP for  $R_1=80\%$ .

states in the upper and lower vibrational levels, respectively. For rotational equilibrium to hold, the rotational levels within the upper and lower vibrational manifolds must be populated according to Boltzmann statistics:

$$P_J = \frac{g e^{\frac{-B_J g}{kT}}}{Q_{rot}(T)} \quad (5.6)$$

where  $Q_{rot}(T)$  is the temperature dependent rotational partition function of the upper or lower vibrational energy levels. Substituting Equation (5.6) into Equation (5.5) gives a expression for the transitional gain distribution in terms of the upper and lower vibrational populations and the temperature:

$$\gamma_{u \rightarrow l}(v_o) = \sigma_{u \rightarrow l}(v_o) \left[ \frac{g_u e^{\frac{-B_v g_u}{kT}}}{Q_{rot}(T)} N_u - g_u \frac{e^{\frac{-B_v g_l}{kT}}}{Q_{rot}(T)} N_l \right] \quad (5.7)$$

If the rotational energy levels within the upper and lower vibrational manifolds are in equilibrium then all the overtone gains shown in Figure 5.101 should be described by Equation (5.7) with the same values for  $N_u$ ,  $N_l$  and  $T$ . The solid curves in Figure 5.101 represent least squares fits of the P(1) – P(5) experimental overtone gain data using Equation (5.7). The curve fits show excellent agreement with the overtone gain data and predict temperatures of 277 and 164 K for the  $R_1=0$  and 80% cases, respectively. The ability to apply a single temperature Boltzmann or equilibrium distribution to the overtone gain data both with and without the presence of laser oscillation on the fundamental band suggests that the  $v = 2$  and  $v = 0$  manifolds are in rotational equilibrium. If a simulated gain distribution with a perfect equilibrium rotational distribution is perturbed by as little as  $\pm 25\%$  on a single line, attempts to fit the data to Equation (5.7) will fail. However, since the curve fit values of  $N_u$ ,  $N_l$  and  $T$  are not unique (i.e., several combinations of  $N_u$ ,  $N_l$  and  $T$  will give good fits), this method is not well suited for precise determinations of the temperature. Hence, the estimated error bars for the temperatures derived from fitting the data with Equation (5.7) are large ( $\pm 20\%$ ). The dashed lines in Figure (5.101) represent curve fits using Equation (5.7) while holding the temperature fixed at  $\pm 20\%$  of the temperature determined from the least squares fit.

The temperatures determined from the lineshape analyses of the individual ro-vibrational gains and the temperature determined from curve fitting Equation (5.7) to the rotational gain distributions are summarized in Table 5.9 and shown in Figure 5.103 for

several OC reflectivities. The upper and lower vibrational level populations determined from the curve fits are also listed in Table 5.9. The translational temperature is given by the average value from the 5 observed lines with error bars of  $\pm 1$  standard deviation. The rotational temperature indicates the temperature that gave the best fit with Equation (5.7) with an estimated error of  $\pm 20\%$ . The error of the temperature determined from the lineshape analysis increases significantly as the OC reflectivity increases due to the significant drop in overtone gain caused by the higher saturation condition. The translation and rotational temperatures are in fairly good agreement at all OC reflectivities and show a general trend of decreasing temperature as OC reflectivity increases.

While the present results make a persuasive case for rotational equilibrium in this cw supersonic HF laser flow, the fundamental question concerning the origin of multi-line lasing remains unanswered. In the limit of infinitely fast rotational relaxation, the output of a molecular laser should be limited to a single ro-vibrational transition per vibrational band. The combination of "slow" stimulated emission and "fast" rotational relaxation should produce a steady state condition where the entire ro-vibrational

**Table 5.9** Results of lineshape and saturated gain data analysis.

Outcoupler Reflectivity (%)	$T_{\text{trans}}$ (K) <sup>a</sup>	$T_{\text{rot}}$ (K) <sup>b</sup>	$[\text{HF}(v = 2)]^b$ ( $\times 10^{14} \text{ cm}^{-3}$ )	$[\text{HF}(v = 0)]^b$ ( $\times 10^{14} \text{ cm}^{-3}$ )
0	$287 \pm 14$	$277 \pm 55$	4.7	2.2
50	$188 \pm 50$	$177 \pm 35$	2.8	2.6
60	$229 \pm 18$	$214 \pm 43$	2.3	0.9
70	$206 \pm 29$	$163 \pm 33$	1.7	1.3
80	$173 \pm 45$	$164 \pm 33$	1.1	1.7
90	$223 \pm 100^c$	$144 \pm 29^c$	0.1	0.7

<sup>a</sup> Average value with 1 standard deviation from lineshape analysis of 5 observed lines.

<sup>b</sup> Best fit to saturated gain data, see Figure 5.101. Error bars are  $\pm 20\%$ .

<sup>c</sup> The 90% outcoupler data was extremely weak and only 3 lines were analyzed.

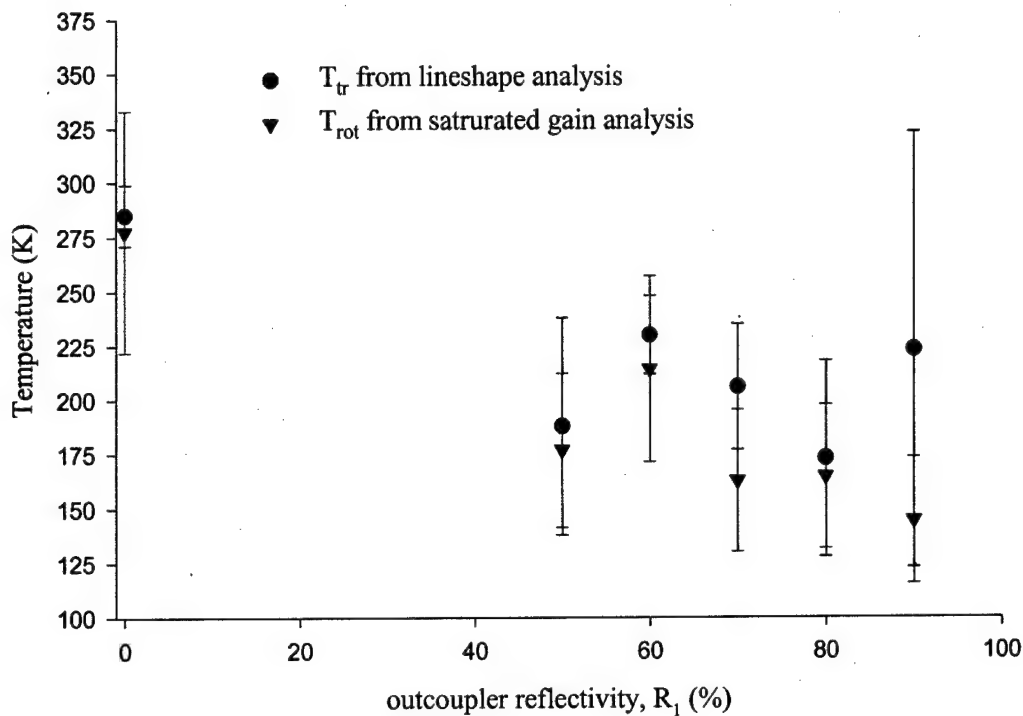


**Figure 5.103** Temperature as a function of OC reflectivity for the ( $F_2=2$ ,  $H_2=10$ ) flow conditions 2.7 cm downstream of the NEP and 3.0 mm above the vertical centerline. Graphical representation of results presented in Table 5.9.

manifold of a given vibrational band is drained via stimulated emission through the transition with the highest gain. This is rigorously true for devices with completely homogeneous gain media and lasers with Fabry-Perot resonators, where communication between upstream and downstream regions of the flow does not occur. According to this model only a change in the gas temperature, which changes the most populated rotational state, is able to change the active laser line.

In fact, it has been suggested that temperature gradients and local inhomogeneities in the gas phase medium region defined by the laser resonator could be responsible for the multiline output of HF lasers (Cohen et al. 1986). This hypothesis is somewhat

problematic because a very large temperature gradient is required to account for the diversity of HF laser lines observed. For example, in the  $v = 2$  vibrational level the Boltzmann distribution is at its maximum of  $J = 2$  for a wide temperature range of  $T = 50$  – 210 K. A single quantum change to a peak population in  $J = 3$  is reasonable since  $220 < T < 500$  is necessary. Small variations or perturbations from the equilibrium distribution may contribute to some of the spectral diversity that is observed. However, the observation of P(6) lines is puzzling given that temperatures in excess of 900 K are necessary to make  $J = 5$  the most populated rotational state in  $v = 2$  and there is no evidence for such a high temperature in our device.

Finally, care must be taken when applying the results of this section, which were specifically derived for a small-scale experimental HF laser, to the flow conditions of a large-scale combustor-driven device. Large-scale devices are likely to have significantly higher gain, temperature and concentration gradients. In addition, longer path length devices that use nozzle banks could have significantly shorter stimulated emission lifetimes than the device investigated here. A shorter stimulated emission lifetime could alter the apparent balance between rotational relaxation and stimulated emission discovered here and change the saturation dynamics within the laser flow field.

## Chapter 6

### Conclusions

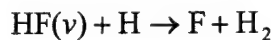
The overtone small signal gain measurements made in this investigation of a small-scale supersonic HF laser show that the gain distribution is highly inhomogeneous in both the vertical and streamwise directions. The inhomogeneity is the result of inefficient mixing between the fuel ( $H_2$ ) and oxidizer (F atom) flow streams created by a combination of nozzle injection geometry and laser cavity flow properties. The shallow  $H_2$  injection angle limits the penetration of the near field reaction zone while the low cavity density and corresponding low Reynolds number result in a highly viscous flow field in which molecular diffusion is the dominant mixing mechanism.

Large increases in  $H_2$  injection flow rate and excess  $F_2$  flow in the laser cavity appear to have only minor effects on the streamwise gain distribution. The most significant increases in gain come from increases in F atom concentration, which were limited in this test series by discharge tube performance. Large increases in overtone gain can therefore be expected for high pressure combustor-driven lasers which eliminate much, if not all, of the primary He diluent flow. The HF absorption measured in the base relief region means there is a significant amount of recirculating HF and may indicate that the base relief region is too large for this low concentration system. Reducing or even eliminating the size of the base purge region would reduce the amount of absorbing molecules in the optical beam path and could prove very beneficial, particularly for nozzle bank laser systems.

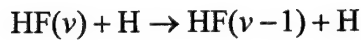
Premixed computer modeling predictions of this HF laser system have shown that the flow system kinetics are dominated by the cold pumping reaction and the HF V-V

energy transfer reactions. All other reactions appear to play a minor role in the predicted streamwise gain distribution for these flow conditions. Unfortunately, large uncertainty in the V-V energy transfer reaction rate constants creates large uncertainty in the predicted gain. The need for reliable V-V rate constants to the HF laser modeling community is paramount. However, constructing an experiment that isolates individual HF V-V reactions with anything other than the ground state is nearly impossible. The V-V rate constants for two vibrationally excited HF molecules are therefore likely to remain the result of extrapolation from a limited number of measured HF( $v$ ) + HF(0) rate constants.

Another major question that remains regarding HF laser kinetics is choosing between the two competing theories concerning the principal reaction path for the reaction of H atoms with vibrationally excited HF for  $v \geq 3$ . The theory of Bartoszek et al (1978) states that the principal reaction path is reactive quenching which creates H<sub>2</sub> and F atom through the reverse cold pumping reaction:



However, Bott and Heidner (1977) attribute the loss of HF( $v \geq 3$ ) to the deactivation reaction:



Since the reported rate constant of the deactivation reaction for  $v = 3$  is larger than the cold pumping reaction into  $v = 3$ , this reaction in essence takes all the HF( $v = 3$ ) created by the cold pumping reaction and places it into HF( $v = 2$ ). The inclusion of the deactivation reaction in the 2-D computer model used in this investigation raised the predicted overtone small signal gain by approximately 25%. To resolve this conflict, Dr.

Heidner (2003) suggests a re-evaluation of the data presented in his original paper using the latest updates of the cold pumping reaction rate constant and equilibrium constant. A new experimental investigation in which both the creation of HF( $\nu = 3$ ) and loss of HF( $\nu = 2$ ) would also be useful.

Inclusion of a k- $\epsilon$  turbulence model in the 2-D computational fluid dynamics code has an insignificant effect on the predicted streamwise gain distribution at the vertical peak gain location but does have a noticeable effect on the predicted gain at the vertical centerline. The small mixing enhancement produced by introducing turbulence into the highly viscous flow field slightly increases the predicted F atom utilization. This modest increase in F atom utilization does however produce a significant increase in the maximum vertically averaged gain. The level of turbulence in the actual laser flow field is unknown. However this computational exercise did show the beneficial effect even small increases in mixing can have on laser performance and that there is likely a large number of unreacted F atoms in the flow far downstream of the NEP.

The results of comparisons between two separate modeling injection schemes (i.e., imesh=2 and imesh=3) and the measured gain profiles indicate that the injected H<sub>2</sub> flow stream is surrounded on both sides by F atoms from the primary laser flow. The F atoms are presumably transported from the region near the vertical centerline to the region between the injected H<sub>2</sub> flow stream and the nozzle wall by large-scale vortex structures created by the H<sub>2</sub> injection dynamics. The complex injection dynamics are modeled by merely re-distributing the F atom flow at the NEP which appears to adequately predict the near and far field vertical gain profiles. This suggest that the large-scale vortex structures dominate the near field mixing, where they are modeled in a

very crude way, but their dominance diminishes in the far field where no modeling attempt is made. The F atom re-distribution results in an additional reaction zone on the side of the H<sub>2</sub> flow stream away from the vertical centerline, which increases the F atom utilization and the maximum vertically averaged gain. Increasing the injection angle of the H<sub>2</sub> jet with respect to the nozzle wall might increase vortex strength providing better mixing and consequently higher F atom utilization and higher average gain. However, the corresponding loss of streamwise momentum caused by the increased injection angle would lower the Mach number and compress the streamwise gain distribution making power extraction more difficult.

The 2-D computer model used to help interpret the measurements consistently overpredicted the overtone gain. Several input parameters were systematically changed in an effort to discover which parameters had the most significant effect on the predicted gain. The results of this exercise showed that increasing the HF V-V energy transfer rate constants was the only computer model input parameter that reduced the predicted gain to the level of the measurements while maintaining the proper streamwise gain distribution trends. A factor of 3.25 increase in all the HF V-V rate constants decreased the predicted maximum small signal gain by almost 60%. This is a relatively small change for a rate constant, particularly for one that has not been experimentally determined, that illustrates the sensitivity of the overtone gain to V-V energy transfer. The fact that the 2-D code predicts the general streamwise trends of the flow field fairly well indicates that the flow field can reasonably be considered two-dimensional and that molecular diffusion is the dominant mixing mechanism in the laser cavity. The biggest benefit of employing a 3-D computer code would likely be in the modeling of the highly three-dimensional injection

process. However, even with a fully elliptic 3-D CFD code, the magnitude of the predicted gain will still only be as good as the rate constants used to represent the chemical kinetics of the system.

There are two main conclusions to all of the data-model comparisons performed in this thesis. The first is that mechanisms influencing reactant mixing (i.e., turbulence and large-scale vortex structures) have a profound effect on the gain averaged in the vertical direction but an insignificant effect on the maximum system gain or the peak gain at a particular streamwise location. Effective mixing increases F atom utilization by quickly transporting fuel to the vertical centerline thereby producing a more homogeneous gain medium. The second main conclusion is that the maximum gain of the laser system is dominated by the system chemical kinetics. The kinetics are defined by the reaction rate constants and reactant concentrations. Therefore

to achieve higher peak gains the system must be operated at higher reactant concentrations and higher pressures. However, the resulting higher HF( $\nu$ ) concentrations will also increase the rate of reaction for the V-V energy transfer reactions, which will compress the streamwise gain distribution. High gain systems therefore require high Mach number nozzles with small throat sizes that have represented serious engineering challenges in the development of fundamental HF laser systems. Development of high gain overtone laser systems is likely to further complicate these engineering challenges. This is because the Boltzmann distribution enforced on the initially inverted vibrational energy levels by V-V energy transfer has a much more detrimental effect on the overtone ( $\nu = 2-0$ ) population inversion than on the fundamental ( $\nu = 2-1$ ) population inversion. This will compress the streamwise gain distribution even more and drive HF overtone

nozzle designs to higher Mach numbers with small throat sizes and increase the importance of reactant mixing.

Finally, the distribution of rotational states in the main flow of a small-scale HF laser has been measured directly for a variety of conditions. In all cases, the distribution appeared to be Boltzmann. These observations challenge the conventional view that HF lasers are characterized by nonequilibrium distributions among rotational levels. It is clear that resolution of the occurrence of multi-line lasing in supersonic HF lasers requires further study. Experimentally, a particularly useful measurement would be to spatially resolve the small signal gain (fundamental and/or overtone) in the streamwise direction, within the region defined by the resonator, while the laser is operating. This could be accomplished by passing the gain probe beam through the laser cavity orthogonal to both the laser optical axis and the streamwise axis. This type of measurement would be critically dependent upon adequate purging of the base region to remove adventitious ground state absorption. In the presence of a laser cavity extracting energy from the flow, a substantial temperature change or large, highly localized, inhomogeneities should be observed. It would also be interesting to observe how the output spectra are affected by extracting power from the laser cavity with an optical aperture that eliminates the base purge region from the active lasing medium. On the computational front, time-dependent 3-D models should be employed to assess the likelihood, magnitude, and effect of large temperature gradients in supersonic chemical HF laser flow fields. However, the inclusion of a multi-line lasing model in a fully 3-D elliptical computational fluid dynamics code represent a serious challenge to the model community.

## References

- 1) Airey, J. R., and McKay, S. F. (1969). "A Supersonic Mixing Chemical Laser." *Appl. Phys. Lett.*, 15(12), 401.
- 2) Arunan, E., Setser, D. W., and Ogilvie, J. F. (1992). "Vibration-Rotational Einstein Coefficients for HF/DF and HCl/DCl." *J. Chem. Phys.*, 97(3), 1734 - 1741.
- 3) Bartoszek, F. E., Manos, D. M., and Polanyi, J. C. (1978). "Effect of Changing Reagent Energy. X. Vibrational Threshold Energies for Alternative Reaction Paths HF(v) + D --> F + HD and --> H + DF." *J. Chem. Phys.*, 69(2), 933 - 935.
- 4) Bashkin, A. S., Igoshin, V. I., Leonov, Y. S., Oraevskii, A. N., and Porodinkov, O. E. (1977). "An Investigation of a Chemical Laser Emitting Due to an Overtone of the HF Molecule." *Sov. J. Quantum Electron.*, 7(5), 626 - 627.
- 5) Basov, N. G., Kulakov, L. V., Markin, E. P., Nikitin, A. I., and Oraevsky, A. N. (1969). "Emission Spectrum of a Chemical Laser Using an H<sub>2</sub> + F<sub>2</sub> Mixture." *JETP Lett.*, 9, 375.
- 6) Batovskii, O. M., Vasil'ev, G. K., Makarov, E. F., and Tal'rose, V. L. (1969). "Chemical Laser Operating on Branched Chain Reaction of Fluorine with Hydrogen." *JETP Lett.*, 9, 200.
- 7) Baulch, D. L., Duxbury, J., Grant, S. J., and Montague, D. C. (1981). "Homogeneous Gas Phase Reactions of Halogen- and Cyanide- Containing Species." *J. Phys. Chem. Ref. Data*, 10(suppl. 1).
- 8) Benedict, R. P. (1983). Fundamentals of Gas Dynamics, Wiley, New York, 185-189.
- 9) Bird, R. B., Stewart, W. E., and Lightfoot, E. N. (1960). Transport Phenomena, Wiley, New York, 569-572.
- 10) Blanchard, J. N., Brunet, Y., and Merlen, A. (1999). "Influence of a Counter Rotating Vortex Pair on the Stability of a Jet in a Crossflow: An Experimental Study by Flow Visualization." *Exper. in Fluids*, 26, 63-74.
- 11) Bollati, L. A., Arguello, G. A., and Staricco, E. H. (1985). "Dependence on Vibrational Excitation of Energy Transfer Processes for HF(v,J) + HF(v = 0)." *J. Chem. Phys.*, 83(11), 6050 - 6052.
- 12) Bollati, L. A., Arguello, G. A., and Staricco, E. H. (1988). "HF Autorelaxation in V = 1 and V = 2." *J. Chem. Soc. Faraday Trans. 2*, 84(6), 599 - 609.
- 13) Bott, J. F., and Heidner, R. F., III. (1977). "The Vibrational Deactivation of HF(V = 3) and HF(V = 2) by H Atoms." *J. Chem. Phys.*, 66(7), 2878 - 2882.

- 14) Bott, J. F., and Heidner, R. F., III. (1978). "Kinetic Study of H + HF(V = 3): Kinetic Isotope Effect and Temperature Dependence." *J. Chem. Phys.*, 68(4), 1708 - 1714.
- 15) Buggeln, R. C., Shamroth, S., Lampson, A. I., and Crowell, P. G. (1994) "Three-Dimensional (3-D) Navier-Stokes Analysis of the Mixing and Power Extraction in a Supersonic Oxygen Iodine Laser (COIL) with Transverse I<sub>2</sub> Injection.", AIAA Paper 94-2435.
- 16) Camussi, R., and Stella, A. (2002). "Experimental Study of a Jet in a Crossflow at Very Low Reynolds Number." *J. Fluid Mech.*, 454, 113-144.
- 17) Carroll, D. L., Sentman, L. H., Theodoropoulos, P. T., Waldo, R. E., and Gordon, S. J. (1993). "Experimental Study of Continuous Wave Hydrogen-Fluoride Chemical Laser Overtone Performance." *AIAA J.*, 31(4), 693 - 700.
- 18) Cengel, Y. A., and Boles, M. A. (1994). *Thermodynamics: An Engineering Approach*, McGraw-Hill, New York, 784-787.
- 19) Chase, M. W., Jr. (1998). "JANAF Thermochemical Tables." *J. Phys. Chem. Ref. Data*, 14(S1), 1099.
- 20) Chou, S. I., Baer, D. S., and Hanson, R. K. (1999a). "Diode Laser Measurements of He-, Ar-, and N<sub>2</sub>-Broadened HF Lineshapes in the First Overtone Band." *J. Mol. Spectrosc.*, 196, 70-76.
- 21) Chou, S. I., Baer, D. S., and Hanson, R. K. (1999b). "Spectral Intensity and Lineshape Measurements in the First Overtone Band of HF Using Tunable Diode Lasers." *J. Mol. Spectrosc.*, 195, 123-131.
- 22) Cohen, N., and Bott, J. F. (1976). "Ch.2 Kinetics of Hydrogen-Halide Chemical Lasers", *Handbook of Chemical Lasers*, R. W. F. Gross and J. F. Bott, eds., Wiley, New York.
- 23) Cohen, N., and Bott, J. F. (1982). "Review of Rate Data for Reactions of Interest in HF and DF Lasers." *SD-TR-82-86*, The Aerospace Corporation.
- 24) Cohen, N., Bott, J. F., Kwok, M. A., and Wilkins, R. L. (1986). "The Status of Rotational Nonequilibrium in HF Chemical Lasers." *SD-TR-86-26*, The Aerospace Corporation.
- 25) Copeland, R. A., and Crim, F. F. (1983). "Rotational Energy Transfer in HF(v = 2): Double Resonance Measurements and Fitting Law Analysis." *J. Chem. Phys.*, 78(9), 5551 - 5563.
- 26) Copeland, R. A., and Crim, F. F. (1984). "Rotational Energy Transfer in HF(v = 2): Energy Corrected Sudden Approximation Scaling Relations Applied to Double Resonance Measurements." *J. Chem. Phys.*, 81(12), 5819 - 5829.

27) Copeland, R. A., Pearson, D. J., and Crim, F. F. (1981). "Laser Double Resonance Measurements of Rotational Energy Transfer Rates in HF(v = 2)." *Chem. Phys. Lett.*, 81(3), 541 - 546.

28) Crowell, P. G. (1983). "Laminar Mixing between Chemically Reacting Parallel Streams of Excited Oxygen and Iodine for an Exact Multicomponent Diffusion Model." 83-A/K-14-0.1984, R&D Associates.

29) Crowell, P. G. (1987). "The Effective Binary Diffusion Model." 87-A/K-3-02-165, RDA Logicon.

30) Crowell, P. G. (1989). "A Vorticity-Stream Function Approach to Calculating Three-Dimensional Mixing for Viscous Parabolic Flows." 87-A/K-03-02-1125, R&D Associates.

31) Crowell, P. G. (2002). "2-D Aerokinetic Mixing Model (HFDFMIX) for HF/DF Chemical Laser Analysis." *Contract F29601-00-D-0202*, Air Force Research Laboratory.

32) Demtroder, W. (1982). *Laser Spectroscopy*, Springer-Verlag, New York, 79-100.

33) DePristo, A. E., Augustin, S. D., Ramaswamy, R., and Rabitz, H. (1979). "Quantum Number and Energy Scaling for Nonreactive Collisions." *J. Chem. Phys.*, 71, 850.

34) DePristo, A. E., and Rabitz, H. (1979). "A Scaling Theoretical Analysis of Vibrational Relaxation Experiments: Rotational Effects and Long-Range Collisions." *Chem. Phys.*, 44, 171.

35) Deutsch, T. F. (1967). "Molecular Laser Action in Hydrogen and Deuterium Halides." *Appl. Phys. Lett.*, 10(8), 234.

36) Duncan, W., Holloman, M., Rogers, B., and Patterson, S. (1989) "Hydrogen Fluoride Overtone Chemical Laser Technology." AIAA Paper-89-1903.

37) Duncan, W., Patterson, S., Graves, B., and Holloman, M. (1991) "Recent Progress in Hydrogen Fluoride Overtone Chemical Lasers." AIAA Paper-91-1480.

38) Duncan, W. A., Patterson, S. P., Holloman, M. E., and Sollee, J. L. (1990) "Progress in Hydrogen Fluoride Overtone Chemical Lasers." *International Conference on Lasers 1990*, 661 - 669.

39) Dunning, T. H. (1976). "The Low-Lying States of Hydrogen Fluoride: Potential Energy Curves for the  $X^1\sigma^+$ ,  $^3\sigma^+$ ,  $^3\pi$ , and  $^1\pi$  States." *J. Chem. Phys.*, 65, 3854.

40) Eppard, W. M., McGrory, W. D., Godfrey, A. G., Cliff, E. M., and Borggaard, J. T. (2000) "Recent Advances in Numerical Techniques for the Design and Analysis of COIL Systems.", AIAA Paper 2000-2576.

- 41) Fric, T. F., and Roshko, A. (1994). "Vortical Structure in the Wake of a Transverse Jet." *J. Fluid Mech.*, 279, 1-47.
- 42) Givi, P., Madnia, C. K., Steinberger, C. J., Carpenter, M. H., and Drummond, J. P. (1991). "Effects of Compressibility and Heat Release in a High Speed Reacting Mixing Layer." *Comb. Sci. Tech.*, 78, 33-67.
- 43) Grosh, G., and Emanuel, G. (1976). "Ch.5 Gas Dynamics of Supersonic Mixing Lasers." *Handbook of Chemical Lasers*, R. W. F. Gross and J. F. Bott, eds., Wiley, New York.
- 44) Gross, R. W. F., Cohen, N., and Jacobs, T. A. (1968). "HF Chemical Laser Produced by Flash Photolysis of F<sub>2</sub>O-H<sub>2</sub> Mixtures." *J. Chem. Phys.*, 48(8), 3821-3822.
- 45) Gross, R. W. F., Giedt, R. R., and Jacobs, T. A. (1969). "Stimulated Emission Behind Overdriven Detonation Waves in F<sub>2</sub>O-H<sub>2</sub> Mixtures." *J. Chem. Phys.*, 51(3), 1250.
- 46) Gruber, M. R., Nejad, A. S., Chen, T. H., and Dutton, J. C. (1997). "Compressibility Effects in Supersonic Transverse Injection Flowfields." *Phys. Fluids*, 9(5), 1448-1461.
- 47) Hager, G. D., Helms, C. A., Truesdell, K. A., Plummer, D., Erkkila, J., and Crowell, P. (1996). "A Simplified Analytic Model for Gain Saturation and Power Extraction in the Flowing Chemical Oxygen-Iodine Laser." *IEEE J. Quant. Elect.*, 32(9), 1525-1536.
- 48) Han, J., Heaven, M. C., and Manke, G. C., II. (2002). "Hydrogen Atom Reactions with Molecular Halogens: The Rate Constants for H + F<sub>2</sub> and H + Cl<sub>2</sub> at 298k." *J. Phys. Chem. A*, submitted.
- 49) Haugen, H. K., Pence, W. H., and Leone, S. R. (1984). "Infrared Double Resonance Spectroscopy of V-T,R Relaxation of HF(v = 1): Direct Measurement of High-J Populations." *J. Chem. Phys.*, 80(5), 1839 - 1852.
- 50) Hecht, J. (1993). "Chemical-Lasers Offer Infrared Power and Tunability." *Laser Focus World*, 29(12), 91.
- 51) Heidner, R. F., III. (2003). Personal Communication.
- 52) Herbelin, J. M., Henshaw, T. L., Rafferty, B. D., Anderson, B. T., Tate, R. F., Madden, T. J., Manke, G. C., II, and Hager, G. D. (1999). "The Measurement of Gain on the 1.315  $\mu$ m Transition of Atomic Iodine in a Subsonic Flow of Chemically Generated NCl(A<sup>1</sup> $\delta$ )."*Chem. Phys. Lett.*, 299(6), 583-588.
- 53) Hirschfelder, J. O., Curtiss, C. F., and Bird, R. B. (1954). *Molecular Theory of Gases and Liquids*, Wiley, New York, 516-517.

54) Hollas, J. M. (1998). High Resolution Spectroscopy, 2<sup>nd</sup> Ed, Wiley, Chichester, 33-38, 39-43, 159-170.

55) Hollo, S. D., McDaniel, J. C., and Hartfield, R. J. (1994). "Quantitative Investigation of Compressible Mixing: Staged Transverse Injection into Mach 2 Flow." *AIAA J.*, 32(3), 528-534.

56) Hon, J. F., and Novak, J. R. (1975). "Chemically Pumped Hydrogen Fluoride Overtone Laser." *IEEE J. Quant. Elect.*, QE-11, 698 - 699.

57) Hough, J. J. T., and Kerber, R. L. (1975). "Effect of Cavity Transients and Rotational Relaxation on the Performance of Pulsed HF Chemical Lasers: A Theoretical Investigation." *Appl. Optics*, 14(12), 2960 - 2970.

58) Jeffers, W. Q. (1988). "Short Wavelength Chemical Lasers." *AIAA J.*, 27(1), 64 - 66.

59) Kiernan, V. (2001). "Lasers Play a Key Role in Missile-Defense Program." *Laser Focus World*, 37(9), 58-59.

60) Kompa, K. L., and Pimentel, G. C. (1967). "Hydrofluoric Acid Chemical Laser." *J. Chem. Phys.*, 47, 857-858.

61) Kwok, M. A., Wilkins, R. L., Segal, G. I., Cross, E. F., Ueunten, R. H., and Foster, K. L. (1985). "In Search of High J States in the HF(v,J) System." *SD-TR-85-21*, The Aerospace Corporation.

62) Launder, B. E., and Sharma, B. I. (1974). "Application of Energy Dissipation Model of Turbulence to the Calculation of Flow near a Spinning Disk." *Lett. Heat Mass Trans.*, 1, 131-138.

63) Levine, I. N. (1975). Molecular Spectroscopy, Wiley, New York, 25-27, 56-63, 114-122, 142-162.

64) Lowe, J. P. (1993). Quantum Chemistry, Academic Press, San Diego, 19-23.

65) Madden, T. J. (1997). "Laminar Mixing between Chemically Reacting Parallel Streams of Excited Oxygen and Iodine for an Exact Multicomponent Diffusion Model," Ph.D. Dissertation, University of Illinois, Urbana-Champaign.

66) Manke, G. C., II. (2002). "Procedure for Extracting Temperature and Concentration from Measured Spectral Lineshapes." Internal Document, Air Force Research Laboratory, Directed Energy Directorate, Kirtland Air Force Base, Albuquerque, New Mexico.

67) Manke, G. C., II, and Hager, G. D. (2001). "A Review of Recent Experiments and Calculations Relevant to the Kinetics of the HF Laser." *J. Phys. Chem. Ref. Data*, 30(3), 713 - 733.

68) Manke, G. C., II, Henshaw, T. L., Madden, T. J., Herbelin, J. M., Rafferty, B. D., and Hager, G. D. (2001). "Characterizing Fluorine and Chlorine Atom Flow Rates Using Iodine Atom Spectrometry." *AIAA J.*, 39(3), 447 - 454.

69) Manke, G. C., II, Hewett, K. B., Wisniewski, C. F., Truman, C. R., and Hager, G. D. (2003). "On the Presence of Rotational Nonequilibrium in a Supersonic HF Laser." *IEEE J. Quant. Elect.*, submitted.

70) McQuarrie, D. A., and Simon, J. D. (1997). *Physical Chemistry: A Molecular Approach*, University Science Books, Sausalito, 157-189, 495-500, 693-700.

71) Mirels, H. (1988). "Effects of Translational and Rotational Nonequilibrium on cw Chemical Laser Performance." *SD-TR-88-40*, The Aerospace Corporation.

72) Nikolaev, V. D., Zagidullin, M. V., Svistun, M. I., Anderson, B. T., Tate, R. F., and Hager, G. D. (2000). "Results of Small Signal Gain Measurements on a Supersonic COIL with an Advanced Nozzle Bank." *IEEE J. Quant. Elect.*, 38(5), 421-428.

73) Parker, J. H., and Pimentel, G. C. (1968). "Hydrogen Fluoride Chemical Laser Emission through Hydrogen-Atom Abstraction from Hydrocarbons." *J. Chem. Phys.*, 48, 5273-5274.

74) Perry, R. H., and Green, D. W. (1997). "Ch.10 Transport and Storage of Fluids." *Perry's Chemical Engineer's Handbook*, McGraw-Hill, New York.

75) Pimentel, G. C., and Kompa, K. L. (1976). "Ch.1 What Is a Chemical Laser? An Introduction", *Handbook of Chemical Lasers*, R. W. F. Gross and J. F. Bott, eds., Wiley, New York.

76) Polanyi, J. C., and Sloan, J. J. (1972). "Energy Distribution among Reaction Products. Vii.  $H + F_2$ ." *J. Chem. Phys.*, 57, 4988 - 4998.

77) Ramshaw, J. D., and Dukowicz, J. K. (1979). "Apache: A Generalized Mesh Eulerian Computer Code for Multicomponent Chemically Reactive Fluid Flow." *LA-7427*, Los Alamos National Laboratory, Los Alamos, NM.

78) Rigrod, W. W. (1965). "Saturation Effects in High-Gain Lasers." *J. Appl. Phys.*, 36(8), 2487 - 2490.

79) Schetz, J. A., and Billig, F. S. (1966). "Penetration of Gaseous Jets Injected into a Supersonic Stream." *J of Spacecraft and Rockets*, 3(11), 1658-1665.

80) Schmidt, T. (1996). "Technical Data for Critical Flow Nozzles." Flow-Dyne Engineering, Inc., Fort Worth, Texas.

81) Sentman, L. H. (1975). "Rotational Nonequilibrium in cw Chemical Lasers." *J. Chem. Phys.*, 62(9), 3523 - 3537.

82) Sentman, L. H. (1977). "Rotational Relaxation of HF." *J. Chem. Phys.*, 67(3), 966 - 969.

83) Sentman, L. H. (1978). "Chemical Laser Power Spectral Performance: A Coupled Fluid Dynamic, Kinetic, and Physical Optics Model." *Appl. Optics*, 17, 2244-2249.

84) Sentman, L. H., Carroll, D. L., and Gilmore, J. (1989a). "Modeling cw HF Fundamental and Overtone Lasers." *AIAA Paper 89-1904*.

85) Sentman, L. H., Eyre, A. J., Cassibry, J. T., and Wootton, B. P. (1999a). "Studies of cw HF Chemical Laser Performance." *AAE TR 99-01, UILU-ENG 99-0501*, University of Illinois.

86) Sentman, L. H., Eyre, A. J., Wootton, B. P., and Cassibry, J. T. (1999b). "Comparison of cw HF Laser Performance for Several Nozzles." *AIAA Paper 99-3469*.

87) Sentman, L. H., Nayfeh, M. H., Renzoni, P., King, K., Townsend, S., and Tsoulos, G. (1984). "Saturation Effects in a Continuous Wave HF Chemical Laser." *AIAA J.*, 23(9), 1392 - 1401.

88) Sentman, L. H., Nayfeh, M. H., Townsend, S. W., King, K., Tsoulos, G., and Bichanich, J. (1985). "Time Dependent Oscillations in a cw Chemical Laser Unstable Resonator." *Appl. Optics*, 24, 3598-3609.

89) Sentman, L. H., Theodoropoulos, P. T., Nguyen, T., Carroll, D. L., and Waldo, R. E. (1989b) "An Economical Supersonic cw HF Laser Testbed." *AIAA Paper 89-1898*.

90) Sentman, L. H., Theodoropoulos, P. T., Waldo, R. E., Nguyen, T., and Snipes, R. (1987). "An Experimental Study of cw HF Chemical Laser Amplifier Performance and Zero Power Gain." Aeronautical and Astronautical Engineering Department, University of Illinois at Urbana-Champaign, Urbana.

91) Skifstad, J. G., and Chao, C. M. (1975). "Rotational Relaxation in a Line-Selected Continuous HF Chemical Laser." *Appl. Optics*, 14(7), 1713 - 1718.

92) Smith, B. A., and Wall, R. (2000). "THEL Laser Kills Short-Range Missile." *Aviation Week & Space Technology*, 152(24), 33.

93) Spencer, D. J., Jacobs, T. A., Mirels, H., and Gross, R. W. F. (1969). "Continuous-Wave Chemical Laser." *Int. J. Chem. Kinet.*, 1, 493-494.

94) Steinfeld, J. I., Francisco, J. S., and Hase, W. L. (1989). Chemical Kinetics and Dynamics, Prentice Hall, Englewood Cliffs, 1-17, 225-231, 293-297.

95) Taatjes, C. A., and Leone, S. R. (1988). "Laser Double-Resonance Measurements of Rotational Relaxation Rates of HF( $J = 13$ ) with Rare Gases, H<sub>2</sub>, and D<sub>2</sub>." *J. Chem. Phys.*, 89(1), 302 - 308.

96) Taatjes, C. A., and Leone, S. R. (1991). "Laser Double-Resonance Studies of Low-Temperature Rotational and Vibrational Relaxation of HF: Rates for HF( $J = 13$ ) + HF from 225 to 298 K and Detection of HF( $v = 1$ ) Deactivation by HF Clusters at 210 - 240 K." *J. Phys. Chem.*, 95, 5870 - 5877.

97) Tate, R. F., Hunt, B. S., Helms, C. A., Truesdell, K. A., and Hager, G. D. (1995). "Spatial Gain Measurements in a Chemical Oxygen Iodine Laser (COIL)." *IEEE J. Quant. Elect.*, 31(9), 1632 - 1636.

98) Tennekes, H., and Lumley, J. L. (1972). *A First Course in Turbulence*, MIT Press, Cambridge, 1-25, 127-129.

99) VanLerberghe, W. M., Santiago, J. G., Dutton, J. C., and Lucht, R. P. (1999). "Mixing of a Sonic Transverse Jet Injected into a Supersonic Flow." *AIAA J.*, 38(3), 470-479.

100) Vasiliev, A. A., Bezmelnitsyn, V. N., Sinianski, V. F., and Chaivanov, B. B. (1999). "Rate Constant for Heterogeneous Dissociation of Fluorine in a Temperature Range of 700 - 900 K on a Nickel Surface." *J. Fluorine Chem.*, 95, 153 - 159.

101) Verdeyen, J. T. (1995). *Laser Electronics*, Prentice Hall, Englewood Cliffs, 172-206.

102) Ward, J., Cooper, J., and Smith, E. W. (1974). "Correlation Effects in the Theory of Combined Doppler and Pressure Broadening - I. Classical Theory." *J. Quant. Spectrosc. Radiat. Transfer*, 14, 555 - 590.

103) White, F. M. (1991). *Viscous Fluid Flow*, McGraw-Hill, New York, 77-78, 227-230, 253-254, 335-349, 358-359.

104) Wilkins, R. L. (1977). "Vibration-Rotation Bands of HF and DF." *SAMSO-TR-77-198*, The Aerospace Corporation, El Segundo.

105) Wisniewski, C. F., Hewett, K. B., Manke, G. C., II, Crowell, P., Truman, C. R., and Hager, G. D. (2003a). "Small Signal Gain Measurements in a Small Scale HF Overtone Laser." *Appl. Phys. A*, 77, 337-342.

106) Wisniewski, C. F., Hewett, K. B., Manke, G. C., II, Truman, C. R., and Hager, G. D. (2003b). "Non-Intrusive Mach Number Measurement in Supersonic Hydrogen Fluoride Laser." *Chem. Phys. Lett.*, 371, 522 - 527.

107) Wisniewski, C. F., Hewett, K. B., Manke II, G. C., Truman, C. R., and Hager, G. D. (2003c). "Direct Measurements of Fluorine Atom Concentration, Gain Length and Small Signal Gain in an Hydrogen Flouride Overtone Laser." *Chem. Phys. Lett.*, 370, 591-596.

108) Wollmann, G. (2003). "Directed Energy Weapons: Fact or Fiction." *Military Technology*, 27(4), 80-85.

109) Wurzberg, E., and Houston, P. L. (1980). "The Temperature Dependence of Hydrogen Abstraction Reactions: F + HCl, F + HBr, F + DBr, and F + HI." *J. Chem. Phys.*, 72(11), 5915 - 5923.

110) Yardley, J. T. (1980). Introduction to Molecular Energy Transfer, Academic Press, New York, 82-127, 130-170.